
**Observation of multiple-muon
seasonal variations in the
NO ν A Near Detector**



Stefano Castro Tognini

PHYSICS PH.D. PROGRAM
INSTITUTE OF PHYSICS
FEDERAL UNIVERSITY OF GOIAS

Thesis presented as a partial fulfillment of the requirements for the degree of

Doctor in Physics

GOIÂNIA

2018

**TERMO DE CIÊNCIA E DE AUTORIZAÇÃO PARA DISPONIBILIZAR VERSÕES ELETRÔNICAS
DE TESES E
DISSERTAÇÕES NA BIBLIOTECA DIGITAL DA UFG**

Na qualidade de titular dos direitos de autor, autorizo a Universidade Federal de Goiás (UFG) a disponibilizar, gratuitamente, por meio da Biblioteca Digital de Teses e Dissertações (BDTD/UFG), regulamentada pela Resolução CEPEC nº 832/2007, sem ressarcimento dos direitos autorais, de acordo com a Lei nº 9610/98, o documento conforme permissões assinaladas abaixo, para fins de leitura, impressão e/ou *download*, a título de divulgação da produção científica brasileira, a partir desta data.

1. Identificação do material bibliográfico: Dissertação Tese

2. Identificação da Tese ou Dissertação:

Nome completo do autor: Stefano Castro Tognini

Título do trabalho: Observation of multiple-muon seasonal variations in the NOVA Near Detector

3. Informações de acesso ao documento:

Concorda com a liberação total do documento SIM NÃO¹

Havendo concordância com a disponibilização eletrônica, torna-se imprescindível o envio do(s) arquivo(s) em formato digital PDF da tese ou dissertação.


Assinatura do(a) autor(a)²

Ciente e de acordo:


Assinatura do(a) orientador(a)²

Data: 23 / 03 / 2018

¹ Neste caso o documento será embargado por até um ano a partir da data de defesa. A extensão deste prazo suscita justificativa junto à coordenação do curso. Os dados do documento não serão disponibilizados durante o período de embargo.

Casos de embargo:

- Solicitação de registro de patente
- Submissão de artigo em revista científica
- Publicação como capítulo de livro
- Publicação da dissertação/tese em livro

²A assinatura deve ser escaneada.



FEDERAL UNIVERSITY OF GOIAS
INSTITUTE OF PHYSICS
PHYSICS PH.D. PROGRAM



Stefano Castro Tognini

Observation of multiple-muon seasonal variations in the $\text{NO}\nu\text{A}$ Near Detector

Thesis submitted to the Physics Ph.D.
Program of the Institute of Physics at
the Federal University of Goiás, in par-
tial fulfillment for the degree of Doctor in
Physics, under the advising of Prof. Dr.
Ricardo Avelino Gomes.

GOIÂNIA

2018

Ficha de identificação da obra elaborada pelo autor, através do Programa de Geração Automática do Sistema de Bibliotecas da UFG.

Castro Tognini, Stefano

Observation of multiple-muon seasonal variations in the NOvA Near Detector [manuscrito] / Stefano Castro Tognini. - 2018. xxvi, 160 f.: il.

Orientador: Prof. Dr. Ricardo Avelino Gomes.

Tese (Doutorado) - Universidade Federal de Goiás, Instituto de Física (IF), Programa de Pós-Graduação em Física, Goiânia, 2018. Bibliografia. Apêndice.

Inclui siglas, fotografias, abreviaturas, símbolos, gráfico, tabelas, lista de figuras, lista de tabelas.

1. NOvA. 2. muon. 3. seasonal. 4. variations. I. Avelino Gomes, Ricardo, orient. II. Título.

CDU 539.12



Universidade Federal de Goiás
Instituto de Física
Programa de Pós-Graduação em Física

Ata Nº 34 de defesa de tese de **Stefano Castro Tognini** para obtenção do título de Doutor em Física.

Aos 26 dias do mês de abril de 2018, às 13h00min, no Anfiteatro I do Instituto de Física da UFG, reuniu-se a Banca Examinadora designada pela Coordenadoria do Programa de Pós-Graduação em Física, composta pelo **Prof. Dr. Ricardo Avelino Gomes** (orientador e presidente da Banca – IF/UFG), **Prof. Dr. Maury Charles Goodman** (ANL), **Prof. Dr. Mauricio Jose Alves Bolzam** (UFJ), **Prof. Dr. Fábio Luis Braghin** (IF/UFG) e **Prof. Dr. Norton Gomes de Almeida** (IF/UFG) para julgar a tese de doutorado de **Stefano Castro Tognini**, intitulada: "**Observation of multiple-muon seasonal variations in the NOvA Near Detector**". O Presidente abriu os trabalhos agradecendo a presença dos membros da Banca Examinadora e concedeu a palavra a **Stefano Castro Tognini**, que expôs detalhadamente seu trabalho. Em seguida, os membros da Banca fizeram suas considerações e procederam à arguição do candidato. Concluída essa etapa, a Banca, em sessão fechada, deu prosseguimento ao julgamento do trabalho, atribuindo os seguintes conceitos:

Prof. Dr. Ricardo Avelino Gomes (orientador)

Aprovado

Prof. Dr. Maury Charles Goodman (ANL)

Aprovado

Prof. Dr. Mauricio Jose Alves Bolzam (UFJ)

Aprovado

Prof. Dr. Fábio Luis Braghin (IF/UFG)

APROVADO

Prof. Dr. Norton Gomes de Almeida (IF/UFG)

APROVADO

Novamente em sessão aberta, o presidente da Banca anunciou o resultado final do julgamento, declarando o candidato **Stefano Castro Tognini** APROVADO pela Banca Examinadora. Nada mais havendo a tratar, a sessão foi encerrada e lavrou-se a presente ata que segue assinada pelos membros da Banca Examinadora.

Goiânia, 26 de abril de 2018.

Ricardo A. Gomes
Prof. Dr. Ricardo A. Gomes

Maury Goodman
Prof. Dr. Maury C. Goodman

Mauricio J. A. Bolzam
Prof. Dr. Mauricio J. A. Bolzam

Fábio Luis Braghin
Prof. Dr. Fábio Luis Braghin

Norton Gomes de Almeida
Prof. Dr. Norton Gomes de Almeida

To my parents.

Acknowledgements

The conclusion of this Thesis marks the end of a long lasting journey which would have been much harder, if not impossible, without the help of a seemingly endless list of people. This short note is, therefore, just a sample of all my unorganized thoughts and memories regarding these last years.

I will start of by thanking my family. My parents, whose unconditional love and support were the foremost decisive reason for most of my important accomplishments in life, and my older brother who, along with my father, taught me to be curious and amused by learning how things work. They have had a huge influence in my interest in the natural rules and peculiarities of the world, shaping my decision to pursue Physics. I also cannot put into words my gratitude to my fiancée Ohana, who has always been by my side, bringing up my best self, as well as enduring and supporting me at my worst and most difficult moments.

Next, I would like to thank CAPES and CNPq for funding this work, and my advisor, Ricardo A. Gomes, for all the conversations, advices, assistance, and opportunities that he made possible. A huge thanks to my co-advisors Maury Goodman and Philip Schreiner for the countless meetings and discussions throughout these years. Your support and advices were fundamental. Thank you all for all the time spent in mentoring and guiding me.

A big thanks to the Fermi National Accelerator Laboratory and Argonne National Laboratory for the financial support, as well as for receiving me at different occasions over the years. Likewise for the NO ν A Collaboration, being involved with this team of people has been a great experience, no pun intended. Among them, I am grateful for all the feedback and assistance from the Exotics Group, especially to Alec Habig, Matthew Strait, Martin Frank, and Craig Dukes. Similarly to Louise Suter for helping me dealing with the Near Detector, Alexander Himmel for guiding me through the work of processing the dataset in the GRID, and to all the other friendly helps along the way that pushed this work forward, in a way or another.

Finally, a huge personal acknowledgment to all my friends, at UFG and otherwise, whose companies resulted in lighter and brighter days throughout this long journey.

“The Cosmos is rich beyond measure – in elegant facts, in exquisite interrelationships, in the subtle machinery of awe.”

Carl Sagan

Abstract

The interaction of a cosmic ray particle with an element of the atmosphere results in a cascade of particles, known as extensive air showers, which can be divided into three main branches, known as the hadronic, the electromagnetic, and the muonic component. As for the latter, since muons can reach high depths underground, they are generally used to study cosmic rays at different underground depths. The dynamics of extensive air showers is directly connected to the density of the atmosphere, as it defines the probability of particles to decay or interact. As muons are mainly produced from the decay of pions and kaons, and a warmer atmosphere results in higher number of meson decays, such particles are prone to suffer a seasonality effect that is directly correlated to the yearly seasonal variations of the atmosphere, an effect that has been verified by a large number of experiments over the past six decades.

In 2015 the MINOS experiment presented an anti-correlation between the effective temperature of the atmosphere and the seasonality of the muon flux for multiplicities higher than one (i.e. more than one muon track per cosmic ray event). Said anti-correlation is not yet fully understood, counting with only a qualitative hypothesis as a probable mechanism. As such, the main goals of this study are to verify the MINOS anti-correlation effect and extend the study to verify the seasonality of the effect as a function of different variables in order to improve the understanding of the phenomenon and possible corroborations with the known hypothesis.

Two full years of the NO ν A Near Detector, ranging from April 2015 to April 2017, were used as the dataset for the analysis. The anti-correlation between the multiple muon flux and the effective temperature of the atmosphere is confirmed by the NO ν A Near Detector, being in full agreement with the results presented by the MINOS Collaboration. The seasonal effect is also broken down by different variables: *i*) track separation, *ii*) zenith angle, *iii*) track angular separation, and *iv*) multiplicity. Different regions of these variables represent different energy ranges for the detected underground muons, their hadron parents or the primary particles that originated the cosmic ray shower, being a way to verify any particular dependency with energy. The results show that there are no clear trends in any of the studied variables, except for the multiplicity, in which the intensity of the seasonal variation increases for higher multiplicities.

Resumo

A interação entre um raio cósmico e algum elemento da atmosfera é responsável por produzir uma cascata de partículas, conhecida como chuva atmosférica extensa. Tal cascata pode ser dividida em três principais componentes, conhecidas como hadrônica, eletromagnética e muônica. O fato de que múons são capazes de alcançar grandes profundidades no subsolo, faz com que a última componente citada seja ideal para ser utilizada por detectores subterrâneos para estudar chuvas atmosféricas extensas. A dinâmica desses chuvas está diretamente associada à densidade da atmosfera, a qual é um fator determinante nas probabilidades de decaimento ou interação das partículas produzidas ao longo da mesma. Em vista do fato de que múons são produzidos à partir do decaimento de píons e káons, e considerando que uma atmosfera mais quente/fria implica em um maior/menor número de decaimento desses mésons, espera-se que o fluxo de múons de raios cósmicos tenha uma sazonalidade anual, um efeito confirmado por um conjunto de experimentos ao longo das últimas 6 décadas.

Em 2015 o experimento MINOS apresentou uma anticorrelação entre a temperatura efetiva da atmosfera e a sazonalidade do fluxo de múons para eventos com multiplicidade maior que um (ou seja, mais de uma trajetória detectada por evento de raio cósmico). Tal correlação inversa não é completamente compreendida, contando apenas com uma hipótese qualitativa como provável mecanismo físico. Portanto, os principais objetivos deste estudo implicam em verificar este efeito sazonal invertido no Near Detector do experimento NO ν A, além de estender a verificação da sazonalidade de múons múltiplos em função de diferentes variáveis, de forma a trazer uma melhor compreensão sobre o fenômeno e trazer conclusões que possam corroborar com a hipótese mencionada anteriormente.

Como forma de atingir os objetivos, desenvolveu-se uma análise usando dois anos de dados do NO ν A Near Detector, acumulados entre abril de 2015 e abril de 2017. A anticorrelação entre o fluxo de múons múltiplos e a temperatura efetiva da atmosfera foi confirmada, estando de acordo com os resultados apresentados pelo experimento MINOS. O efeito sazonal foi estudado de acordo com diferentes variáveis: *i*) separação entre trajetórias, *ii*) ângulo zenital, *iii*) separação angular e *iv*) multiplicidade. Diferentes regiões de valores destas variáveis representam diferentes regiões de energia dos múons detectados, dos hádrons que os originaram ou dos respectivos primários. Os resultados mostram que não existem claras correlações em nenhuma das variáveis estudadas, exceto pela multiplicidade, a qual mostra que a intensidade da variação sazonal de múons múltiplos aumenta à medida que a multiplicidade do evento aumenta.

Contents

Acknowledgements	ix
Abstract	xiii
Resumo	xv
1 Introduction	1
2 Cosmic Rays	5
2.1 Brief historical introduction	5
2.2 Origins and characteristics	6
2.3 Extensive air showers (EAS)	8
2.3.1 EAS dynamics	8
2.3.2 EAS at the surface level	13
2.3.3 EAS underground	14
3 The seasonal effect	17
3.1 Overview	17
3.2 The Earth's atmosphere	17
3.2.1 Structure and composition	17
3.2.2 Pressure, density and mass	19
3.3 The seasonal effect of the muon flux	20
3.3.1 Muon production in the atmosphere	22
3.3.2 The effect of the temperature in the muon intensity	23
3.3.3 Theoretical prediction of α_T	28
3.4 Experimental results on the seasonal variations of the muon flux	28
3.4.1 Single muons	29
3.4.2 Multiple-muons	45

4	The NOνA Experiment	55
4.1	Overview	55
4.2	The Fermilab accelerator complex	58
4.3	The NuMI beamline	59
4.3.1	NuMI in the NO ν A Era	60
4.4	The concept of an off-axis neutrinos experiment	61
4.5	The NO ν A detectors	63
4.5.1	The detector design	64
4.5.2	The Near Detector	67
4.5.3	The Far Detector	70
5	The data acquisition	73
5.1	Overview	73
5.2	The triggering system	75
5.3	The Near Detector Data Driven Activity trigger	77
5.3.1	Change in the requirements of the Activity trigger	78
5.4	The DAQ data formats	78
6	The pre-analysis	81
6.1	Overview	81
6.2	The reconstruction process	81
6.2.1	The Hough Transform	81
6.2.2	NO ν A's Multi-Hough Transform method	82
6.2.3	Multi-Hough 3D track reconstruction	84
6.3	The Monte Carlo	90
6.3.1	Monte Carlo software for simulating multiple-muon events	90
6.3.2	Data and Monte Carlo track reconstruction	91
6.3.3	Monte Carlo true and reconstructed information	93
6.4	The selection criteria	98
6.4.1	Data quality selection criteria	98
6.4.2	Data analysis selection criteria	104
6.5	The data processing	107
6.5.1	The definition of the dataset	107
6.5.2	The data processing chain	107
6.6	Consistency checks	109
6.6.1	Data and Monte Carlo after all selection criteria	109
6.6.2	Near Detector operation consistency over time	111
6.7	The ECMWF temperature data	113
6.7.1	The effective temperature	115
6.7.2	The systematic errors	116

6.8	Frequency analyses	119
6.8.1	The Rayleigh power	119
6.8.2	The classic periodogram	120
6.8.3	The Lomb-Scargle method	121
7	Multiple-muon physics results	123
7.1	Periodicity consistency checks	123
7.2	Seasonal variations using different time bins	124
7.3	Seasonal variations as a function of different event variables	131
7.3.1	By track separation	131
7.3.2	By zenith angle	135
7.3.3	By angle between tracks	138
7.3.4	By multiplicity	143
8	Conclusions	147
A	List of acronyms and abbreviations	151

List of Figures

2.1	Cosmic rays: all-primaries spectra & fluxes of nuclei	7
2.2	Heitler’s model of the electromagnetic component	9
2.3	Heitler-Matthews’ model of the hadronic component	11
2.4	Vertical flux of particles according to the atmosphere’s depth	14
3.1	Earth’s atmosphere layers	18
3.2	Barrett <i>et al.</i> experimental apparatus and measured α_T	30
3.3	MACRO’s $\Delta R_\mu/\langle R_\mu \rangle$ and $\Delta T_{\text{eff}}/\langle T_{\text{eff}} \rangle$ as a function of month of year	33
3.4	AMANDA’s $\Delta R_\mu/\langle R_\mu \rangle$ and $\Delta T_{\text{eff}}/\langle T_{\text{eff}} \rangle$ as a function of day of year	34
3.5	Muon intensity variations as seen by LVD	35
3.6	IceCube muon seasonal variations and α_T	35
3.7	MINOS FD muon and T_{eff} seasonal variations, and α_T	36
3.8	MINOS ND muon and T_{eff} seasonal variations, and α_T	37
3.9	Borexino’s muon and T_{eff} seasonal variations, and α_T	38
3.10	GERDA’s muon and T_{eff} seasonal variations, and α_T	39
3.11	Double Chooz’ muon and T_{eff} seasonal variations, and α_T	41
3.12	Daya Bay’s α_T results for each experimental hall	42
3.13	Theoretical prediction of α_T compared to the experimental data	45
3.14	MINOS FD track separation and multiple-muon seasonal variations	47
3.15	MINOS Near Detector track separation distribution	48
3.16	MINOS ND seasonal variations for both single and multiple-muons	48
3.17	ECMWF modulation amplitudes and phases	50
3.18	Monte Carlo muon production altitudes for the FD track separation regions	51
3.19	MACRO and MINOS multiple-muon amplitudes and phases	53
4.1	The NO ν A beam line	56
4.2	Fermilab’s accelerator complex	59
4.3	The NuMI beam target	60
4.4	The NuMI beam line	60

4.5	Neutrino flux and energy according to its production angle	63
4.6	NO ν A detector cells, APD and FEB boards	65
4.7	NO ν A detector concept	67
4.8	The NO ν A Near Detector	69
4.9	The NO ν A Far Detector	71
5.1	Diagram of the NO ν A DAQ system	75
5.2	Activity trigger date rate change	78
6.1	The Hough Transform	82
6.2	Multi-Hough Transform applied to a multiple-muon event	84
6.3	Example of gaps within 2D track hits	86
6.4	YZ view of a 2 muon event with rogue tracks	88
6.5	Schematic view of the multiple-muon Monte Carlo allowed region	90
6.6	Multiple-muon data and Monte Carlo comparison	92
6.7	Multiple-muon data and Monte Carlo comparison	93
6.8	True and reconstructed values from the multiple-muon Monte Carlo	94
6.9	Single muon reconstruction efficiency according to zenith angle	96
6.10	Properties of the raw reconstructed dataset	99
6.11	Properties of the reconstructed dataset after the data quality selection criteria	101
6.12	Event displays of two “identical” event triggers	103
6.13	Fiducial volume cut	105
6.14	Time difference between tracks	106
6.15	Detector daily and total exposure time	108
6.16	Comparison between UTC ECMWF daily data and Near Detector runs	108
6.17	The data processing chain	109
6.18	Multiple-muon data and Monte Carlo comparison after the analysis cuts	110
6.19	Multiple-muon data and Monte Carlo comparison after the analysis cuts	111
6.20	Near Detector operation consistency check	112
6.21	ECMWF grid area and the area of muon production	114
6.22	ECMWF temperature, $W(X)$, and weight as a function of altitude or pressure	115
6.23	Daily effective temperature and its percentual variation as function of time	116
6.24	Weighted temperature variance as a function of time	117
6.25	Effective temperature variance in the 2×2 grid as a function of time	118
7.1	Lomb-Scargle results for both multiple-muon rate and T_{eff} data	124
7.2	Daily multiple-muon and effective temperature seasonalities, and α_T	126
7.3	Weekly multiple-muon and effective temperature seasonalities, and α_T	127
7.4	Monthly multiple-muon and effective temperature seasonalities, and α_T	128
7.5	Week of year multiple-muon and effective temperature seasonalities, and α_T	129

7.6	Month of year multiple-muon and effective temperature seasonalities, and α_T	130
7.7	Multiple-muon seasonal variations for different regions of track separation	134
7.8	Calculated α_T for each region of track separation squared	135
7.9	Multiple-muon seasonal variations for different regions of $\cos(\text{zenith})$	137
7.10	Calculated α_T for each region of $\cos(\text{zenith})$	138
7.11	Angular separation between tracks for different multiplicities	139
7.12	Multiple-muon seasonal variations for different regions of angular separation	141
7.13	Calculated α_T for each region of angular separation	142
7.14	Number of events as a function of multiplicity	143
7.15	The multiple-muon event with the highest reconstructed multiplicity	145
7.16	Multiple-muon seasonal variations for different multiplicities	145

List of Tables

2.1	Cosmic ray primaries' composition	6
2.2	Energy loss parameters values for standard rock	15
3.1	Composition of the Earth's atmosphere	18
3.2	Mesons main decay channels that contribute to the muonic component	21
3.3	$W_{\pi,K}(X)$ parameters	26
3.4	Compilation of experiments that measured α_T	44
3.5	η and ρ dimuon decay channels and their branching ratios	49
4.1	NO ν A scintillator oil composition	64
4.2	NO ν A Near Detector specifications	68
4.3	NO ν A Far Detector specifications	70
5.1	Triggers used by NO ν A	77
5.2	Runs and dates of both Activity trigger configurations	78
5.3	The DAQ data formats	80
6.1	Track reconstruction criteria	89
6.2	Single muon reconstruction efficiency according to zenith angle	96
6.3	Multiple-muon reconstruction efficiency and purity	97
6.4	Single muon angular resolution according to track length	98
6.5	Multiple-muon angular resolution according to track length and separation	98
6.6	Data quality selection criteria	100
6.7	Effects of the quality selection criteria	102
6.8	Analysis selection criteria	105
6.9	Effects of the analysis selection criteria	106
6.10	Dataset processed for the analysis	107
6.11	Tabular representation of the ECMWF temperature data	114
7.1	Multiple-muon α_T fitted values according to different time bins	125
7.2	Binned Rayleigh power results for each track separation squared region	133

7.3 Best fit values for each region of track separation 133

7.4 Multiple-muon α_T fitted values according to different regions of track separation 133

7.5 Binned Rayleigh power results for each $\cos(\text{zenith})$ region 136

7.6 Best fit values for each region of $\cos(\text{zenith})$ 136

7.7 Multiple-muon α_T fitted values according to different regions of $\cos(\text{zenith})$. . 136

7.8 Binned Rayleigh power results for each angle between tracks region 140

7.9 Best fit values for each region of angular separation 140

7.10 Multiple-muon α_T values according to different regions of angular separation . 143

7.11 Total number of events according to multiplicity 144

7.12 Best fit values for each multiplicity 144

Chapter 1

Introduction

The interaction between a cosmic ray particle with a nucleus of the Earth's atmosphere is responsible for starting a sequence of hadronic and decay processes that produces cascade of particles known as an extensive air shower. The produced particles can be split into three main branches, known as the hadronic, the electromagnetic, and the muonic component. The development of these extensive air showers depends on the atmosphere's composition, temperature, and density profile, as the interactions and decay process that the produced particles may undergo are tightly linked to the characteristics of the mean traversed by them. In this scenario, the changes in the Earth's atmosphere due to its yearly seasons should provoke a quantifiable effect in the measured flux of each of the aforementioned components.

Due to their high penetrative power, the muons produced by extensive air showers have the capacity to reach deep underground detectors, being one of the background signals in many experiments, but they are also a powerful tool to better understand the dynamics of cosmic ray induced showers. As such, many experiments since the late 1950's have been verifying seasonalities in the measured muon flux, at different depths, and comparing the periodicity of said flux with the temperature of the atmosphere. Since the probability of a cosmic ray to interact with the atmosphere decreases as its kinetic energy increases (following a power law), lesser energetic showers are more likely to occur. Therefore, given the higher likelihood of lower energetic events to happen, allied with a finite, and usually small detector¹, cosmic ray muon events containing one single muon track represent the vast majority of the data when compared to events with two or more muons.

Comparing a muon flux measurement with the temperature of the atmosphere is not straightforward, as the atmosphere has large temperature variations from the surface up to the end of the stratosphere. To overcome this complication, an effective temperature of the atmosphere is adopted, in which a weighted average over several temperature measurements throughout different altitude levels is performed. The weighting choice is a model based on the muon production processes, in which the model tries to add higher weights to regions of the atmosphere

¹In comparison with the area that a cosmic ray shower may cover.

where muons are more likely to be produced via the direct decay of secondary pions and kaons.

The seasonality of said majority of single muon events has been reported by a long list of experiments, and it is known to follow a direct correlation with the effective temperature of the atmosphere, which is expressed as

$$\frac{\Delta R_\mu}{\langle R_\mu \rangle} = \alpha_T \frac{\Delta T_{\text{eff}}}{\langle T_{\text{eff}} \rangle}, \quad (1.1)$$

where ΔR_μ represents the variation of the muon rate at a given time t with respect to the global muon rate average $\langle R_\mu \rangle$, α_T is the temperature correlation coefficient, and ΔT_{eff} is the effective temperature variation at a given time t with respect to the global effective temperature average $\langle T_{\text{eff}} \rangle$. The direct correlation is explained by the fact that during summer (winter), the atmosphere's density is lower (higher), which in turn decreases (increases) the probability of pions and kaons to interact. The lower (higher) interaction probability results in more (less) mesons decaying into muons and neutrinos, producing a higher (lower) measured flux.

The theoretical prediction of the temperature correlation coefficient α_T is based on the premise that the measured muon flux is originated solely via the direct decay of secondary pions and kaons in the tropopause. In this scenario, it only predicts positive values, yielding a direct correlation with the effective temperature and not taking into account any contributions for further hadronic interactions down the atmosphere, being well suited only for single muons, as multiple-muon events may contain muons that have been originated at very different altitudes.

In 2015 the MINOS Experiment² reported unexpected results from both of its detectors: in the Near Detector, the seasonality of the muon flux for events with 2 or more muons showed an anticorrelation between its modulation phase and the effective temperature phase. The inverted seasonality was also accompanied by another not fully understood effect, verified by the Far Detector, in which the seasonality of the flux of multiple-muon events showed different phase trends according to different track separations: Shorter distances between tracks followed a direct correlation with the effective temperature seasonality, whilst muons with large separations showed an inverted phase.

Qualitative hypotheses on the mechanism that causes the phase inversion have been proposed, but the effect has not been verified by any other experiment, which leads to the goals of the analysis presented in this Thesis:

- i) Analyze the seasonal variation effect in the multiple-muon flux using the NO ν A Near Detector in order to validate the results presented by MINOS.
- ii) Quantify seasonal effect suffered by the multiple-muon flux in order to make possible the comparison of the seasonality of different valid ranges of different variables of interest, namely: track separation, zenith angle, angle between tracks, and multiplicity. Each of

²The details will be covered in Chapter 3.

these variables will be broken down into different regions and the seasonality of the muon flux from each will be verified and quantified in an attempt to search for any particular trend.

In order to accomplish said goals, this Thesis is organized in the following order:

- Chapter 2 describes the characteristics and dynamics of cosmic rays and extensive air showers.
- Chapter 3 provides theoretical background on the seasonal effect of the muon flux, along with the calculation of the effective temperature, as well as a thorough review of experimental results regarding muon seasonal variations.
- Chapter 4 describes in depth the NO ν A Experiment, from its goals to its experimental apparatus.
- Chapter 5 describes the data acquisition system developed and used by NO ν A, including details on how cosmic ray data is recorded by the detectors.
- Chapter 6 describes all the necessary steps that take place prior to the data analysis, including: the reconstruction algorithm; the Monte Carlo, used to validate the reconstruction method and to define the analysis selection criteria; the definition of the selection criteria; the description of the datasets used (both from the NO ν A detector, as well as the atmospheric temperature data); the data processing; detector operation consistency checks; and the systematic errors.
- Chapter 7 presents the analysis results.
- Chapter 8 outlines the conclusions of the study.

Chapter 2

Cosmic Rays

2.1 Brief historical introduction

During the 16th century, Coulomb reported an effect showing spontaneous discharges in electroscopes, a conundrum whose explanation only emerged four centuries later, in the beginning of the 20th century, starting with the discovery of radioactivity by Becquerel, and Pierre and Marie Curie. Their studies led to the conclusion that ionized particles coming from radioactive sources were crossing the electroscope's enclosure and discharging it. The further work of Wilson, Elster and Geitel significantly improved the electroscope's insulation, providing the possibility to quantitatively measure its discharge rate [1]. These improvements gave Thomas Wulf the opportunity to test if such radioactivity was indeed coming from the ground. By 1910, he carried an insulated vessel containing an electroscope to the top of the Eiffel Tower with the hypothesis that the radiation from the ground would be absorbed by the larger volume of air, resulting in a lower discharge rate. The comparison between his predictions with the measured data showed that the discharge rate was much higher than expected, leading to the radical claim that part of the radiation should have its origin coming from the atmosphere. In 1912, said hypothesis resulted in a balloon experiment, led by Victor Hess, whose purpose was to measure such discharge rate as a function of the altitude. The experiment showed that the radiation levels increased drastically above 5 km of altitude [1]. A few months later, Hess presented his study to the community with a very significant conclusion [2]:

“The results of my observations are best explained by the assumption that a radiation of very great penetrating power enters our atmosphere from above.”

Hess was responsible for one of mankind's revolutionary scientific discoveries and paved the way for a new era of research in physics, which field is now known as Cosmic Ray Physics¹.

¹Hess was awarded with a Nobel prize in 1936 for the discovery of Cosmic Rays, which was shared with Carl Anderson for the discovery of the positron.

2.2 Origins and characteristics

The flux of cosmic rays that reach the Earth's atmosphere can be described by a power formula proportional to their energy [3]

$$\frac{dN}{dE} \propto E^{-\gamma} \left(\frac{1}{\text{m}^2 \text{ sr s GeV}} \right), \quad (2.1)$$

where γ is the integral spectral index and varies according to the primaries' energy range, as can be seen in figure 2.1 (a): up to 10^{15} eV, $\gamma = 2.68 \pm 0.02$ [4]. Near 10^{15} eV the spectral index suffers its first change, which is referred to as the *knee*. From this point up to 10^{17} eV, $\gamma = 3.02 \pm 0.03$ [5]. Around 10^{17} eV, γ suffers a second change, which is called the *second knee*. Within the range of 10^{17} eV and 10^{19} eV, where the upper limit is known as *the ankle*, $\gamma = 3.33 \pm 0.04$ [6]. For primaries with energy above 10^{19} eV, the spectral index falls to $\gamma = 2.68 \pm 0.04$ [6]. The decrease in the γ value above the ankle may be caused by the GZK suppression² [7], an effect known to cause a drastic decrease in the primaries' flux originated by extragalactic sources due to their energy loss caused by the interaction between the cosmic ray particle and the cosmic microwave background. Said suppression, predicted to happen at the value of $\text{GZK}_{\text{cut-off}} \approx 6 \times 10^{19}$ eV, was seen by the HiRes Experiment³ [8] and the Auger Collaboration⁴ [9]. Although the suppression was measured, there are rare events that were found to have an energy significantly above 10^{19} eV and, for these cases where $E > \text{GZK}_{\text{cut-off}}$, $\gamma = 4.2 \pm 0.1$ [6].

As shown in table 2.1, cosmic rays are composed mostly of protons ($\sim 79\%$) and helium ($\sim 20\%$), resulting in $\sim 1\%$ or less for heavier nuclei, which are composed mainly by carbon, nitrogen and oxygen. Figure 2.1 (b) shows the flux for different cosmic ray primaries, as a function of their energy. Note that each one of the curves was scaled by a factor of 10^{-n} for visual purposes. The difference in the flux for different primary nuclei is a direct consequence

Primary composition	Fraction of the total flux
Proton	$\sim 79\%$
Helium	$\sim 20\%$
Other (from C, N, and O to Fe)	$\sim 1\%$

Table 2.1 | Cosmic ray primaries' composition

Table shows the proportion of different elements found in the flux of cosmic rays [3].

of their abundance in the galaxy.

²Abbreviation for Greisen-Zatsepin-Kuzmin. The effect is also known in the literature as the GZK cut-off and the GZK limit.

³Acronym for High Resolution Fly's Eye Experiment, an observatory located in the desert of Utah.

⁴Located in Malargüe, Argentina. It is the biggest experiment for detecting ultra high energy cosmic rays, with Cherenkov radiation detectors spread over an area larger than 3,000 km².

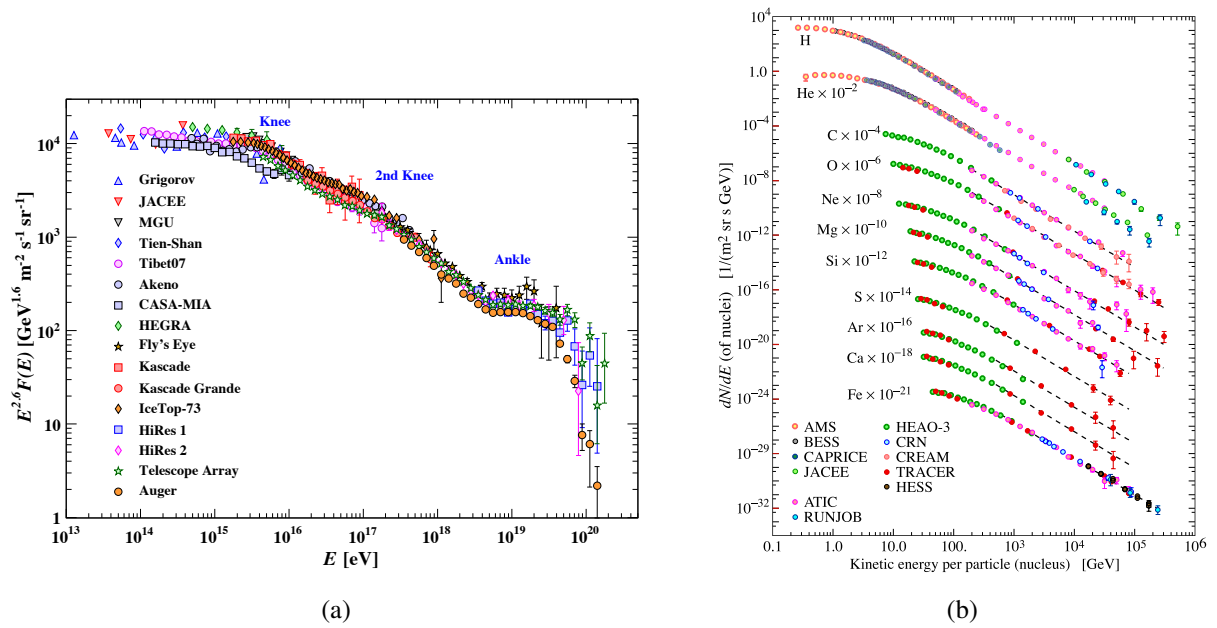


Figure 2.1 | Cosmic rays: all-primaries spectra & fluxes of nuclei

(a) The all primaries spectrum according to their energy and (b) the primaries' flux according to their energy and composition [3].

Although the vast majority of low energy cosmic rays have their origin in the Sun, there are open questions on what are the main sources of acceleration of high energy primaries. A widely accepted idea is known as the Fermi mechanism [10], also known as *diffusive shock acceleration*, which uses the premise that the acceleration suffered by charged particles is caused by a repeated pattern of electromagnetic shock waves⁵. A rewarding consequence of this mechanism is the conclusion that the spectrum of the cosmic radiation must obey an inverse power law formula, which traces back to the experimental description of the flux provided in equation 2.1. The limitation of this mechanism is known as the injection problem, which shows that charged particles must have a sufficiently high minimum energy to start the acceleration process in the first place. For protons, the threshold is as low as 200 MeV, but it increases rapidly for heavier nuclei, being estimated as 1 GeV for α particles and reaching 300 GeV for Fe nuclei⁶. Finally, ultra high energetic primaries may be explained by Active Galactic Nuclei (AGN) and Gamma Ray Bursts (GRB) – the latter, originated by hypernovae – but the question is still open to debate [12].

It is worth quoting Pierre Auger, one of the discoverers of extensive air showers (see session 2.3), at the 1939 Symposium held in Chicago [13, 14]:

“One of the consequences of the extension of the energy spectrum of cosmic rays up to 10^{15} eV is that it is actually impossible to imaging a single process able to

⁵The origins of the shock waves should come from astronomical radio sources, such as stars, supernovae remnants, pulsars or even black holes.

⁶A more detailed description of the model can be seen in Ref. [11].

give a particle such an energy. It seems much more likely that the charged particles which constitute the primary cosmic radiation acquire their energy along electric fields of very great extension.”

Nowadays, Auger’s mechanism is considered to be very unlikely, given the unavailability of electric fields of great extensions due to the conductivity of interstellar plasma [14], but by having observed cosmic rays with energies greater than 10^{20} eV, his first statement still holds true: identifying all the mechanisms that could provide such an astounding range of kinetic energy for charged particles remains a great challenge. Mainly, when another issue is put into perspective, which is related to the primaries’ direction: said particles are constantly scattered and deflected by interstellar magnetic fields, resulting in the loss of the information of their original direction.

2.3 Extensive air showers (EAS)

The resulting set of hadronic and electromagnetic interactions and decay processes that take place after an incident cosmic ray collision with an element in the Earth’s atmosphere is known as an Extensive Air Shower (EAS). This phenomenon was discovered by Rossi, Schmeiser, Bothe, Kohlhörster and Auger during the 1930’s and can reach energy scales many orders of magnitude above any man-made experiment was able to achieve. Despite the work done by Rossi and the others, the discovery is usually credited to Auger and his collaborators [14].

2.3.1 EAS dynamics

The cascade of particles in an extensive air shower can be divided into two main cascades: the electromagnetic and the hadronic component – the latter, can be subdivided into a hadronic and a muonic component. In this section, we will consider Heitler’s model [16] for the electromagnetic cascade development and extend it to the case of extensive air showers. The reason for this choice is that although there are more sophisticated models⁷, this approach already predicts the most important features of an EAS.

Heitler’s model of the electromagnetic component

Heitler’s approximation for the electromagnetic component considers an electron, a positron and a photon undergoing two-body splittings, either a bremsstrahlung or e^+e^- pair production, after a distance proportional to one radiation length in the medium, as seen in figure 2.2.

After n splittings, two conclusions can be inferred:

- (i) The total number of particles in the shower is $N(n) = 2^n$.

⁷For more sophisticated approaches, see Gaisser, T. K. **Cosmic Rays and Particle Physics**, Cambridge University Press, Cambridge (1990).

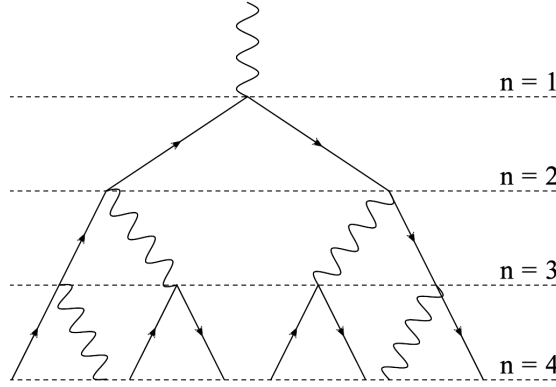


Figure 2.2 | Heitler's model of the electromagnetic component

Visual representation of Heitler's model for the electromagnetic component, showing 4 different levels of particle splittings.

- (ii) The energy per particle can be approximated by $E(n) = E_0/N(n)$, where E_0 is the energy of the primary particle.

This behavior changes below the critical energy ϵ_e , at which collisional energy losses surpass radiative losses and are more likely to be absorbed or decay. In air, $\epsilon_e = 81$ MeV [3]. Therefore, the highest number of particles in the component is simply $N_{\max} = 2^{n_c}$ and the total energy is $E_0 = \epsilon_e N_{\max}$, leading to

$$E_0 = \epsilon_e 2^{n_c}$$

$$n_c = \frac{\ln(E_0/\epsilon_e)}{\ln(2)}, \quad (2.2)$$

which is the number of splitting iterations needed for the shower to reach its maximum size. The length of each layer that represents the splitting distance is a constant, defined as $d_s \equiv \lambda_r \ln(2)$, where λ_r is the radiation length in the medium [17]. Following this definition, one can calculate the penetration depth of the shower after n splittings:

$$X(n) = n\lambda_r \ln(2). \quad (2.3)$$

The combination of expressions 2.2 and 2.3 provides the maximum of the electromagnetic shower

$$X_{\max} = \lambda_r \ln \left(\frac{E_0}{\epsilon_e} \right), \quad (2.4)$$

which represents the depth in the atmosphere where the electromagnetic cascade reaches its maximum number of particles. Below this distance, particles will be below the critical energy and start to be absorbed by the atmosphere.

Heitler's approximation shows two important aspects of the electromagnetic shower, which

are

$$N \propto E_0 \quad \text{and} \quad X_{\max} \propto \ln(E_0), \quad (2.5)$$

but it has known limitations:

- (i) The electron to photon ratio is overestimated by the model [16]. After a few iterations, $N_e \approx \frac{2}{3}N_{\max}$. This is way too large, mainly due to two factors: first of all, not one, but multiple photons can be produced via bremsstrahlung and, second, several e^\pm are absorbed in the atmosphere, resulting in a much larger number of photons than e^\pm . The outcome, confirmed by simulations, is a number of photons that exceed the number of electrons by a factor of 6 when both are at their respective maxima [17].
- (ii) Considering item (i) and that photons produce a much weaker signal in scintillator detectors than e^\pm do, the number N_{\max} predicted by the model will significantly differ from what an experiment would measure.
- (iii) In simulations, the maximum electron number N_{\max} is one order of magnitude smaller than the one predicted by Heitler. Said correction remains nearly identical up to PeV scales for proton air showers. Therefore, an electron/positron reduction factor $N_e = N_{\max}/g$, where $g \approx 10$, can be used to correct Heitler's original prediction.

Heitler-Matthews' model of the hadronic component

Matthews [17] extends Heitler's approach to develop the hadronic part of extensive air showers. His approximation consists of a few main premisses:

- (i) Hadrons are the primaries producing the hadronic cascade.
- (ii) Using an analogue to the splitting distance $d_s = \lambda_r \ln(2)$, the hadronic shower will interact after every fixed interaction distance $d_I = \lambda_I \ln(2)$, where λ_I is the interaction length. It can be assumed as constant for primaries from 10 GeV to 1 TeV.
- (iii) An hadronic interaction produces N_{π^\pm} charged pions and $\frac{1}{2}N_{\pi^\pm}$ neutral pions⁸. The resulting π^0 's will instantly decay into photons, initiating electromagnetic cascades. A schematic view of this set of interactions and decays can be seen in figure 2.3.
- (iv) Charged pions will continue to interact until they reach their critical energy ϵ_π , below which they will all decay, yielding muons.

After n interactions, a primary with E_0 will produce a total number of pions $N_\pi^{\text{tot}}(n) = \left(\frac{3}{2}N_{\pi^\pm}\right)^n$. Assuming an equal division of energy, each pion will bear

$$E_\pi(n) = \frac{E_0}{\left(\frac{3}{2}N_{\pi^\pm}\right)^n}. \quad (2.6)$$

⁸The model does not considers kaon production.

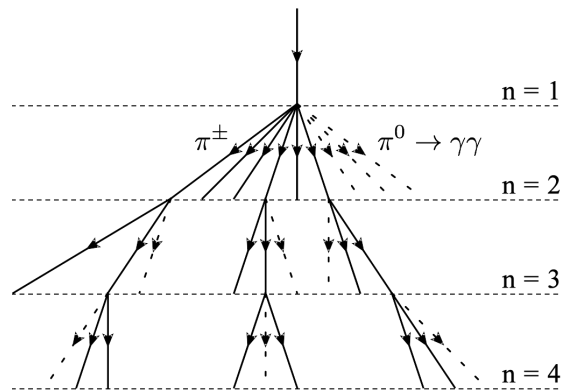


Figure 2.3 | Heitler-Matthews' model of the hadronic component

Visual representation of Heitler-Matthews's model for the hadronic component, showing 4 different layers of interactions. Hard lines show charged pions produced in the interaction, while the dashed lines show the neutral pion production, which in the model instantaneously decays into photons. Some of the pion lines were omitted in order to avoid clutter.

Since there are $N_{\pi^\pm}^{\text{tot}}(n) = (N_{\pi^\pm})^n$ charged pions, they carry a total energy $E_{\pi^\pm}^{\text{tot}}(n) = (2/3)^n E_0$. The rest of the energy is carried away with neutral pions decaying into photons and producing electromagnetic showers.

The critical energy ϵ_π is reached after n interactions and it can be defined as the energy at which the decay length of a charged pion becomes smaller than the interaction distance d_I . Using equation 2.6, one can infer the maximum number of interactions needed for the hadronic cascade to reach it:

$$E_\pi = \epsilon_\pi$$

$$n_c = \frac{\ln(E_0/\epsilon_\pi)}{\ln\left(\frac{3}{2}N_{\pi^\pm}\right)}. \quad (2.7)$$

Following the same line of thought developed in Heitler's electromagnetic shower model, the maximum penetration depth can be calculated using equation 2.7

$$X_{\text{max}}^{\text{had}} = n_c \lambda_I \ln(2)$$

$$X_{\text{max}}^{\text{had}} = \frac{\lambda_I \ln(2)}{\ln\left(\frac{3}{2}N_{\pi^\pm}\right)} \ln(E_0/\epsilon_\pi). \quad (2.8)$$

The results show that Heitler-Matthews' model of hadronic showers have the same qualitative behavior as the electromagnetic component model:

$$N_{\pi^\pm} \propto E_0 \quad \text{and} \quad X_{\text{max}}^{\text{had}} \propto \ln(E_0). \quad (2.9)$$

The fact that every charged pion below ϵ_π decays into a muon allows the calculation of the number of muons produced by the shower.

Heitler-Matthews' model of the muonic component

The primary energy must be conserved and divided into both hadronic and electromagnetic cascades. After reaching the critical number of interactions or splittings, all electrons and positrons will be absorbed by the atmosphere and all charged pions will decay through the channel $\pi^\pm \rightarrow \mu^\pm \nu_\mu (\bar{\nu}_\mu)$, leading to the following straightforward relation

$$N_{\mu^\pm} = N_{\pi^\pm}^{\text{tot}} = (N_{\pi^\pm})^{n_c}. \quad (2.10)$$

From equations 2.10 and 2.7 it is easy to notice that

$$\begin{aligned} \ln(N_{\mu^\pm}) &= \ln(N_{\pi^\pm})^{n_c} \\ \ln(N_{\mu^\pm}) &= \frac{\ln(N_{\pi^\pm})}{\ln\left(\frac{3}{2}N_{\pi^\pm}\right)} \ln(E_0/\epsilon_\pi) \equiv \beta \ln(E_0/\epsilon_\pi) \end{aligned}$$

$$\ln(N_{\mu^\pm}) = \ln\left(\frac{E_0}{\epsilon_\pi}\right)^\beta$$

$$N_{\mu^\pm} = \left(\frac{E_0}{\epsilon_\pi}\right)^\beta. \quad (2.11)$$

Therefore, it is different from the pion cascade, $N_{\mu^\pm} \propto E_0^\beta$, with $\beta \approx 0.9$ being reported from Monte Carlo studies [17].

A limitation of this approach is that it does not take into account the longer path of higher energy muons that come from the decay of leading pions after the primary's hadronization process.

The primary energy

The primary interaction produces $N_{\pi^\pm}^{\text{tot}}$ pions in the hadronic component plus N_{max} particles in the electromagnetic component. Since $N_{\pi^\pm}^{\text{tot}} = N_{\mu^\pm}$, the total energy of the primary can be written simply as a function of the critical energies ϵ_e and ϵ_π , and the number of electrons, photons and muons:

$$E_0 = \epsilon_e N_{\text{max}} + \epsilon_\pi N_{\mu^\pm}. \quad (2.12)$$

Including the scaling factor⁹ g , in which $N_e = N_{\max}/g$, equation 2.12 becomes

$$E_0 = g\epsilon_e N_e + \epsilon_\pi N_{\mu^\pm}, \quad (2.13)$$

showing that the relative contributions from N_μ and N_e is determined by their respective critical energies.

2.3.2 EAS at the surface level

At the surface, near sea level, most of the EAS has died out and the electromagnetic cascade has ranged out in the atmosphere. Mesons have already decayed or interacted, resulting in a small final set of particles consisting of protons, neutrons, electrons, muons, photons and neutrinos.

The hadronic component

The nucleons above 1 GeV represent the final stages of a long chain of interactions and decays that started in the stratosphere, resulting in mainly neutrons and protons. At sea level, the vertical intensity of protons is known to be $I_p \approx 0.9 \text{ m}^{-2} \text{ s}^{-1} \text{ sr}^{-1}$.

The electromagnetic component

The electrons, positrons and photons detected at sea level originate from two main sources: *i*) the electromagnetic cascades produced by meson decays, mainly pions and kaons, and *ii*) Michel electrons/positrons, which are the result of muons decaying via the channel $\mu^\pm \rightarrow e^\pm \nu_e (\bar{\nu}_e) \nu_\mu (\bar{\nu}_\mu)$, with the latter source only becoming dominant at low energies. The intensity of electromagnetic showers depends highly on altitude and zenith angle.

The muonic component

Muons are by far the largest number of charged particles produced by an EAS that reach the surface (see figure 2.4). Most of them are produced at ~ 15 km altitude and their intensity at sea level is measured to be $I_{\mu^\pm} \approx 70 \text{ m}^{-2} \text{ s}^{-1} \text{ sr}^{-1}$ [3].

The muon flux also varies according to the zenith angle, whose distribution at the surface level is expected to be

$$I_{\mu^\pm} \propto \cos^2 \theta. \quad (2.14)$$

A geometrical demonstration of this result can be found in Ref. [18], which shows that this correlation is a direct consequence of the fact that the primaries's vertical flux as a function of energy obeys a power law of the kind $I(E) \propto E^{-n}$. For muons with enough energy to neglect

⁹See limitation (iii) of Heitler's model of the EM shower in subsection 2.3.1.

muon decays ($E_\mu > 100/\cos\theta$ GeV), the pion and kaon contribution to the total muon flux can be approximated using the following parameterized equation [3]

$$\frac{dN_\mu}{dE_\mu d\Omega} \approx 0.14 E_\mu^{-2.7} \left[\frac{1}{1 + \frac{1.1 E_\mu \cos\theta}{\epsilon_\pi}} + \frac{0.054}{1 + \frac{1.1 E_\mu \cos\theta}{\epsilon_K}} \right] \text{ cm}^{-2} \text{ s}^{-1} \text{ sr}^{-1} \text{ GeV}^{-1}, \quad (2.15)$$

where $\epsilon_\pi = 115$ GeV and $\epsilon_K = 850$ GeV are the critical energies for both pions and kaons.

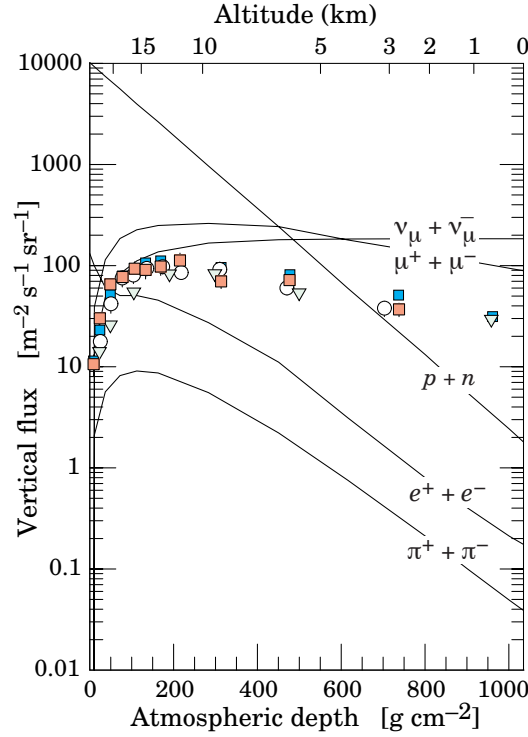


Figure 2.4 | Vertical flux of particles according to the atmosphere's depth

The plot shows the vertical flux of the different components of extensive air showers as they develop in the atmosphere. Since muons are highly penetrating, they are the only particles (apart from the almost non-interactive neutrinos) that do not suffer a drastic decrease in their vertical flux as the shower approaches sea level. The data points show the flux of negative muons with $E > 1$ GeV [3].

2.3.3 EAS underground

The only highly penetrating particles in extensive air showers are muons and neutrinos and they are the only direct component of the EAS that can be detected by deep underground experiments. Any other detected particle will come from neutrino and muon interactions with the surrounding rock/environment of the detector.

The intensity of muons underground can be estimated by calculating their energy loss after traversing an amount of matter X (in g/cm^2) using the following parameterized equation [3, 19]

$$-\frac{dE_\mu}{dX} = a(E_\mu) + \sum_{i=1}^3 b_i(E_\mu) E_\mu, \quad (2.16)$$

where a is the collisional term (i.e. the energy loss through ionization processes) and $\sum b_i = b_{\text{brem}} + b_{\text{pair}} + b_{\text{DIS}}$ takes into account, respectively, bremsstrahlung, pair production and deep inelastic scattering. As specified, these parameters vary for different energy ranges and are subject to different values for different rock compositions, having to be evaluated to match with the desired location. Table 2.2 shows the values of a and b_i for different muon energy ranges considering “standard rock”.

E_μ [GeV]	a [MeV cm ² /g]	b_{brem}	b_{pair} [10 ⁻⁶ cm ² /g]	b_{DIS}	$\sum b_i$
10	2.17	0.70	0.70	0.50	1.90
10 ²	2.44	1.10	1.53	0.41	3.04
10 ³	2.68	1.44	2.07	0.41	3.92
10 ⁴	2.93	1.62	2.27	0.46	4.35

Table 2.2 | Energy loss parameters values for standard rock

Table shows the values of the muon energy loss parameters a and b_i for different muon energy ranges for standard rock [19].

A direct integration of equation 2.16 yield

$$E_\mu^{\text{surf}} = (E_\mu + \xi)e^{-b_T X} - \xi, \quad (2.17)$$

where $\xi = a/b_T$ represents the critical energy below which ionization processes are more important than radiative processes and $b_T = \sum b_i$. Using equations 2.16 and 2.17 it is possible to calculate the muon intensity at a given depth X

$$\frac{dN_\mu}{dE_\mu}(X) = \frac{dN_\mu}{dE_\mu^{\text{surf}}} \frac{dE_\mu^{\text{surf}}}{dE_\mu}$$

$$\frac{dN_\mu}{dE_\mu}(X) = \frac{dN_\mu}{dE_\mu^{\text{surf}}} e^{-b_T X}. \quad (2.18)$$

Notice that the intensity underground diminishes exponentially as the muon component propagates through the rock and that depends on the rock chemical composition, characterized by a and $\sum b_i$ terms.

Chapter

The seasonal effect

3.1 Overview

The interaction between a cosmic ray particle and the atmosphere produces a set of 3 primary branches, defined as the hadronic, electromagnetic and muonic components. The latter is the most evident in underground detectors. The dynamics of these extensive air showers, covered in Chapter 2, already showed that the development of each of their components is intrinsically tied to the characteristics of the atmosphere.

The Earth is subject to different seasons each year due to its axial tilt, resulting in several systems following the same yearly trend. In this context, its atmosphere has a set of parameters that change in a yearly basis, ranging from temperature and density to CO₂ levels. Given the close connection between the dynamics of extensive air showers and the atmosphere, it is expected that the seasonal variations suffered by the atmosphere's density profile results in quantifiable seasonal modulations in the muonic component of extensive air showers.

This Chapter thereby provides information on the structure of the atmosphere of the Earth, and connects its yearly seasonal variation to the muonic component of extensive air showers, describing how changes in the atmosphere should affect the measured muon flux in surface and underground detectors.

3.2 The Earth's atmosphere

3.2.1 Structure and composition

The atmosphere is a mixture of gases held by Earth's gravity. Its composition is fairly simple, with approximately 99% of it being composed only by nitrogen and oxygen, and the 1% rest being mainly argon and carbon dioxide, as it is shown in table 3.1 [20].

The atmosphere is conventionally divided into a set of vertical layers based on their thermal qualities. Starting from the sea level up to 100 km of altitude, the atmosphere is composed by

Component	Volume fraction (%)
Nitrogen (N ₂)	78.08
Oxygen (O ₂)	20.95
Argon (Ar)	0.93
Carbon dioxide (CO ₂)	0.04
Other	~ 0.05

Table 3.1 | Composition of the Earth's atmosphere

The table presents the constituents of the Earth's atmosphere. The numbers represent data for the atmosphere only up to 25 km of altitude. Nonetheless, the 2 main components (which comprise ~99% of it) are known to remain constant until about 100 km. The other gases, representing less than 1% of the atmosphere's total composition, are mainly Ne, Kr, CH₄, Xe, He, O₃, and H, by order of significance [20].

3 main layers, with a smaller intersection layers between each of the three, as can be seen in figure 3.1. The vast majority of cosmic ray interactions and decays happen below 40 km of altitude. Therefore, the lower 2 main layers, plus their intersection, comprise the region of the atmosphere that plays a significant role in the dynamics of extensive air showers.

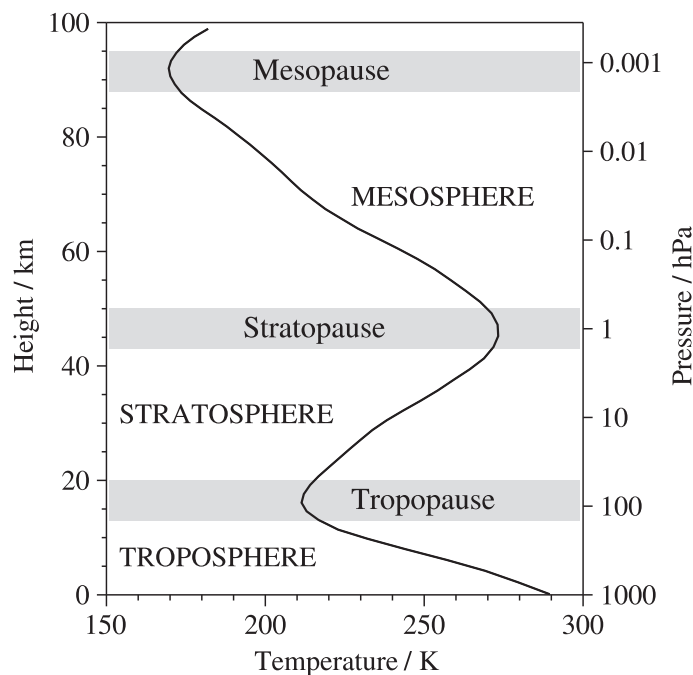


Figure 3.1 | Earth's atmosphere layers

The graph shows the average temperature of the atmosphere as a function of both altitude and pressure, along with the definition of each of the Earth's atmosphere layers. It is worth mentioning that, since the atmosphere is not static, these boundaries suffer small shifts over time [21].

The lowest of these 2 layers is the troposphere, and it finishes at about 10 km to 15 km of altitude. This is the densest of all three, with its temperature decreasing with height. The next

layer is the stratosphere, which ends at about 45 km, and whose temperature now follows an inverted trend, increasing with altitude. The few kilometers long boundary between both layers, in which the temperature trend inverts, is called the tropopause. This temperature inversion perceived in the stratosphere depends on the main source of heat in each layer. In the case of the troposphere, the ground itself is the main source, and, therefore, as the altitude increases, the atmosphere loses thermal energy. However, the stratosphere is filled by ozone (O_3), with higher amounts closer to the top of it [21]. The ozone is responsible for absorbing most of the UV radiation emitted by the Sun and, therefore, it becomes the predominant element for conducting heat to the stratosphere. This disparateness in which the heat is emanated from both the ground, with its gradient pointing upward in the troposphere, and by the ozone in the stratosphere, with its gradient pointing downward, is the responsible mechanism for the flip in the temperature trend and, thereby, the existence of the tropopause.

3.2.2 Pressure, density and mass

There is little interaction between the components of the atmosphere, making the ideal gas a good approximation. For an atmosphere at rest, the hydrostatic balance dictates that the pressure at any level of the atmosphere is proportional to the mass above it. The pressure axis in figure 3.1 shows that approximately 90% of the total mass of the atmosphere must lie in the troposphere [21]. The stratosphere comprises around 10%, resulting in a close to negligible amount of mass in the mesosphere and above¹.

Starting from the two premises above, in which the atmosphere is approximately an ideal gas, and that it is, at a given time, in hydrostatic balance, it is possible to show how its pressure varies as a function of altitude. The two premises imply that

$$\frac{dp}{dz} = -\rho g, \quad \text{and} \quad pV = Nk_B T, \quad (3.1)$$

Where p is the pressure, z is the vertical axis with respect to the ground, ρ is the air density, g is the acceleration of gravity, V is volume, N is the number of molecules of air, k_B is the Boltzmann constant and, finally, T is temperature. By rewriting the density ρ as

$$pM = \frac{NM}{V} k_B T = \rho k_B T \quad \Rightarrow \quad \rho = \frac{pM}{k_B T}, \quad (3.2)$$

where M is the mean mass of a molecule of air, it is easy to notice that

$$\frac{dp}{dz} = -\frac{pMg}{k_B T}. \quad (3.3)$$

¹Such small amount of matter above 100 km of altitude is, indirectly, the reason for which the 100 km threshold separates aeronautics from astronautics. This threshold, called the Kármán line, represents the region in which the role of the aerodynamics of a flying object becomes meaningless.

The temperature also depends on z , and, therefore, after a simple integration, one may find

$$\int_{P_0}^P \frac{dp}{p} = - \int_0^h \frac{Mg}{k_B T(z)} dz$$

$$P(h) = P_0 \exp \left(- \frac{Mg}{k_B} \int_0^h \frac{dz}{T(z)} \right), \quad (3.4)$$

where P_0 is the pressure at sea level. The result in equation 3.4 shows that the pressure (and, as a consequence of equation 3.2, also the density) of the atmosphere decreases exponentially with respect to the altitude. In the case of an isothermal atmosphere, $T(z) = T$ and, thus, equation 3.4 becomes simply

$$P(h) = P_0 \exp \left(- \frac{h}{H(T)} \right), \quad (3.5)$$

where $H(T) \equiv k_B T / Mg$ is known as the pressure scale height, and it defines the height over which the pressure falls by a factor of e .

An important parameter is the atmospheric depth X (in g/cm^2), which represents the column of matter above a certain altitude h . Since the pressure at a given depth X_i is simply $X_i = P_i$, equation 3.5 can be rewritten in terms of the depth solely by replacing the pressure:

$$X(h) = X_0 \exp \left(- \frac{h}{H(T)} \right). \quad (3.6)$$

At sea level, $X_0 = 1,030 \text{ g}/\text{cm}^2 = 1,010 \text{ hPa}$.

As for the the total mass of the atmosphere, it is known that it varies over time due to several aspects, such as the total water vapor loading, carbon dioxide emission and absorption, interstellar gas, dust, and meteors, volcanic eruptions, and so on. Considering all reasons, water vapor is the main contributor to these fluctuations, but they still do not produce variations higher than roughly 1 hPa [22]. Given the fact that the fluctuations in the pressure at sea level represent around 0.1% of its total value of approximately 10^3 hPa , it is safe to say that, for the purposes of this study, the total mass of the atmosphere can be considered constant over time.

3.3 The seasonal effect of the muon flux

The interaction of a primary cosmic ray particle takes place mostly in the stratosphere, and the result is a cascade of electromagnetic and hadronic events. Most of the hadrons produced in the first interaction are mesons, mainly pions and kaons. The bulk of the muonic component of an EAS originates solely from these two mesons flavors, as their most probable decay channels contribute, directly or indirectly, to the production of muons, as it is shown in table 3.2. In the case of underground detectors, the vast majority of the detected muons must come from $(\pi^\pm, K^\pm) \rightarrow \mu\nu_\mu$, as other direct channels hold much smaller branching ratios and, in the case

of indirect channels, there is much less energy transferred to the final muon, which may not reach the detector depth.

Channel	Fraction ($\Gamma_i/\Gamma_{\text{total}}$)
$\pi^\pm \rightarrow \mu^\pm \nu_\mu(\bar{\nu}_\mu)$	$(99.98770 \pm 0.00004) \%$
$\eta \rightarrow \pi^+ \pi^- \pi^0$	$(28.10 \pm 0.34) \%$
$\eta \rightarrow \pi^+ \pi^- \gamma$	$(22.92 \pm 0.28) \%$
$K^\pm \rightarrow \mu^\pm \nu_\mu(\bar{\nu}_\mu)$	$(63.56 \pm 0.11) \%$
$K^\pm \rightarrow \pi^0 \mu^\pm \nu_\mu(\bar{\nu}_\mu)$	$(3.352 \pm 0.033) \%$
$K^\pm \rightarrow \pi^\pm \pi^0$	$(20.67 \pm 0.08) \%$
$K^\pm \rightarrow \pi^\pm \pi^\pm \pi^-$	$(5.583 \pm 0.024) \%$
$K^\pm \rightarrow \pi^\pm \pi^0 \pi^0$	$(1.760 \pm 0.023) \%$
$\rho^\pm \rightarrow \pi^\pm \pi^0$	$\sim 100 \%$
$\rho^0 \rightarrow \pi^+ \pi^-$	$\sim 100 \%$

Table 3.2 | Mesons main decay channels that contribute to the muonic component

The table presents the most common branching ratios that are likely to contribute to the muonic component of an EAS [3]. Charged pions always produce muons, as a first approximation, while at least 63% of the charged kaons directly decay into muons as well. The other channels do have a non negligible effect in the final muon flux at the surface, but lose influence when it comes to producing underground detectable muons, as *i)* their branching ratios are small, *ii)* the resulting pions may interact and, *iii)* the resulting muons are less likely to carry enough energy to reach the detector depth.

While the temperature variations in the stratosphere can be very high, reaching differences of 70 K in a matter of days², and the variations in the troposphere can vary by up to ~ 20 K during winter in temperate zones, the tropopause has a temperature profile that only shows variations over longer timescales, such as seasons. Although muons are expected to be produced throughout most of the development of an EAS, the most energetic muons, originated from the decay of secondary mesons, are more likely to be produced while still at altitudes within the tropopause. These more energetic muons are more likely to reach deeper underground depths and, therefore, be measured by underground detectors.

The probability of a meson to decay or interact depends on its energy and on the density of the medium that said particle is traversing. Therefore, it is expected that a denser (thinner) atmosphere profile increases the probability of a meson to interact (decay). Considering that the tropopause temperature (and density) varies following a yearly seasonality, and that the cosmic ray flux is isotropic and homogeneous for most of its energy spectrum, it is reasonable to expect that the muon rate measured by underground detectors should follow the same sea-

²This effect, in which the stratosphere suffers a drastic increase in temperature in a short period of time, is known as a Sudden Stratospheric Warming (SSW) effect.

sonality pattern as the one measured from the troposphere and tropopause temperatures. This relation between the muon flux measured underground and the temperature of the atmosphere is described in the following sections.

3.3.1 Muon production in the atmosphere

The process of quantifying the muon flux at a given underground depth starts by calculating the intensity of muons at the Earth's surface level. This intensity is directly related to the production of mesons in the atmosphere, which is considered to fall exponentially, as of e^{-X/Λ_N} , where X is the slant depth of traversed atmosphere (following the direction of the parent particle), and Λ_N is the absorption mean free path of the cosmic ray particle responsible for producing the mesons. The total intensity of muons at surface level is the integral of the differential intensity of muons at ground level produced by the EAS. Said differential intensity is given by the integral of the production \mathcal{P}_μ of muons from mesons (π and K) over the atmosphere [23]

$$\frac{dI_\mu}{dE_\mu} = \int_0^\infty \mathcal{P}_\mu(X, E_\mu) dX, \quad (3.7)$$

where \mathcal{P}_μ takes into account only the two body decay of pions and kaons into muons ($M \rightarrow \mu\nu_\mu$), being written as

$$\mathcal{P}_\mu(X, E) = \sum_{M=\pi, K} \frac{\epsilon_M}{X \cos \theta (1 - r_M)} \int_{E_\mu}^{E_\mu/r_M} \frac{\mathcal{M}(X, E) dE}{E} \frac{dE}{E}. \quad (3.8)$$

The equation above has one term for each considered meson, $r_M \equiv m_\mu^2/m_M^2$, and \mathcal{M} is the meson production spectrum

$$\mathcal{M}(X, E) = e^{(-X/\Lambda_M)} \frac{Z_{NM}}{\lambda_N} E_M^{(\gamma-1)} \int_0^\infty \left(\frac{X'}{X}\right)^{\epsilon_M/E \cos \theta} \exp\left(\frac{1}{\Lambda_M} - \frac{1}{\Lambda_N}\right) dX', \quad (3.9)$$

where Λ_M and Λ_N are the atmospheric attenuation lengths for mesons (M) and nucleons (N), λ_N is the nucleon interaction length, Z_{NM} is the spectrum-weighted inclusive cross section moment³, γ is the muon spectral index, and ϵ_M is the meson critical energy. Said energy defines the threshold in which the probabilities for a meson to decay or interact are equal, and it is written as

$$\epsilon_M = \frac{m_M c^2 H(T)}{c\tau_M}, \quad (3.10)$$

which, for the mesons of interest, yields $\epsilon_\pi = 115$ GeV and $\epsilon_K = 850$ GeV.

³The quantity Z_{NM} is better understood in the following terms: it determines the fluxes of uncorrelated particles in the atmosphere, as it measures the fraction of energy that is transferred to the particles of type M .

The solution of equation 3.7 is shown to be [24]

$$\frac{dI_\mu}{dE_\mu} \simeq AE_\mu^{-(\gamma+1)} \left(\frac{A_\pi^1}{1 + 1.1E_\mu \cos \theta / \epsilon_\pi} + \frac{0.635A_K^1}{1 + 1.1E_\mu \cos \theta / \epsilon_K} \right), \quad (3.11)$$

where A is an adjustable parameter, and

$$A_M^1 \equiv \frac{Z_{NM}(1 - r_M^{\gamma+1})}{(1 - r_M)(\gamma + 1)}. \quad (3.12)$$

Using numerical values from [23], equation 3.11 becomes

$$\frac{dI_\mu}{dE_\mu} \simeq 0.14E_\mu^{-(\gamma+1)} \left(\frac{1}{1 + 1.1E_\mu \cos \theta / \epsilon_\pi} + \frac{0.054}{1 + 1.1E_\mu \cos \theta / \epsilon_K} \right) \frac{\text{muons}}{\text{cm}^2 \text{ sr GeV}}, \quad (3.13)$$

which is the same result mentioned in Chapter 2, equation 2.15. This equation is used to find the total intensity of muons at surface, given by

$$I_\mu(E) = \int_{E_{\text{th}}}^{\infty} \frac{dI_\mu}{dE_\mu} dE_\mu. \quad (3.14)$$

Equation 3.14 returns the total intensity of muons at surface above an energy threshold E_{th} . Plugging equation 3.11 into equation 3.14 and integrating should result in [24]

$$I_\mu \simeq B \times E_{\text{th}}^{-\gamma} \left(\frac{1}{\gamma + (\gamma + 1)1.1E_{\text{th}} \cos \theta / \epsilon_\pi} + \frac{0.054}{\gamma + (\gamma + 1)1.1E_{\text{th}} \cos \theta / \epsilon_K} \right), \quad (3.15)$$

where B is an adjustable scalar parameter. Equation 3.15 describes the intensity of muons at surface level originated by the direct decays of charged pions and kaons into muons and neutrinos, whose propagation happened in an isothermal atmosphere that follows a density profile which decays exponentially with altitude. The $E_{\text{th}} \cos \theta$ term represents the vertical muon energy threshold needed, at surface level, for a muon to reach a given detector depth. In the case of the NO ν A Near Detector, $E_{\text{th}} \cos \theta \simeq 54$ GeV.

3.3.2 The effect of the temperature in the muon intensity

The changes in the final muon intensity caused by variations in the atmospheric temperature is quantitatively intricate. As shown in figure 3.1, the atmospheric temperature obeys a non uniform and complicated profile. A second problem is that mesons and muons are not produced at particular depths, with the task to trace back at which level a particular muon was produced using surface or underground detector measurements being very complicated (if not impossible). Furthermore, the model presented in Section 3.3.1 is, by premise, isothermal, with its connection with the atmospheric temperature lying inside the pions and kaons critical energies ϵ_M (equation 3.10), since they are written as a function of the atmospheric scale height $H(T)$

(defined in equation 3.5).

A form of solving these problems is achieved by defining an effective temperature of the atmosphere T_{eff} , which represents an average temperature that matches the measured muon intensity I_{μ}^0 , in case the atmosphere were indeed isothermal. Since a variation in the temperature would result in a change in the value of the critical energy ϵ_M , a new parameter η is defined as

$$\eta(X) \equiv \frac{T(X) - T_{\text{eff}}}{T_{\text{eff}}}, \quad (3.16)$$

such that the critical energy can be rewritten as

$$\epsilon_M(X) = \epsilon_M^0 [1 + \eta(X)], \quad (3.17)$$

where ϵ_M^0 is the critical energy of the meson when $T = T_{\text{eff}}$. This new critical energy, which now includes variation in the temperature as being a part of the production spectrum of muons, implies that an increment in the average temperature of the atmosphere should affect equation 3.7 as following

$$\frac{dI_{\mu}}{dE_{\mu}}(X, E_{\mu}, T_{\text{eff}} + \Delta T) = \int_0^{\infty} \mathcal{P}_{\mu}(X, E_{\mu}, T_{\text{eff}} + \Delta T) dX. \quad (3.18)$$

The muon production spectrum \mathcal{P}_{μ} , as shown in equation 3.8, is written as a function of the meson production spectrum \mathcal{M} (defined in equation 3.9). Therefore, by defining

$$\Delta \mathcal{M} \equiv \mathcal{M} - \mathcal{M}^0, \quad (3.19)$$

where \mathcal{M}^0 is the meson production spectrum for $T = T_{\text{eff}}$, allows one to use the new $\Delta \mathcal{M}$ to write $\Delta \mathcal{P}_{\mu}$, which in turn leads to the variation in the differential muon intensity [24]

$$\Delta \frac{dI_{\mu}}{dE_{\mu}} = \sum_{M=\pi, K} \alpha_M(X) \frac{\Delta T(X)}{T_{\text{eff}}}, \quad (3.20)$$

in which $\alpha_M(X)$ is defined as

$$\alpha_M(X) = \int_{E_{\text{th}}}^{\infty} \frac{A_M^1 E_{\mu}^{-(\gamma+1)} e^{-X/\Lambda_M}}{1 + B_M^1 K(X) (E_{\mu} \cos \theta / \epsilon_M^0)^2} dE_{\mu}. \quad (3.21)$$

The parameter A_M^1 is described in equation 3.12, while

$$B_M^1 \equiv \frac{(\gamma + 3)(1 - r_M^{\gamma+1})}{(\gamma + 1)(1 - r_M^{\gamma+3})}, \quad (3.22)$$

and

$$K(X) \equiv \frac{(1 - X/\Lambda'_M)^2}{(1 - e^{-X/\Lambda'_M}) \Lambda'_M / X}, \quad (3.23)$$

with

$$\frac{1}{\Lambda'_N} = \frac{1}{\Lambda_N} - \frac{1}{\Lambda_M}. \quad (3.24)$$

The $\alpha_M(X)$ term is known as the temperature correlation coefficient, as it is the scaling factor that connects the variation in the muon intensity with the variation in the temperature. It is important to stress the fact that any variation is always taken with respect to I_μ^0 and T_{eff} , being I_μ^0 the muon intensity when $T = T_{\text{eff}}$.

The integration of equation 3.20 over the atmospheric depth X provides the variation of the total intensity ΔI_μ at the surface level due to temperature effects and it is written as [24]

$$\Delta I_\mu = \sum_{M=\pi, K} \int_0^\infty \alpha_M(X) \frac{\Delta T(X)}{T_{\text{eff}}} dX, \quad (3.25)$$

with T_{eff} still being an undefined parameter. Naturally, T_{eff} cannot be a random average, as it must reflect the temperature in which most muons are produced. As such, in order to find T_{eff} , one may start by expanding the term $\Delta T(X)$ in equation 3.25, which results in

$$\Delta I_\mu = \sum_{M=\pi, K} \left[\frac{1}{T_{\text{eff}}} \int_0^\infty \alpha_M(X) T(X) dX - \int_0^\infty \alpha_M(X) dX \right]. \quad (3.26)$$

As previously stated, for $T(X) = T_{\text{eff}} \rightarrow I_\mu = I_\mu^0$ and, as a result, $\Delta I_\mu = 0$. In this case, equation 3.26 must yield zero, and the following statement can be made

$$\frac{1}{T_{\text{eff}}} \sum_{M=\pi, K} \int_0^\infty \alpha_M(X) T(X) dX = \sum_{M=\pi, K} \int_0^\infty \alpha_M(X) dX$$

$$T_{\text{eff}} = \frac{\sum_M \int_0^\infty T(X) \alpha_M(X) dX}{\sum_M \int_0^\infty \alpha_M(X) dX}, \quad (3.27)$$

which shows that the effective temperature is a weighted average over the temperatures of the atmosphere, whose values are weighted by the function that governs the muon production from the decay of pions and kaons. Experimentally, the data for $T(X)$ is collected at discrete levels of the atmosphere and, as such, it is reasonable to convert the integral in equation 3.27 into the following summation

$$T_{\text{eff}} = \frac{\sum_M \sum_{i=1}^n T(X_i) \alpha_M(X_i) \Delta X_i}{\sum_M \sum_{i=1}^n \alpha_M(X_i) \Delta X_i}$$

$$T_{\text{eff}} = \frac{\sum_{i=1}^n T(X_i) [\alpha_\pi(X_i) + \alpha_K(X_i)] \Delta X_i}{\sum_{i=1}^n [\alpha_\pi(X_i) + \alpha_K(X_i)] \Delta X_i}, \quad (3.28)$$

which considers the contributions from both pions and kaons ($M = \pi, K$), and sums the data

over n discrete levels of the atmosphere. In the literature, equation 3.28 is also commonly written as

$$T_{\text{eff}} = \frac{\sum_{i=1}^n T(X_i)[W_{\pi}(X_i) + W_K(X_i)]\Delta X_i}{\sum_{i=1}^n [W_{\pi}(X_i) + W_K(X_i)]\Delta X_i}, \quad (3.29)$$

in which

$$W_{\pi,K}(X) = \frac{A_{\pi,K}^1(1 - X/\Lambda'_{\pi,K})^2 e^{-X/\Lambda_{\pi,K}}}{\gamma + (\gamma + 1)B_{\pi,K}^1 K(X)(E_{\text{th}} \cos \theta / \epsilon_{\pi,K})^2} \quad (3.30)$$

is referred to as the weighting function. The values for the terms of $W_{\pi,K}$ can be seen in table 3.3 [44]. The result presented in equation 3.29 emerges naturally and is compatible to the result shown in equation 3.28 by defining

$$\alpha(X) \equiv \frac{T_{\text{eff}}}{I_{\mu}^0} W(X), \quad (3.31)$$

where

$$W(X) \equiv \sum_{M=\pi,K} W_M(X) = W_{\pi}(X) + W_K(X), \quad (3.32)$$

and replacing $\alpha(X)$ in equation 3.25 by its definition from equation 3.31, being the rest of the development analogous to the one herein stated.

Parameter	Value	Definition
A_{π}^1	1	Defined in equation 3.12
A_K^1	$0.38 \cdot r_{K/\pi}$	–
$r_{K/\pi}$	0.149 ± 0.06	Kaon/pion ratio
B_{π}^1	1.469 ± 0.007	Defined in equation 3.22
B_K^1	1.740 ± 0.028	–
Λ_N	120 g/cm^2	Attenuation length of the primary nucleon
Λ_{π}	180 g/cm^2	Pion attenuation length
Λ_K	160 g/cm^2	Kaon attenuation length
$E_{\text{th}} \cos \theta$	–	Vertical threshold energy for muons to reach a given depth
γ	1.7 ± 0.1	Muon spectral index
ϵ_{π}	$114 \pm 3 \text{ GeV}$	Pion critical energy
ϵ_K	$851 \pm 14 \text{ GeV}$	Kaon critical energy

Table 3.3 | $W_{\pi,K}(X)$ parameters

The table presents the parameters included in the weighting function $W_{\pi,K}(X)$, which accounts for both pions and kaons [44]. The only unknown parameter is the vertical threshold energy for muons, as it is an *a posteriori* value that can only be determined after the assessment of the depth and rock composition above a given underground detector. In the case of the NO ν A Near Detector, $E_{\text{th}} \cos \theta = 54 \text{ GeV}$.

Similarly to the fact that there is a defined effective temperature T_{eff} that accounts for all values of $T(X)$, it is useful to define an effective temperature coefficient α_T that also accounts for all $\alpha_M(X)$ coefficients

$$\alpha_T = \frac{1}{I_\mu^0} \sum_{M=\pi, K} \int_0^\infty \alpha_M(X) dX. \quad (3.33)$$

In view of the fact that the data is collected at discrete levels, equation 3.25 can be rewritten as

$$\Delta I_\mu = \frac{\Delta T_{\text{eff}}}{\langle T_{\text{eff}} \rangle} \sum_{M=\pi, K} \int_0^\infty \alpha_M(X) dX, \quad (3.34)$$

and substituting the definition of α_T from equation 3.33 in equation 3.34, one should find

$$\frac{\Delta I_\mu}{I_\mu^0} = \alpha_T \frac{\Delta T_{\text{eff}}}{\langle T_{\text{eff}} \rangle}, \quad (3.35)$$

where $\Delta T_{\text{eff}} \equiv T_{\text{eff}}^j - \langle T_{\text{eff}} \rangle$, in which T_{eff}^j is the j -th effective temperature, that represents the T_{eff} at a specific time, and $\langle T_{\text{eff}} \rangle$ is the average of all discrete effective temperatures measured over the period of time of interest.

Experiments measure the intensity of muons by calculating the muon rate, which is the number of counted muons divided by the detector exposure time. Furthermore, the muon rate depends on the detector's efficiency (ξ), effective area (A_{eff}), and solid angle acceptance (Ω). On that premise, the intensity of muons is related to the rate as following

$$I_\mu = \frac{N_\mu / \Delta t}{\xi A_{\text{eff}} \Omega}, \quad (3.36)$$

where N_μ is the number of muons counted over the time Δt . Taking in consideration that equation 3.35 is written as $\Delta I_\mu / I_\mu^0$, equation 3.36 can be rewritten as

$$\frac{\Delta I_\mu}{I_\mu} = \left[\frac{\Delta N_\mu / \delta t}{\xi A_{\text{eff}} \Omega} \right] / \left[\frac{N_\mu / \Delta t}{\xi A_{\text{eff}} \Omega} \right] = \left[\frac{\Delta N_\mu}{\delta t} \right] / \left[\frac{N_\mu}{\Delta t} \right] \equiv \frac{\Delta R_\mu}{\langle R_\mu \rangle}, \quad (3.37)$$

in which $\Delta N_\mu = N_\mu^i - N_\mu$, with N_μ^i being the muon count over a period of time δt that is shorter and within the total period Δt . As a result, $\Delta N_\mu / \delta t \equiv \Delta R_\mu$ represents the variation of the muon rate with respect to the global average $N_\mu / \Delta t \equiv \langle R_\mu \rangle$. Finally, the combination of equations 3.35 and 3.37 leads to

$$\frac{\Delta R_\mu}{\langle R_\mu \rangle} = \alpha_T \frac{\Delta T_{\text{eff}}}{\langle T_{\text{eff}} \rangle}. \quad (3.38)$$

Equation 3.38 connects the variations in the muon rate with respect to the total average rate measured by the detector over a time period, with the variations in the effective temperature

with respect to the total average effective temperature of the atmosphere over the same time period by the effective temperature coefficient α_T .

3.3.3 Theoretical prediction of α_T

The theoretical prediction of α_T can be inferred from equation 3.35, which, with a small rearrangement, yields

$$\alpha_T = \frac{T}{I_\mu^0} \frac{\partial I_\mu}{\partial T}. \quad (3.39)$$

A complication with equation 3.39 is that the muon intensity (equation 3.15) has no direct dependence with temperature, as such variable is carried in the meson critical energies. Therefore, a more useful form of equation 3.39 is [24]

$$\alpha_T = -\frac{E_{\text{th}}}{I_\mu^0} \frac{\partial I_\mu}{\partial E_{\text{th}}} - \gamma. \quad (3.40)$$

From equation 3.40, and using equations 3.11 and 3.15, it is possible to show that

$$\alpha_T = \frac{1}{D_\pi} \frac{1/\epsilon_K + A_K^1 (D_\pi/D_K)^2/\epsilon_\pi}{1/\epsilon_K + A_K^1 (D_\pi/D_K)/\epsilon_\pi}, \quad (3.41)$$

where

$$D_{\pi,K} = \frac{\gamma}{(\gamma + 1)} \frac{\epsilon_{\pi,K}}{1.1 E_{\text{th}} \cos \theta} + 1. \quad (3.42)$$

The contribution from the kaon decays ($K^\pm \rightarrow \mu\nu$) come from the term A_K^1 and, as such, if one sets $A_K^1 = 0$, the theoretical prediction of α_T is reduced to the pion contribution only:

$$(\alpha_T)_\pi = 1 / \left[\frac{\gamma}{(\gamma + 1)} \frac{\epsilon_\pi}{1.1 E_{\text{th}} \cos \theta} + 1 \right]. \quad (3.43)$$

3.4 Experimental results on the seasonal variations of the muon flux

The experimental evidence of the correlation between atmospheric temperature variations and the measured muon flux at surface or underground has been reported by several experiments since 1952, and not always showing good agreement with the theoretical prediction. The compilation of the published experimental results related to single muon seasonal variations is presented in Refs. [25–53], while Refs. [54–56] show the results exploring multiple-muon seasonal modulations. Therefore, the next sections are dedicated to briefly outline these experiments and their main contributions. In this compilation of results, some early experiments were named after the first author of the published paper or its location, as there was not a scientific collaboration, and/or the experimental apparatus itself did not have any official designation, as

it became customary after the 1970's. Finally, the list is organized by chronological order. Experiments that have more than one published result will have all their results listed in the same subsection, causing a few results to be out of chronological order, but the caveat is that at least the first result of every listed experiment is presented following a timely fashion.

3.4.1 Single muons

The effective correlation coefficient so far was presented as a dimensionless number. However, earlier experiments used to present their results in $\%/K$ or $\%/^{\circ}C$, which depends upon the measured $\langle T_{\text{eff}} \rangle$ at the time and location of each experiment. As a consequence, each conversion from $(\alpha_T)_{\%/[K,^{\circ}C]}$ to α_T needs its respective $\langle T_{\text{eff}} \rangle$. In the cases in which the $\langle T_{\text{eff}} \rangle$ was not informed by the authors, a standard $\langle T_{\text{eff}}^0 \rangle = 223 \text{ K}$ was adopted for the conversion.

Barrett [26,28]

The experiment carried out by P. Barrett *et al.* interprets a series of measurements by a detector placed underground in a salt mine near Ithaca (NY), at 1574 mwe⁴, using a telescope that consisted of a stack of horizontal planes of Geiger counter tubes and lead absorbers. In order to provide 3D resolution, alternating instrumented planes were rotated horizontally by 90° with respect to each other, as shown in figure 3.2 (a).

The first published result [26], represents the first measurement of the temperature coefficient α_T . The experiment took data during 2 periods, named Series I and Series II. The first represents data collected between August, 1950, and February, 1951, while Series II collected data from July to October of 1951. The temperature information used to calculate the effective temperature was provided by the U.S. Weather Bureau from radiosonde observations, made by the Air Force station at Rome (NY), which is located 75 miles northeast of the salt mine. The reported value of the effective temperature coefficient was $(\alpha_T)_{\%/K} = 0.79 \pm 0.20$, which yields $\alpha_T = 1.76 \pm 0.45$.

A new measurement was published two years later [28], after improvements in the experimental apparatus. In this second work, the data was taken by 3 independent telescopes, similars to the one described in [26], aiming to reach smaller statistical uncertainties. The experiment recorded data between November, 1952, and August, 1953. The combined data of all telescopes yielded an effective temperature coefficient of $(\alpha_T)_{\%/K} = 0.33 \pm 0.12$, or $\alpha_T = 0.73 \pm 0.26$. The combination of both α_T values results in a final $(\alpha_T)_{\%/K}^{\text{Total}} = (\alpha_T)_{\%/K} [26] + (\alpha_T)_{\%/K} [28] = 0.46 \pm 0.11$, which, after conversion, yields $\alpha_T = 1.02 \pm 0.24$. Figure 3.2 (b) shows the last experimental value for $(\alpha_T)_{\%/K}$ found by Barrett *et al.*, along with $(\alpha_T)_{\%/K}^{\text{Total}}$.

⁴Meters of water equivalent, used to normalize different depths under different densities of overburden.

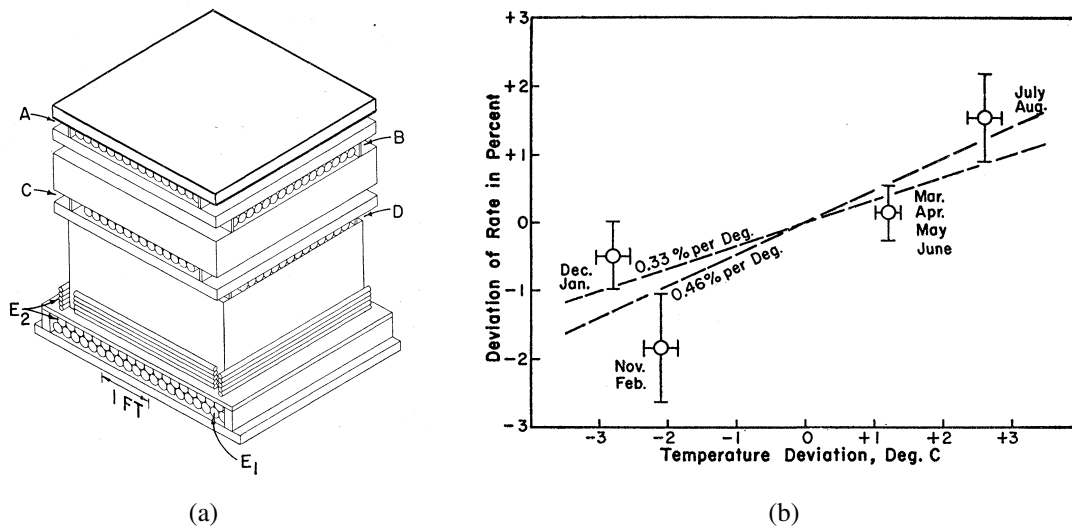


Figure 3.2 | Barrett *et al.* experimental apparatus and measured α_T

(a) Schematic figure of the telescope used in the experiment, showing the alternating planes of Geiger counters, separated by slabs of lead [26]. (b) Plot showing the muon rate deviations as a function of the effective temperature deviations, along with 2 measured values for the correlation coefficient: $(\alpha_T)_{\%/K} = 0.33\%/K$ represents the findings in [28], while $(\alpha_T)_{\%/K} = 0.46\%/K$ is the combined results from [26] and [28].

Sherman [27]

N. Sherman's experiment reported muon seasonal variations from a detector placed at an underground depth of 846 mwe, in a salt mine in Detroit, Michigan. The experimental apparatus is similar to the one described in the previous section, being a set of trays with Geiger tubes separated by slabs of lead.

There were 4 intervals of data taking, being: (1) September to December of 1951; (2) December, 1951, to March 1952; (3) May to August of 1952; and (4) August, 1952 until June 1953. The atmospheric temperature was supplied by radiosonde observations taken by an Air Force weather squadron, made at Selfridge Field, Michigan, about 50 miles from the mine.

The correlation coefficient was found to be $(\alpha_T)_{\%/K} = 0.22 \pm 0.06$, which is equivalent to $\alpha_T = 0.48 \pm 0.13$.

Hobart [29]

This experiment detailed the observation of underground muons at Hobart, in the Australian island of Tasmania. The detector was placed in a disused railway tunnel, providing an overburden of 42 mwe, and consisted of a set of two 1 m² trays with Geiger tubes, with a vertical separation of 50 cm between both planes. Although not strictly specified, the used data was collected within years 1958 and 1959.

The value of the reported effective temperature coefficient was $(\alpha_T)_{\%/K} = 0.028 \pm 0.009$,

which after conversion results in $\alpha_T = 0.06 \pm 0.02$.

Torino [30]

This experiment was build in the *Monte dei Cappuccini* Laboraty, located in Turin, Italy. The detector sat under an overburden of 70 mwe, and was composed by 4 plastic scintillators covering a total area of 2 m². The analysis comes from a data sample recorded over 280 days in the years of 1965 and 1966. The temperature data was provided by the radiosonde station Milano Linate, located in Milan.

The reported value for the effective temperature coefficient was $(\alpha_T)_{\%/K} = 0.041 \pm 0.010$, or $\alpha_T = 0.09 \pm 0.02$.

Poatina [31]

This paper presents the results from a detector placed in Poatina, which is a small city located in Tasmania, Australia. The detector itself was placed at a depth of 357 mwe, and it is a set of geiger tubes displaced in three planes, similarly as described in [29]. In this study, the data was collected within 1972 and 1977, while the temperature data was provided by the Australian Bureau of Meteorology.

The experiment reported a temperature correlation coefficient of $(\alpha_T)_{\%/K} = 0.063 \pm 0.008$ ($\alpha_T = 0.14 \pm 0.02$), proving to be much smaller than the expected value from Monte Carlo simulations, which yielded $(\alpha_T)_{\%/K}^{MC} = 0.22 \pm 0.05$ ($\alpha_T = 0.49 \pm 0.01$). The lower value was attributed to a possible kaon contribution to the measured muon flux, which would affect the predicted value by diminishing it. Although the hypothesis was outlined, no further results were presented to explain the discrepancy.

Utah [32]

This subsection briefly describes the study of atmospheric effects on the muon flux presented by the Utah Anisotropy Detector, located in Salt Lake City, Utah. The detector is under a total overburden of 486 mwe, and consists of 3 layers of plastic scintillators [57]. Weather data were obtained from the Salt Lake City weather station of National Oceanic and Atmospheric Administration (NOAA).

The published result was found to be $(\alpha_T)_{\%/K} = 0.134 \pm 0.004$, which is equivalent to $\alpha_T = 0.299 \pm 0.009$.

Matsushiro [33]

The results present data from the Matsushiro underground telescope, located in the city of Matsushiro, in Japan. The telescope is located at an underground depth of 250 mwe, and it consists of two horizontal layers of plastic scintillators of 1 m² each, separated by a vertical distance of 1.5 m. The results correlate the muon seasonal variations with barometric variations

and temperature variations. The barometric correlation with the muon flux is a topic that is not discussed in this study, as it is only relevant at surface/shallow detectors. Given the fact that the authors combine both parameters (the barometric and the temperature coefficients) in their result, and such measurement is not easily comparable with the other results.

Sagisaka [34]

The results presented by S. Sagisaka show the muon seasonal variations at 3 underground stations located in Matsushiro, Misato, and Sakashita, Japan. Matsushiro has a total of 250 mwe, while Misato and Sakashita are under 34 mwe and 80 mwe, respectively. The findings correlate the muon seasonal variations with barometric variations and temperature variations, as two of detectors are at shallower depths. Similarly to the case described in Matsushiro, the author combines both parameters (the barometric and the temperature coefficients) in his result, not being easily comparable.

Baksan [35]

The Baksan Underground Scintillator Telescope is located in the small town of Baksan, in Russia, under a depth of 850 mwe. Not much information is found describing in details the apparatus, except that there is a total of 6 telescopes with different apertures and directions, in order to provide flexibility to verify correlations with different zenith angles. In this particular study, only the data from the telescope with the widest aperture was used, which represents a total of 5 years of exposure time, ranging from January of 1983 to December of 1987.

The measured effective temperature correlation coefficient yielded $(\alpha_T)_{\%/K} = 0.372 \pm 0.038$ ($\alpha_T = 0.829 \pm 0.084$).

Matsushiro and Kamiokande II [36,37]

Muon seasonal variations observed by the Matsushiro underground telescope and the Kamiokande II Experiment are compared. The Kamiokande⁵ II Experiment was located in the Kamioka Observatory, in the city of Mizum, Japan, being 79 km west of Matsushiro. The detector consisted of a large cylindrical steel tank, containing 2,400 tons of water and surrounded by 948 PMTs used to detect Cherenkov radiation. The main purpose of the experiment was to search for nucleon decay.

The data used in the analysis ranged from January, 1987, to April, 1990, and it used to compare the deviations seen in the muon flux with respect to the average in both detectors. Although no temperature correlation coefficient is presented, the results confirm that more energetic events are more susceptible to atmospheric temperature variations. This conclusion is reached by comparing the amplitude of the muon seasonal deviations with respect to average

⁵Kamiokande is an acronym for Kamioka Nucleon Decay Experiment.

muon flux found by each experiment. Matsushiro presented an amplitude deviation of approximately 0.5%, while Kamiokande II reported an average amplitude close to 1%. The ratio between both amplitudes yields $(\text{Kamiokande-II/Matsushiro}) = 1.92 \pm 0.98$, showing that the atmospheric temperature induced modulation of the muon flux increases with energy.

MACRO [38]

The MACRO⁶ Experiment is the first large detector to report the value of α_T . The detector was located in the National Laboratories of the Gran Sasso (LNGS), in the city of L'Aquila, in central Italy. The LNGS lies inside a mountain which the laboratory carries the name from. As a consequence of being in the core of a mountain, the MACRO detector is under a great overburden, with a minimum of 3,100 mwe. It is a large liquid scintillator detector, with dimensions of 77 m long, 12 m wide, and 9 m high.

The data used in the presented result represents 4 years of detector exposure time, from 1991 to 1994, while the temperature data were provided by the *Ispettorato Telecomunicazioni ed Assistenza Volo dell'Aeronautica Italiana*. The resulting $\Delta R_\mu / \langle R_\mu \rangle$ and $\Delta T_{\text{eff}} / \langle T_{\text{eff}} \rangle$ as a function of month of year (i.e., the 4 years average of each month) are presented in figure 3.3.

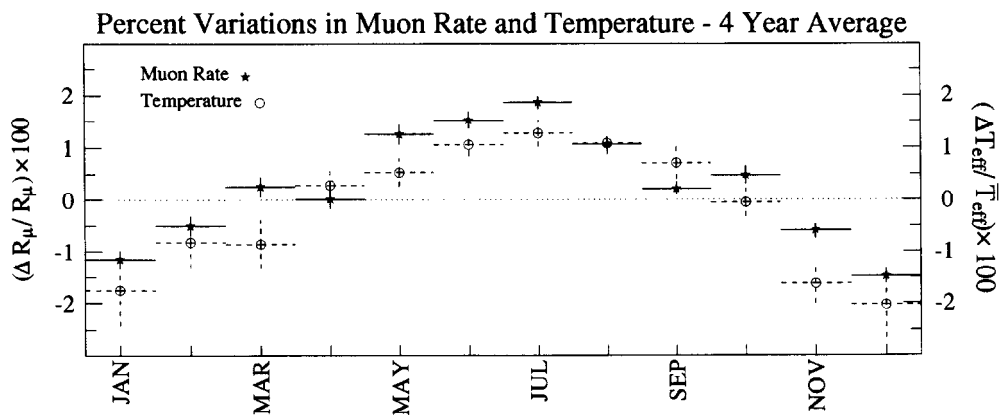


Figure 3.3 | MACRO's $\Delta R_\mu / \langle R_\mu \rangle$ and $\Delta T_{\text{eff}} / \langle T_{\text{eff}} \rangle$ as a function of month of year

Figure shows the average monthly data for both $\Delta R_\mu / \langle R_\mu \rangle$ and $\Delta T_{\text{eff}} / \langle T_{\text{eff}} \rangle$ considering a total of 4 years of detector exposure time. The data shows a correlation very close to unity [38].

The measured value of the effective correlation coefficient for the 4 years of detector exposure yielded $\alpha_T = 0.98 \pm 0.12$.

AMANDA [39]

The AMANDA⁷ Experiment is a deep underground detector located in the South Pole. The detector is buried under the Antarctic ice cap, ranging from 1,500 m and 2,035 m below surface,

⁶Acronym for Monopole, Astrophysics, and Cosmic Ray Observatory.

⁷Acronym for Antarctic Muon and Neutrino Detector Array.

with its center is located at 1,730 m underground, representing a total of 1,590 mwe of overburden. The detector concept is based on a large set cylindrical excavated vertical holes in the ice cap, from which long strings of spherical modules containing PMTs are deployed, creating a grid of over 700 detectors spread over a large underground volume.

The data encompasses a total of 225 days collected during 1997, while the weather information is collected by the Antarctic Support Associates (ASA) and made available by the Antarctic Meteorology Research Center (AMRC).

The final result for the correlation coefficient holds $\alpha_T = 0.86 \pm 0.05$.

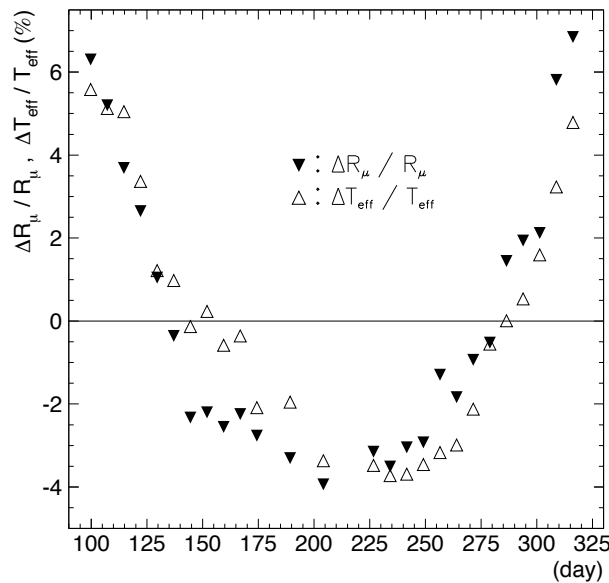


Figure 3.4 | AMANDA's $\Delta R_\mu / \langle R_\mu \rangle$ and $\Delta T_{\text{eff}} / \langle T_{\text{eff}} \rangle$ as a function of day of year

Figure shows the data for both $\Delta R_\mu / \langle R_\mu \rangle$ and $\Delta T_{\text{eff}} / \langle T_{\text{eff}} \rangle$ for the day of the year. Since the detector is in the South Pole, the winter and summer are inverted when compared to the north hemisphere, hence, the inversion of the minimum and maximum in the graph. The temperature data was scaled to the measured value of α_T [39].

LVD [41]

The LVD⁸ is also located in LNGS, similar to MACRO. The detector is a 1 kton liquid scintillator detector, whose main purpose is to search for neutrino burst originated by cataclysmic stellar events, such as supernovae. There is a total of 840 scintillator counters, arranged in a structure of 3 rectangular towers parallel to each other, resulting in a total volume of $13 \times 23 \times 10 \text{ m}^3$.

The result presented in [41] shows the muon seasonal variations from the data taken during a period that ranged from January, 2001, to December, 2008, resulting in a total live time of 2907 days. No temperature coefficient is calculated, nor the data is compared to temperature, with only the average muon intensity being compared to expected results. Despite the lack

⁸Acronym for Large Volume Detector.

of temperature comparison, given the location of the detector, the data shows a clear positive correlation with the expected temperature phase, as shown in figure 3.5.

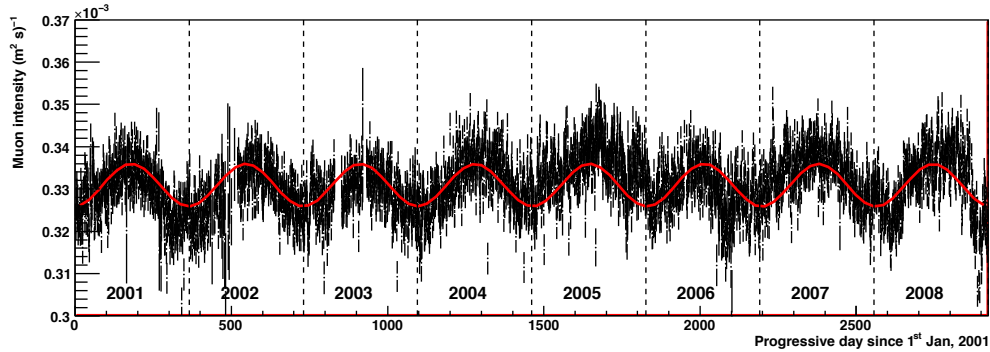


Figure 3.5 | Muon intensity variations as seen by LVD

Figure shows the muon intensity variations as a function of time registered by LVD [41].

IceCube [42]

The IceCube Experiment is a larger and newer version of the already mentioned AMANDA Experiment. After 2005, this new version of the experiment has been incrementally growing. In this result, data from 2007 up to 2009 was analyzed, and the weather data was provided by the Antarctic Meteorology Research Center, and NOAA's Polar Orbiting Environmental Satellites (POES). Both data is shown in figure 3.6 (a). The resulting correlation is shown in figure 3.6 (b), along with the effective temperature correlation coefficient, which yielded $\alpha_T = 0.901$.

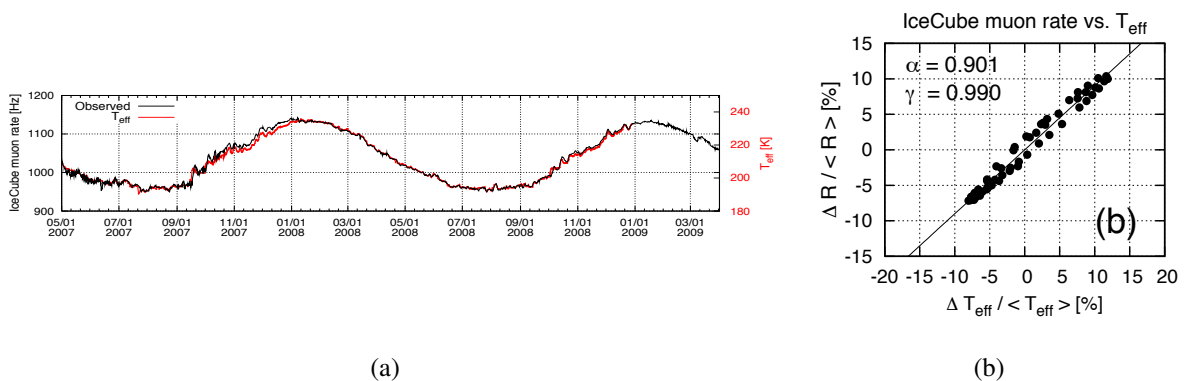


Figure 3.6 | IceCube muon seasonal variations and α_T

(a) Figure shows the muon rate measured by the IceCube detector (black curve) along with the effective temperature of the atmosphere (red curve). (b) Figure shows $\Delta R / \langle R \rangle$ vs. $\Delta T_{\text{eff}} / \langle T_{\text{eff}} \rangle$, along with the measured effective temperature coefficient $\alpha_T = 0.901$ [42].

MINOS [44,49]

The MINOS⁹ Experiment was developed for detecting neutrino oscillations. As such, the experiment is comprised of two functionally identical detectors, namely the Near Detector (ND) and the Far Detector (FD). The first is located at the Fermi National Accelerator Laboratory, in Batavia, Illinois, in a 104 m below surface cavern, resulting in a total of 225 mwe of overburden. The latter was located in the Soudan Underground Mine State Park, in northern Minnesota, 731 km far from the Near Detector. The depth of the mine is 715 m below surface level, resulting in a total overburden of 2100 mwe.

The concept of both detectors is based on a collection of vertical octagonal planes, following an intercalated pattern between plastic scintillators, and steel planes. Every active plane is composed by several long strips of plastic scintillators. The orientation of the strips is intercalated in such a way that the planes are rotated by 90° with respect to one another, enabling for 3D track reconstruction. The Near Detector is made of 3.8 m × 4.8 m planes, and it is 17 m long, resulting in a total mass of 0.98 ktons, while the Far Detector was composed by 8.0 m × 8.0 m planes, and it is 31 m long, yielding a total mass of 5.4 ktons. Each detector produces a ~1.4 T toroidal magnetic field, allowing for charge reconstruction.

The MINOS experiment presented results for the single muon seasonal variations in both detectors. Chronologically, the first measurement [44] used data from the Far Detector from 2003 to 2008. The temperature data for the location of the detector was provided by the European Center For Medium-Range Weather Forecast (ECMWF). The muon seasonal effect, along with the effective temperature variations over the period of the detector live time can be seen in figures 3.7 (a) and (b). The measured correlation coefficient yielded $\alpha_T = 0.873 \pm 0.009$ and is presented in figure 3.7 (c).

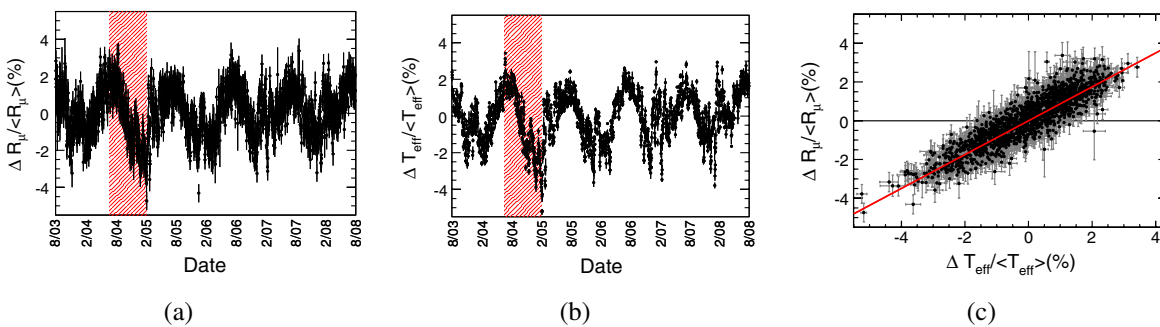


Figure 3.7 | MINOS FD muon and T_{eff} seasonal variations, and α_T

Figure shows (a) the muon seasonal variations, (b) the seasonal variation of the effective temperature of the atmosphere, and (c) the effective correlation coefficient α_T . The hatched region in both (a) and (b) plots represent a period of time in which the detector run with its magnetic field reversed from the normal configuration [44].

The second MINOS result [49] was published 4 years after the first result, aiming to verify

⁹Acronym for Main Injector Neutrino Oscillation Search.

the effect in its smaller Near Detector. The data used in the analysis was collected over the period between 2006 and 2012. Similarly to the previous result, the analysis used the temperature data provided by ECMWF, but systematic uncertainties were calculated by comparing ECMWF data with data from the Integrated Global Radiosonde Archive (IGRA). The muon seasonal effect, along with the effective temperature variations are shown in figures 3.8 (a) and (b). The measured correlation, seen in figure 3.8 (c), reporting an $\alpha_T = 0.428 \pm 0.003$ (stat.) ± 0.059 (syst.). Said result is consistent with the theoretical prediction of $\alpha_T^{\text{theory}} = 0.390 \pm 0.004$ (stat.) ± 0.028 (syst.).

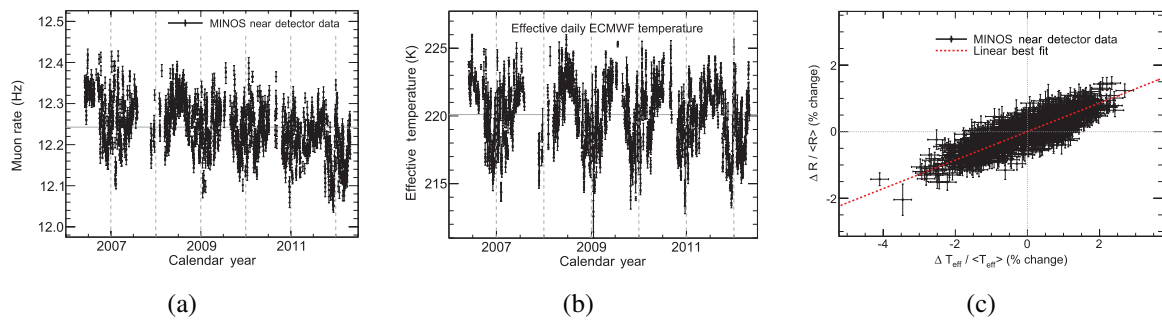


Figure 3.8 | MINOS ND muon and T_{eff} seasonal variations, and α_T

Figure shows (a) the muon seasonal variations, (b) the seasonal variation of the effective temperature of the atmosphere, and (c) the effective correlation coefficient α_T [49].

Another important result presented in [49] shows a new approach to calculate α_T . Previously, α_T calculations were integrated over the zenith angle. However, extensive air showers with higher zenith angles traverse longer lengths in less dense layers of the atmosphere, and therefore their pions and kaons are more prone to decay, resulting in higher α_T values. This discrepancy is overcome by creating a weighted effective temperature

$$T_{\text{eff}}^{\text{weighted}} = \sum_{i=1}^N F_i \cdot T_{\text{eff}}(\theta_i), \quad (3.44)$$

where N is the number of bins in which the zenith angle distribution is divided, F_i is the fraction of the single muon events counted in bin i , and $T_{\text{eff}}(\theta_i)$ is the angular effective temperature in bin i (i.e., applying the corresponding $E_{\text{th}} \cos \theta_i$ in the calculation of the effective temperature). This alternative approach yielded a final value of $\alpha_T^{\text{weighted}} = 0.352 \pm 0.003$ (stat.) ± 0.046 (syst.), also consistent with the aforementioned expected α_T^{theory} .

Borexino [46,48]

The Borexino Experiment is located at LNGS, in Italy, covered by 3,800 mwe of overburden from the Gran Sasso. The main objective of the experiment is to study low-energy solar neutrinos. Given its large overburden, it is also a powerful tool for studying high energy cosmic ray muons. The detector encompasses two parts. The first is a spherical volume filled with 278 tons

of an organic liquid scintillator, whose light is detected by 2212 inward facing PMTs lying in the surrounding shell, is known as the Inner Detector. The Outer Detector comprises the second part, which is a cylindrical tank with 18 m of diameter and 16.9 m high, holding 2,100 tons of pure water and equipped with 208 PMTs for detecting Cherenkov radiation.

The data taking occurred within 2007 and 2011, and the temperature data for the detector location was provided by ECMWF. Figure 3.9 (a) shows both data, and effective temperature as a function of time, while figure 3.9 (b) shows the correlation data reported by the experiment, whose nominal value is $\alpha_T = 0.93 \pm 0.04$, being compatible to the result reported by MACRO [38], and to the theoretically expected value.

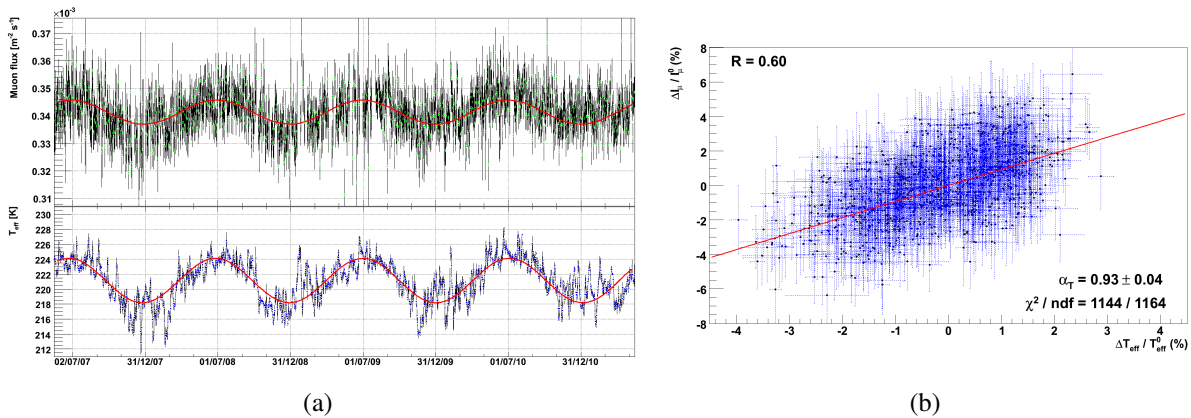


Figure 3.9 | Borexino’s muon and T_{eff} seasonal variations, and α_T

Figure shows (a) the muon seasonal variations (top), the seasonal variation of the effective temperature of the atmosphere (bottom), and (b) the effective correlation coefficient α_T [48].

GERDA [50]

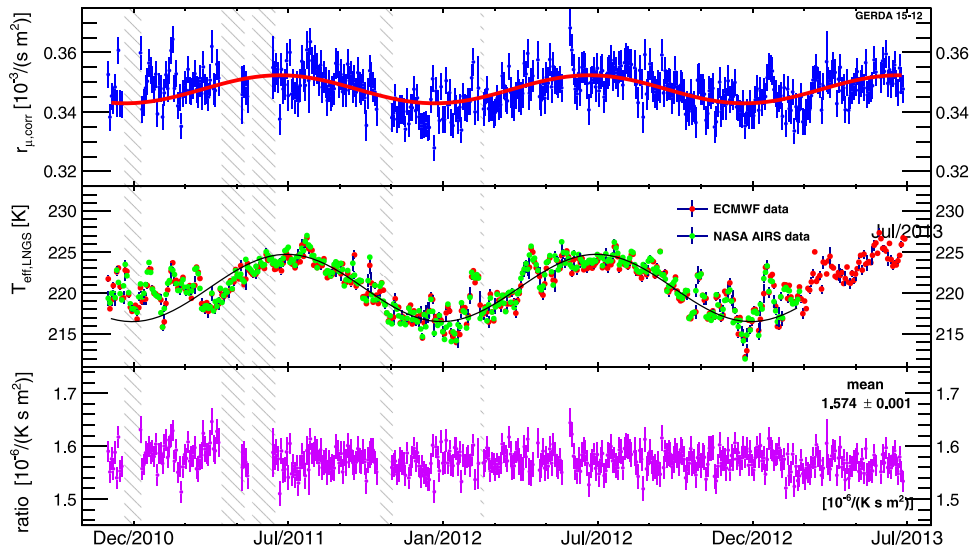
The GERDA¹⁰ Experiment is designed to search for the neutrinoless double beta decay of the ^{76}Ge , and it is located in the LNGS complex. Its overburden is around 3,100 mwe. The detector is composed by a cryostat filled with liquid argon and with germanium crystals in center. In order to remove background originated by cosmic ray muons and surrounding activities, the detector counts with a veto shield. The muon veto consists of two parts: a 590 m³ water tank in which the cryostat lies fully submerged, equipped with PMT’s in its surroundings; and a plane of plastic scintillators connected to PMTs at the top of the tank.

The data used in the seasonal analysis is a result of 806 days of the muon veto exposure time, between November, 2010, and July 2013. Two sets of data were used for the aforementioned period. The first is provided by ECMWF, while the second comes from NASA’s Atmospheric Infrared Sounder (AIRS), on board of the NASA AQUA satellite.

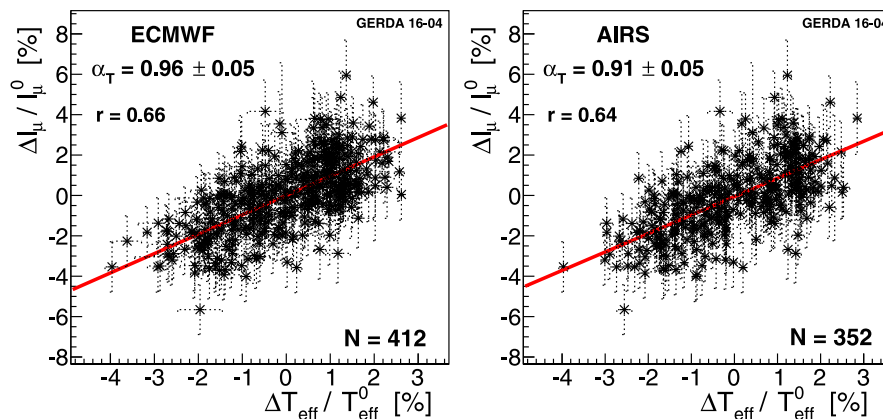
The seasonality of both muon flux and effective temperature measured by the experiment, along with their rates, are presented in figure 3.10 (a). Finally, the correlation coefficient, was

¹⁰Acronym for Germanium Detector Array.

calculated using each temperature dataset, and is presented in figure 3.10 (b). From ECMWF, $\alpha_T = 0.96 \pm 0.05$, while using AIRS, $\alpha_T = 0.91 \pm 0.05$.



(a)



(b)

Figure 3.10 | GERDA's muon and T_{eff} seasonal variations, and α_T

Figure shows (a) the muon seasonal variations (top), the seasonal variation of the effective temperature of the atmosphere (middle), and their respective ratios (bottom). The grey hatched areas represent periods in which there was no muon data taking. Figure (b) shows the effective correlation coefficient α_T for each temperature dataset, where ECMWF and AIRS yielded $\alpha_T = 0.96 \pm 0.05$ and $\alpha_T = 0.91 \pm 0.05$, respectively [50].

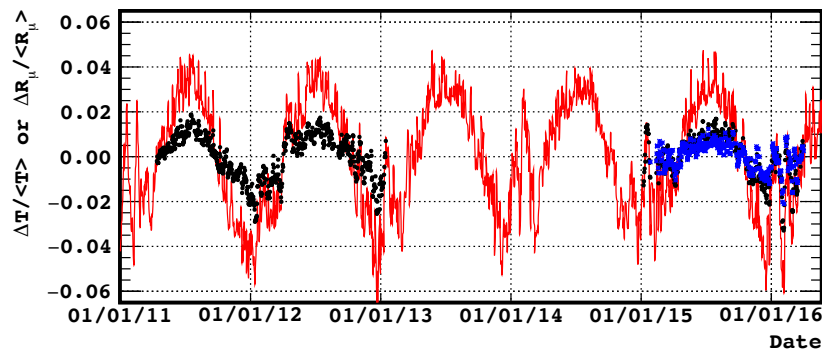
Double Chooz [52]

The Double Chooz Experiment is located in the city of Chooze, France, and its main goal is to measure neutrino oscillations using the neutrinos emitted by the Chooz nuclear power plant. Similar to MINOS, the experiment counts on two detectors, a Near Detector (ND), and a Far

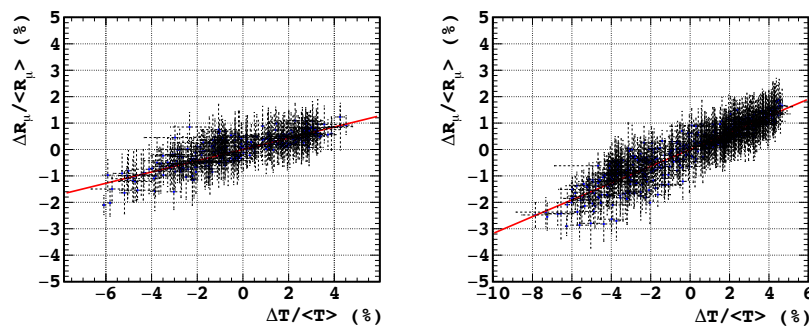
Detector (FD), located respectively at ~ 400 m and $\sim 1,050$ m from the nuclear power plant. Their overburdens are 120 mwe for the ND, and 300 mwe for the FD.

The detectors are based on the same concept, which consists of a set of concentric cylinders with an outer muon veto at the top. The inner vessel is filled with a liquid scintillator doped with Gd. A surrounding vessel allows for full containment of energy deposited by gamma rays, and a third vessel, filled with mineral oil, isolates the inner parts of the detector from surrounding radioactivity. A stainless steel vessel holds in place 390 inward facing PMTs. This set of vessels is called the Inner Detector, and it is surrounded by the Inner Veto, which is a 50 cm thick volume filled with liquid scintillator and equipped with PMTs. Finally, both Inner Detector and Inner Veto are surrounded by 1 m of water in the ND and 15 cm of steel in the FD. A final outer veto, made of plastic scintillator strips, is placed on top of each detector.

The data used in the analysis represents 3 years of Near Detector exposure, with 2 years ranging from January, 2011, until January, 2013, and 1 year ranging from January, 2015, until January, 2016. In the same latter period, data from FD was also used. The temperature data is provided by the NASA AIRS instrument. Figure 3.11 (a) shows the muon rate change for the ND (black), FD (blue), and AIRS temperature data (red). Finally, figure 3.11 (b) presents the correlation coefficients for the ND (left) and FD (right), which yields $\alpha_T = 0.212 \pm 0.013$ (stat.) ± 0.011 (syst.), and $\alpha_T = 0.355 \pm 0.002$ (stat.) ± 0.017 (syst.), respectively.



(a)



(b)

Figure 3.11 | Double Chooz' muon and T_{eff} seasonal variations, and α_T

Figure shows (a) the muon and effective temperature seasonal variations for the ND (black), FD (blue) and AIRS (red) data. Figure (b) shows the effective correlation coefficient α_T for the ND (left) and FD (right), yielding $\alpha_T = 0.212 \pm 0.013$ (stat.) ± 0.011 (syst.), and $\alpha_T = 0.355 \pm 0.002$ (stat.) ± 0.017 (syst.), respectively [52].

Daya Bay [53]

Daya Bay is a neutrino oscillation experiment located in Daya Bay, Shenzhen, China, approximately 50 km northeast of Hong Kong. The experiment detects neutrinos emitted by the Day Bay Nuclear Power Plant complex, which encompasses a total of 6 nuclear reactors. For that, it uses 8 functionally identical detectors placed in 3 underground Experimental Halls, known as EH1, EH2, and EH3, with 250 mwe, 265, and 860 mwe of overburden, respectively.

The detector concept is similar to the detector used by the Double Chooz Experiment, with an inner vessel filled with gadolinium-doped liquid scintillator, which is the fiducial volume used to detect the interacting neutrinos, surrounded by an outer vessel filled with undoped liquid scintillator designed to detect the gamma rays emitted by the inner vessel. A final outermost vessel is filled with mineral oil, and carries a total a 192 PMTs facing inward to the inner vessel. The whole apparatus lies inside a muon detection system, which is a water tank with PMTs to detect Cherenkov light, being the top an array of resistive plate chambers.

The dataset used encompasses data collected between December, 2011, and November,

2013. The first 7 months of this time span, only 6 of the 8 detectors were operating, while the rest of the time all detectors remained operant. The temperature data was provided by ECMWF, and a comparison with IGRA data was performed for defining the temperature systematic uncertainties.

The effective temperature correlation results combining all detectors in each Experimental Hall are shown in figure 3.12, which yields $(\alpha_T)_{EH1} = 0.362 \pm 0.031$, $(\alpha_T)_{EH2} = 0.433 \pm 0.038$, and $(\alpha_T)_{EH3} = 0.641 \pm 0.057$. The results are compatible with the predicted values for α_T .

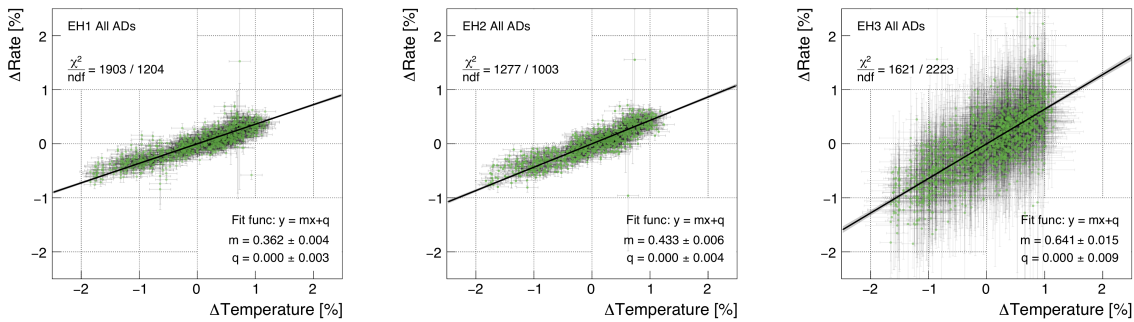


Figure 3.12 | Daya Bay's α_T

Figure shows the α_T results combining all detectors in each Experimental Hall, being $(\alpha_T)_{EH1} = 0.362 \pm 0.031$, $(\alpha_T)_{EH2} = 0.433 \pm 0.038$, and $(\alpha_T)_{EH3} = 0.641 \pm 0.057$ [53].

Final overview of the single muon results

A range of experimental results regarding single muon seasonal modulations was outlined in the previous subsections. It is worth mentioning that a few of the references that were previously listed were left out of the former subsections. The reason for this choice resides in the fact some results did present a clear muon seasonality, but their main results diverged from the topic covered in this Thesis. These references are briefly mentioned now.

Ref. [25]: The findings reported by A. Duperier in 1949 did not show any muon seasonality effect, but it is worth mention, as it shows that temperature variations at approximately 100 mbar (i.e., about 15 km of altitude) are an important factor controlling the meson intensity at surface level, being a strong indicative that such effect must also take place for muons. The results also indicate that the meson component reaches its maximum at about 15 km of altitude, meaning that most muons reaching underground detectors must be produced in the region of the tropopause.

Ref. [40]: The annual seasonality of the trigger of the Soudan 2 detector is reported. The signal modulation shows an amplitude of $\pm 15\%$ with respect to the average, reaching a much higher amplitude than expected if only cosmic ray muons were contributing to the signal (which should oscillate with an amplitude of $\pm 2\%$). The higher trigger variation is confirmed to be caused by a seasonality in the radon levels in the mine's air. This effect verified in the radon levels is explained by less (more) ventilation inside the mine during summer (winter).

Ref. [43]: The MINOS experiment, among muon seasonal variations, verified a Sudden Stratospheric Warming (SSW) effect. This effect is caused by Rossby waves, which are atmospheric waves induced by conservation of potential vorticity¹¹, the Coriolis force, and pressure gradients. These waves have thousands of km of horizontal wavelength, and propagate from the troposphere to the stratosphere during winter and are associated to high latitude vortex structures, usually happening at the poles. These vertical waves can be slowed down or have their direction reversed, causing a sudden rise in the temperature of the stratosphere over the course of a few days, increasing its temperature by over 50 K.

Ref. [45]: The correlation between the muon seasonal variations and the effective temperature of the upper atmosphere is connected to the relative contribution of kaon and pion production and decay. In this scenario, this paper presents a method to estimate the K/π ratio using the measured seasonal modulations of the muon rate at a given detector. As these measurements can be performed by deep underground detectors, this method provides the possibility to estimate the K/π ratio in energy regions previously unexplored by fixed target experiments.

Ref. [47]: Following Ref. [45], the IceCube Collaboration used their muon seasonal variation measurements for estimating the K/π ratio. Given its depth of 1,570 mwe, it was possible to estimate the K/π ratio for cosmic ray primaries at energies of about 20 TeV.

Ref. [51]: The LVD Collaboration presents a direct correlation between the variations in the muon flux and the production of muon induced neutrons in the detector. A higher muon flux represents a higher number of neutrons generated by the interaction of muons with the detector material.

A full compilation of the experiments that provided an α_T value is presented in table 3.4, which shows the assigned name to the experiment, the detector depth, the reported value of the effective temperature correlation coefficient, the reference, and the publication year.

¹¹Potential vorticity is the dot product between vorticity and stratification. Vorticity describes the tendency of a fluid to rotate around a local point, while stratification happens when layers with different properties act as barriers, increasing the difficulty for different layers to mix.

Experiment	Depth (mwe)	Measured α_T	Ref.	Year
Barrett	1,574	$\alpha_T = 1.76 \pm 0.45$	[26]	1952
–	–	$\alpha_T = 0.73 \pm 0.26$	[28]	1954
–	–	$\alpha_T = 1.02 \pm 0.24$ (combined)	–	–
Sherman	846	$\alpha_T = 0.48 \pm 0.13$	[27]	1954
Hobart	42	$\alpha_T = 0.06 \pm 0.02$	[29]	1961
Torino	70	$\alpha_T = 0.09 \pm 0.02$	[30]	1967
Poatina	357	$\alpha_T = 0.14 \pm 0.02$	[31]	1979
Utah	486	$\alpha_T = 0.299 \pm 0.009$	[32]	1981
Baksan	850	$\alpha_T = 0.829 \pm 0.084$	[35]	1990
MACRO	3,800	$\alpha_T = 0.98 \pm 0.12$	[38]	1997
AMANDA	1,590	$\alpha_T = 0.86 \pm 0.05$	[39]	1999
IceCube	1,590	$\alpha_T = 0.901$	[42]	2009
MINOS [FD]	2,100	$\alpha_T = 0.873 \pm 0.009$	[44]	2010
[ND]	225	$\alpha_T = 0.428 \pm 0.059$	[49]	2014
[ND]	–	$\alpha_T^w = 0.352 \pm 0.046$ (weighted)	–	–
Borexino	3,800	$\alpha_T = 0.93 \pm 0.04$	[48]	2012
GERDA	3,500	$\alpha_T = 0.96 \pm 0.05$ (ECMWF)	[50]	2016
–	–	$\alpha_T = 0.91 \pm 0.05$ (AIRS)	–	–
Double Chooz [ND]	120	$\alpha_T = 0.212 \pm 0.017$	[52]	2017
[FD]	300	$\alpha_T = 0.355 \pm 0.017$	–	–
Daya Bay [EH1]	250	$\alpha_T = 0.362 \pm 0.031$	[53]	2017
[EH2]	265	$\alpha_T = 0.433 \pm 0.038$	–	–
[EH3]	860	$\alpha_T = 0.641 \pm 0.057$	–	–

Table 3.4 | Compilation of experiments that measured α_T

The table compiles all experimental results previously listed for α_T by publication year and experiment. Different results from the same experiment are gathered for practicality. To avoid cluttering, columns marked with a “–” imply that its content is the same as the one stated in the previous line.

The data presented in table 3.4 is also compared to the theoretical values of α_T in figure 3.13, which shows the predicted α_T considering the pion contribution (dashed line), the kaon contribution (dotted line), and the sum of both (solid red line) for the expected π/K ratio. Both data points shown at 3,500 mwe were published by the GERDA experiment. The higher value is the GERDA result using ECMWF data, while the lower uses temperature data from the NASA AIRS system. Several experimental data points are presented within 50 mwe and 400 mwe and, in order to avoid clutter, some of these results were colored and specified in a separate legend.

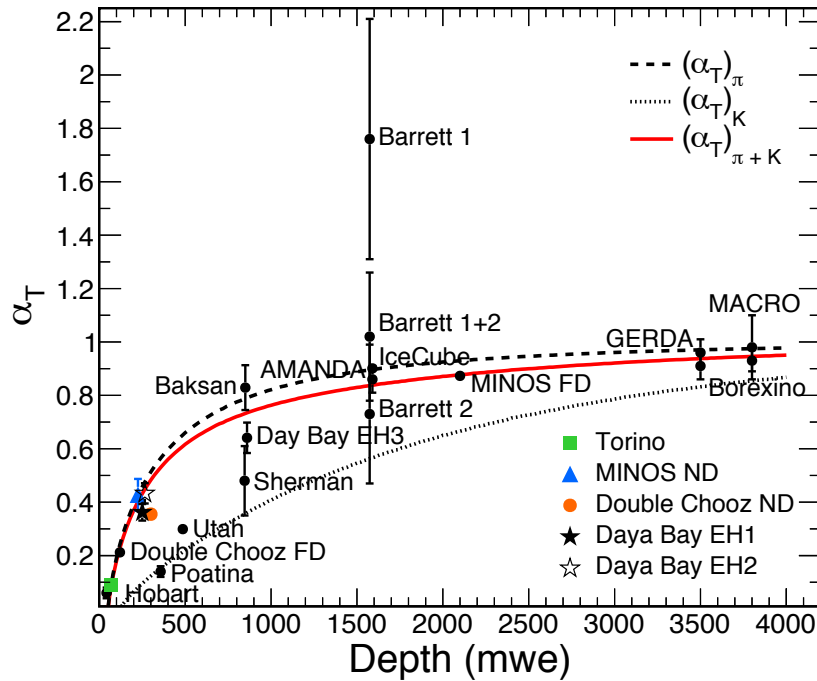


Figure 3.13 | Theoretical prediction of α_T compared to the experimental data

Figure shows the theoretical prediction for α_T considering only pions (dashed line), only kaons (dotted line), and both (solid red line). Both data points at 3,500 mwe belong to the GERDA experiment, in which the one yielding the higher α_T represents the GERDA result using ECMWF data, while the lower one uses temperature data from the NASA AIRS system. Some data points within 50 mwe and 400 mwe were colored in order to be labeled without producing too much clutter.

3.4.2 Multiple-muons

Data analyses focusing on multiple-muon seasonal variations are very recent. The IceCube observatory presented in Ref. [54] the correlation between the variation in the muon multiplicity as a function of the variation of the effective temperature of the atmosphere. Nonetheless, it did not present the seasonal effect that occurs with multiple-muon events. This study was carried forward by the MINOS Collaboration, which noticed an inversion of phase between single and multiple-muon seasonal modulations. Said phase also had a dependency with the separation between multiple-muon tracks in the Far Detector data. Later on, F. Ronga revisited old data from the MACRO Experiment searching for similar trends [56].

Effective temperature coefficients developed for single muons have little meaning in the case of multiple-muons, as the primaries are in general more energetic, resulting in observed muons that could have been originated by mesons that decayed in very different regions of the atmosphere. As such, these studies did not report any parameter to quantify the correlation between muon flux and temperature seasonalities. The following subsections are dedicated to explore in further details the aforementioned results.

MINOS [55]

The publication presents the first reported results on seasonal modulations of multiple-muon events, and it does so for both Near Detector (225 mwe) and Far Detector (2100 mwe). Therefore, the results from each is presented separately.

Far Detector

The MINOS Far Detector is located in the Soudan Underground Mine State Park (MN), being 715 m under the surface level, which yields 2,100 mwe of overburden. The detector is a large set of horizontally displaced octagonal planes, following an intercalated pattern between plastic scintillator and steel planes. The scintillator planes are a collection of long thin scintillator strips with wavelength shifting fibers connected to electronics. The strips in the scintillator planes are rotated by 90° with respect to each other, allowing for 3D track reconstruction. With 484 planes with dimensions of $8 \text{ m} \times 8 \text{ m}$, the detector is 30 m long, and yields a total mass of 5.4 ktons.

The analyzed data comprises a total of 9 years of detector exposure time, from August, 2003, until April, 2012. Seasonalities based on track separation were found by calculating distance of closest approach for every pair of multiple-muon tracks in every event, and by dividing the resulting distribution into 3 regions of equal statistics, as it is shown in figure 3.14 (a). The regions of track separation are defined, in meters, as

$$\begin{aligned}
 \text{Region A: } & 0.6 \leq \Delta S \leq 4.5 \\
 \text{Region B: } & 4.5 < \Delta S \leq 8.0 \\
 \text{Region C: } & \Delta S > 8.0
 \end{aligned}
 \tag{3.45}$$

and present different modulation phases, as it is shown in figure 3.14 (b). Short track separation events show a clearly inverted modulation phase compared to large track separation events, which follow the same phase trend as verified in the single muon results. The midrange track separation shows a modulation phase in between the other result. The short track separation seasonality also presents a clear upward going trend, as it is shown by the linear fit (black solid line). Although it is speculated that solar activity may play a role in the increasing yearly average muon rate, there is no clear evidence for that.

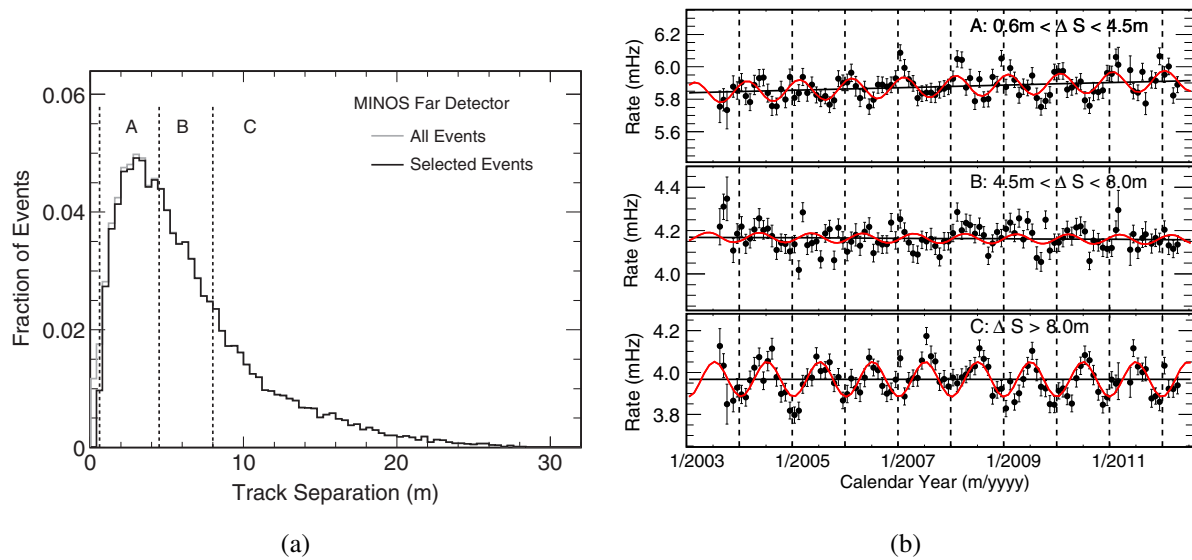


Figure 3.14 | MINOS FD track separation and multiple-muon seasonal variations

Figure (a) shows the distance of closest approach between every pair of muon tracks, along with the 3 regions of equal statistics. The seasonality of each of these regions is presented in (b), along with a cosine fit (red) and a linear fit (black). Given the large data set, each data point is equivalent to one calendar month, and the vertical dashed lines are the boundaries of each year. Tracks with short separations follow an inverted pattern as qualitatively expected, reaching their maximum rate during winter. Midrange separations show a less clear trend, and large track separation events follow the same modulation phase as reported by the single muon results.

Near Detector

The MINOS Near Detector is located at the Fermi National Accelerator Laboratory, in Batavia (IL). The detector lies in an 104 m underground cavern, which provides 225 mwe of overburden. It is a smaller, functionally identical version to the Far Detector, being made of 282 $3.8 \text{ m} \times 4.8 \text{ m}$ hexagonal planes, resulting in a total of 17 m of extent.

The used data encompasses 6 years of detector activity, ranging between June of 2006, and April of 2012. Similarly to the FD analysis, the track separation of multiple-muon events was broken down into 3 regions of equal statistics, as it is shown in figure 3.15. The regions are divided, in meters, as follow

$$\begin{aligned}
 \text{Region A: } & 0.6 \leq \Delta S \leq 1.8 \\
 \text{Region B: } & 1.8 < \Delta S \leq 3.0 \\
 \text{Region C: } & \Delta S > 3.0
 \end{aligned}
 \tag{3.46}$$

All three regions reported the same phase, with minimal differences. Nonetheless, the measured phase is opposite to the one obtained in the single muon data, as it is clearly evident in figure 3.16. Each data point represents the average of every said month throughout the dataset.

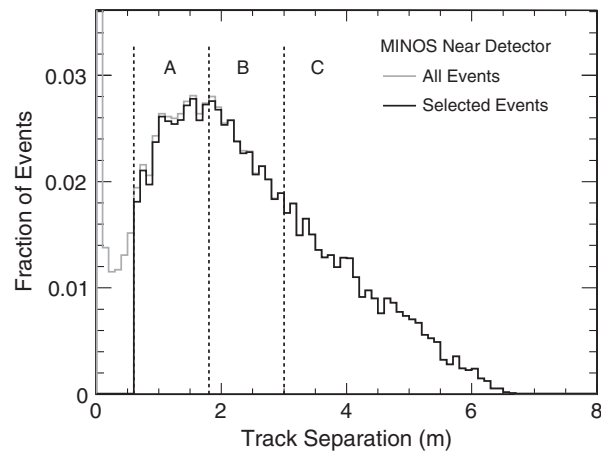


Figure 3.15 | MINOS Near Detector track separation distribution

Figure shows the distance of closest approach between every pair of muon track in the ND, along with the 3 regions of equal statistics.

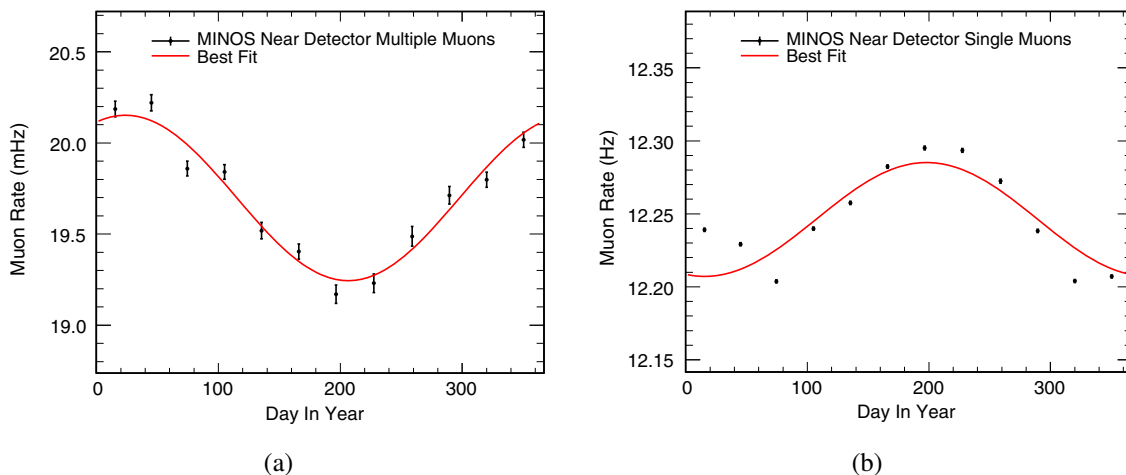


Figure 3.16 | MINOS ND seasonal variations for both single and multiple-muons

Figure shows the Near Detector seasonal modulation of (a) multiple-muons, compared to (b) single muons, as a function of day of year. Each data point represents the average of said month throughout the whole dataset. The inverted phase with respect to the single muon result is verified in all track separations.

Given the not fully understood scenario, a set of hypotheses was outlined in an attempt to suggest possible mechanisms for the phase inversion.

Hypothesis 1: Hadronic dimuon decays

In this scenario, mesons decaying into dimuons are taken into consideration. Although pion and kaon probabilities of interaction suffer noticeable change with seasonal temperature variations, other mesons, such as η 's and ρ 's, do not. This leads to the possibility of a competing mechanism, in which the higher number of pion and kaon interactions during winter is responsi-

ble for increasing the number of η and ρ mesons, leading to a higher number of detected muons at the detector level.

The branching ratios of the aforementioned decays are shown in table 3.5 [3]. The yearly

Channel	Fraction ($\Gamma_i/\Gamma_{\text{total}}$)
$\eta \rightarrow \mu^+\mu^-\gamma$	$(3.1 \pm 0.4) \times 10^{-4}$
$\rho \rightarrow \mu^+\mu^-$	$(4.55 \pm 0.28) \times 10^{-5}$

Table 3.5 | η and ρ dimuon decay channels and their branching ratios

The table presents the two meson dimuon decay channels taken into consideration in this hypothesis, along with their branching ratios [3].

variation in the pion interaction is known to be at the order of $\pm 2\%$ [44]. Also, the multiple-muon rates observed are at least 2 orders of magnitude smaller than that observed for the single muon data – being 1% of the single muon rates in the FD, and 0.16% of the single muon rates in the ND. Those considerations, added to the fact that the branching ratios of the η and ρ meson dimuon decays are at the order of 10^{-4} and 10^{-5} , respectively, the meson decay contribution to the observed rates must be at most at the order of 10^{-6} . Therefore, its too small to explain the effect.

Hypothesis 2: A geometry effect

The hypothesis considers the change in the altitude of the primary cosmic ray interaction due to changes in the atmosphere over the seasons. An expanded atmosphere during summer would cause primaries to interact, on average, at higher altitudes in the atmosphere. This would increase the average altitude of meson decay and, as a consequence, would produce a larger muon spread at the detector level. As such, one would consider the possibility of the multiple-muons from region A in the FD track separation distribution (figure 3.14 (a)), whose rates peak during winter, to move to region C during the summer, shifting the peak exactly as experimentally observed.

Calculations show that for a particular muon event, with a given decay angle, a shift from region A to region C (for the FD), solely by changing the altitude of the meson decay, would imply in an increase in said decay altitude by at least ~ 60 km. In a parallel observation, the smaller Near Detector does not show any track separation dependence, preserving the same phase as shown by Region A in figure 3.14 (a). These statements show that the effect does not account for the multiple-muon phase inversion.

Hypothesis 3: A temperature effect

This idea suggests the possibility of single and multiple-muons seasonalities to follow different altitude dependencies. Different altitude temperature trends could be leading the different phase trends in each case. This hypothesis can be verified by combining two different informations: *i*) The seasonal phase and amplitude of the temperature trend as a function of altitude, and *ii*) the altitude of muon production for each of the 3 track separation regions of the FD.

The temperature modulation as a function of altitude is produced by fitting a cosine function over the temperature data for data from different altitude levels. The temperature data is provided by ECMWF, which presents the interpolated temperature for 37 different pressure levels in a daily basis. The resulting amplitudes and phases retrieved from the fit, for each pressure level, is presented in figure 3.17 (a) and (b), respectively.

The verification of the muon production altitudes for each track separation regions was per-

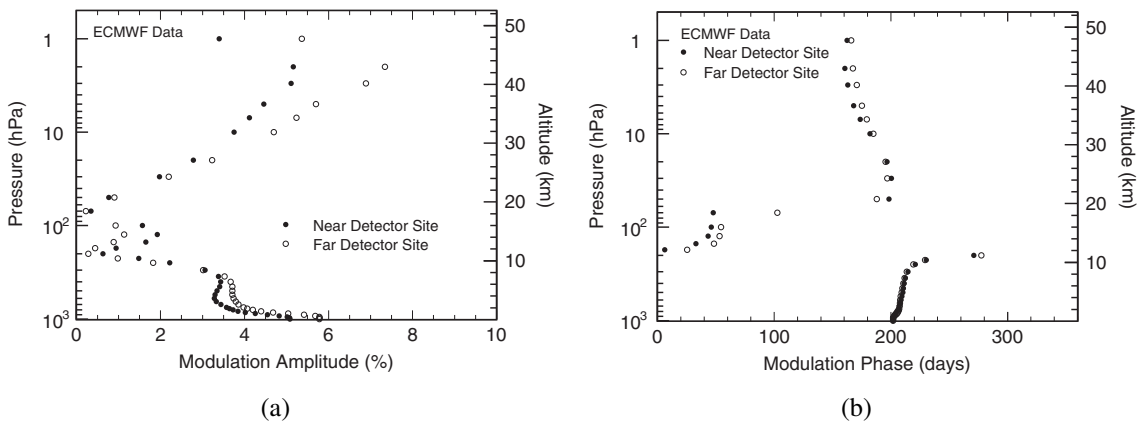


Figure 3.17 | ECMWF modulation amplitudes and phases

Figure shows the resulting (a) amplitudes, and (b) phases, from the cosine fit of the temperature data for different pressure levels.

formed using CORSIKA¹² [58]. The Monte Carlo provides relevant information of the cosmic ray simulated particles at surface level. For muons only, the additional information of their production altitude is stored as well. For each simulated EAS, the muons at surface level are propagated through the rock using

$$E_{\text{loss}}(X) = \frac{a}{b_T} (e^{b_T X} - 1), \quad (3.47)$$

where X is the rock overburden, a represents the ionization energy loss, and b_T takes into account the energy loss for deep inelastic scattering, bremsstrahlung, and pair production. The numerical values of a and b_T are shown in table 2.2. The track separation is calculated for

¹²Acronym for Cosmic Ray Simulation for KASCADE. The latter, being an acronym for Karlsruhe Shower Core Array Detector, a cosmic ray experiment located in Karlsruhe, Germany.

muons that crossed the simulated volume of the Far Detector at 715 m of depth. Finally, the production altitudes of muons within each region are plotted, and can be seen in figure 3.18. The same study was performed using 3 different high energy hadronic interaction models, namely QGSJET-01C, QGSJET-II, and EPOS, all yielding similar and consistent results.

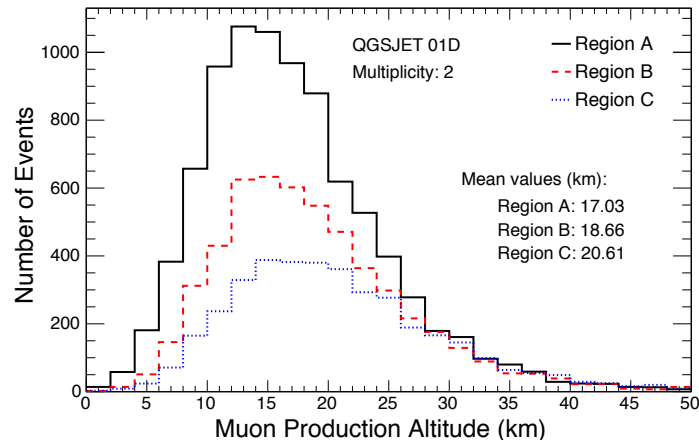


Figure 3.18 | Monte Carlo muon production altitudes for the FD track separation regions

Figure shows the Monte Carlo results of the muon production altitudes for the muons that reached the FD volume underground, based on their track separations. The average altitude of the muon production increases as the separation increases, indicating that the effect outlined in hypothesis 2 does play a small role in the dynamics of the cosmic ray shower.

The difference in the average muon production altitude for each region varies from ~ 17 km for Region A, to ~ 21 km for Region C. The resulting amplitudes and phases related to the muon production altitude of the 3 track separation regions, assuming that the rates and temperatures are correlated, produce seasonal modulations that peak during the summer months for all 3 regions. Therefore, it does not appear that this hypothesis can account for the inverted phase seen for Region A of the FD, nor for the inverted phase seen in the ND.

Hypothesis 4: Anti-correlation between secondary and further meson decays

This hypothesis may be the one that best fits as a concise explanation for the phase inversion effect. Although most single muons are originated from secondary pion and kaon decays in the upper atmosphere, multiple-muons events may be originated from further hadronic interactions. As such, while during the summer there is a higher likelihood of these secondary mesons to decay into muons, the increase in their interaction probability during winter acts as a mechanism for increasing the meson production and decay further in the atmosphere, which leads to a larger number of observed muons.

The hypothesis provides a probable mechanism for the phase inversion, with the important caveat that further hadronic interactions imply less kinetic energy per particle. As a result, only more energetic cosmic ray primaries will have enough energy to produce muons (from these

further interactions) that are able to reach the detector depth.

This is more evident if compared with the single muon data, whose absolute rates are at least 2 orders of magnitude higher than multiple-muon rates, which implies that they are, on average, originated by less energetic primaries. As such, the main mechanism that governs the single muon seasonal variations is tied to the competition between decay and interaction probabilities of mainly the secondary mesons over the different seasons of the year. As a consequence, the single muon seasonal modulation follows the same trend of the atmospheric temperature variations. Multiple-muons are, on average, produced by higher energetic primaries. Further hadronic interaction are not just more likely to produce detectable muons at the detector depth, but an increase in the meson interaction probability results in an overall increase in the number of muons observed underground. Hence the fact that the multiple-muon phase peaks during winter.

The mechanism only exists as a qualitative concept. A quantitative study and validation has still yet to be done.

Revisited data from MACRO [56]

In this unpublished study from 2017, F. Ronga, from INFN¹³, revisited the data from the MACRO experiment in an attempt to verify the multiple-muon trends observed by MINOS [55] in 2015. The dataset used ranges from December, 1995, to December, 2000. The temperature data at the detector location was retrieved from ECMWF.

The revisited analysis reported a new value for the single muon temperature correlation coefficient, yielding $\alpha_T = 1.03 \pm 0.01$ (stat.), being higher than the former MACRO result $\alpha_T = 0.98 \pm 0.12$ [38], and the expected $\alpha_T^{\text{theory}} \simeq 0.92$.

For multiple-muons, the track separation distribution was divided into 4 regions, defined, in meters, as follow:

$$\text{Region 1: } 0.05 \leq \Delta S \leq 0.30$$

$$\text{Region 2: } 0.30 < \Delta S \leq 2.20$$

$$\text{Region 3: } 2.20 < \Delta S \leq 10.00$$

$$\text{Region 4: } \Delta S > 10.00$$

These regions are then fitted by a cosine function, whose phase and amplitude values are shown in figure 3.19 (a), and directly compared to the MINOS results, in figure 3.19 (b). In these polar representations, a null phase represents winter, a phase at π matches with the summer, and the radial distance from the center represents the absolute amplitude value. Different than the MINOS results, all MACRO phases peak at summer, showing no multiple-muon phase inversion nor a track separation phase dependency.

¹³Italian acronym for National Institute for Nuclear Physics. INFN is responsible for the management of the LNGS, in Italy.

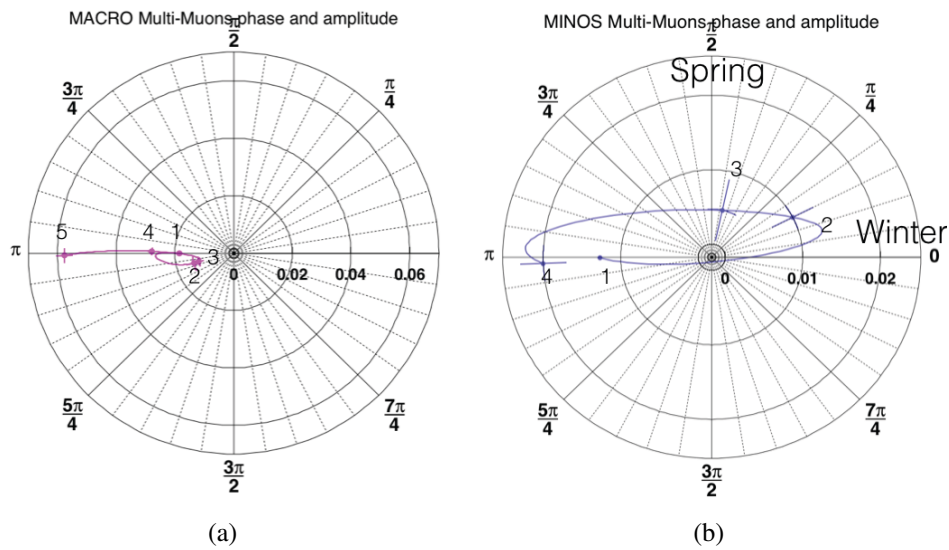


Figure 3.19 | MACRO and MINOS multiple-muon amplitudes and phases

Figure shows the resulting amplitudes and phases from the cosine fit for (a) MACRO, and (b) MINOS. The number 1 label represents the data for single muons. Labels 2 and higher represent the different track separation regions for multiple-muons, by order of increasing track separation.

Although the result seems to be in disagreement with MINOS, the MACRO detector lies under 3,800 mwe of solid rock overburden and, as such, the threshold energy for muons is very high ($E_{th} \simeq 1.3$ TeV [38]). This is an indication that the vast majority of muons, even for the multiple-muon data, is produced from the secondary meson decays, still in the upper atmosphere. As a consequence, their seasonality follows the same trend as the single muon data.

Chapter

The NO ν A Experiment

4.1 Overview

The NuMI Off-axis ν_e Appearance Experiment (NO ν A) is located at the Fermi National Accelerator Laboratory and it was proposed in 2005 [59] with the main purpose to study neutrino oscillations using the NuMI¹ beam line, originally built to provide an intense beam of muon neutrinos for the MINOS² Experiment. Its main proposal involves measuring or at least establishing experimental limits on the Pontecorvo–Maki–Nakagawa–Sakata (PMNS) matrix³, which parameterizes the currently accepted model for explaining neutrino oscillations and it determines the mixing proportion between different neutrino quantum states. It is an analogue of the Cabibbo-Kobaiashi-Maskawa (CKM) matrix, which delineates the transition states within different quark families. The experiment’s current goals can be summarized as

- (i) measure the octant of the θ_{23} mixing angle,
- (ii) measure the CP symmetry violation phase (δ_{CP}) in the leptonic sector and
- (iii) provide the answer for the neutrino mass ordering problem, which will depend on the achieved significance of the measurement of δ_{CP} .

In order to measure neutrino oscillations from the NuMI beam line, the NO ν A Experiment relies on two large, functionally identical detectors separated by a distance of 810 km, as shown in figure 4.1. The Near Detector, located at Fermilab, is 1 km downstream from the neutrino source and is responsible for measuring the initial neutrino flux, while the Far Detector, located in Ash River (MN) is responsible for measuring the spectrum of the final states of neutrinos. The difference in the event ratio measured between the initial and final states allows the determination of the oscillation parameters.

¹Acronym for Neutrinos at the Main Injector, one of Fermilab’s accelerators.

²Acronym for Main Injector Neutrino Oscillation Search. After updates in the Main Injector in 2013, MINOS became known as MINOS+ and started a new round of data taking and analysis. The experiment stopped taking data in June 29, 2016, after 11 years of operation.

³Also known as the lepton (or neutrino) mixing matrix.

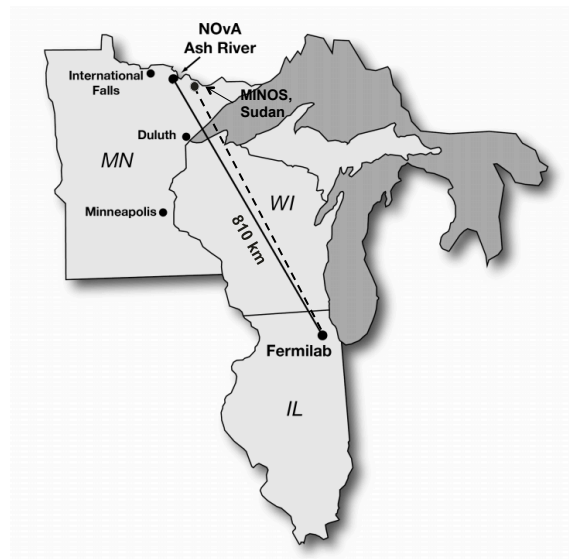


Figure 4.1 | The NO ν A beam line

A schematic figure representing the off-axis path traveled by the neutrino beam. The 810 km distance is measured from the neutrino source, 1 km before the Near Detector, up to the Far Detector, located in Ash River (MN). The dashed line shows the on-axis neutrino path, ending in Soundan (MN), where the MINOS Far Detector is located. In the on-axis path, the neutrinos travel a total distance of 735 km [60].

Beyond its primary goals, the experiment's detectors are very well suited for non oscillation physics as well, including the detection of supernovae, cosmic ray physics and the search for exotic phenomena, such as Weakly Interactive Massive Particles (WIMPS), which are possible candidates for dark matter, and magnetic monopoles.

Supernovae can be found based on the fact that $\sim 99\%$ of the energy released during a supernova event is emitted in the form of low energy neutrinos [61]. Hence, a neutrino avalanche during a short period of time⁴ with its origin pointing to a defined direction is a sign of a supernova event.

The detection of WIMPS is also based on neutrino detection: a hypothetical WIMP particle-antiparticle pair may be captured by the Sun's gravity and annihilate, which could produce mesons that would finally decay, producing muon neutrinos. Said ν_μ 's would escape the Sun's gravity and interact with one of the NO ν A detectors.

Magnetic monopole searches are based on the energy deposition of particles in the detector. Monopoles have a different dE/dX function when compared to known particles, and NO ν A is sensitive to a yet to be explored region of $\beta = v/c$ and mass. Therefore, NO ν A can provide new limits on this phenomenon.

NO ν A consists of two large detectors at two different depths constantly exposed to cosmic ray particles. This provides the opportunity to explore a variety of topics associated with cosmic ray physics. Thus, beyond the scope of the muon seasonal variation analysis presented in this

⁴In this scenario, the magnitude of the signal's length is at the order of several minutes.

Thesis, the experiment is also able to supply data for other cosmic ray physics topics, such as:

- (i) The Sun/Moon shadowing effect, in which a deficit of cosmic rays coming from the Sun/Moon direction is measured and quantified.
- (ii) The East/West effect, which is an expected asymmetry between the flux of muons coming from the East and West due to the non uniformity of the Earth's geomagnetic field.
- (iii) Multiple-muon studies in the Far Detector, with the intention of determining properties of cosmic rays showers based on their observables in the NO ν A Far Detector.

In order to provide a clear understanding on the different aspects of the experiment, the next sections will cover in detail the following topics:

- (i) The Fermilab accelerator complex, from the source to the final proton beam provided to the NuMI beam line.
- (ii) The NuMI beam line, responsible for producing an intense $\nu_\mu(\bar{\nu}_\mu)$ beam using the protons supplied by the Main Injector.
- (iii) The concept of an off-axis experiment and why NO ν A chose this configuration.
- (iv) The technology and the characteristics of both the Near and Far detectors.

4.2 The Fermilab accelerator complex

The first step of the process of accelerating a proton beam starts with a cylinder containing hydrogen gas at room temperature. Said gas is ionized, becoming H^- , and inserted in the first linear accelerator of the chain, the Radio Frequency Quadrupole (RFQ). The RFQ became operational in 2013, when it replaced a much older linear accelerator called Cockcroft-Walton, which although it has received many upgrades over time, it has been used by Fermilab since the late 1960's. The RFQ is responsible for accelerating the beam pulse up to 750 keV, when it becomes suitable for being inserted in the LINAC⁵, a 150 m long accelerator made of radio-frequency cavities. This accelerator increases the beam energy up to 400 MeV [62]. When exiting the LINAC, the beam traverses a thin carbon sheet, responsible for removing the electrons of the H^- , making it a pure proton beam pulse, now compatible to be accelerated by the Booster, a circular accelerator with a radius of 75 m. This process in which a beam of H^- coming from a linear accelerator is transformed into a beam of H^+ and inserted into a circular accelerator is known as Charge Exchange Injection [63]. The Booster accelerates the proton beam up to 8 GeV and sends it to the Main Injector, the largest accelerator currently in operation at Fermilab. It is a circular accelerator with 530 m radius that pushes the energy of the beam pulses up to 120 GeV and sends them to different beam lines, including NuMI.

Until 2011, the Main Injector was also responsible for delivering proton batches to the Tevatron, a 1 km radius' synchrotron that could reach a 1 TeV beam in the laboratory frame. The Tevatron was responsible for producing $p\bar{p}$ collisions and, therefore, the accelerator complex had to produce a \bar{p} beam as well. This was aided by the Recycler, a circular accelerator of the same size of the Main Injector. The antiproton beam was produced by colliding protons with a nickel target located at the Target Hall [64]. Anti-protons produced by the collision were then separated and stacked in the Accumulator Ring, now referred as Muon Ring – shown simply as Muon in figure 4.2, which is a schematic of Fermilab's accelerator complex. Said triangular area was formerly known as the Antiproton Source and, after Tevatron's decommissioning in September 2011, was updated to serve for new muon experiments, hence the new name. When the antiprotons reached the desired intensity, they were moved back to the Main Injector, accelerated to 120 GeV and transferred to the Tevatron, which would finally accelerate them to provide $p\bar{p}$ collisions for the CDF⁶ and D0 experiments or transfer the proton beam to a set of fixed target experiments located in three main areas, now referred as MTest, SeaQuest and Switchyard in figure 4.2.

⁵Acronym for Linear Accelerator.

⁶Acronym for Collider Detector at Fermilab.

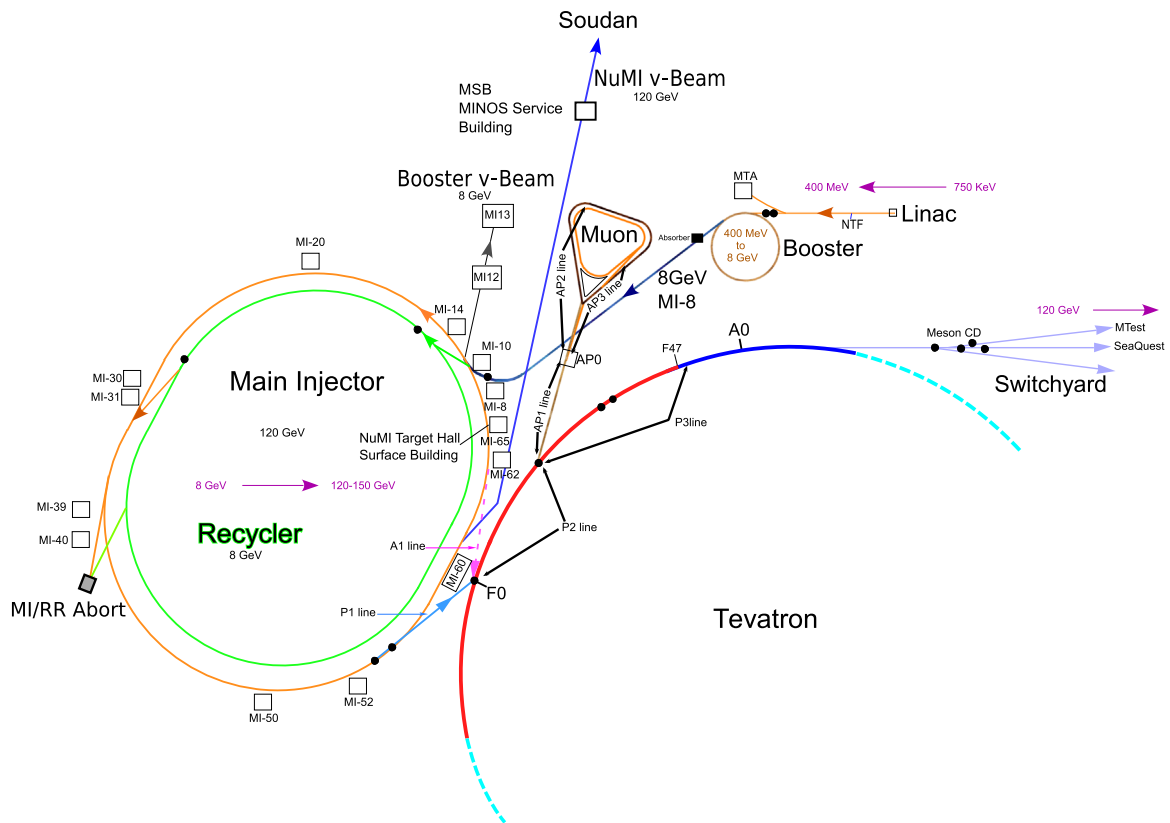


Figure 4.2 | Fermilab's accelerator complex

Schematic view of Fermilab's accelerator complex, showing each accelerator along with its operational energy range. The $\text{NO}\nu\text{A}$ Near Detector is located in the MINOS Service Building (upper part of the figure) and receives neutrinos produced by the NuMI beam. This beam line operates using 120 GeV protons delivered by the Main Injector. The Tevatron, a circular accelerator of 1 km of radius and responsible to provide ~ 2 TeV $p\bar{p}$ interactions in the center of mass frame for the D0 and CDF experiments, was decommissioned on September 30, 2011. A fraction of the Tevatron remains active with the sole purpose to direct protons to the SeaQuest Experiment, the Switchyard and to the Test Beam Facility (MTest), an infrastructure where beam tests are conducted and detector prototypes are built and tested [62].

4.3 The NuMI beamline

The NuMI beam line's purpose is to deliver an intense and collimated neutrino beam using the batches of 120 GeV protons provided by the Main Injector. The first step is to collide the proton pulse with a graphite target built with 47 fins, each with dimensions of 20 mm of length (in the beam direction), 15 mm of height and 6.4 mm of width. Each fin is spaced 0.3 mm apart, resulting in a total length of 95 cm long for the target itself. These fins are welded to two steel pipes for the water coolant. The structure of the target can be seen in figure 4.3. Although the choice for graphite as the target material was to maximize the meson production [65], it is known that the current choice is being replaced by a Beryllium one during $\text{NO}\nu\text{A}$ [66].

The next step after the interaction between the proton batches and the target makes use of a pair of horn-shaped magnetic lenses, which are used to collimate positive (negative) particles

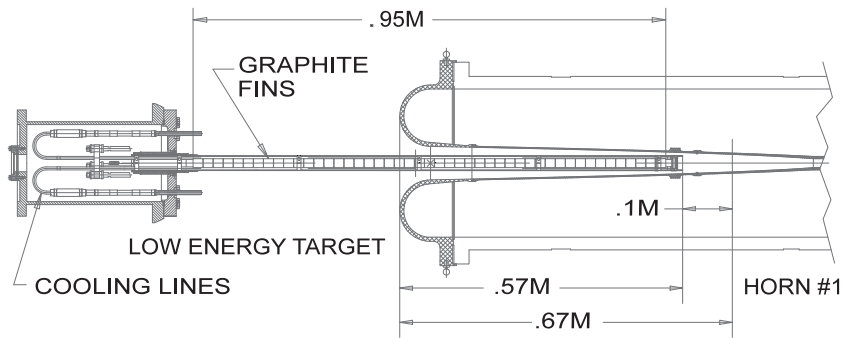


Figure 4.3 | The NuMI beam target

Schematic view of the NuMI beam target, showing the 47 fins along with the stainless steel pipes for the water coolant. The right side of the figure also shows the front half of Horn 1. The beam direction is oriented from left to right [62].

in order to produce a beam of neutrinos (anti-neutrinos) depending on their polarity, resulting in two operation modes, the Forward Horn Current (FHC, also known as neutrino mode) and the Reverse Horn Current (RHC, also known as anti-neutrino mode). Since the incident beam is positively charged, the anti-neutrino mode still carries a much larger amount of neutrinos compared to the amount of anti-neutrino contamination present in the neutrino mode. After being focused by the horns, the charged particles enter a 675 m long decay pipe to maximize their chance to decay into leptons. Following the decay region there is a hadron counter and an absorber, followed by a set of muon monitors intercalated with solid rock. This whole set of monitors and absorbers (rock included) is made for giving a quantitative idea of the neutrino flux, whilst it stops any other particle than neutrinos from reaching the Near Detector. The full schema is shown in figure 4.4.

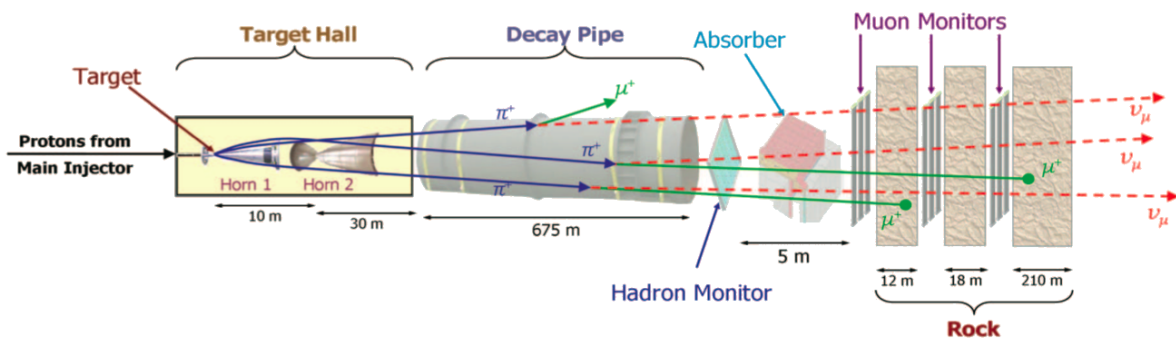


Figure 4.4 | The NuMI beam line

Schematic view of the NuMI beam line, showing pair of magnetic lenses (Horns 1 and 2), the decay pipe and the structure used to estimate the neutrino flux and stop all other undesired particles [62].

4.3.1 NuMI in the NO ν A Era

The NuMI beam line received a set of upgrades to deliver a more intense neutrino beam for NO ν A. During the MINOS Era, the Main Injector delivered a power of ~ 350 kW and, after all

the upgrades, the power was ramped up to ~ 700 kW⁷.

To achieve the new intensity profile, the Main Injector cycle-time was reduced from 2.2 to 1.33 seconds. The Recycler, formerly used to inject \bar{p} into the Main Injector, is now used as an injection accelerator for the Main Injector, in a technique called slip-stacking⁸. In this procedure, the Booster Ring injects 6 batches of $\sim 5 \times 10^{12}$ protons each into the Recycler Ring, which will gradually decelerate them by reducing the frequency in the RF cavities. Since the Recycler is 7 times larger than the Booster, there is room for an extra batch, which is injected with a slightly different momentum than the other 6. The momentum difference drifts the seventh batch towards one of the 6 former batches, increasing its density. At this point, an eighth batch is inserted in the now empty seventh slot. The process is repeated until all 6 batches have twice the number of protons. These new batches are transferred altogether to the Main Injector and sent to the NuMI beam line. This process results in beam spills that last 10 μ s and carry $\sim 5 \times 10^{13}$ protons delivered at a rate of 1.33 Hz [67].

4.4 The concept of an off-axis neutrinos experiment

Different from MINOS, which is perfectly aligned with the neutrino beam, the axis that links the NO ν A Near and Far Detectors makes a 14 mrad (0.8°) angle with the NuMI beam direction. Said difference is a ground breaking conceptual design between both experiments and its main reason lies in the fact that an off-axis configuration significantly reduces beam background contaminations in the $\nu_\mu \rightarrow \nu_e$ analysis⁹.

The reason why there is less contamination is due to the fact that pions and kaons decay isotropically with respect to their center of mass. In the case of pions and kaons decaying into muons and neutrinos, the neutrino flux and the neutrino energy of neutrinos that decayed with small angles with respect to their mother particle can be described by equations [59]

$$\Phi_\nu = \left(\frac{2\gamma}{1 + \gamma^2\theta^2} \right)^2 \frac{A}{4\pi z^2} z \quad (4.1)$$

and

$$E_\nu = \alpha \frac{E_{\pi,K}}{1 + \gamma^2\theta^2}, \quad \text{where } \gamma = \frac{E_{\pi(K)}}{m_{\pi(K)}} \quad \text{and } \alpha = \left(1 - \frac{m_\mu^2}{m_{\pi,K}^2} \right). \quad (4.2)$$

In equation 4.1, Φ_ν is the neutrino flux for a detector with area A , located at a distance z from the meson decay and θ is the angle between the neutrino and its mother particle. In equation 4.2, $E_{\pi,K}$ is the energy of the mother particle and α is referred to as the hadron's boost. Experimentally, the detector's area A is a constant and the hadrons' energy distribution $E_{\pi,K}$

⁷This is the main reason why MINOS became known as MINOS+ after 2013. Due to the upgrades and changes in the NuMI beam line, the neutrino energy range shifted leaving an opportunity to collect new data in a new energy region. Therefore, MINOS updated its detectors and was renamed to MINOS+.

⁸For more details, see Ref. [59].

⁹The Tokai to Kamioka (T2K) Experiment was the first to make use of the off-axis neutrino experiment concept.

depends solely on the energy of the proton beam coming from the Main Injector. The remaining variables, θ and z can be selected by defining the location of the Far Detector in a way that the oscillation probability $P(\nu_\mu \rightarrow \nu_e)$ is maximized. A distance of 810 km between the beam line and the detector showed a maximum in the oscillation probability curve, remaining only the θ angle to be defined. Figures 4.5 (a) and (b) shows how equations 4.1 and 4.2 behave for different values of θ . The decision of placing the detectors 14 mrad off-axis is explained in figures 4.5 (c) and (d). The peak of the oscillation probability $P(\nu_\mu \rightarrow \nu_e)$ in figure 4.5 (d) happens close to 2 GeV, an energy value that coincides with the peak in the red narrow distribution shown in figure 4.5 (c). The narrow energy distribution reduces contamination from neutral current events and prevents contamination from tau neutrinos, as their minimum energy is already at the high end tail of the CC events distribution.

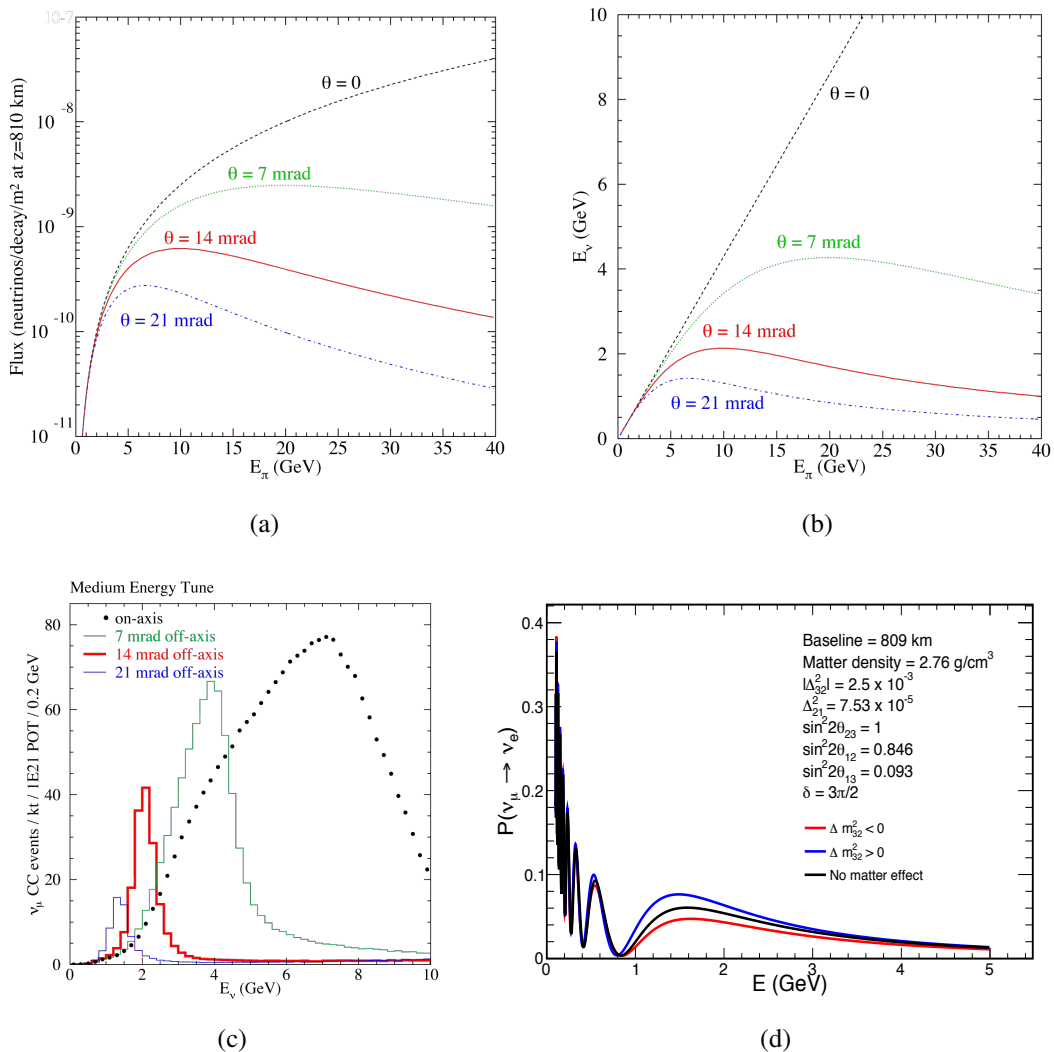


Figure 4.5 | Neutrino flux and energy according to its production angle

(a) The flux and (b) energy of neutrinos for different values of θ , considering the proton beam energy provided by the Main Injector and a Far Detector located at ~ 810 km from the beam line. (c) Estimated number of neutrino CC events for different values of θ in function of energy, considering the same aforementioned conditions considered in plots (a) and (b). The plot shows a clear suppression of the high neutrino energy tail. (d) Oscillation probability curves for a detector located 809 km considering the lack of matter effects and the two mass ordering scenarios [59, 67].

4.5 The NO ν A detectors

The two NO ν A detectors are conceptually identical. They are highly active and fine grained tracking calorimeters made of reflective extruded plastic cells and filled with liquid scintillator and a wavelength shifting (WLS) fiber whose ends are readout and processed by the detector's electronics.

The readout of the light signals is done by avalanche photodiodes (APDs), which produce electrical signals from the photons transmitted by the WLS fibers. APDs operate by a pro-

cess called impact-ionization, which occurs due to an internal high electric field created in the photodiode from a high voltage applied to the APD pixel. Electrons excited by photons are accelerated by the high electric field and quickly interact with the surrounding electrons of the material, moving these electrons to the conduction band of the semiconductor. The new free electrons will repeat the process, being accelerated by the electric field and removing other electrons from their valence band. This avalanche of charge carriers in the diode results in a significantly amplified photocurrent.

The use of APDs is favored over photomultiplier tubes (PMTs) due to their much higher quantum efficiency for the spectrum of light delivered by the WLS fibers, being 85% for APDs whilst PMTs can only provide somewhat between 10% and 20% [67]. This is specially important for NO ν A, given the length of its cells.

4.5.1 The detector design

The detector is made of rectangular extruded modules of polyvinyl chloride (PVC). Each extrusion creates 16 cells with a cross-section of 3.9 cm width and 6 cm depth each, as can be seen in figures 4.6 (a) and (b). A set of two extrusions glued together in parallel form a so called module. Therefore, each module in the detector is a flat row of 32 cells. These cells are coated with titanium dioxide (TiO₂), making them 90% reflective to 430 nm wavelength light. The liquid scintillator that fills each cell is, by mass, 94.63% mineral oil, 5.23% pseudocumene (scintillator), 0.14% PPO (2,5-diphenyloxazole, a wavelength-shifter), 0.0016% bis-MSB ((1,4-bis-(o-methyl-styryl)-)benzene, also a wavelength-shifter), 0.001% Stadis-425 (anti-static, increases conductivity), and 0.001% vitamin E (anti-oxidant) [68]. This information is summarized in table 4.1. The pseudocumene typically emits light in the range of 360-

Composition	Purpose	Mass fraction
Mineral oil	Solvent	94.63%
Pseudocumene	Scintillator	5.23%
PPO	Wavelength-shifter	0.14%
bis-MSB	Wavelength-shifter	0.0016%
Stadis-425	Anti-static	0.001%
Vitamin E	Anti-oxidant	0.001%

Table 4.1 | NO ν A scintillator oil composition

The table shows the composition of the liquid scintillator used by the NO ν A detectors, which is essentially a mineral oil, along with the purpose and mass fraction of each used additive [68].

390 nm, which is shifted to 400-450 nm by both PPO and bis-MSB. Along with the scintillator oil, each cell has a Kuraray wavelength-shifting (WLS) fiber (figure 4.6 (a)), which is looped at the bottom of it (figure 4.6 (b)) and has both ends connected to an APD pixel.

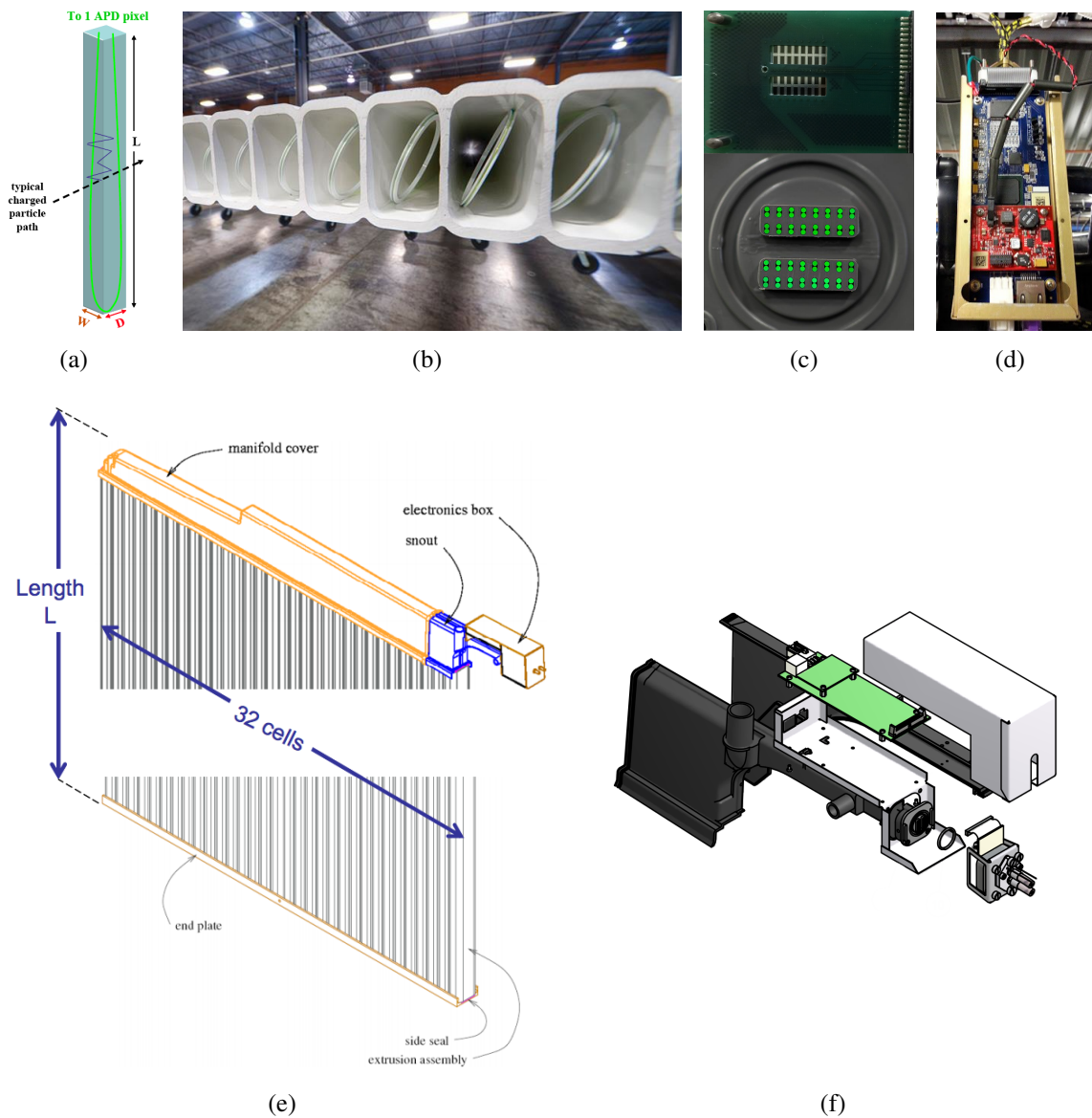


Figure 4.6 | NO ν A detector cells, APD and FEB boards

(a) Visual representation of a NO ν A cell filled with scintillator oil and a with a wavelength shifting fiber [69]. (b) Picture showing an extruded PVC block with a wavelength shifting fiber looping at the end of each cell [70]. (c) Top image shows the Hamamatsu APD silicon board and bottom image shows the enclosure base to which the APD is connected, along with both ends of each wavelength shifting fiber reaching the area in which an APD pixel will stand [68]. (d) Picture of an FEB [71]. (e) Image showing a module with the manifold cover installed on top of it, responsible for directing the WLS fibers to the APD+FEB set, placed inside the electronics box [72]. (f) Schematic figure of the snout used in the detectors. The small box at the bottom right end of the figure is the APD's base, the green area is where the FEB is mounted on and the box shown at the right top is the enclosure of the electronics box [73].

The experiment uses custom built Hamamatsu APD silicon boards, each one containing 32 pixels of $2 \times 1 \text{ mm}^2$ each, whose size was designed to fit both ends of the WLS fiber in each one of the pixels (figure 4.6 (c)) [68, 69]. Given the size of the detector, in order to detect signal

from dark current¹⁰ from the far end of each WLS fiber, APDs are operated at a temperature of -15 °C. The low temperature reduces the noise from dark current and is achieved by a thermoelectric cooler (TEC) connected directly above the APD silicon board. The heat from the TEC is removed by a water cooling system that circulates cold water through all TECs. An air system ventilates dry air directly at the APDs pixels to prevent the condensation of water from the ambient's humidity on their surface due their low temperature of operation. This minimizes surface currents and avoids the possibility of short circuits.

Since a module contains 32 cells, each module is serviced by one APD. At the top of each module, the fibers are embedded into fiber raceway grooves and conducted to an optical connector (bottom of figure 4.6 (c)) that contains 32 holes, one for each APD pixel. A manifold cover encloses the fiber's raceway tracks, as shown in figure 4.6 (e). The optical connector, responsible for joining the fibers' ending points with the APD pixels, lies inside the snout of the manifold cover. The fiber tracks, manifold cover and snout are all made of black injection plastic, reducing light reflection and, therefore, cross-talk between the fibers. Each APD is connected to a Front End Board (FEB) (figure 4.6 (d)) and each set of APD+FEB is placed inside the electronics box. The FEB amplifies the APD signal, digitizes it, formats and time stamps the data before sending it to a Data Concentrator Module (DCM) [72], and hosts the circuit responsible for cooling and controlling the temperature of the APD.

Modules of 32 cells each are disposed in parallel to produce a layer of cells, known as a detector plane. Adjacent planes are orthogonally rotated with respect to one another to allow for 3D track reconstruction, as it is shown in figure 4.7. The detectors are assembled in units of blocks, each one consisting of 32 planes glued together in alternating vertical and horizontal orientations, following the aforementioned pattern. Each APD+FEB handles 32 cells and every DCM reads out the data of 64 FEBs, resulting in a total of 2,048 cells plugged into each DCM. The accumulated data in the DCMs is sent to buffer nodes, which are responsible for packing it into subruns and recording it in data disks [69].

¹⁰Noise current produced by the APD due to thermally created electron-hole pairs.

**3D schematic of
NO ν A particle detector**

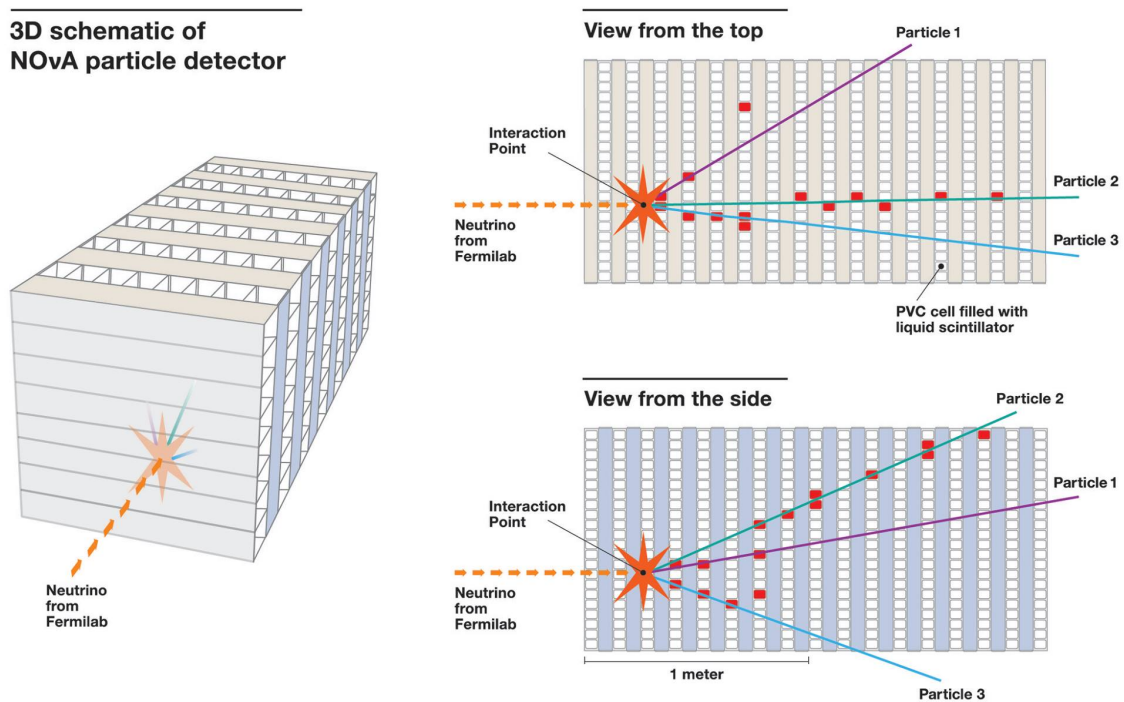


Figure 4.7 | NO ν A detector concept

Schematic concept of NO ν A detector. Figure shows the orthogonal alternating planes pattern that allows for 3D track reconstruction. A pair of planes provides information for a tridimensional space point. A bigger set of planes provides a set of points in space, enabling the reconstruction of a trajectory path [67, 74].

4.5.2 The Near Detector

NO ν A's Near Detector is located at Fermilab and it sits ~ 100 m underground, near where the MINOS detector was built and it is placed at a 1 km distance from the NuMI target. The detector became fully operational in August of 2014 and it is divided into 2 regions, called the Active Region and the Muon Catcher, the latter being positioned at the far end of the detector. The Active Region is only made of active scintillator planes while the Muon Catcher intercalates every pair of PVC planes with a 10 cm thick steel plane to increase the stopping power of the detector and increase the chance of fully containing muons produced by neutrino interactions.

In the Active Region a detector plane comprises 3 PVC modules, resulting in 96 cells per plane. The Muon Catcher is smaller, with each plane being made of 3 modules placed vertically or only 2 horizontally, which results in 96 vertical cells and only 64 horizontal cells. The total number of scintillator planes consists of 192 in the Active Region plus 22 in the Muon Catcher, resulting in a total of 20,192 cells. In the muon catcher, a steel plane is added after every 2 scintillator planes, yielding a total of 10 steel planes. The Active Region is divided into 3 units called diblocks, with 64 planes each. The diblock definition is due to the readout system, in which each DCM handles the data of a set of modules that, in the z direction, is

equivalent of two detector blocks¹¹. Since the Muon Catcher has only 22 planes, it is still counted as one diblock, but the DCMs data input ports are only partially used. The detector is 4 m wide, 4 m tall and 15.6 m long with 132 tons of scintillator, 78 tons of steel planes and 83 tons of PVC, resulting a total mass of 293 tons [68, 75, 76]. These numbers are summarized in table 4.2. Figure 4.8 is a set of screenshots taken from the GEANT4 simulation geometry file used in NO ν A, which shows the ND dimensions and the NuMI coordinate system, whose origin is placed in the geometrical center of the first plane of the detector. The z -axis of the NuMI coordinate system is rotated by $38^\circ 16' 48''$ from the geographic north, while its y -axis is parallel to the zenith [77].

Quantity	Active region	Muon catcher	Total
Modules per plane	3	3 (x) / 2 (y)	–
Number of planes	192	22 + 10 (steel)	214 + 10
Number of cells	18,432	1,760	20,192
Number of diblocks	3	1	4
Extensions (NuMI coordinate system)			
x (cm)	[-200, 200]	[-200, 200]	[-200, 200]
y (cm)	[-200, 200]	[-200, 70]	–
z (cm)	[0, 1,275]	[1,275, 1,560]	[0, 1,560]
Mass (metric tons)	195	98	293
PVC	74	9	83
Scintillator	121	11	132
Steel	–	78	78

Table 4.2 | NO ν A Near Detector specifications

The table shows the Near Detector technical specifications for the Active Region, the Muon Catcher and both [68, 75, 76].

¹¹For more details, see Chapter's section 5.1.

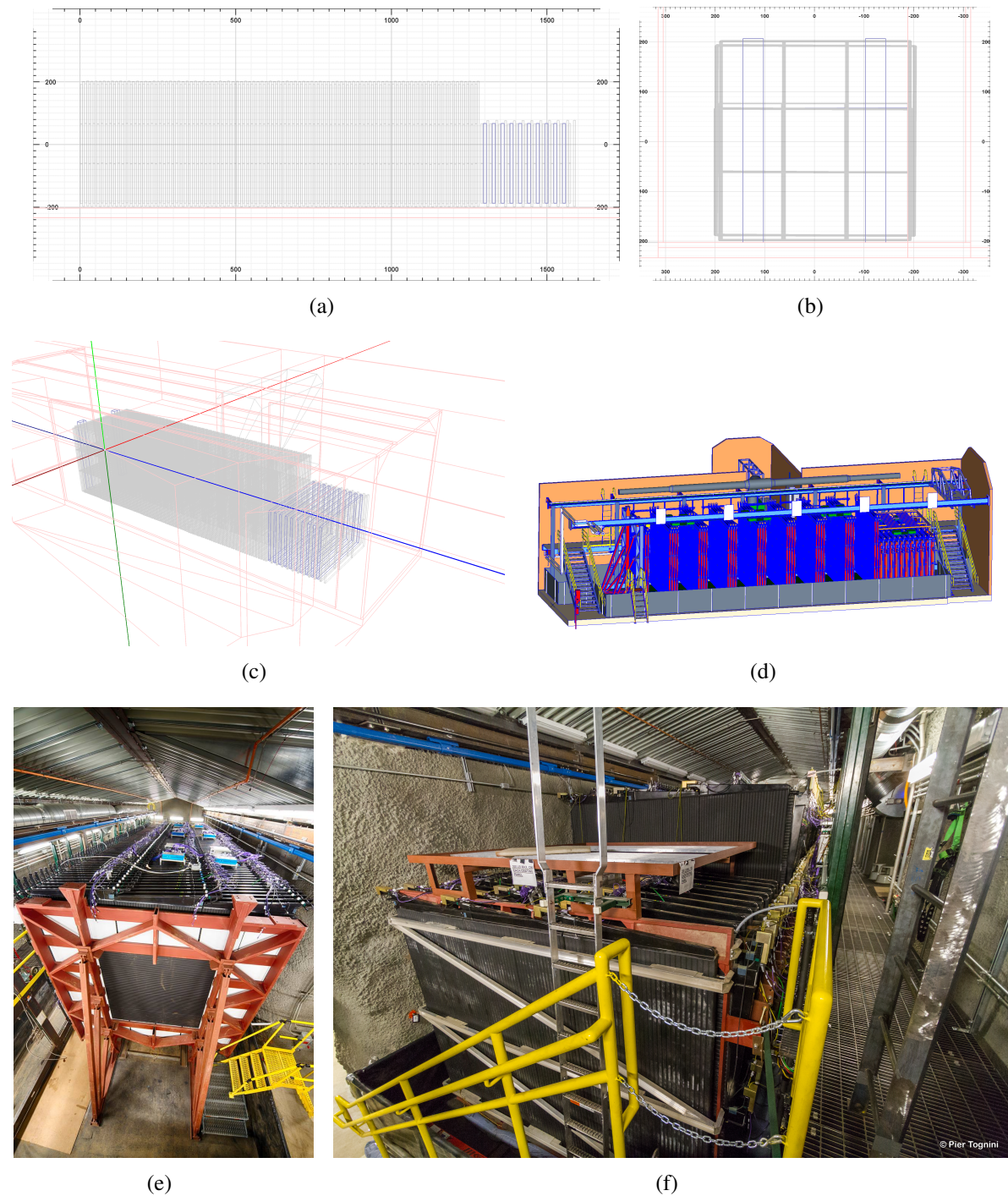


Figure 4.8 | The NO ν A Near Detector

Figures (a), (b) and (c) were taken from the Near Detector's GEANT4 geometry file showing (a) its YZ view, (b) its XY view, and (c) a tridimensional perspective of the ND, including the NuMI coordinate system axis. The blue color in (a) and (c) represent the steel planes. It is worth noticing that between every steel plane there are 2 scintillator planes, in order to provide a tridimensional position of the particle before it reaches the next steel plane. (d) A technical drawing of the ND. For picture clarity, some scintillator planes have been omitted [78]. (e) View from the top of the front face of the detector, showing the DCM modules responsible for the vertical planes and their power supplies [68]. (f) Picture of the back end of the detector. In evidence is the Muon Catcher, along with the difference in height between the Muon Catcher and the Active Region.

4.5.3 The Far Detector

NO ν A's Far Detector was built in Ash River (MN), 809 km distant from the Near Detector, and its construction ended in July of 2014. Different from the ND, the Far Detector was built near surface level, at an altitude of ~ 380 m [79], being vastly exposed to cosmic rays. In an attempt to diminish the effect, the building has a small overburden composed by 1.2 m of concrete and 0.15 m of loose barite rock, which decreases significantly the observed intensity of photons and electrons due to its high Z nuclei [68, 79]. The Far Detector is a much more massive detector, comprised of 896 planes made of 12 modules each, resulting in a total of 344,064 cells. The detector is composed by 28 blocks, which were assembled and moved into place by the block pivoter¹² (see figures 4.9 (a), (b) and (c)), resulting in a total of 14 diblocks units with 64 planes each. The final result is a detector that is 15.5 m wide, 15.5 m tall and 60 m long, weighting a total of approximately 14 metric tons. The scintillator represents roughly 65% of the total weight and the remaining is PVC [78]. Table 4.3 summarizes the aforementioned specifications, while figure 4.9 shows several pictures of the Far Detector, including the (a) assembly area, (b) and (c) the pivoter, (d) the detector's top and (e) the dates in which each block was complete.

Quantity	Value
Modules per plane	12
Total number of diblocks	14
Total number of planes	896
Total number of cells	344,064
Extensions (NuMI coordinate system)	
x (cm)	[-758, 768]
y (cm)	[-749, 765]
z (cm)	[0, 5,962]
Mass (metric kilotons)	14
Scintillator	9*
PVC	5*

Table 4.3 | NO ν A Far Detector specifications

The table shows the technical specifications of the Far Detector. Elements marked with (*) were not found and, therefore, are estimated values calculated from the available information in Refs. [75, 78].

¹²The block pivoter is a movable horizontal platform. Upon completion of each block, the pivoter moves on rails down the building hall until it reaches the position in which the block will be installed. An axis enables the platform to pivot to a vertical configuration to allow the installation of the block. At the end of the process, the pivoter returns to the assembly area and the procedure is repeated.

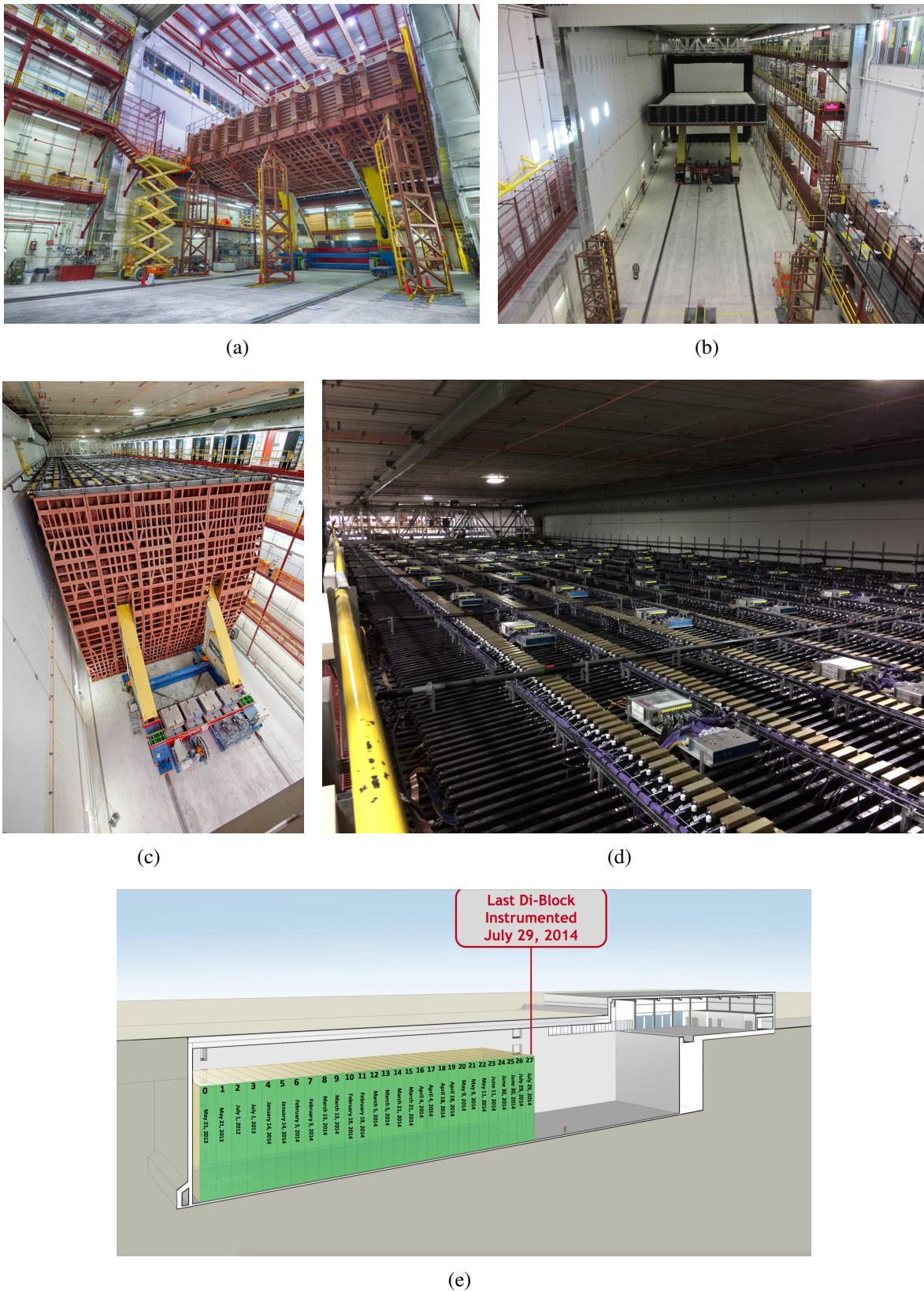


Figure 4.9 | The NO ν A Far Detector

(a) The assembly area in which the detector blocks are built [80]. (b) The pivoter moving a block into place [80]. (c) The detector, after its completion, along with the pivoter [74]. (d) The top of the detector. Each pair of electronics boxes seen in the picture takes care of 1 detector module per plane, spanned through one diblock. (e) Schematic picture showing the completion date of each detector block [81].

Chapter 5

The data acquisition

This Chapter describes the data acquisition system (DAQ) developed for the NO ν A Experiment, starting from the readout of the front-end electronics to the triggering system. In particular, the Activity trigger has received special attention.

5.1 Overview

The data acquisition system (DAQ) developed in NO ν A is based on a continuous readout of the front end electronics, whose data is temporarily stored in buffer nodes and processed by a global triggering system, responsible to decide if any portion of the data must be transferred to a long term data disk storage.

Each detector module (i.e. 32 cells) readout is performed by a set of APD+FEB. The APD converts the photon signal into an amplified electric current and sends it to the FEB, which digitizes, formats and time stamps the data. The FEB sends its preprocessed data to a DCM in batches called *nanoslices*. On the other end, each DCM collects *nanoslices* of data from 64 FEBs and assembles them into a collection, called a *microslice*, that has a duration of 50 μ s. Each DCM accumulates *microslices* until it gathers 5 ms of data, called a *millislice*, and transfers it to a pool of buffer nodes in such a way that the same buffer node receives the data from all DCMs related to the same 5 ms. This method guarantees that each individual buffer node in the pool possesses 5 ms of full detector activity, a unit of data called a *milliblock*. Each milliblock is processed by the triggering system of the buffer node, which decides if the data must be kept. In an affirmative case, the data logger gathers all the accumulated data, packs it into data files divided into runs, subruns and events, and sends it to a permanent storage system [67, 72]. Figure 5.1 is a schematic view of the DAQ system, showing the data flow from the APD readout to a raw data file being sent to the long term storage system.

A single DCM can handle 2 consecutive modules per plane in a span of 32 planes. Since each DCM only reads data from planes of the same view, and each detector block has 16 planes per view, a full DCM encompasses 2 detector blocks, a unit called *diblock*. As a consequence,

although the detector assembly is organized in units of blocks, the readout system is based on units of diblocks [67, 69]. Given the number of modules per plane (see tables 4.2 and 4.3), the NO ν A Near Detector is operated by 16 DCMs (4 diblocks \times 4 DCMs), whilst the Far Detector is readout by 168 DCMs (14 diblocks \times 12 DCMs) [67].

In order to synchronize all the electronics, from the NuMI facility to the farm of buffer nodes of each detector, the experiment uses a timing sync system connected to a GPS link. To accomplish this, each detector diblock is connected to a Slave Timing Distribution Unit (STDU). The STDUs are then connected to a Master Timing Unit Distribution (MTDU), which is connected to a GPS receiver. The MTDU is responsible to sync its clock with the GPS and synchronize all STDUs which will, at the end, put all DCMs and APD+FEBs in the same time frame. Since the NuMI facility is also connected to a GPS link, both the Near and Far detectors are placed in the same time frame as the NuMI beam spills [68].

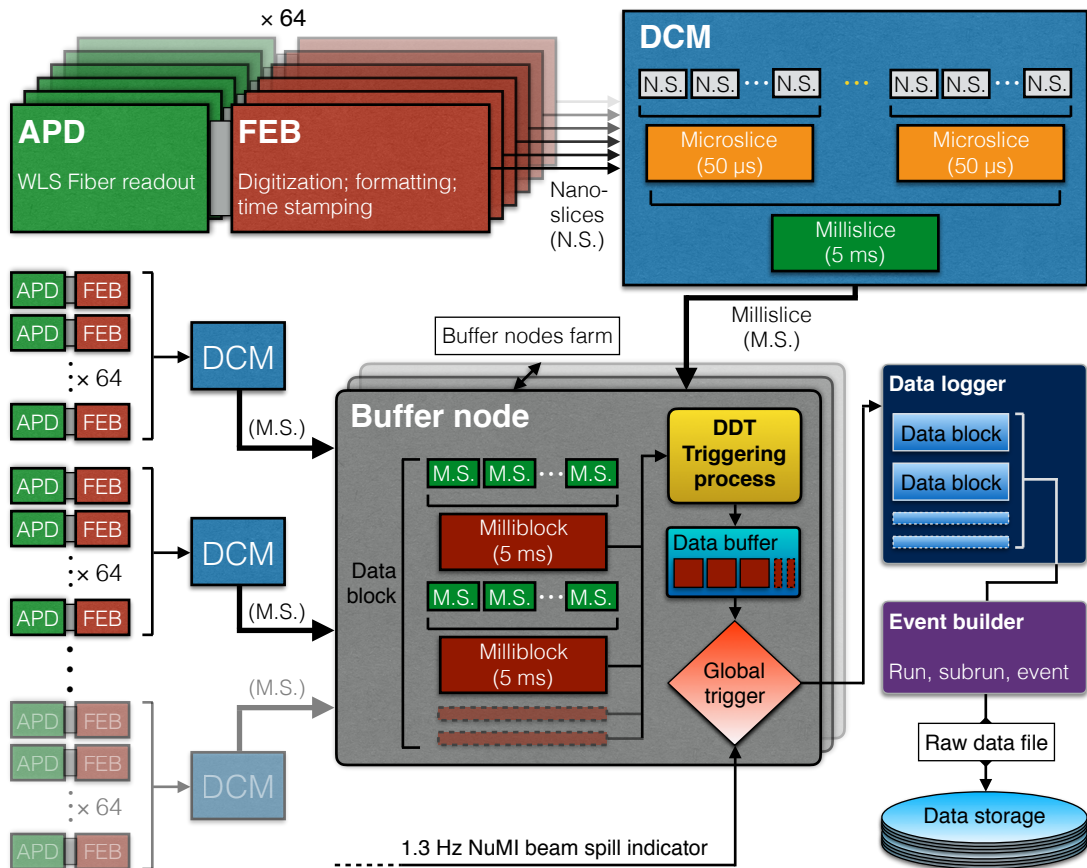


Figure 5.1 | Diagram of the NOνA DAQ system

Schematic view of the DAQ system built for NOνA. The figure shows in details the data flow and processing, from the APD readout to the final raw data file written to the storage system. The top of the figure shows 64 APD+FEBs connected to one DCM. The FEB sends nanoslices to the DCM, which forms microslices of $50 \mu\text{s}$ each and gathers them until it has a total of 5 ms of data, called a millislice. Each DCM sends its 5 ms data to a buffer node in a way that at the end, the buffer node packs all millislices into one milliblock, which has 5 ms of full detector activity. A triggering system is used to decide if the milliblock should be stored or not. The stored milliblocks are accumulated to produce a data block. The set of data blocks is processed by the data logger to produce a raw data file with run, subrun and event numbers, which is sent to a permanent data storage system. The time synchronization is handled by having all DCMs and buffer nodes connected to the STDUs and MTDU.

5.2 The triggering system

The high amount of data collected by both detectors, together with the DAQ link speed, the physical limit of the network cabling and the used bandwidth, implies that it is impractical to write to disk all the data recorded¹. Therefore, in order to store all the relevant data, a global triggering system is used.

The buffer nodes receive the data from the DCMs in a *round-robin* system [75]: the first 5 ms recorded by all DCMs is sent to one buffer node. The next 5 ms of data is sent to the second

¹Details about NOνA link speeds can be found in Ref. [82].

buffer node and so forth, until all nodes received one milliblock. At this point, the first node will have received a new milliblock, overwriting the former data. This system is designed to provide enough time for each node to process the data and decide if it should be deleted or sent to long term storage². If a set of data complies with the conditions predefined by one of the many triggers available, the buffer node will save the data in a permanent storage system. The NO ν A triggers can be separated into two categories [83]:

- 1. Standard Triggers:** This set of triggers uses the timestamp as the parameter responsible to issue a trigger. The triggers in this category are the the NuMI trigger and the Cosmic Pulsar. The first fires a fixed time during every NuMI beam spill, while the second sets off at a defined frequency, currently 10 Hz, and records one detector's time window, which lasts 550 μ s in both ND and FD.
- 2. Data Driven Triggers (DDT):** As the name suggests, these triggers analyze the data information that is temporarily stored in the shared memory segment of the nodes to decide whether it is a set of data with interesting physics or not. There is a large list of DDT triggers being used, from detector calibration purposes to physics, including search for magnetic monopoles and supernovae.

Every issued trigger is processed by the Global Trigger before being sent to a long term storage system. This process ensures that the data processed by one specific trigger conforms with the necessary standards. The requirements, although details being considerably more complicated³, can be summarized by three main informations:

- (i) the start time,
 - (ii) the duration of the data, and
 - (iii) the trigger mask, which contains the information on the type of the trigger being issued,
- allowing a virtually infinite flexibility when it comes to define a trigger. Currently, the set of triggers used in the experiment are summarized in table 5.1.

²Currently the system has no more than a few seconds to make a decision for each milliblock.

³For a detailed description of the DAQ trigger format, see Ref. [84].

Trigger	Category	Detector	Nominal rate [Hz]	Readout size [μ s]
NuMI Beam	Standard	Both	1.3	550
Cosmic Pulsar	Standard	FD	10	550
Activity	DDT	ND	40	50
High Energy	DDT	FD	8	50
Calibration muon	DDT	ND	24	50
Upward going muon	DDT	FD	0.8	50
Contained upward going muon	DDT	FD	8	50
Fast Magnetic Monopole	DDT	FD	17	50 – 100
Slow Magnetic Monopole	DDT	FD	1	50 – 5,000
SNEWS	DDT	Both	0.02	2,000,050

Table 5.1 | Triggers used by NO ν A

A summary of all triggers being used in NO ν A, detailing their category, rate, and time window. The Activity trigger, highlighted in the table, is the one responsible to collect cosmic data from the Near Detector and it is the trigger used in this analysis. The SNEWS trigger is an acronym for SuperNova Early Warning System, a trigger used worldwide to provide the scientific community a prompt alert of the occurrence of a core-collapse supernova signal.

5.3 The Near Detector Data Driven Activity trigger

Although the Far Detector operates using the Cosmic Pulsar trigger for collecting cosmic ray data, the Near Detector is not only much smaller (roughly 55 times smaller in volume), but it is also located under approximately 100 m of a solid rock overburden, vastly diminishing the amount of cosmic ray activity. This results in not just a clean neutrino data, but also a small enough cosmic ray activity that a sampling process, as the Far Detector’s Cosmic Pulsar, becomes unnecessary. Therefore, the collaboration developed a trigger whose purpose is to record any reconstructable activity found to be outside of the NuMI beam pulse time window. A reconstructable activity is a defined minimum amount of hits that are close in space and time. The effort resulted in what it is now known as the Data Driven Activity trigger (or Activity trigger), shown in table 5.1, and which has three basic requirements [85]:

- 1. Number of hits** – There must be a minimum number of hits recorded concomitantly throughout the detector. Currently this threshold is set to be at 10.
- 2. Number of planes** – There must be at least one hit in a minimum number of planes in each view of the detector. Currently, the trigger considers a minimum of 8 planes in total, with at least 3 planes per view.
- 3. Continuity** – There must be a minimum number of active planes within a minimum number sequential planes. Currently, the trigger considers that there was an activity if the readout shows at least 5 planes with hits in a window of 6 sequential planes.

5.3.1 Change in the requirements of the Activity trigger

The Data Driven Activity trigger changed its requirement values in April 8, 2015. The minimum number of planes and the continuity premisses remained intact, but the minimum number of hits changed from 60 to 10 [86]. The reason behind the reassignment of this parameter lies in Monte Carlo studies that showed that the trigger efficiency for single muons is almost twice as high when the minimum number of hits is lowered to 10, meaning that the old trigger definition resulted in the loss of almost 50% of the reconstructable cosmic data. Table 5.2 shows the date when the trigger changed and figure 5.2 shows the increase in the DD-Activity trigger rate before and after the trigger configuration change has been implemented.

	Original trigger		Current trigger	
	Run number	Date	Run number	Date
Start	10332	07 / 31 / 2014	10876	04 / 08 / 2015
End	10875	04 / 08 / 2015	Present	Present

Table 5.2 | Runs and dates of both Activity trigger configurations

Table showing the date and the Near Detector run related to when the Activity suffered the change from 60 to 10 hits threshold.

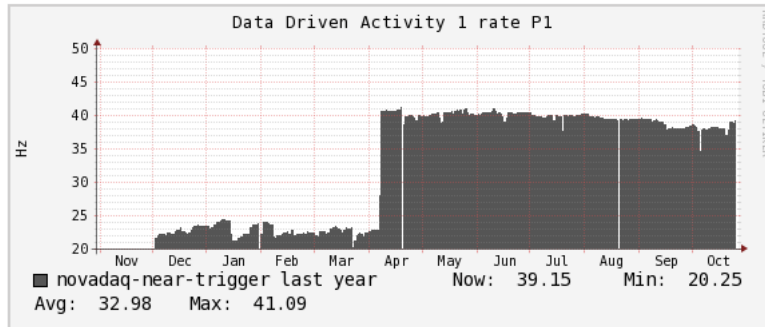


Figure 5.2 | Activity trigger date rate change

Figure showing the change in the NO ν A DAQ recording response rate from ~ 20 Hz to ~ 40 Hz after the Activity trigger changed its minimum hits threshold from 60 to 10 hits on April 08, 2015.

5.4 The DAQ data formats

NO ν A organizes its raw data in a hierarchical format that is the result of the concatenation of different data blocks from different levels of the data acquisition chain. The following list shows the data units by order of hierarchy, with the first item being the one with the highest value in the hierarchy rank [84].

1. **RUN** – The run is a chronologically ordered sequence of triggered events that were written out to permanent storage and correspond to a specific period of time. A run normally encompasses a time range at the magnitude of hours and carries the necessary information to describe the detector and the run time parameters of the DAQ system. For each detector, the run number ranges from 0 to infinity.
2. **SUBRUN** – Each run is divided into units called subruns. A new subrun is started when the data stream reaches a defined size limit, currently set to 1 GB, or a defined time limit, currently set to 1 hour [72]. Either way, if any of the two aforementioned conditions is satisfied, a new subrun is started by the DAQ system. For the Far Detector, the subrun number ranges from 0 to 63, yielding a total of 64 subruns per each run. Since each subrun takes minutes to complete, the FD records a handful of runs within 24h. In the Near Detector, as a result of its much lower data stream, each subrun finishes after 1 hour. In light of this fact, the number of subruns is defined to vary from 0 to 23. This yields a comfortable way of dividing the data into one run per day with 24 subruns each.
3. **EVENT** – A readout window recorded to the permanent storage as a result of a trigger response. The recorded time window will depend on the trigger, varying from $50 \mu\text{s}$, which is the minimum time window allowed by the DAQ system, up to a few seconds.
4. **SLICE** – Events can be divided into slices for better performance of the analyses algorithms. Since different studies require different forms of slicing, the slicing method may vary according to the reconstructed data file, resulting in different events holding different numbers of slices.
5. **TRIGGER** – A specified amount of detector activity data that is considered of interest for further analysis. The size of the recorded time window varies according to the trigger's definition. This information consists of the starting time of the activity, its duration, the type and the source of the trigger, along with the data itself, which consists of a chronologically ordered set of data blocks.
6. **DATA BLOCK** – The collection of milliblocks extracted from the buffer nodes farm upon a trigger request. Size and duration of the data block will depend on the trigger and the recorded activity.
7. **MILLIBLOCK** – The collection of all millislices collected from all the DCMs of the same 5 ms period. Therefore, a milliblock contains all the detector activity recorded within a 5 ms time window. This is the information that is processed by the triggering system.
8. **MILLISLICE** – A collection of readout windows (microslices) that are combined to form a data block of 5 ms, appropriate for network transmission. This format is used for the data transmission between the DCMs and the buffer nodes.

9. **MICROSLICE** – A 50 μs long collection of individual FEB nanoslices. Each FEB communicates with the DCMs in packages of microslices and, therefore, this is the shortest detector activity time window recorded in the permanent storage system. Even if the activity responsible for a trigger issue only lasted for a few ns, such as a cosmic shower, the event recorded in the data file will show a time window of 50 μs containing the much shorter detector activity.
10. **NANOSLICE** – The data readout by the FEB, including the APD’s pulse height and the timestamp of individual detector cells’ activities. A nanoslice is usually referred to as a detector hit.

The information presented in former sections is summarized in table 5.3 which shows each data unit, along with its source, composition and size.

Name	Source	Composed by	Size
RUN	Data logger	Subruns	64 (FD) / 24 (ND)
SUBRUN	Data logger	Events	Variable
EVENT	Data logger	Data blocks	Variable
TRIGGER	Buffer node	Millislices	Variable
DATA BLOCK	Buffer node	Milliblocks	Variable
MILLIBLOCK	Buffer node	Millislices	5 ms
MILLISLICE	DCM	Microslices	5 ms
MICROSLICE	DCM	Nanoslices	50 μs
NANOSLICE	FEB	APD readouts	Sampling clock

Table 5.3 | The DAQ data formats

A summary of the listed DAQ data formats, showing their respective sources, what they are composed of and their respective size.

Chapter

The pre-analysis

6.1 Overview

This Chapter covers all necessary software processing steps that come prior to the physics analysis itself. The first section describes the track reconstruction algorithm developed for the analysis. The following section describes the method used to produce a multiple-muon Monte Carlo for validating the reconstruction software, finding its efficiency and purity, and measuring the accuracy of the simulation with the data. The Monte Carlo is also important for highlighting the limitations of the reconstruction, and in defining the selection criteria applied in the analysis. Next, the data processing chain is described from the raw data up to the final analysis files. With the data processed, a few consistency checks are applied to ensure that there is no anomaly in the analysis criteria, nor is there a detector degradation or an unexpected hardware/configuration change over time. The next section describes the meteorological data used to compare the variations in the muon flux with variations in the temperature of the atmosphere. The last section is dedicated to outline the frequency analyses methods, used to quantify the periodicity and likelihood of the seasonal effect.

6.2 The reconstruction process

6.2.1 The Hough Transform

In $\text{NO}\nu\text{A}$, an event is a collection of hits from its rectangular cells stored after a trigger response from the DAQ system. The extraction of patterns from said collection of hits, such as track-like trajectories, is the first step towards a full event reconstruction. The chosen method to achieve this goal is the Hough Transform [87], which is a standard method for line and shape recognition in two dimensional images composed of points or pixels. The method is known for its robustness to noise. Since every cosmic ray muon event in $\text{NO}\nu\text{A}$ is a combination of two two-dimensional views of the detector each containing a set of channel hits forming a straight

line, this is an ideal method for finding track-like patterns.

The Hough Transform maps space points to curves in a polar coordinate system, known as the Hough map. The Hough map is built from the premise that each space point in a (x, y) coordinate system is intersected by an infinite set of lines of the form

$$\rho(\theta) = x \cos \theta + y \sin \theta, \quad (6.1)$$

where ρ is the perpendicular distance between the line and the origin of the (x, y) coordinate system, and θ is the angle between ρ and the x -axis. Therefore, each space point in (x, y) is described by a curve in the Hough map. This parameterization is necessary to allow for vertical lines, which are unachievable if written in the form $y(x) = ax + b$.

In the case of two space points, $P_1 = (x_1, y_1)$ and $P_2 = (x_2, y_2)$, both curves in the Hough map must share one solution (ρ_0, θ_0) , as shown in figure 6.1, which describes the line that intersects both space points in the (x, y) coordinate system. As more points are added, more Hough curves will intersect at different points, creating a score of how many (x, y) space point pairs are included in a specific (ρ, θ) line. The Hough map coordinate with the highest number of curve intersections defines the line that connects the highest amount of data points in the (x, y) coordinate system.

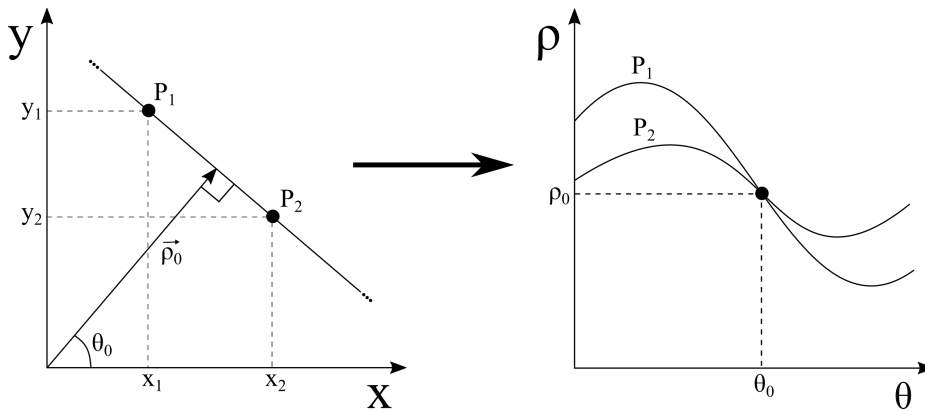


Figure 6.1 | The Hough Transform

Figure shows the Hough transform curve for two cartesian space points, P_1 and P_2 , in the Hough map. The coordinate (ρ_0, θ_0) , which is the intersection between the curves describing points P_1 and P_2 in the Hough map, defines the line that intersects both points in (x, y) .

Although the Hough Transform was originally designed to find straight lines, over time the method was generalized to detect arbitrary shapes [88].

6.2.2 NOVA's Multi-Hough Transform method

NOVA uses a modified Hough Transform, outlined in Refs. [89, 90], in which the method is applied separately to each view of the detector by calculating (ρ, θ) values for every line that intersects every pair of hits. For each line calculated, the Hough map is filled with a Gaussian

smearred weight, defined as

$$w = \exp\left(-\frac{\rho - \rho_0}{2\sigma_\rho^2}\right) \exp\left(-\frac{\theta - \theta_0}{2\sigma_\theta^2}\right), \quad (6.2)$$

where

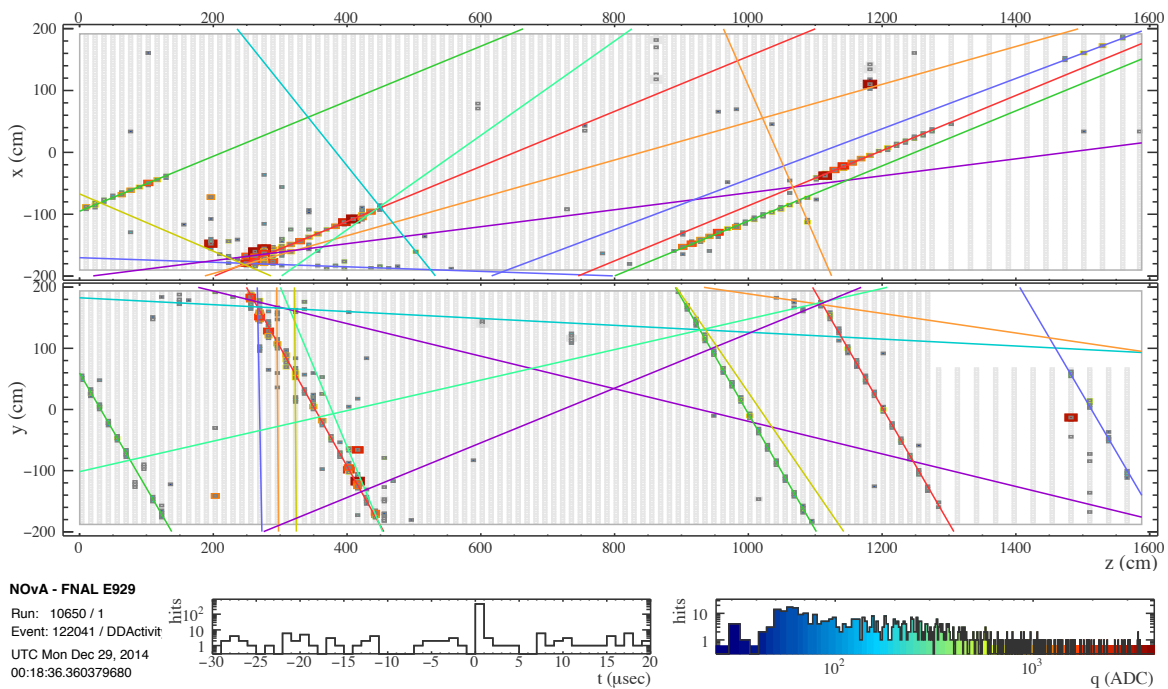
$$\sigma_\rho = \frac{3}{\sqrt{12}} \text{ [cm]}, \quad (6.3)$$

$$\sigma_\theta = \frac{3 \text{ [cm]}}{d\sqrt{6}}, \quad (6.4)$$

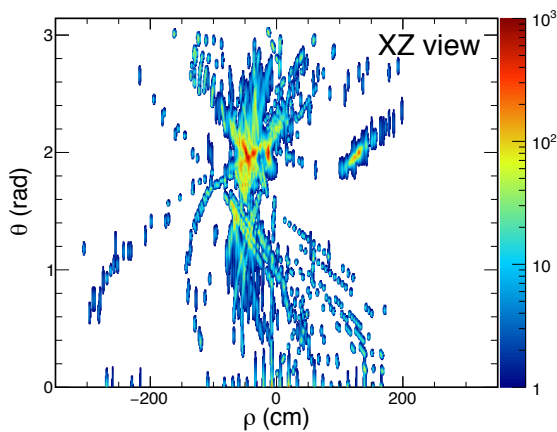
and d is the distance between pairs. Two restrictions were added to the algorithm for the NO ν A ND: the first limits the distance between pairs to be $d \leq \sqrt{15,000}$ cm, to avoid heavy computing time lost in pairs of hits that are unlikely to represent a real track. The second defines a minimum distance of $0.25\sqrt{15,000}$ cm for hit pairs that are in the same horizontal line, whether in the XZ or YZ view of the ND. Since these points have the same x or y value depending on the detector view, they create a strong tendency to produce Hough lines that are completely horizontal and do not represent real data. Figure 6.2 shows a 5 muon event recorded by the Near Detector, the lines found by the Multi-Hough Transform, and the respective Hough map for each view.

The Multi-Hough loop

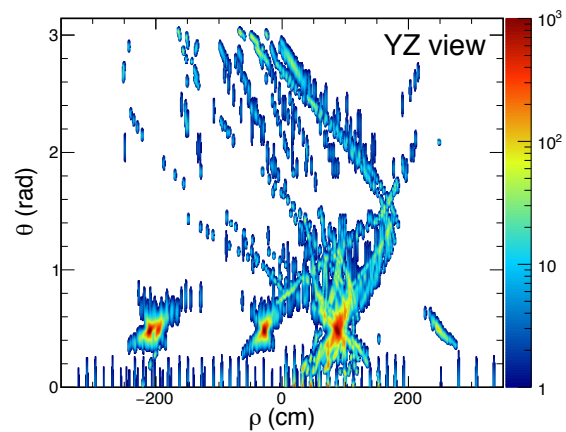
The Hough Transform can produce better results if is applied multiple times to the same event. After the highest peak is identified from the Hough map, the hits associated with said line are removed from the sample and a new Hough map is produced. The hits associated to the tallest peak are again removed, and the procedure is repeated. The loop ends when there are no more peaks above a defined threshold or if a predefined number of loops is achieved, whichever comes first.



(a)



(b)



(c)

Figure 6.2 | Multi-Hough Transform applied to a multiple-muon event

(a) Event display of a 5 muon event recorded by the Near Detector. The colored lines are the solutions found by the Multi-Hough Transform. (b) The Hough map for the XZ and (c) YZ views of the detector. The Hough peaks produce the lines shown in (a). Since the 5 muon tracks must produce the highest peaks in the Hough map, the 5 highest peaks in figures (b) and (c) define the 5 lines that are overlapping the hits produced by the 5 muons seen in the event display.

6.2.3 Multi-Hough 3D track reconstruction

The reconstruction process described in this section is repeated for every trigger recorded. For organization purposes, the reconstruction chain is summarized in the following set of steps, each one being fully described in its own subsection.

- **Multi-Hough 2D track reconstruction:** All possible 2D tracks in each view are found and stored.
- **Removal of far away hits in 2D tracks:** Real track hits are close together. Hits found with a big gap¹ from each 2D track cluster of hits are removed.
- **Removal of rogue 2D tracks:** The Multi-Hough transform commonly finds shorter rogue tracks overlapping the real track. This step removes these rogue tracks from the list of 2D tracks in each view.
- **2D track merge:** The remaining 2D tracks in each view are compared and merged to produce 3D tracks.

1. Multi-Hough 2D track reconstruction

Multi-Hough lines are created from the (ρ, θ) solutions found in the Multi-Hough map. Due to the Multi-Hough loop, the final Multi-Hough maps are very clean, with only a small set of lines found per event. Given this scenario, no Multi-Hough peak threshold was used, in order to avoid the removal of short tracks. These lines are used in the first step of the reconstruction, which gathers hits along each Multi-Hough line and creates vectors of hits that represent every possible 2D track for each detector view. This is accomplished by looping over the Multi-Hough lines in each detector view and selecting hits whose perpendicular distance is 10 cm or less from the Multi-Hough line. At the end of this process, both sets of 2D tracks found for each view are ordered by decreasing number of hits. This ordering is necessary for the 3rd step of the reconstruction.

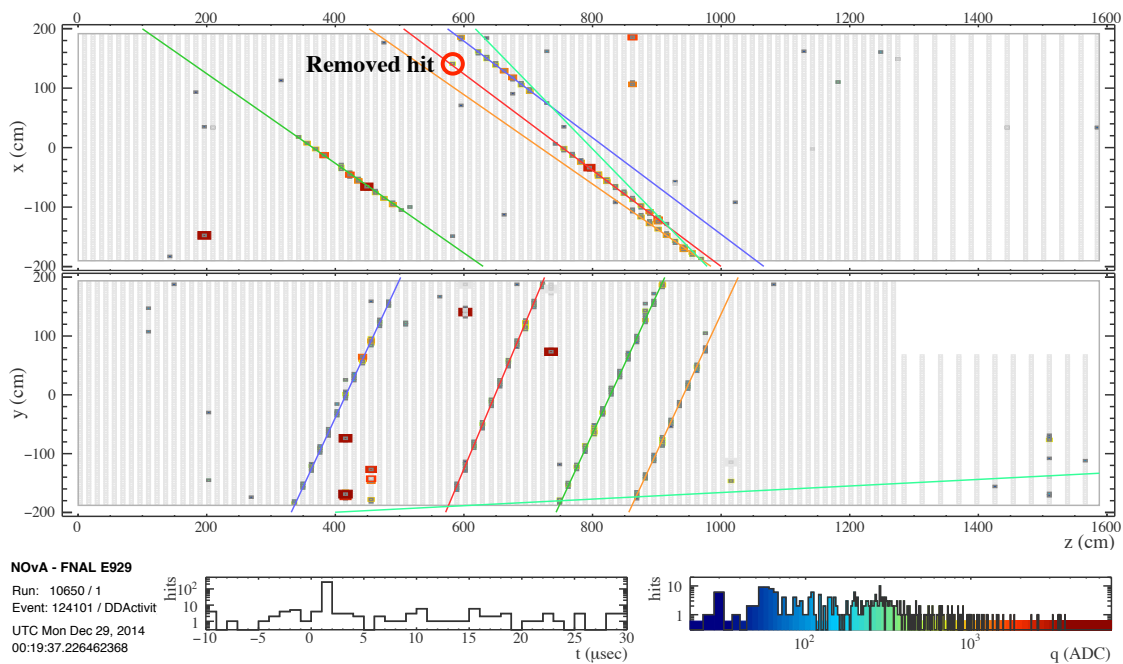
2. Removal of far away hits in 2D tracks

A charged particle traversing the detector produces a set of hits close in space and time. Therefore, any collected hit in step 1 that is farther than a threshold distance from the cluster of hits should be ignored, as it may be a noise hit (figure 6.3 (a)) or belong to another track (figure 6.3 (b)). Due to the detector geometry, the distance between hits widens as the angle between the 2D track with respect to the detector planes decreases. Therefore, the gap threshold Δr_{\max} is angle dependent, and is defined as

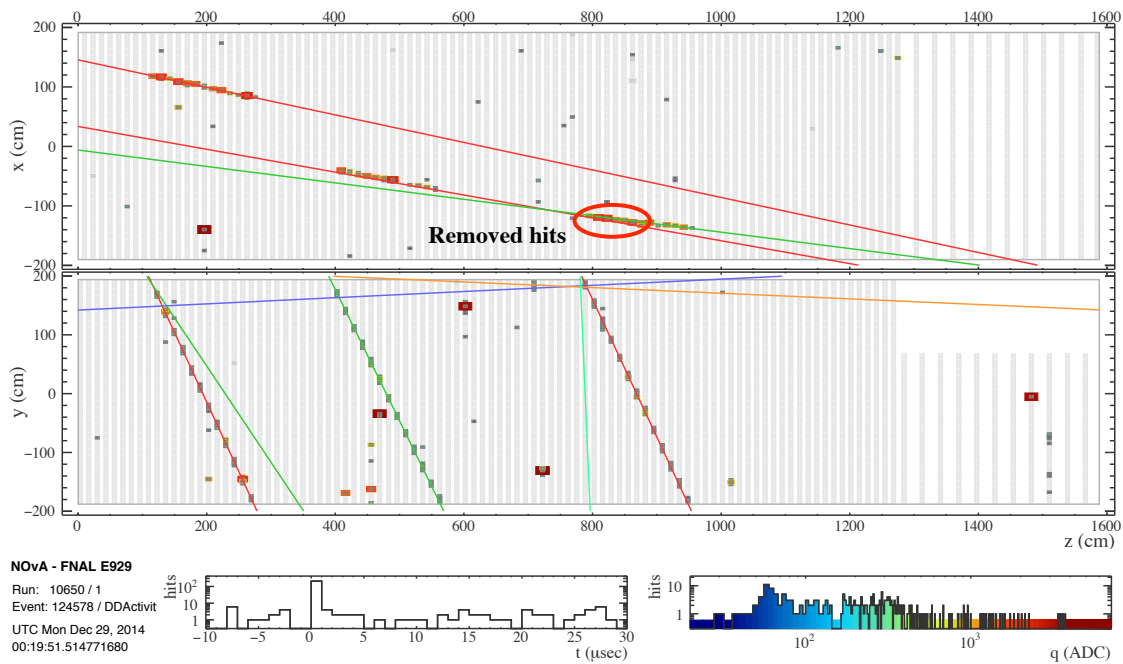
$$\Delta r_{\max} = d_{\text{gap}} + d_{\text{gap}} \sin \theta, \quad (6.5)$$

where $d_{\text{gap}} = 70$ cm and θ is the slope of the Multi-Hough line. This allows the maximum gap distance to vary within $70 \text{ cm} \leq \Delta r_{\max} \leq 140 \text{ cm}$, being 70 cm for tracks parallel to Z, and 140 cm for tracks parallel to the plane surface.

¹In this context, a big gap represents a gap that is larger than a predefined threshold distance.



(a)



(b)

Figure 6.3 | Example of gaps within 2D track hits

(a) Event display of a 4 muon event. Highlighted, the removed hit from the list of hits belonging to the 3rd track from left to right in the XZ view. (b) Event display of a 3 muon event. In this case, the set of highlighted hits were originally included in the list of hits belonging to the 2nd track from left to right in the XZ view.

3. Removal of 2D rogue tracks

The Multi-Hough transform produces solutions that fit the real tracks, but also creates rogue results due to the proximity of the hits belonging to the real track with noise hits². This consideration is clearly shown in figures 6.2 (a) and 6.3, in which several other Multi-Hough lines are crossing the real trajectories. This is particularly problematic, as rogue 2D tracks may result in a single muon event being flagged as a multiple-muon one. Diminishing the Hough peak threshold was a bad strategy, as a higher threshold causes the removal of shorter real tracks, decreasing statistics and possibly adding a bias to the analysis. Hence, a method was developed for removing 2D rogue tracks based on the following set of premises:

- i)* The Activity trigger is expected to only records reconstructable data, as mentioned in section 5.3. Therefore, for every recorded event there must be at least one real track.
- ii)* In the case of overlapping tracks, the longest track is the correct one.
- iii)* In the case of a multiple-muon event, real tracks do not intercept each other within the detector volume.

The method is applied to each detector view separately. In order to define which are the real 2D tracks in a specific view, a boolean matrix \mathbb{M} of order $k \times k$, where k is the number of 2D tracks found in said view, is built with the purpose to select only non overlapping tracks. The matrix values \mathbb{M}_{nm} , with $n < m$, represent all pair combinations between tracks and can be TRUE or FALSE, with the latter meaning that track m overlapped track n . To define each \mathbb{M}_{nm} value, 2D tracks are ordered by descending number of hits and every possible pair of tracks is checked. For every pair, the distance in the Z axis between every hit of one track and every hit of the other track is calculated. If the condition

$$\Delta Z = |\text{hit}_{\text{track}_n}^i - \text{hit}_{\text{track}_m}^j| < 10 \text{ [cm]} \quad (6.6)$$

is satisfied, where $\text{hit}_{\text{track}_n}^i$ is the i^{th} hit of the n^{th} track and $n < m$ for avoiding duplicate combinations, then track _{m} (shorter) is considered to be a rogue track and the position \mathbb{M}_{nm} is defined as FALSE. The main diagonal of \mathbb{M} is always TRUE, since a track cannot be compared to itself, and every value below it is filled with TRUE as well, as they are not used. At the end of the process, the columns of \mathbb{M} that are filled only with TRUE values represent the 2D tracks that did not overlap and are most likely to be real tracks.

The predefined condition that the main diagonal of \mathbb{M} is always TRUE, implies that $\mathbb{M}_{n1} = \text{TRUE}$ and, along with the fact that tracks are ordered by descending number of hits, this already defines the first and longest track recorded as a real track for every event, satisfying premises *i)*

²There are different reasons for the noise hits, not just APD channels with low thresholds. For example, more energetic events can cause an effect known as an APD flash. When enough energy is dumped on one or more channels of the same APD, it causes the baseline of the APD to sag, producing fake hits as it restores.

and *ii*). The existence of any other non overlapping track is conditioned to the existence of any other column of \mathbb{M} that is only filled with TRUE values, satisfying premise *iii*).

Figure 6.4 shows a 2 muon event that produced 5 Multi-Hough lines in the YZ view of the detector, labeled in descending order of number of hits. The resulting \mathbb{M}_{YZ} matrix, after applying the condition stipulated by equation 6.6, is shown in equation 6.7, whose only tracks considered to be real are the tracks from columns 1 and 2, representing the tracks labeled as 1 and 2 in figure 6.4.

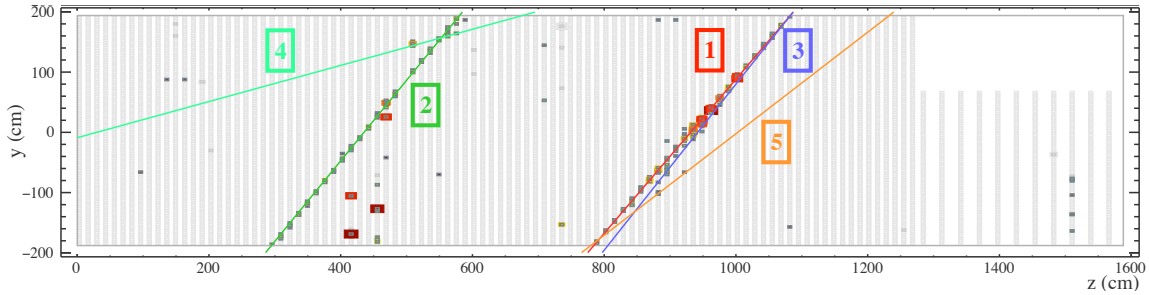


Figure 6.4 | YZ view of a 2 muon event with rogue tracks

Figure shows the YZ view of the detector for a 2 muon event that produced a total of 5 Multi-Hough lines, that were responsible for producing 5 2D tracks, of which only 2 represent a correct muon trajectory. The lines are labeled by descending order of number of hits.

$$\mathbb{M}_{(YZ)} = \begin{array}{c} \text{Track} \\ \begin{array}{c} 1 \\ 2 \\ 3 \\ 4 \\ 5 \end{array} \end{array} \begin{array}{ccccc} 1 & 2 & 3 & 4 & 5 \\ \left[\begin{array}{ccccc} \text{True} & \text{True} & \mathbf{FALSE} & \text{True} & \mathbf{FALSE} \\ \text{True} & \text{True} & \text{True} & \mathbf{FALSE} & \text{True} \\ \text{True} & \text{True} & \text{True} & \text{True} & \text{True} \\ \text{True} & \text{True} & \text{True} & \text{True} & \text{True} \\ \text{True} & \text{True} & \text{True} & \text{True} & \text{True} \end{array} \right. & \end{array} \quad (6.7)$$

A final consideration is that, if applied to a single view, a rogue track that has no overlaps could indeed exist and will be considered as a TRUE 2D track. This does not constitute a problem, as said track would not have its 2D track counterpart found in the other detector view and, in such cases, the 2D track merging will fail and will not produce any 3D track. This method has proven to be robust to deal with noisy events, such as the one presented in figure 6.2 (a), in which the resulting matrices selected only the 5 expected muon tracks for each view.

4. 2D track merge

At this point of the reconstruction, the remaining 2D tracks from each view are compared and, if possible, merged to produce 3D tracks. Since individual hit time showed to be unreliable to define their order within a track, the hits of every track, in both views, are ordered by increasing value of Z . This allows the comparison of the Z coordinate of both ends of every

track (i.e. the first and last hits) from one detector view with the Z coordinates of both ends of every track in the other view. If conditions

$$\Delta\text{start}Z = Z_{\text{hit}_0}[\text{XZ}]_{\text{track}_n} - Z_{\text{hit}_0}[\text{YZ}]_{\text{track}_m} < 50 \text{ cm}, \quad (6.8)$$

$$\Delta\text{end}Z = Z_{\text{hit}_{\text{last}}}[\text{XZ}]_{\text{track}_n} - Z_{\text{hit}_{\text{last}}}[\text{YZ}]_{\text{track}_m} < 50 \text{ cm}, \quad (6.9)$$

and

$$\sum \text{hit}[\text{XZ}]_{\text{track}_n} + \sum \text{hit}[\text{YZ}]_{\text{track}_m} \geq 6, \quad (6.10)$$

the latter selecting only 3D tracks with at least 6 hits, are satisfied at the same time, then 2D track_n and 2D track_m are merged together and they cannot be used in any other 3D track merging. The loop ends if there are no more combinations that can satisfy conditions 6.8, 6.9, and 6.10, or if there are no more 2D tracks left in at least one of the views.

Since hits are ordered by increasing values of Z , the final step calculates the first and last hits of each 3D track and defines the starting hit as the one with the highest Y value. This implies that the reconstruction does not consider the existence of upward muon tracks, a limitation that is not relevant for this analysis.

All the selection criteria used during the reconstruction process are summarized in table 6.1.

Criteria	Value
2D tracks	
Multi-Hough peak threshold	0
Allowed distance from the Multi-Hough line	10 cm
Maximum gap within hits (d_{gap} in 6.5)	70 cm
Minimum distance between tracks	10 cm
3D tracks	
Allowed $\Delta\text{start}Z$ and $\Delta\text{end}Z$ for 3D track merging	50 cm
Minimum number of 2D hits for 3D track merging	6

Table 6.1 | Track reconstruction criteria

The table shows the criteria used for both 2D and 3D track reconstruction. The Multi-Hough peak was kept as zero due to the Multi-Hough loop, which produces final Hough maps with small sets of Hough line solutions for each event. For that reason, any non zero threshold could result in the non reconstruction of short tracks that crossed the corners of the detector.

6.3 The Monte Carlo

6.3.1 Monte Carlo software for simulating multiple-muon events

NO ν A uses CRY as its standard cosmic ray Monte Carlo. It is a simulation based on pre-computed tables derived from full MCNPX simulations of primary cosmic rays [91]. CRY's simulation outputs are propagated through a full GEANT4 simulation of the Near Detector geometry and cavern. The final output is a ROOT file with the same structure as the files produced by the NO ν A DAQ system, along with the inclusion of an extra set of data holding the true information of the simulation. Although CRY provides a fast simulation process, it has a few known limitations, which include a short list of simulated particles³ and the underestimation of the neutron flux at low energies. For this analysis' purpose, the Monte Carlo faces an even bigger limitation, which is the fact that it only simulates samples containing single muon events and hence fails to provide useful samples for testing the efficiency and limitations of the multiple-muon reconstruction code. For single muon studies, a standard set of CRY Monte Carlo simulation files are used, but there was the need to produce multiple-muon samples.

The solution was to develop a mock-up of multiple-muon events from the original single muon samples. The method consists of reading a single muon sample and replicating the original simulated muon in each event (i.e., keeping its original momentum) and assigning a new randomly chosen location. This replication process is repeated until the desired multiplicity is achieved. To ensure that every new replicated muon will cross the detector's volume, the starting position of the muon is placed in an area that is defined according to its momentum direction, which is described by the angles θ_{XY} and θ_{YZ} , as shown in figure 6.5. These two angles

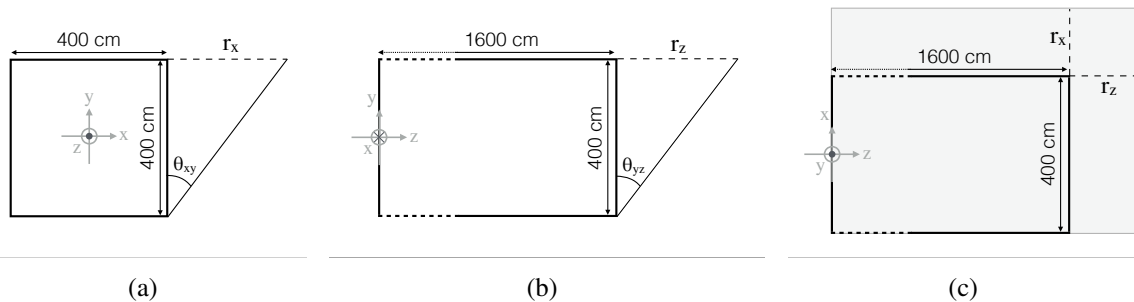


Figure 6.5 | Schematic view of the multiple-muon Monte Carlo allowed region

(a) XY view and (b) YZ view of the detector, showing the limit range in directions X and Z in which a particle with angles θ_{XY} and θ_{YZ} would still cross the detector volume. Figure (c) shows the allowed area for the case shown in (a) and (b), in which both r_x and r_z are positive values.

allow the calculation of the distance limits r_x and r_z at the top of the detector in which the new

³CRY only considers protons, neutrons, muons, pions electrons and photons in its simulation, lacking, for example, the neutrinos produced by meson and lepton decays.

particle track can be placed and still reach the detector volume:

$$r_x = \text{ND}_{\text{height}} \tan(\theta_{xy}) = \text{ND}_{\text{height}} \left(\frac{p_x}{p_y} \right) \quad (6.11)$$

and

$$r_z = \text{ND}_{\text{height}} \tan(\theta_{yz}) = \text{ND}_{\text{height}} \left(\frac{p_z}{p_y} \right), \quad (6.12)$$

where p_x , p_y and p_z are the momentum components in the NuMI coordinate system, and $\text{ND}_{\text{height}} = 400$ cm. The output of the mock-up is a text file written in the HEPEVT format that is used as an input for the GEANT4 simulation. Each DAQ output file will contain a specified number of events, all with the same predefined multiplicity. This file is used to create a reconstructed file with both true information and the 3D track reconstruction based on the Hough Transform. As this method produces a continuous stream of events with the same multiplicity, resulting in an unrealistic flux of particles, it can only be used to study reconstruction efficiency, purity, and limitations.

6.3.2 Data and Monte Carlo track reconstruction

It is important to verify if the Monte Carlo simulation reflects the data measured by the detector. To do so, the multiple-muon Monte Carlo simulation is reconstructed using the same process as applied to the Near Detector data and a set of distributions is made. The distributions presented in figure 6.6 show approximately 15,000 two-muon Monte Carlo reconstructed events compared with multiple-muon events collected from a full day of detector exposure. Both MC and data were normalized with respect to their number of events. For validation purposes, no additional selection criteria were included, except the ones used in the reconstruction process.

The first set of distributions shown in figure 6.6 provides a comparison between the track start and end points, along with the directional cosine of every reconstructed track for both data and Monte Carlo. The bump seen at approximately 50 cm in the track start [Y] distributions (figure 6.6 (e)) is caused by the Muon Catcher, which is also evident at the end of the track start [Z] plot (figure 6.6 (f)). The big peaks at zero in the directional cosines [X] and [Z] (figures 6.6 (g) and (i)) are caused by poorly reconstructed tracks that crossed the detector parallel to the NuMI x-axis (i.e. parallel to the detector planes) or were very steep tracks (i.e., with very small zenith angles). The multiple-muon reconstruction of both Monte Carlo and data agree to a satisfactory level.

Figure 6.7 shows a second set of distributions, being the (a) number of hits, (b) number of detector planes, (c) track length, (d) cosine of the zenith angle, (e) the ϕ angle, which is defined as the angle in the NuMI XZ plane between the track and the NuMI x-axis ($\phi = 0$ points to the x+ axis direction), and (f) shows the distance between every pair of tracks in each event. There are two issues that can be noticed from these plots: *i*) the odd data points in the ϕ plot, which show spikes at 0° , 90° , 180° and 270° are produced by the same reasons that produced the spikes

in the directional cosines plots. *ii*) The track separation plot shows a discrepancy between data and MC for tracks closer than 70 cm. The excess seen in the data is caused by muons that interact with the surrounding cavern and produce small activities at the edges of the ND. Said interactions are not taken into account by the Monte Carlo simulation, and are reconstructed as one or more short tracks close to the muon track, resulting in a mistagged multiple-muon event.

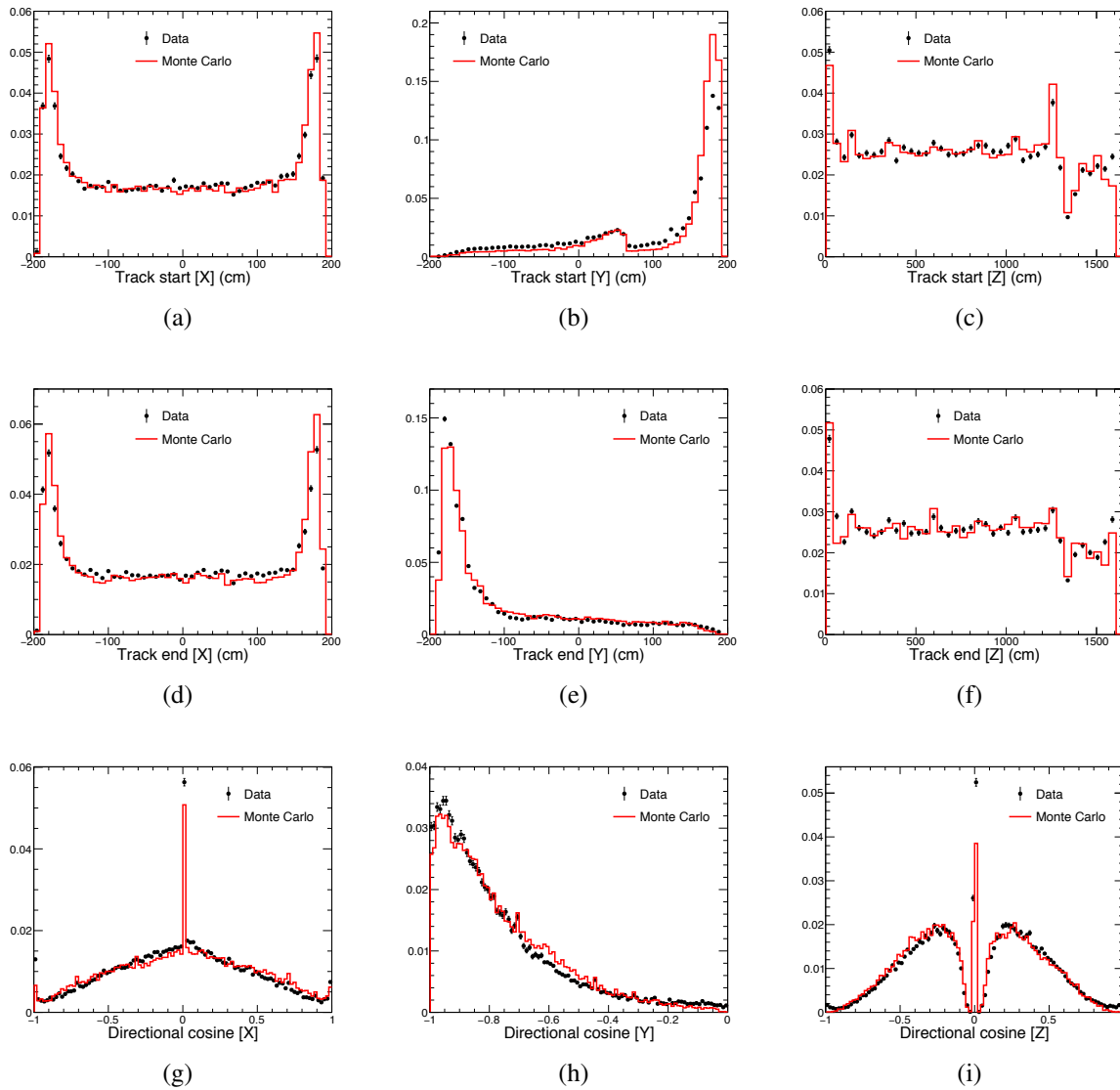


Figure 6.6 | Multiple-muon data and Monte Carlo comparison

Figure shows, for every reconstructed track, its starting vertex in the (a) [X], (b) [Y], and (c) [Z] coordinate, along with (d, e, f) their respective ending vertices in each coordinate. Plots (g, h, i) present their respective directional cosines in each NuMI coordinate.

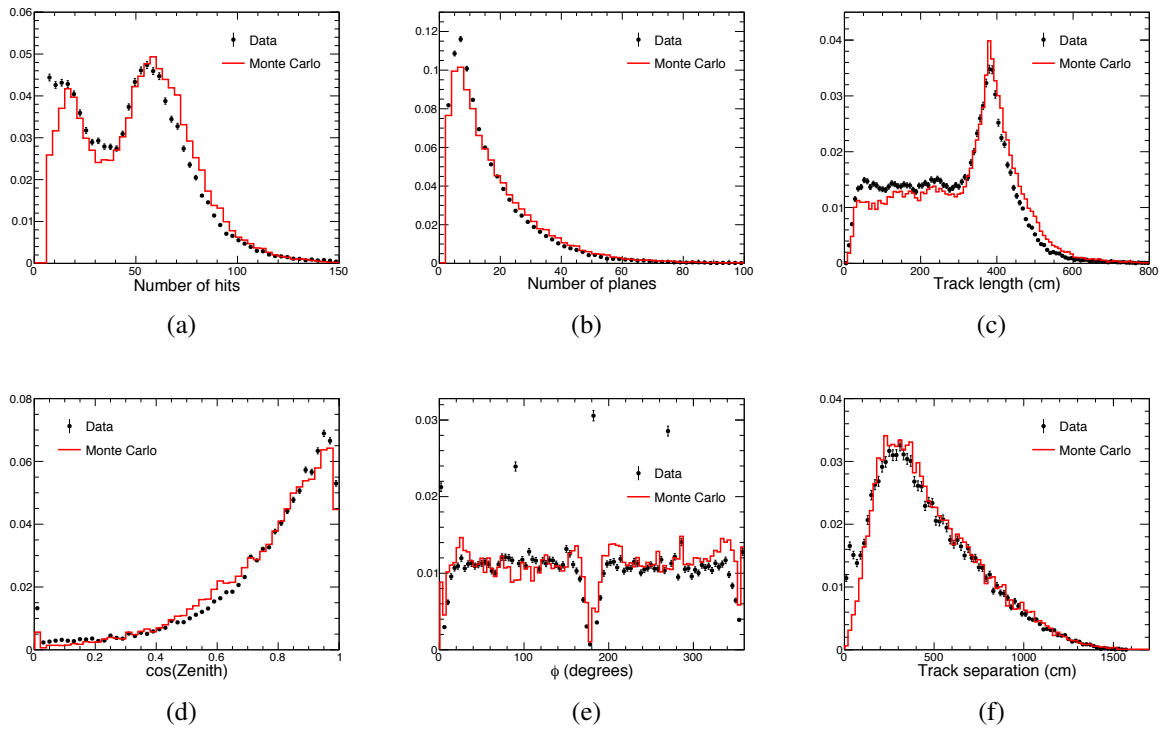


Figure 6.7 | Multiple-muon data and Monte Carlo comparison

Figure shows, for every reconstructed track, (a) number of hits; (b) number of planes; (c) track length; (d) cosine of the zenith angle; (e) ϕ angle, which provides the angle of the track in the XZ plane and is defined as 0° in the X+ NuMI axis; and (f) the distances between tracks for each multiple-muon event.

6.3.3 Monte Carlo true and reconstructed information

Although the validation of the Monte Carlo with the data in figures 6.6 and 6.7 shows good agreement, it does not provide any information on the quality of the reconstruction process itself. Therefore, it is important to compare the Monte Carlo's true information with the reconstructed results. Figure 6.8 compares the true particle information with the respective reconstructed variable: (a) through (f) shows the start and ending points, (g) through (i) their directional cosines, (j) zenith and (k) ϕ angle, and (l) particle/track separation. The peaks close to zero seen in the reconstructed directional cosines X and Z (figures 6.8), which are not present in the true information confirms that the reconstruction fails for tracks that are closely parallel to X, which in turn also results in a poor Z reconstruction. Figure 6.8 compares the particle and track length, zenith and ϕ angles and the particle and track separation.

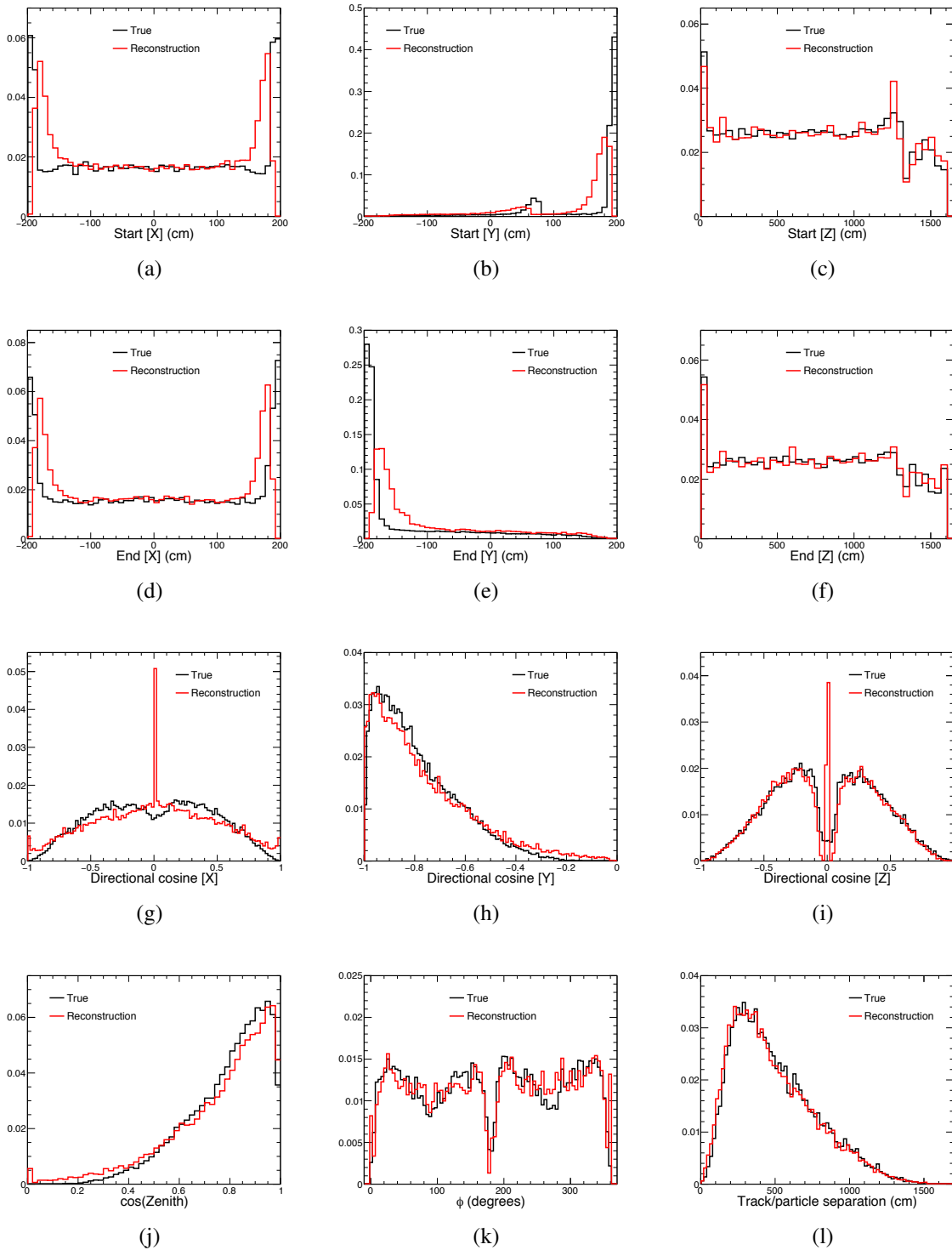


Figure 6.8 | True and reconstructed values from the multiple-muon Monte Carlo

Figure shows for every simulated particle (true) and its respective track (reconstruction), their starting vertex in the (a) [X], (b) [Y], and (c) [Z] coordinate, along with (d, e, f) their respective ending vertices in each coordinate. Plots (g, h, i) present their respective directional cosines in each NuMI coordinate. The last three plots show the (j) cosine of their zenith angles, (k) their ϕ angle, which provides the angle of the track in the XZ plane and is defined as 0° in the X+ NuMI axis, and (l) the distances between particles/tracks for each multiple-muon event.

Reconstruction efficiency and purity

The efficiency and purity are numbers that show how well the reconstruction performs with regards to finding cosmic ray muon events. The efficiency is defined as being the fraction of muon events that were successfully reconstructed as such (including multiplicity), being provided by the Monte Carlo, as it includes both true and reconstructed information. The purity measures by how much the reconstruction process fails by mistagging muon events, and it is defined as being the fraction of the number of reconstructed muon events by how many of these were correctly tagged as such. As the Monte Carlo only simulates pure cosmic ray muon events, it fails to provide an estimate for the purity, which is a measure of how much non cosmic ray muon activity ends up being tagged as such. Both definitions can be written as

$$e \equiv \frac{\text{number of reconstructed muon events}}{\text{number of true muon events}}, \quad (6.13)$$

and

$$p \equiv \frac{\text{number of muon events correctly tagged by the reconstruction}}{\text{number of reconstructed muon events}}. \quad (6.14)$$

Single muons

The single muon Monte Carlo sample is produced from a set of pre-processed files from the NO ν A standard CRY MC that undergoes through the reconstruction algorithm in order to compare true and reconstructed data. The resulting efficiency is considerably low, being at the 35% level:

$$e = \frac{57,827}{165,827} = 0.349 \pm 0.005. \quad (6.15)$$

The purity cannot be estimated from the Monte Carlo only, but a hand-scan of nearly 4,000 events showed only a handful of events that were not single or multiple-muons, being mostly short activities originated from the interaction of the cosmic ray muon with the surrounding cavern. As such, it is safe to state that for single muons $p > 99\%$.

The efficiency has a dependency on zenith angle, as it is shown in figure 6.9 and table 6.2, which shows the efficiency of the reconstruction algorithm for 10° wide bin regions of zenith angle. The reconstruction suffers small changes within 10° and 70°, but for angles above 80° the specific planar geometry of the Near Detector strongly affects the capacity of the reconstruction, resulting in a very small amount of near vertical events reconstructed.

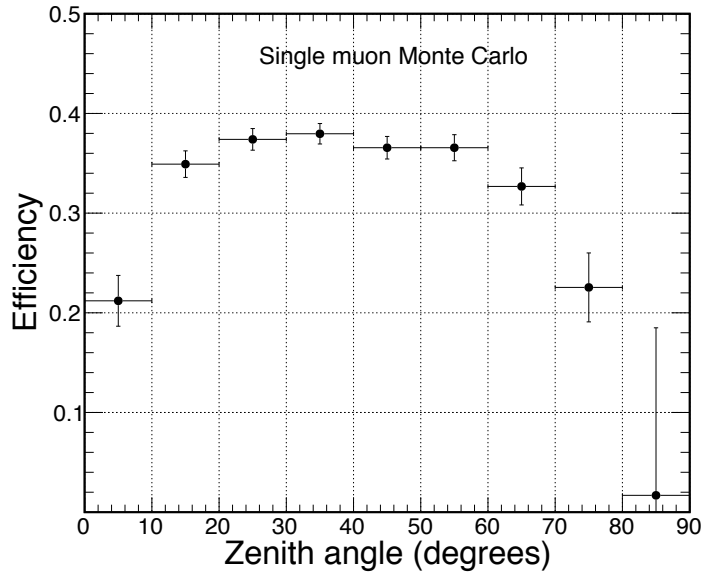


Figure 6.9 | Single muon reconstruction efficiency according to zenith angle

Figure shows the single muon reconstruction efficiency for 10° wide bin regions of zenith angle, showing that the efficiency is similar within 10° and 70°. Above the higher thresholds the detector geometry is highly significant, resulting in nearly no good reconstruction of very steep tracks (above 80°).

Single muon reconstruction quality	
True zenith angle bin	Efficiency
0° – 10°	$\frac{1,866}{8,801} = 0.212 \pm 0.025$
10° – 20°	$\frac{7,604}{21,779} = 0.349 \pm 0.013$
20° – 30°	$\frac{11,685}{31,244} = 0.374 \pm 0.011$
30° – 40°	$\frac{13,118}{34,555} = 0.380 \pm 0.010$
40° – 50°	$\frac{10,677}{29,202} = 0.366 \pm 0.011$
50° – 60°	$\frac{7,973}{21,807} = 0.366 \pm 0.013$
60° – 70°	$\frac{3,843}{11,760} = 0.327 \pm 0.019$
70° – 80°	$\frac{1,025}{4,546} = 0.225 \pm 0.034$
80° – 90°	$\frac{36}{2,133} = 0.017 \begin{matrix} + 0.17 \\ - 0.017 \end{matrix}$
Total	$\frac{57,827}{165,827} = 0.349 \pm 0.005$

Table 6.2 | Single muon reconstruction efficiency according to zenith angle

The table shows the efficiency of the reconstruction calculated CRY Monte Carlo samples. The reconstruction efficiency has its higher efficiency levels within 10° and 70°. Above the higher limit the detector geometry strongly affects the reconstruction efficiency, being close to zero for near vertical tracks (above 80°).

The expected average rate of cosmic ray muon events, whose vast majority is comprised by single muons, is $\sim 37 \text{ s}^{-1}$ (see figure 5.2), resulting in a total count at the order of 2.5×10^6

single muons per day of detector exposure. With such high volume of events, the current 35% level of efficiency represents a capability for reconstructing roughly 9×10^5 single muons per day, being far from imposing a statistical limitation on studying their seasonal modulation.

Multiple-muons

The multiple-muon sample is produced using the method outlined in Section 6.3.1. The limitation of the Monte Carlo was overcome by hand scanning a set of 4,000 cosmic ray events from the detector data, and manually defining the list of all multiple-muon events found within the sample. A total of 88 multiple-muon events were found and, before any selection criteria, apart from those used in the 3D track reconstruction itself, the efficiency is determined to be at the 60% level in both Monte Carlo and the hand scan. The purity of multiple-muon events after reconstruction is at the 90% level. Table 6.3 summarizes these results. Given the statistical uncertainties in the efficiency values, both hand scan and Monte Carlo results are in good agreement. The $\sim 10\%$ of mistagged multiple-muon events, resulting in a $\sim 90\%$ purity, is due to short tracks generated in the surrounding cavern, and due to muon pairs with large time differences. The table presents the numbers prior to any analysis selection cut, which will be discussed further. After the analysis criteria are applied, all the hand scanned mistagged events are removed, resulting in $p > 99\%$.

Multiple-muon reconstruction quality		
Variable	Monte Carlo	Hand scan
Efficiency	$\frac{15,710}{25,640} = 0.61 \pm 0.01$	$\frac{59}{88} = 0.7 \pm 0.2$
Purity	–	$\frac{59}{65} = 0.9 \begin{matrix} + 0.1 \\ - 0.2 \end{matrix}$

Table 6.3 | Multiple-muon reconstruction efficiency and purity

The table shows the efficiency and purity numbers for both Monte Carlo reconstruction and hand scan. The efficiency of the reconstruction using the two methods is in good agreement.

Angular resolution studies

A set of studies using both single muon and multiple-muon Monte Carlo samples was performed in order to assess the reconstruction's angular resolution. True and reconstructed data were compared for different ranges of track length. The single muon sample was used to find information on the accuracy of the reconstructed angle considering the angle between the track with respect to each NuMI axis. Shorter tracks have fewer hits and are prone to poorer angular resolution. The findings are summarized in table 6.4.

The multiple-muon Monte Carlo was used to provide information on the angular reconstruction resolution for different track lengths as a function of different track separation distances.

Track length (cm)	θ_X	θ_Y	θ_Z	θ (degrees)
10 to 200	6.4	5.1	3.6	5.09
200 to 350	3.8	3.2	2.0	3.16
350 to 1,400	1.9	1.6	1.2	1.63
All	3.4	2.8	1.9	3.29

Table 6.4 | Single muon angular resolution according to track length

The table shows the angular resolution of the reconstruction for directional angle with respect to the NuMI coordinate system, along with the resolution of the final reconstructed zenith angle.

As the multiple-muon sample produced follows the procedure outlined in Section 6.3.1, all multiple-muon events have parallel muons. The global average resolution is found to be 3.29° , with better resolution as both track length and track separation increase. The data is shown in table 6.5

Angular resolution			
Track length (cm)	Track separation (cm)		
	30 to 350	350 to 450	> 450
30 to 350	4.71°	–	–
350 to 450	3.72°	1.74°	–
> 450	3.24°	1.52°	0.93°

Table 6.5 | Multiple-muon angular resolution according to track length and separation

The table shows the angular resolution of the reconstruction for multiple-muons according to different regions of track length and separation. The global average resolution is found to be 3.29° .

6.4 The selection criteria

The selection criteria are a set of cuts applied to the data to guarantee that the final dataset includes only good subrun data and that the list of selected single and multiple-muon candidates have as little as possible contamination of non cosmic ray muons. This is accomplished by using two sets of selection criteria: the data quality cuts, and the analysis cuts.

6.4.1 Data quality selection criteria

The data quality cuts are the first criteria applied to the reconstructed dataset. They are included to avoid carrying forward any particular issue that may have happened during the

recording of the data. Figure 6.10 shows a set of distributions used to verify the integrity of the raw dataset: (a) and (b) show the raw single and multiple-muon reconstructed rates, (c) shows the subrun time length (each subrun is defined to last 1 hour), and (d) shows the number of subruns per run of the full reconstructed data (each run is expected to have no more than 24 subruns). Both rate histograms make it clear that part of the dataset counts very low rates –

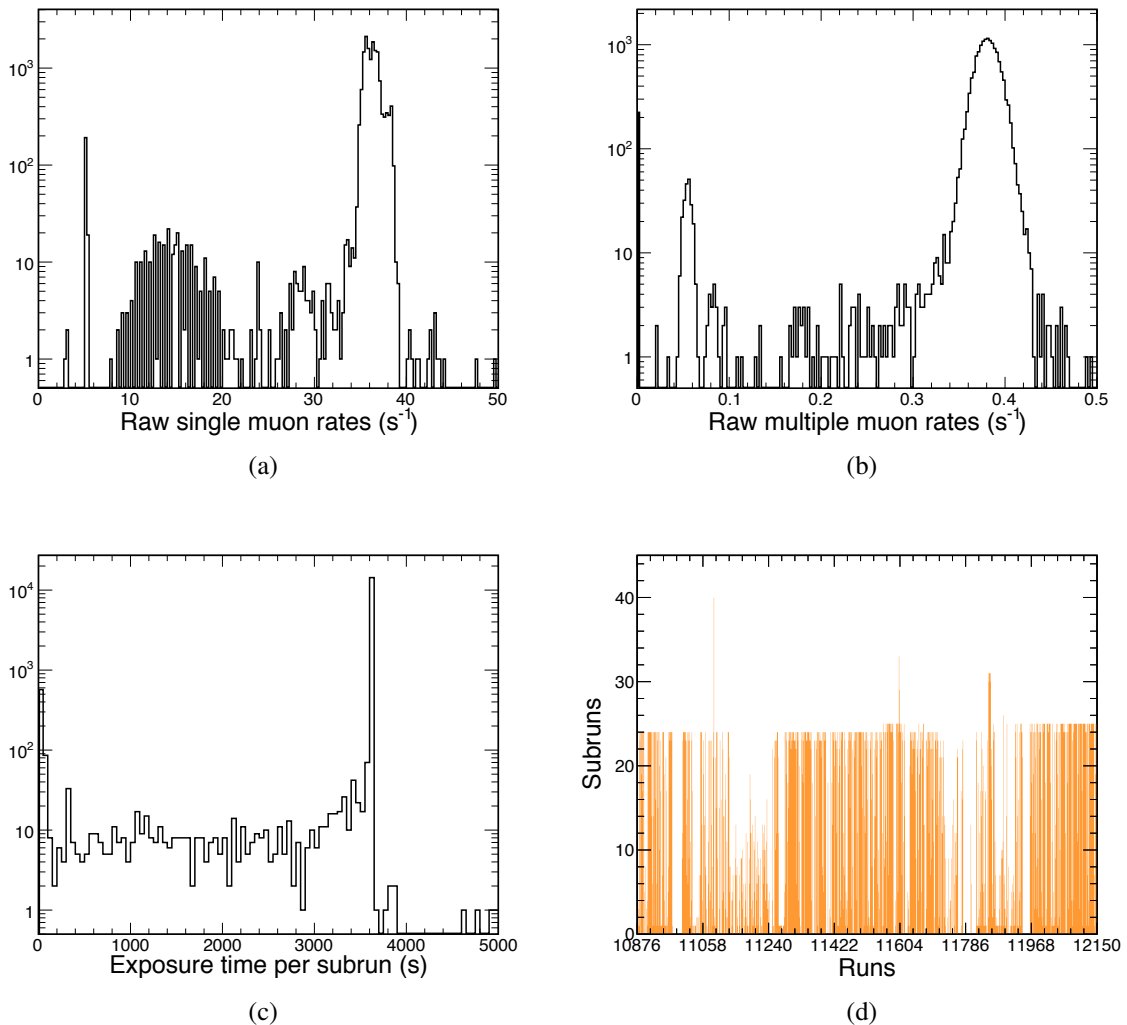


Figure 6.10 | Properties of the raw reconstructed dataset

Figure shows the raw (a) single, and (b) multiple-muon reconstructed rates. Figure (c) shows the subrun time length, and (d) shows number of subruns per run throughout the dataset. Notice that low values of rates and runs with unexpectedly high numbers of subruns are a clear hint that some of the data may be faulty.

including zero –, compared to the peaks centered in $\sim 36 \text{ s}^{-1}$ for single muons and $\sim 0.38 \text{ s}^{-1}$ for multiple-muons. The low rates were thoroughly checked, and it is understood that for both single and multiple-muon data, the set of low (and zero) values are due to a few specific runs bunches, each bunch being recorded continuously over a small amount of detector live time, indicating that they represent momentary DAQ problems.

The subrun time length (figure 6.10 (c)) is expected to have a flat distribution from zero up to 1 hour, as the probability of both a manual stop of the run or a detector run crash caused by any DAQ issue is the same at any given time. Very long subruns (i.e. longer than ~ 3600 s) are also linked to low or high single and multiple-muon rates.

As can be seen in figure 6.10 (d), a few runs recorded a high number of subruns, reaching up to 40 subruns for one run. The unexpected high number of subruns is most likely caused by a very high data flow, as the DAQ conditions for a subrun to end are: (1) the subrun time length reached 1 hour long or (2) the subrun data file reached 1 GB of disk size. Many technical reasons can cause a fake high data flow, including a wrong configuration of the detector's APD thresholds.

In order to remove all of the above issues, two data quality cuts were implemented:

- 1. Raw rates cut:** The single muon rate must be within $32 \text{ s}^{-1} \leq R \leq 39 \text{ s}^{-1}$, while the multiple-muon rates must be within $0.33 \text{ s}^{-1} \leq R \leq 0.43 \text{ s}^{-1}$. The cut is implemented at the file level, meaning that if a file does not comply with the cut, it is discarded. Each file represents one subrun.
- 2. Subrun time length cut:** Since shorter subruns are not necessarily a problem, there was the necessity of defining a subrun time threshold in which there would be a balance between the loss of statistics and removing unwanted biased data due to DAQ issue. Tests showed that discarding subruns whose time length is not within $3000 \text{ s} \leq \Delta t \leq 3650 \text{ s}$ fitted our purposes.

Table 6.6 summarizes the data quality cuts, and figure 6.11 shows the same distributions shown in figure 6.10 after going through the data quality selection criteria. It is interesting noticing that in figure 6.11 (d), after the selection criteria removed the faulty subrun files, the final number of subruns per run has lowered to its expected limit of 24 throughout the whole dataset.

Data quality selection criteria	
Criteria	Value
Single muon rate	$32 \text{ s}^{-1} \leq R \leq 39 \text{ s}^{-1}$
Multiple-muon rate	$0.33 \text{ s}^{-1} \leq R \leq 0.43 \text{ s}^{-1}$
Subrun time length	$3000 \text{ s} \leq \Delta t \leq 3650 \text{ s}$

Table 6.6 | Data quality selection criteria

The table shows the criteria used for removing subrun files that may be affected by DAQ issues.

The effects of the data quality selection criteria are summarized in table 6.7, which shows the number of remaining subruns and fraction of the total data after each data quality criterion is applied. The total amount of subrun files removed represent a loss of $\sim 9\%$ of the number of subruns. As the cuts are applied by removing subruns, and considering that faulty subruns

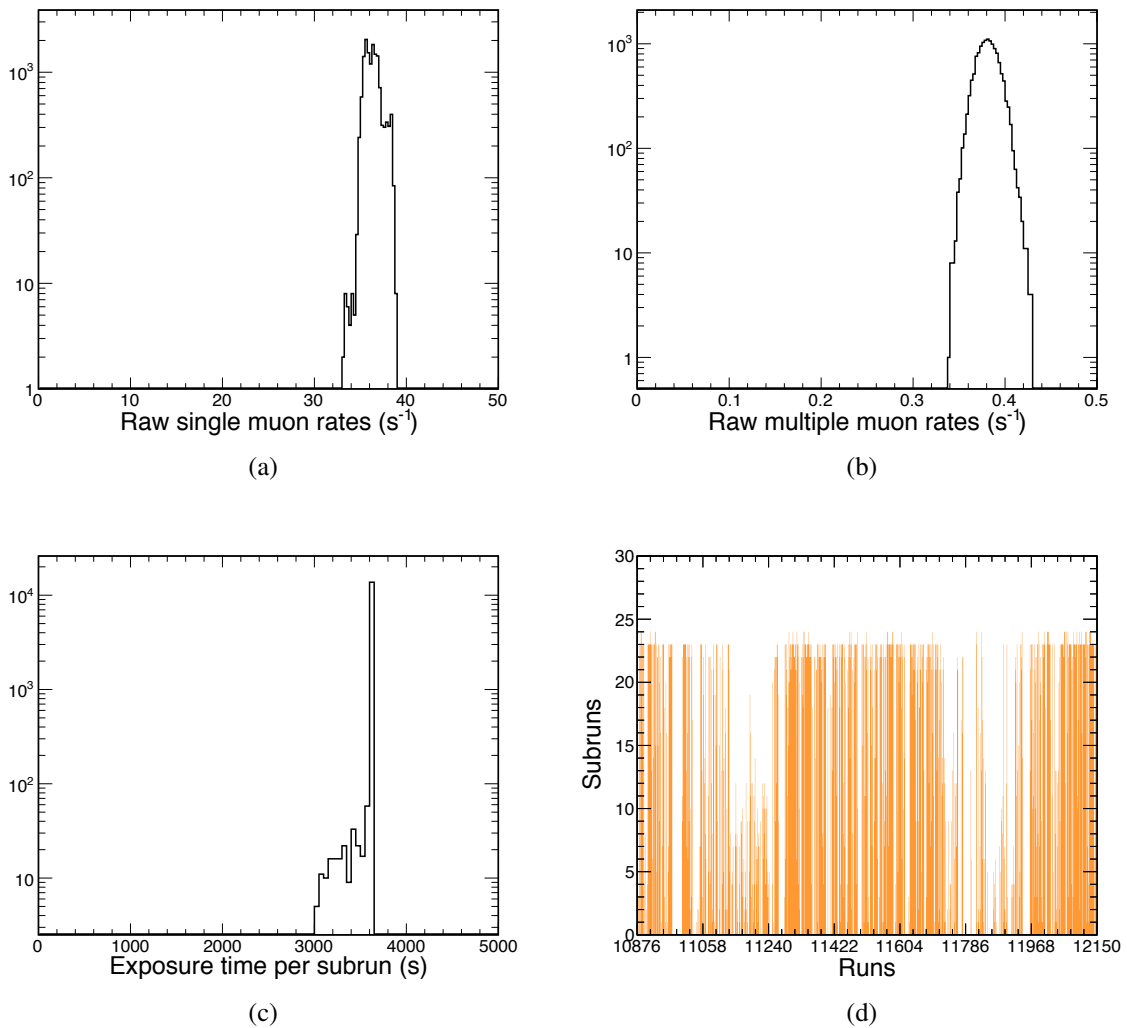


Figure 6.11 | Properties of the reconstructed dataset after the data quality selection criteria
 Figure shows the (a) single, and (b) multiple-muon reconstructed rates. Figure (c) shows the subrun time length, and (d) shows number of subruns per run throughout the dataset.

have different time lengths, a removal of 9% of all subruns does not represent a 9% loss of total detector exposure time.

Duplicated trigger events

The Data Driven Activity trigger, which was previously described in table 5.1 and in Section 5.3, is known to have an issue of storing the same detector activity in different event triggers in some specific cases. This is caused for two reasons:

1. Events are defined as a continuous readout time of $50 \mu\text{s}$ that triggers whenever there is any detector activity that meets the Activity trigger criteria⁴.

⁴The reason for this specific event length lies in the data acquisition system, which does not record chunks of data shorter than said readout time length.

Effects of the data quality selection criteria	
Criteria	Remaining number of subruns (fraction)
None	15,724 (1.00)
Single muon rate	14,806 (0.94)
Single + multiple-muon rate	14,698 (0.93)
Single + multiple-muon rate + Subrun time length	14,273 (0.91)

Table 6.7 | Effects of the data quality selection criteria

The table shows the total number of subruns, and the remaining number (and fraction) after each of the data quality selection criteria is applied. The inclusion of all criteria represent a loss of $\sim 9\%$ of the total used data.

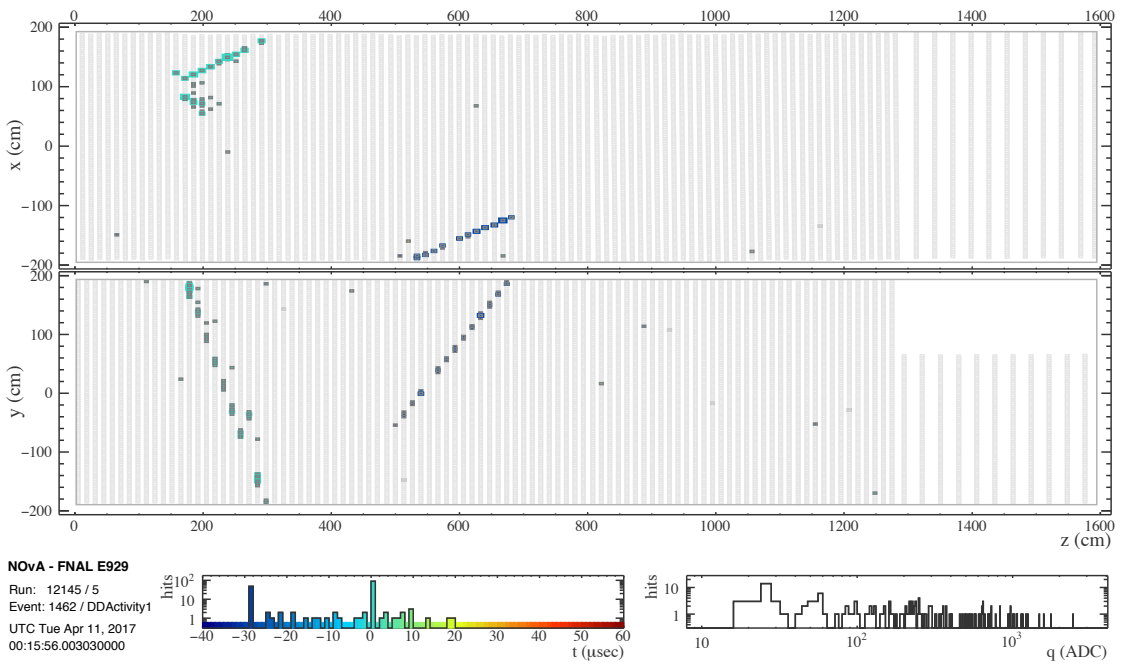
2. The trigger does not remain idle throughout its readout time window duration.

As a consequence, any two or more cosmic ray induced activities that are less than $50 \mu\text{s}$ apart will trigger 2 or more events, lasting $50 \mu\text{s}$ each, with their readout time windows partially overlapping. Therefore, any activity within the overlapped readout time will be recorded twice by the data acquisition system. Figure 6.12 shows an example of two uncorrelated single muons that were recorded in two separate triggers.

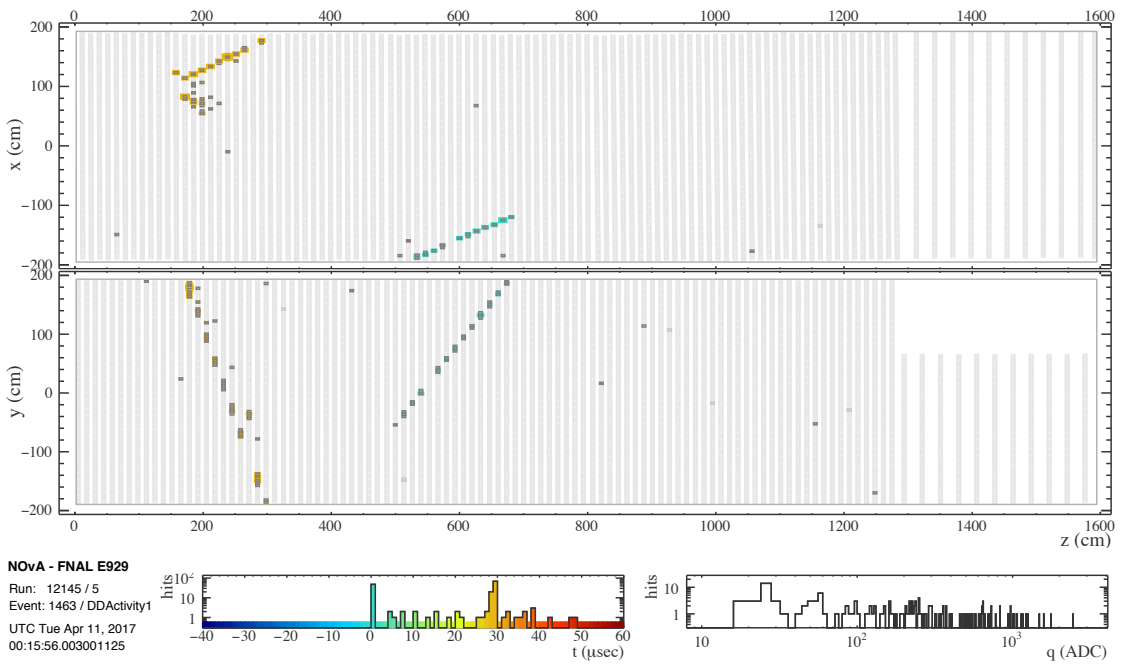
The solution was to compare the timestamp of the start time of triggered events in a pair by pair basis, such that if the difference of the starting time of 2 consecutive events, namely event i and $i + 1$, is $\Delta t < 50 \mu\text{s}$, the code proceeds to search if any further event (i.e. $i + 2$, $i + 3$, and so on) also has a starting time that is less than $50 \mu\text{s}$ apart from event i . When a further event has a timestamp outside the readout time of event i , all gathered events whose starting times are within $50 \mu\text{s}$ from event i are eliminated⁵, and the code returns to check events in a pair by pair basis until it finds another overlapping set of events, or the file ends.

For one hour of detector exposure time, the average number of muon events is at the order of 1×10^5 , with about 6×10^2 removed events. As such, removing the duplicate events represents a loss of $\sim 0.6\%$ of the data.

⁵Event i is included in the list of eliminated events.



(a)



(b)

Figure 6.12 | Event displays of two “identical” event triggers

Figures (a) and (b) show two sequential events that were triggered due to two separate single muons. Given the short time distance between each muon, both were recorded by both readout time windows.

6.4.2 Data analysis selection criteria

Having removed the data files that could contain DAQ failures, the next step is to ensure that the selection of single and multiple-muon events is as pure as possible. This is achieved by adding three more selection criteria, referred to as the analysis cuts. Two of the criteria were defined by comparing the reconstruction from both data and multiple-muon Monte Carlo, which is described in Section 6.3.2. They aim to remove the peaks in the directional cosines [X] and [Y] (figures 6.6 (g) and (i)), caused by poorly reconstructed tracks, and the excess seen in the data in figure 6.7 (f) for track pairs whose distance is shorter than ~ 70 cm, caused by interaction of muons with the surrounding rock of the detector. These rock interactions cause short activities at the top or sides of the ND that are reconstructed as 2 or more short tracks, very close to each other. The last data analysis cut is added to remove muon tracks that, although recorded in the same DAQ event, their time difference is such that they cannot have been produced by the same cosmic ray shower.

- 1. Directional cosines cut:** This cut aims to remove poorly reconstructed tracks. Due to the detector's geometry, specific situations are prone to produce wrong reconstruction values. Such cases happen with tracks that are almost parallel to the x or y axis of the NuMI coordinate system, which cross a small number of planes.
- 2. Fiducial volume cut:** This cut aims to remove the contamination of rock events from the muon interaction with the Near Detector cavern by selecting only through-going muons. This is achieved by requiring that tracks start and end at distances less than 50 cm from the borders of the detector. Figure 6.13 shows the starting and ending points of the trajectories after the cut is applied.
- 3. Time cut:** A selection criteria is needed to avoid mistagging events as multiple-muon candidates when their tracks are coming from different primaries. In this cut, the time difference between the first hit of the first track and the first hit of any further track of the same event cannot exceed 100 ns. Figure 6.14 shows the time distributions between tracks, along with the 100 ns threshold.

Table 6.8 summarizes all the analysis cuts used and their values.

The analysis cuts have different effects for single or multiple-muon data, as shown in table 6.9. For single muon events, the directional cosines cut removes 5% of the data, while the fiducial volume cut is responsible for diminishing the total number of events by a further 15%. As for the multiple-muons, the cuts are more prominent. The directional cosines criterion is responsible for removing about 20% of the data, being in roughly in accordance with what is observed from the data sample. This can be confirmed by verifying that the total contribution of the peaks near zero seen in figures 6.6 (g) and (i) represent roughly 14% of the fraction of events in both distributions. The timing cut diminishes the total number of events by further

Analysis selection criteria	
Criteria	Value
Directional cosine X	$\text{dirX} \leq 0$ or $\text{dirX} \geq 0.02$
Directional cosine Z	$\text{dirZ} \leq -0.02$ or $\text{dirZ} \geq 0.02$
Fiducial volume (from the edges of the detector)	$d \leq 50$ cm
Time between tracks	$\Delta t \leq 100$ ns

Table 6.8 | Analysis selection criteria

The table shows the criteria applied in the data analysis. The directional cosines cut is implemented to remove poorly reconstructed tracks, the fiducial volume cut aims to select only through going muons – thus, avoiding short activities from muon interactions with the surrounding cavern –, and the timing cut removes non multiple-muon events that are eventually recorded within the same trigger time window.

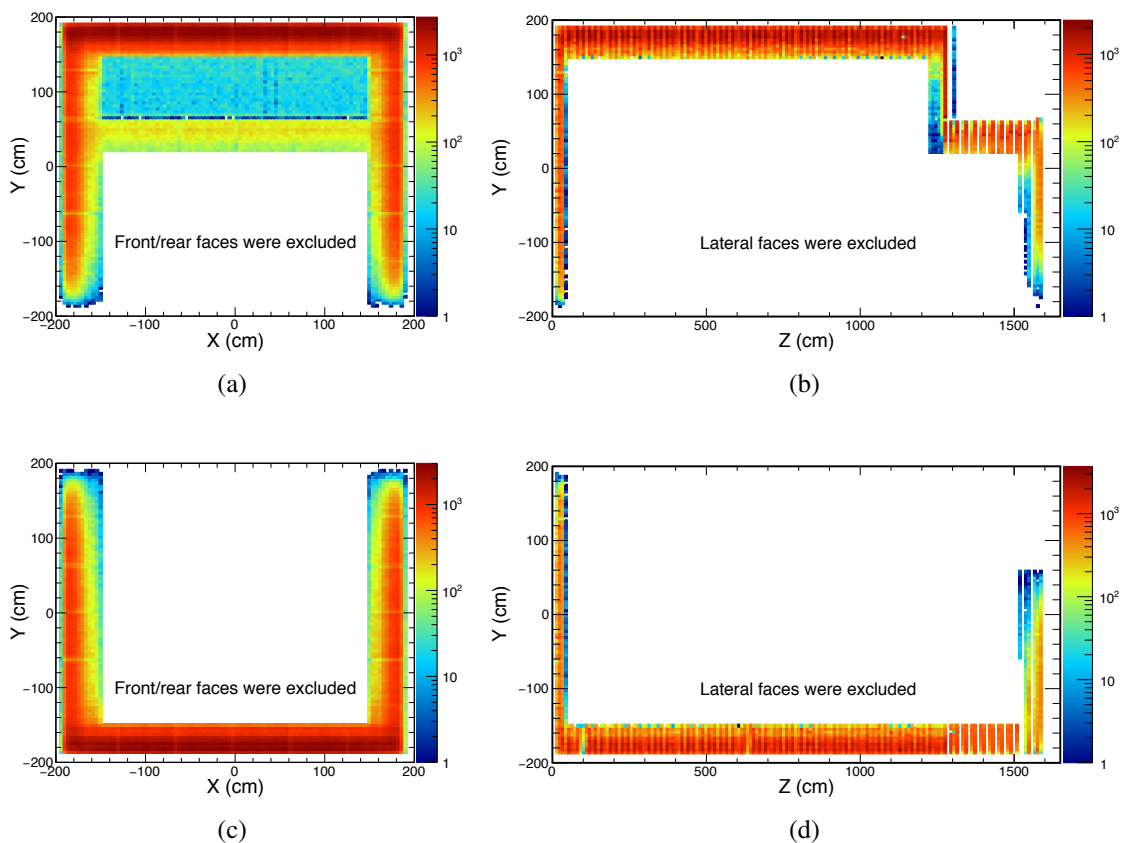


Figure 6.13 | Fiducial volume cut

Figures show the start and ending vertices of selected events after the fiducial volume cut is applied. The XY view is shown in (a) and (c), while the YZ view is presented in (b) and (d). In the XY view, both front and rear faces of the detector were intentionally removed for visual clarity. The same consideration applies for the YZ view, in which the lateral faces were removed as well.

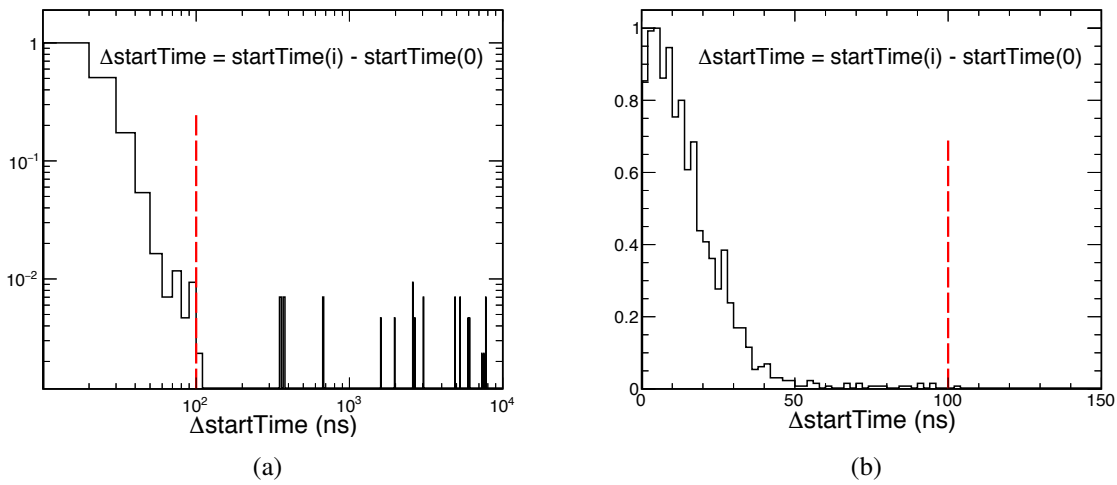


Figure 6.14 | Time difference between tracks

Figure shows the time differences between a track i and the first track of each event for one full day of detector exposure. Histogram (a) shows that only a small fraction of events record tracks from different primaries (both axes are in log scale, for easier visualization). Figure (b) shows the same distribution of (a) in more detail.

9%, while the fiducial volume restriction produces the highest effect in removing events, being responsible for removing 23% of the events alone. Table 6.9 summarizes the effects of the analysis' selection criteria for both single and multiple-muons, showing the number and fraction of events that remained after each cut is applied. The numbers presented in the table are taken from one full day (24 h) of detector exposure.

Selection criteria	Number of events (remaining fraction)	
	Single muons ($\times 10^6$)	Multiple-muons ($\times 10^3$)
None	3.22 (1.00)	32.01 (1.00)
Dir[X, Z]	3.08 (0.95)	25.52 (0.80)
Dir[X, Z] + Time	3.08 (0.95)	22.83 (0.71)
Dir[X, Z] + Time + Fiducial	2.57 (0.80)	15.43 (0.48)

Table 6.9 | Effects of the analysis selection criteria

The table shows the number of events and the total fraction of the data that remained after each selection criteria is applied considering one full day of detector exposure. The effects of the cuts are smaller for single muons due to the fact that several multiple-muon events can be tagged as single muons, compensating the discard of originally single muon events that do not meet all criteria.

The analysis criteria, when applied to the single and multiple-muon Monte Carlo samples, produce a similar very little effect on both reconstructed and true information. The directional cosine cut removes less than 1% of the simulated events, while the time and the fiducial criteria

have a null effect. The time cut does not cause any differences due to the fact that all secondary muons are a replicas of the single muon originally simulated by CRY, with their times being almost identical⁶. The fiducial cut has no effect, as all simulated particles are ideally simulated muons, resulting in only through-going particles.

6.5 The data processing

6.5.1 The definition of the dataset

The processed data comprises 2 full years of data taking time, ranging from April 8 of 2015 to April 16 of 2017. Table 6.10 provides the details of the dataset used, while figure 6.15 shows the detector live time per day, along with the integrated exposure time.

Activity trigger		
	Run / subrun	Date (time)
Start	10876 / 01	04 / 08 / 2015 (16:43:49)
End	11250 / 24	04 / 16 / 2017 (13:45:02)

Table 6.10 | Dataset processed for the analysis

The table shows the trigger used, and start and ending runs, subruns, date, and time of the analysis dataset.

Accounting for all downtimes and removed data due to the data quality selection criteria, the final integrated detector exposure time is 55.29×10^6 s. Given that for the same period the total elapsed time is 63.85×10^6 s, the average duty cycle of this analysis is 86%.

6.5.2 The data processing chain

This section provides an overview of the sequence of steps in which the data is processed, how it is structured and at which step of the chain each analysis criteria is included.

The raw data collected by the data acquisition system is pre-processed to produce raw ROOT files. The raw root files, defined as DAQ files, are used in the first step of the processing chain, which produces reconstructed files from the DAQ data. In this step only the Multi-Hough transform information is processed and included in the ROOT files, which are defined as RECO files. The next step now uses the Multi-Hough Transform data available in the RECO files to build 3D tracks and store their information in an n-tuple structured ROOT file. Since all of the former steps of the chain have an equivalent number of files (i.e., one input file produces one

⁶The differences happen when a muon located at the top of the detector is replicated to a position in which the starting vertex of the replica ends up at one of the sides of the detector, resulting in a different starting Y position at a slightly different time.

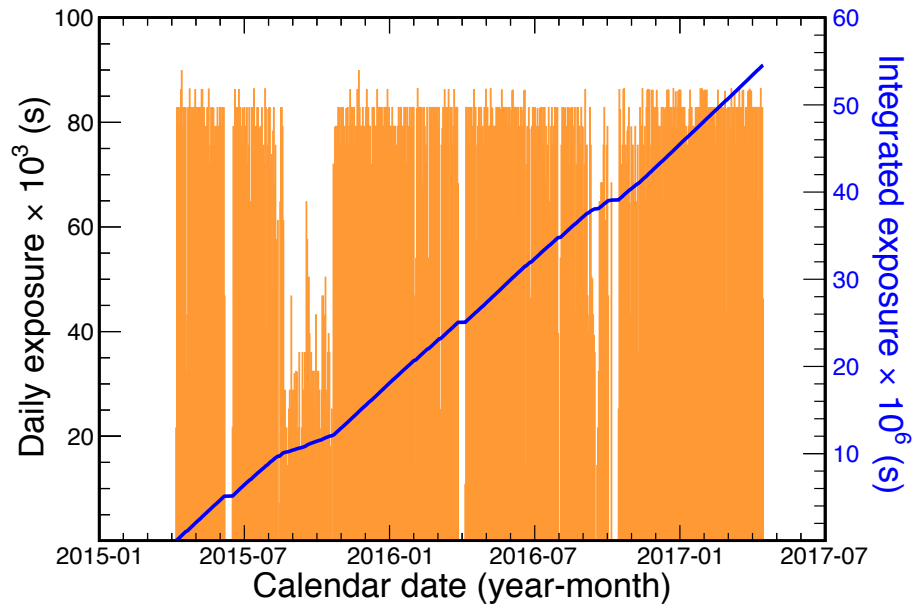


Figure 6.15 | Detector daily and total exposure time

Figure shows the daily exposure time of the detector (orange), along with the integrated exposure time curve (blue). The total integrated exposure time, after 2 years of data taking, is 55.29×10^6 s.

output file), the n-tuple files are still organized in a way such that each file represents one subrun of the detector.

The run/subrun file structure is sufficient for most analyses, but in order to compare the Near Detector data with the meteorological data from ECMWF (more details in section 6.7) in an orderly fashion, it is helpful to convert the run/subrun data into daily data files. The ECMWF data is ordered in UTC days, while the Near Detector's run/subrun structure has a chaotic connection with calendar days, as is exemplified in figure 6.16. The complication is overcome by merging subrun files that start in the same UTC day into one file that represents one UTC day of the year.

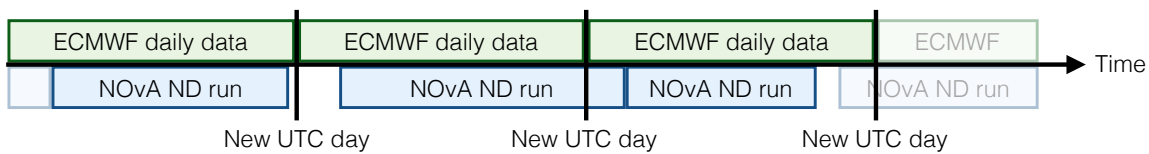


Figure 6.16 | Comparison between UTC ECMWF daily data and Near Detector runs

Figure illustrates the lack of direct correlation between the Near Detector run numbers with an UTC day and, thereby, the UTC daily temperature data provided the ECMWF.

The data quality cuts described in Section 6.4.1 are applied at the subrun level, discarding any subrun file that do not comply with the pre-defined criteria. Hence, the data quality cuts are applied in this step, while the subrun n-tuple files are being merged to produce UTC daily n-tuple files.

The UTC daily data files comprises a set of ~ 700 files, consuming up to 1.3 GB each.

Adding the analysis cuts and producing a new set of files with roughly the same size would cost more disk space and would not speed up the data processing for the single and multiple-muon results. Therefore, the final step applies the analysis cuts into the UTC daily n-tuples and produces only one final file, with only relevant information for specific results. This means that this step must be done multiple times during the analysis, each time storing different relevant sets of information. Each final file, which may vary from a few kB to a few GB, is then used to extract the analysis results.

A scheme of the different data processing steps is presented in figure 6.17, showing at which steps the data quality and the analysis cuts are applied.

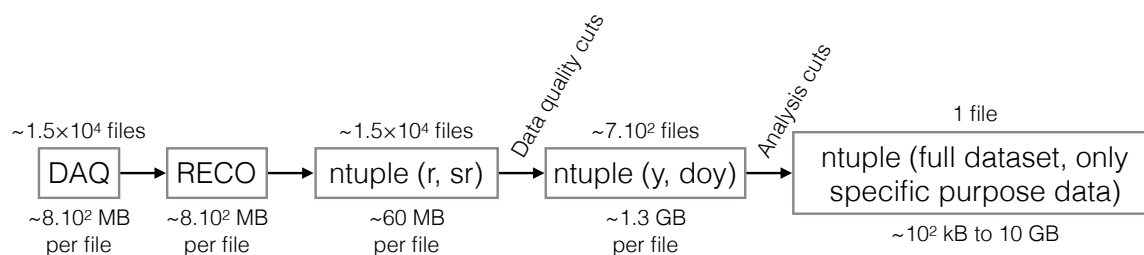


Figure 6.17 | The data processing chain

Schematic representation of the processing chain developed for the analysis. The DAQ files only carry information at the hit level. In the second stage, the produced RECO files also carry the Multi-Hough Transform information, which is used to produce 3D track information that is stored into ntuple files. The ntuples, ordered by run and subrun, are gathered together to produce files such that one file represents one UTC day. During this step the data quality cuts are included and subruns that do not pass the criteria are discarded. Finally, the daily ntuples are processed to include the analysis cuts and produce a single file with specific sets of data for specific plots and results.

6.6 Consistency checks

6.6.1 Data and Monte Carlo after all selection criteria

In order to confirm that the analysis criteria are behaving as expected, the same distributions presented in figures 6.6 and 6.7 are reprocessed taking these cuts into account. The new distributions comparing data and MC are shown in figures 6.18 and 6.19. The agreement is excellent.

The peaks near zero in both directional cosines [X] and [Z] (figures 6.18 (g) and (i)) are now gone, and both reconstructed data and reconstructed Monte Carlo are in good agreement. The spikes at 0° , 90° , 180° , and 270° , caused by vertical tracks, and tracks that are parallel to the detector planes, do not appear anymore in the ϕ plot (figure 6.19 (e)). Finally, the track separation plot (figure 6.19 (f)), also does not carry any excess of tracks with short separation, confirming that these events were caused by short tracks, which were successfully removed by including the constraint that only through-going tracks are included in the analysis.

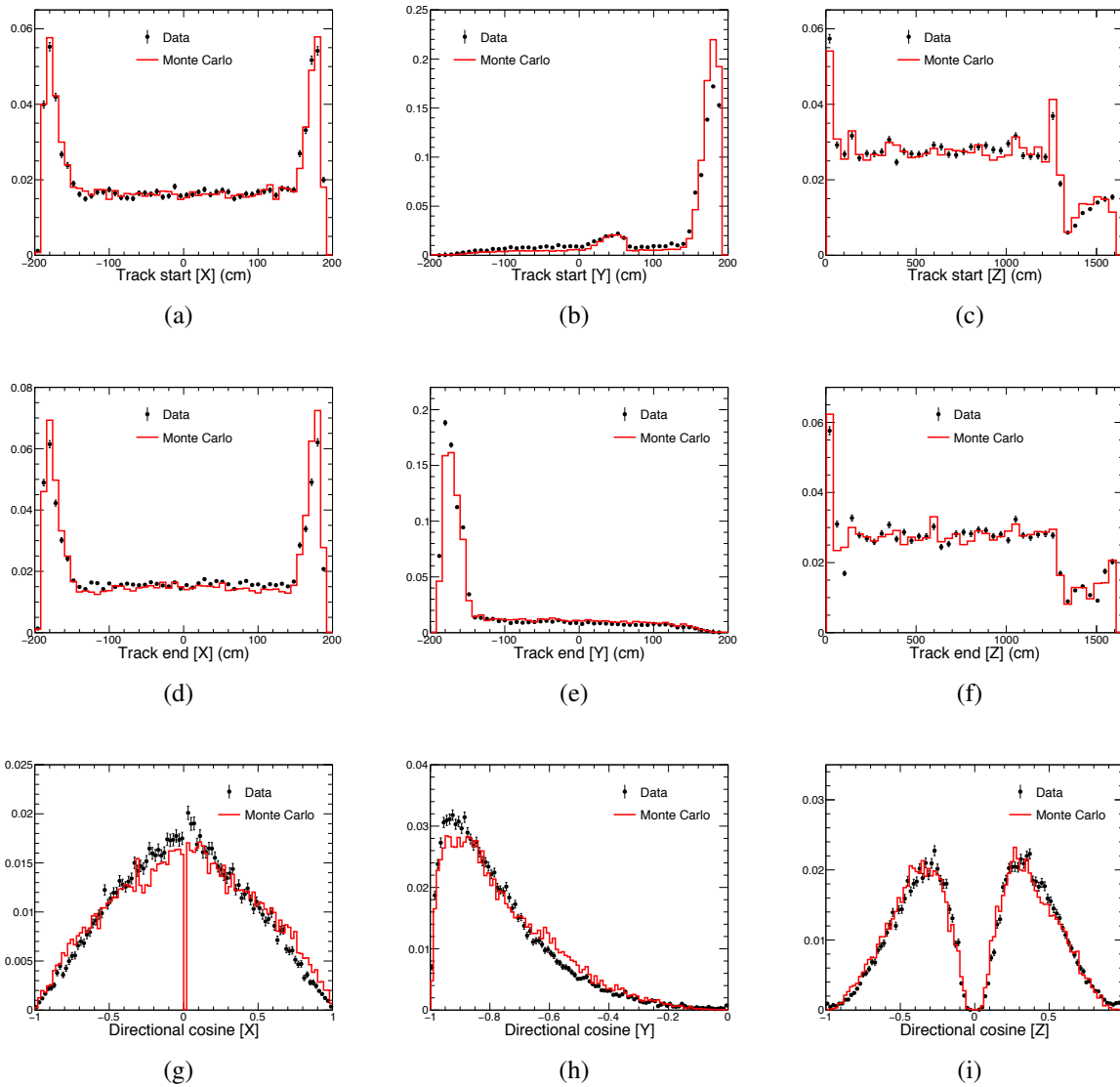


Figure 6.18 | Multiple-muon data and Monte Carlo comparison after the analysis cuts

Figure shows, for every reconstructed track in both data and Monte Carlo, its starting vertex in the (a) [X], (b) [Y], and (c) [Z] coordinate, along with (d, e, f) their respective ending vertices in each coordinate. Plots (g, h, i) present their respective directional cosines with respect to each NuMI coordinate axis.

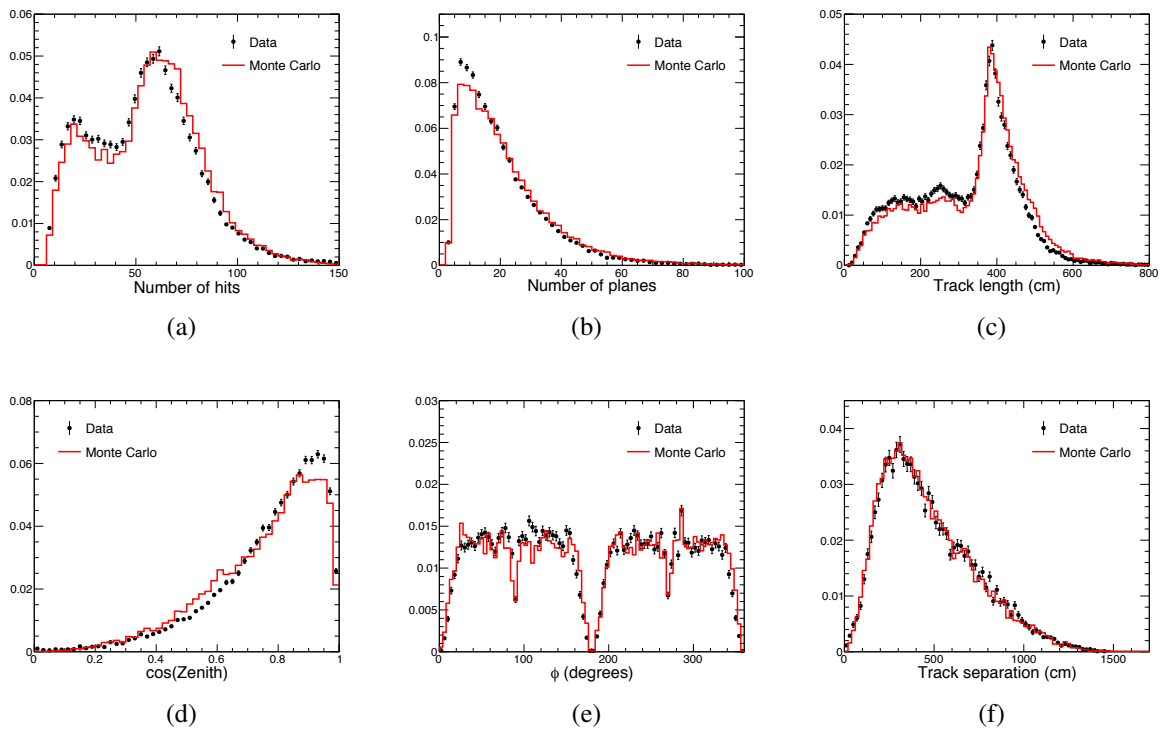


Figure 6.19 | Multiple-muon data and Monte Carlo comparison after the analysis cuts

Figure shows, for every reconstructed track, (a) number of hits; (b) number of planes; (c) track length; (d) cosine of the zenith angle; (e) ϕ angle, which provides the angle of the track in the XZ plane and is defined as 0° in the X+ NuMI axis; and (f) the distances between tracks for each multiple-muon event.

6.6.2 Near Detector operation consistency over time

These consistency checks are made in order to ensure that the detector operation remained constant throughout the whole dataset. This can be verified by splitting the analysis data into different sub datasets, each representing a specific period of time, and comparing them. In this case, the data was split into two years: the first year comprises data from April 2015 to March 2016, whilst the second sub dataset encompasses the data from April 2016 until April 2017.

The comparison of the two sub datasets was done by normalizing and overlapping a set of distributions related to the reconstructed 3D tracks for single-muon events, after both data quality and analysis cuts. These distributions are presented in Figure 6.20. For easier comparison, the ratio $r = [2015-2016]/[2016-2017]$ of each distribution is also shown.

Figures 6.20 (a), (b), and (c) shows the track vertices of the single-muon data, along with their ratios. Next, distributions (d), (e), and (f) represent the directional cosines of the data and their ratio. Finally, histograms (g), (h), and (i) show the track length, zenith, and azimuth distributions, respectively.

The detector remained fully operative during both years of data taking and no hardware differences are noticed. Faulty planes, dead channels, or even channels with low/high threshold

configurations would cause depletions or peaks in the vertex and directional cosines reconstruction.

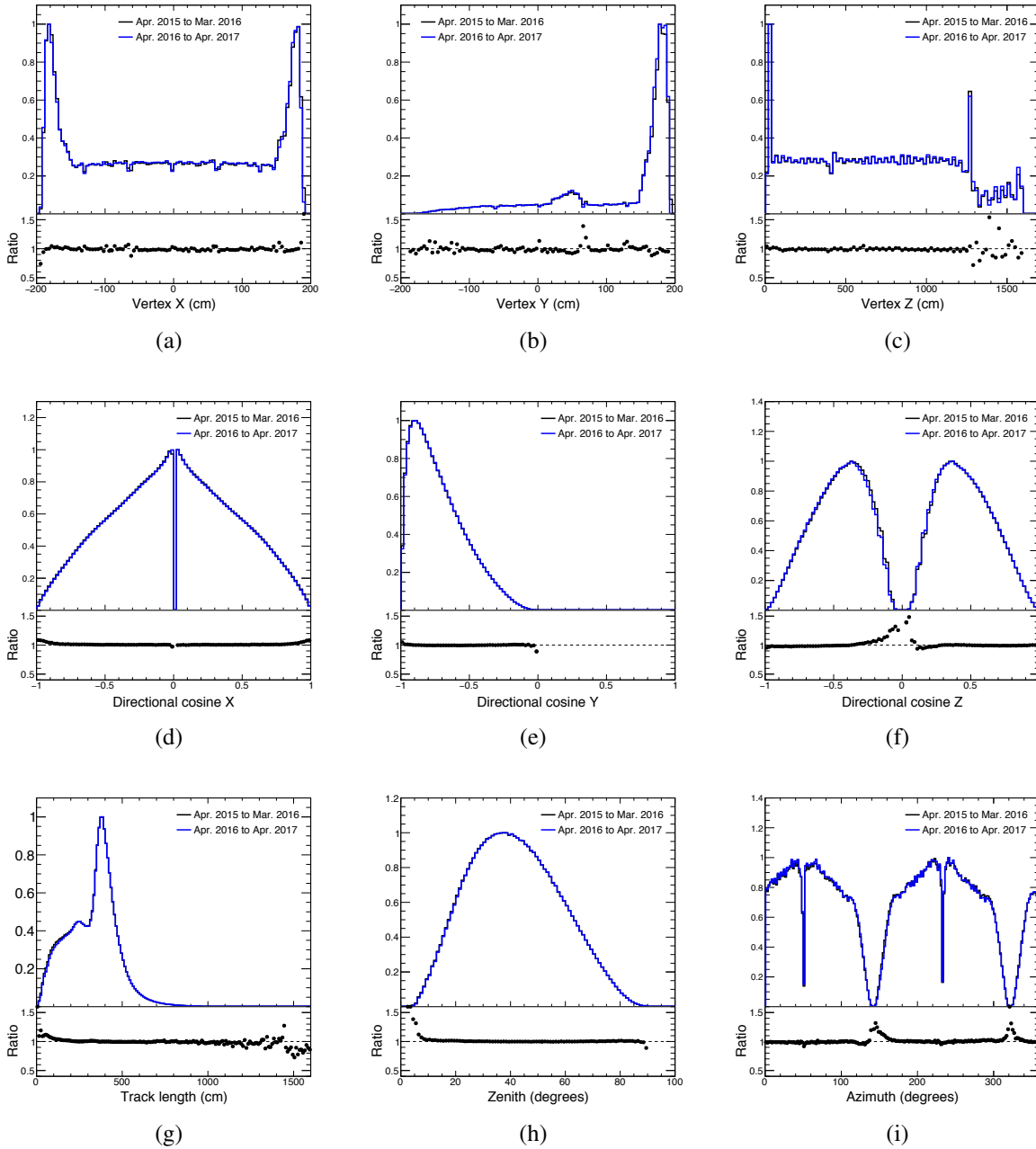


Figure 6.20 | Near Detector operation consistency check

The figure shows a set of distributions from 3D reconstructed tracks compared in a yearly basis. The distributions consider only single-muon data, and already includes the full set of selection criteria (i.e. data quality and analysis cuts). Each distribution also shows its bin by bin ratio, with the first year being the numerator. The track vertex reconstruction is shown in (a), (b), and (c), whilst their directional cosines are presented in (d), (e), and (f). Finally, distribution (g) shows the track length, (h) the zenith, and (i) the azimuth angles.

6.7 The ECMWF temperature data

The atmospheric temperature data is provided by the European Center for Medium-Range Weather Forecast (ECMWF), which is an independent intergovernmental organization whose purpose is to produce global numerical weather forecasts⁷. The ECMWF center provides several forecast parameters, including the temperature, for different pressure levels and spanning the whole globe via the ERA-Interim reanalysis [92], which covers a time range from January 1st, 1989, until today⁸.

For the atmospheric temperature data related to the NO ν A Near Detector, ERA-Interim data from April 1st, 2015 until April 30th, 2017 was retrieved. The data provides measurements of 4 different times of the day (0 h, 6 h, 12 h, and 18 h), all in UTC time. The data at each of these four times includes 37 pressure levels, ranging from 1 hPa to 1,000 hPa⁹, with 4 temperature values each. Each temperature is the result of an interpolation from surface, balloon, and satellite measurements to fit specific latitude and longitude coordinates. In the case of the Near Detector region, for each pressure level, the 4 temperature measurements represent the interpolated temperatures of the corners of a 2 \times 2 grid, whose latitude and longitude values range from (41.25 $^\circ$ N, 87.75 $^\circ$ W) to (42.00 $^\circ$ N, 88.50 $^\circ$ W) with a 0.75 $^\circ$ incremental step in each direction¹⁰.

The angular limits of this, which will be used for the effective temperature calculations, represents a surface area of $62.5 \times 85.0 = 5,312.5 \text{ km}^2$, as shown in figure 6.21 (a). As such, in order to fairly compare the muon flux and the effective temperature of the atmosphere, the solid angle in which most detected muons are produced must be encompassed or at least comparable to the ECMWF grid area. Muons are mainly produced at an altitude of $\sim 15 \text{ km}$ and follow a zenith angle distribution as shown in figure 6.20 (h). At 15 km of height, the area produced by the solid angle is equal to the ECMWF grid area when $\theta \approx 70^\circ$, which already covers most of the zenith spectrum of the detected muons. This result confirms the compatibility between the size of the grid of the temperature data and the region where the observed muons are produced.

⁷Information and data are available at <https://www.ecmwf.int>.

⁸The ERA-Interim reanalysis replaces the ERA-40, which covers meteorological data forecasts back from January of 1979. The extension of the ERA-Interim project to include data from 1979 to 1989 is in preparation.

⁹The pressure levels are not evenly distributed over said pressure range. As such, one cannot recover the level values by dividing 1,000 hPa by 37 levels.

¹⁰The coordinates of the MINOS Service Building, which leads to the NO ν A Near Detector cavern, are (41.84 $^\circ$ N, 88.27 $^\circ$ W).

Pressure level	Day 1				...	Day N			
	00h	06h	12h	18h	...	00h	06h	12h	18h
1	$T_1 T_2$	$T_1 T_2$	$T_1 T_2$	$T_1 T_2$...	$T_1 T_2$	$T_1 T_2$	$T_1 T_2$	$T_1 T_2$
	$T_3 T_4$	$T_3 T_4$	$T_3 T_4$	$T_3 T_4$...	$T_3 T_4$	$T_3 T_4$	$T_3 T_4$	$T_3 T_4$
2	$T_1 T_2$	$T_1 T_2$	$T_1 T_2$	$T_1 T_2$...	$T_1 T_2$	$T_1 T_2$	$T_1 T_2$	$T_1 T_2$
	$T_3 T_4$	$T_3 T_4$	$T_3 T_4$	$T_3 T_4$...	$T_3 T_4$	$T_3 T_4$	$T_3 T_4$	$T_3 T_4$
.
.
.
37	—	—	—	—	...	—	—	—	—
	—	—	—	—	...	—	—	—	—

Table 6.11 | Tabular representation of the ECMWF temperature data

The table is a representation of the structure of the temperature data provided by ECMWF. Each daily data consists of temperature measurements from 4 available times of the day. Each time encompasses 4 temperature values from the 2×2 grid over 37 pressure levels, covering a pressure range that goes from 1 hPa to 1,000 hPa. Said pressure range is divided unevenly and, thus, $1,000/37$ does not represent the pressure value at each step.

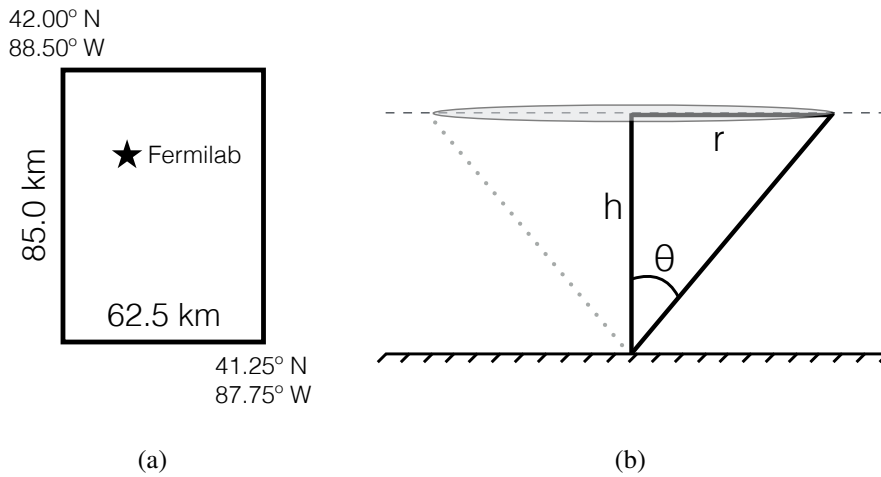


Figure 6.21 | ECMWF grid area and the area of muon production

Figure (a) shows the size of the 2×2 grid of the temperature data provided by ECMWF, along with a rough approximation for where Fermilab is located within the grid. Figure (b) schematically shows the area at a certain altitude of the atmosphere that encompasses all detected muons with angles up to θ . At ~ 15 km of altitude, a $\theta \approx 70^\circ$ produces an area that is equal to the ECMWF grid area. Since 70° encompasses the vast majority of muons that reach the detector, the ECMWF grid size is compatible for this study.

6.7.1 The effective temperature

The calculation of the effective temperature at the Near Detector location is carried forward using equations 3.29 and 3.30. The process is repeated for each available time of each day, resulting in 4 effective temperatures per day. The daily effective temperature is simply the average of the effective temperatures from all 4 available hours. Figure 6.22 shows the ECMWF temperature (red curve) and the $W(X)$ weighting function (dashed curve) according to altitude or pressure level. Since different days produce different temperature profiles, the temperature curve shown in figure 6.22 represents the average temperature of the 2 full years of data. The $\int W(X)dX = W(X).X$ (blue curve) shows the integrated weight used in the T_{eff} calculation according to depth, which demonstrates that the region in which the temperature data receives the highest weights is between ~ 10 km and ~ 25 km of altitude, which is where most muons from the decay of secondary mesons are produced.

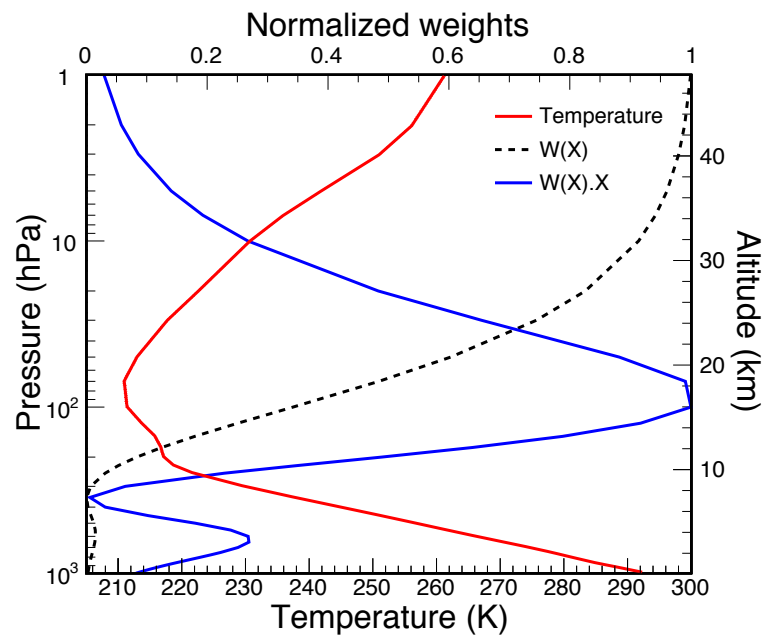


Figure 6.22 | ECMWF temperature, $W(X)$, and weight as a function of altitude or pressure

Figure shows the average temperature value, along with the normalized $W(X)$ weighting function, as a function of altitude or pressure level. The blue curve represents the normalized integral $\int W(X)dX = W(X).X$ as a function of depth, which shows that the region of the atmosphere in which the the weight used to calculate T_{eff} assume its higher values is within ~ 10 km and ~ 25 km of altitude, which is where most muons from the decay of secondary mesons are produced.

Figure 6.23 (a) shows the daily effective temperature for each UTC day, along with the total effective temperature average (red line), which yields $\langle T_{\text{eff}} \rangle = 222.15 \pm 0.01$ K. Figure 6.23 (b) shows the percentual variation of each daily effective temperature with respect to $\langle T_{\text{eff}} \rangle$ in function of time.

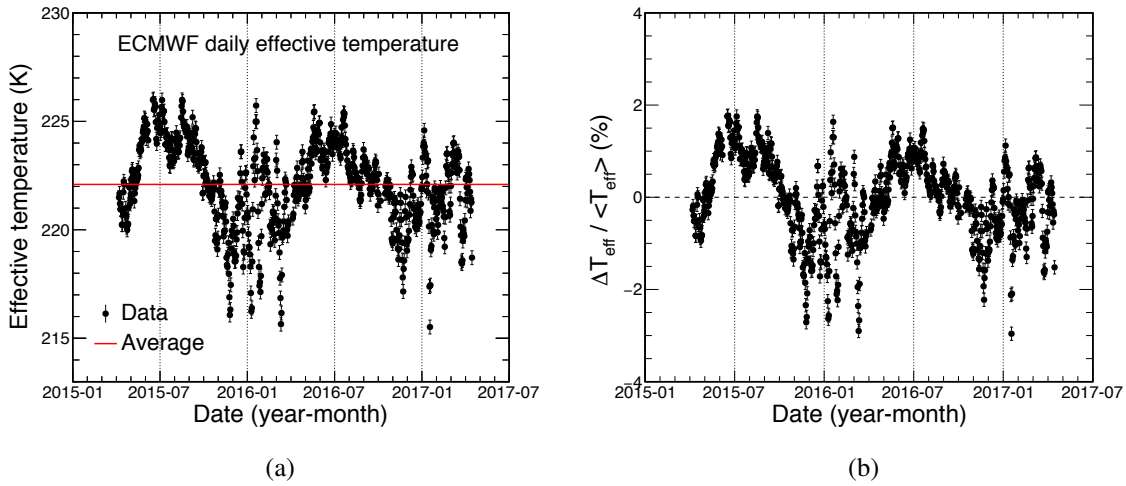


Figure 6.23 | Daily effective temperature and its percentual variation as function of time

Figure (a) shows the daily effective temperature for the NO ν A Near Detector location, along with the total average (red line), which yields $\langle T_{\text{eff}} \rangle = 222.15 \pm 0.01$ K. Figure (b) represents the percent variation of each daily T_{eff} with respect to $\langle T_{\text{eff}} \rangle$.

6.7.2 The systematic errors

The systematic uncertainty of the temperature data arises from limitation in the data taking and on the models used to interpolate the data for different pressure levels and geographic locations, as not all values come from direct measurements. As such, there are three components that are taken into account to select the final systematic error: the variance of the temperature data as a function of *i*) altitude, *ii*) time, and *iii*) over the ECMWF area in which the effective temperature is calculated. The following subsections describe each case and present the total systematic uncertainty, which is the sum in quadrature of each of the aforementioned components.

The temperature variance as a function of time

The effective temperature of the atmosphere is calculated as a weighted average of the temperatures at different pressure levels (equation 3.29), in which the weighting function $W_{\pi,K}(X)$ takes into account the muon production from the decay of secondary pions and kaons. As such, in order to verify the average variance as a function of altitude, the same weighting function is applied. As a result, the final daily variances found are adding more weight to the temperature variances at the region of muon production, whilst dimming the importance to variances close to the surface or at very high altitudes (higher half of the stratosphere).

To include the weighting function and calculate an average variance per day¹¹, one must start

¹¹The procedure may be easier to understand if table 6.11 is reviewed in parallel with the description herein stated.

by finding the variance per pressure level per available hour per day, which can be calculated by computing

$$\sigma_{j,k} = \sqrt{\frac{1}{4} \sum_{i=1}^4 (T_i - \bar{T})^2}, \quad (6.16)$$

where $\sigma_{j,k}$ is the variance of the four temperatures of the j -th level of the k -th available time per day, T_i represents each of the four available temperatures per day per level per available hour, and \bar{T} is simply the arithmetic average of the four temperatures used in the variance. The next step is to calculate the weighted variance of all 37 level variances for each k -th available time per day, written as

$$\bar{\sigma}_{\text{hour}}^{\text{day } k} = \frac{\sum_{j=1}^{37} W(X_j) \Delta X_j \sigma_{j,k}}{\sum_{j=1}^{37} W(X_j) \Delta X_j}. \quad (6.17)$$

The output is one weighted temperature variance per each available hour per day, which is then averaged over the four available times per day

$$\bar{\sigma}_{\text{day}} = \frac{1}{4} \sum_{k=1}^4 \bar{\sigma}_{\text{hour}}^{\text{day } k}, \quad (6.18)$$

resulting in a daily weighted variance. This calculation is repeated for every day of the sample and plotted as a function of calendar date, as shown in figure 6.24. Since the daily data represents the altitude weighted variance, the plot considers both variance as a function of altitude and as a function of time. The average of all daily weighted variances is found to be $\sigma_{\text{avg}} = 0.09 \pm 0.02$, which is also included in figure 6.24, with the average being represented by the solid red line and its $\pm 1\sigma$ defined by the red shaded region.

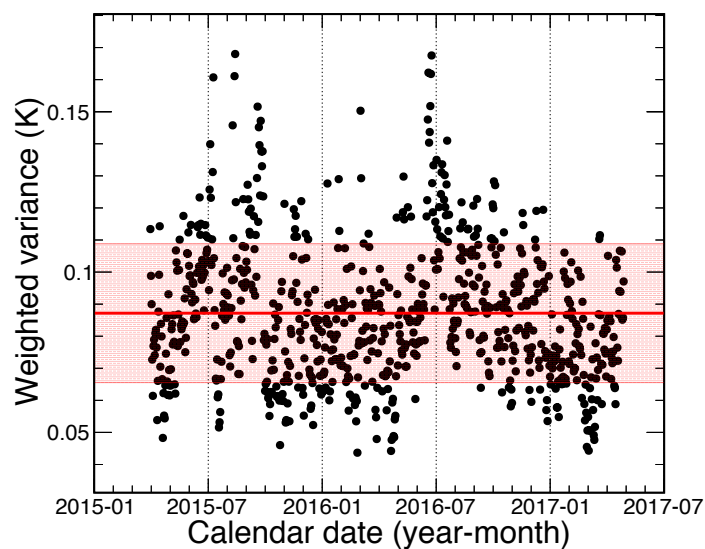


Figure 6.24 | Weighted temperature variance as a function of time

Daily weighted variance as a function of time, along with the average (solid red line) and $\pm 1\sigma$ of the average (red shaded region), which yields $\sigma_{\text{avg}} = 0.09 \pm 0.02$.

The effective temperature variance within the ECMWF grid

As described in Section 6.7, shown in figure 6.21 (a), the ECMWF temperature data comes from 4 temperatures per day per level per available time, representing a 2×2 grid that covers an area of $5,312.5 \text{ km}^2$.

To assess the effect of the temperature differences within the 2×2 grid area, two daily effective temperatures were calculated, in order to provide the lowest and highest effective temperature per day. Each one is calculated using the temperature extremes of each pressure level per available time – which results in a high and a low effective temperature per available time –, and averaging each group of four effective temperatures per day to reach two daily effective temperature values, representing the highest and the lowest daily T_{eff} . The daily variance of the effective temperature is calculated by computing

$$\sigma_{\text{day}_j}^{T_{\text{eff}}} = \sqrt{\frac{1}{2} \sum_{i=1}^2 (T_{\text{eff}_i} - \bar{T}_{\text{eff}})^2}, \quad (6.19)$$

where $\sigma_{\text{day}_j}^{T_{\text{eff}}}$ is the variance between the high and low effective temperatures of the j -th day, T_{eff_i} is the high or low T_{eff} of said day, and \bar{T}_{eff} is the average daily T_{eff} .

The daily temperature variance $\sigma_{\text{day}_j}^{T_{\text{eff}}}$ in the 2×2 grid is plotted as a function of time and presented in figure 6.25, which also includes the average of the variance (solid red line) and its uncertainty (red shaded region). The average is found to be $\bar{\sigma}_{T_{\text{eff}}} = 0.31 \pm 0.07$.

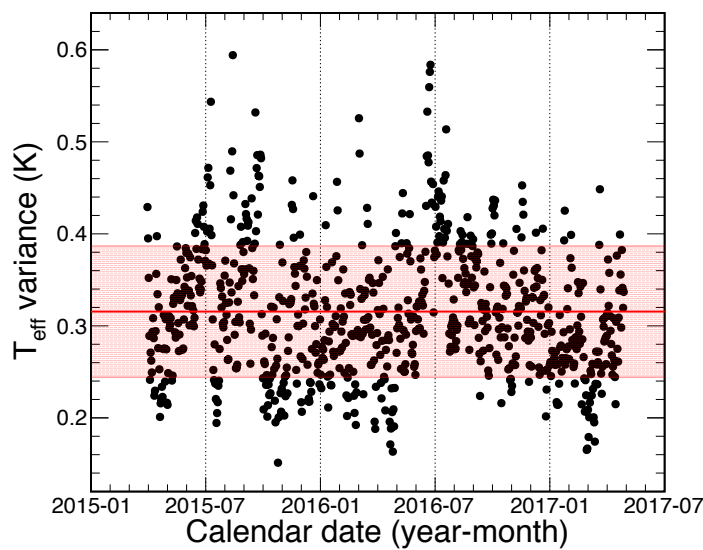


Figure 6.25 | Effective temperature variance in the 2×2 grid as a function of time

High/low effective temperature variance as a function of time, along with the average (solid red line) and $\pm 1\sigma$ of the average (red shaded region). The average yields $\bar{\sigma}_{T_{\text{eff}}} = 0.31 \pm 0.07$.

Total systematic uncertainty

The total systematic uncertainty of the effective temperature data is simply the sum in quadrature of the effect of the weighted variance of the temperature data over time and the effect of the variance seen in the effective temperature due to the temperature differences over the 2×2 grid region. Therefore, the resulting systematic uncertainty yields

$$\sigma_{\text{syst}} = \sqrt{(\sigma_{\text{avg}})^2 + (\bar{\sigma}_{T_{\text{eff}}})^2} = 0.32 \text{ K.} \quad (6.20)$$

6.8 Frequency analyses

Several methods were developed to find patterns in data signals, and the search for periodicities is commonly used in Physics. As both temperature and muon flux are known to follow a seasonal modulation, this section describes a set of techniques that are further applied to the data analysis.

6.8.1 The Rayleigh power

The Rayleigh power $P_{\text{R}}(\omega)$ is a method developed for finding and quantifying a periodicity of a given signal. It is specifically tailored to search for periodicity in events as a function of time and is defined as [93, 94]

$$P_{\text{R}}(\omega) = \frac{1}{N} \left\{ \left[\sum_{i=1}^N \sin(\omega t_i) \right]^2 + \left[\sum_{i=1}^N \cos(\omega t_i) \right]^2 \right\}, \quad (6.21)$$

where ω is the tested frequency over a set of N time measurements $t_i = \{t_1, t_2, \dots, t_N\}$. Equation 6.21 states that if t_i contains a sinusoidal component of frequency ω_0 , then when $\omega \approx \omega_0$ the t_i terms are in phase with $\cos(\omega t_i)$ and $\sin(\omega t_i)$, making large contributions to the sum. For random values of ω , the terms in the sum are randomly positive and negative, yielding a small final P_{R} value.

The importance of this tool is that the calculated Rayleigh power $P_{\text{R}}(\omega)$ can be compared to the expected $P_0(\omega)$ value in case P_0 is calculated from uniform noise. In said case, the functional form of the probability distribution follows an exponential [93, 94], meaning that the probability that the calculated P_{R} value exceeds the expected value P_0 for uniform noise at a given frequency ω is simply $\exp(-P_{\text{R}})$.

The binned Rayleigh power

In this study, the periodicity of the signal happens with event counts instead of time counts. As such, equation 6.21 is changed to a binned Rayleigh power, where each bin contains the counted number of events over a defined time interval that represents the bin width. In this

scenario, the binned Rayleigh power must sum over the number of bins, and its normalization factor is simply the total number of events, being expressed as

$$P_R^{\text{bin}}(\omega) = \frac{1}{N} \left\{ \left[\sum_{i=1}^{N_{\text{bins}}} X_i \sin(\omega i) \right]^2 + \left[\sum_{i=1}^{N_{\text{bins}}} X_i \cos(\omega i) \right]^2 \right\}, \quad (6.22)$$

where $X_i = R_i \langle t \rangle$ is the calculated number of events in bin i using the measured muon rate R_i in said bin multiplied by the bin width $\langle t \rangle$, $N = \sum X_i$ is the total number of events, N_{bins} is the chosen number of bins, and ω is a selected frequency. Since the bin width must be the same for all bins (being the analogue of having an evenly spaced data), $\langle t \rangle$ is defined as

$$\langle t \rangle = \frac{\Delta\tau}{N_{\text{bins}}} \varepsilon, \quad (6.23)$$

where $\Delta\tau$ is the total elapsed time of the dataset, and ε is the average duty cycle of the detector. Definition 6.23 can be easily interpreted by rewriting it as the equality of the two products $\varepsilon\Delta\tau = \langle t \rangle N_{\text{bins}}$, which are just two different forms of describing the total detector exposure time.

Similarly to the standard Rayleigh power, equation 6.22 states that if X_i contains a sinusoidal component of frequency ω_0 , $P_R^{\text{bin}}(\omega)$ must yield a high final value when $\omega \approx \omega_0$. This happens due to the fact that near the expected frequency ω_0 , the $\cos(\omega i)$ and $\sin(\omega i)$ terms make large contributions to the total summation, whilst for any other values of ω , said terms will be randomly positive and negative, cancelling each other out and producing a small P_R^{bin} .

The binned Rayleigh power holds the same property as the standard Rayleigh power, in which it can be compared to the probability $\exp(-P_R^{\text{bin}})$ of being pure noise. As a consequence, since it quantifies the absolute likelihood of a given signal to be periodic, it also provides a mean to compare seasonality trends between two or more datasets and assess which has a more or less prominent effect with respect to one another.

6.8.2 The classic periodogram

The classic periodogram is a method based on the discrete-time Fourier transform (DTFT)

$$\mathcal{F}(\omega) = \sum_{j=1}^{N_{\text{bins}}} X(t_j) \exp(-i\omega t_j), \quad (6.24)$$

applied to a sampled data $X(t_j) = \{X(t_1), X(t_2), \dots, X(t_{N_{\text{bins}}})\}$ with N_{bins} data bins evenly distributed in time, calculated for any particular frequency ω one may choose, in order to determine the magnitude of the DTFT for said frequency. As such, the classic periodogram definition

is

$$P_c(\omega) = \frac{1}{N_{\text{bins}}} |\mathcal{F}(\omega)|^2 = \frac{1}{N_{\text{bins}}} \left| \sum_{j=1}^{N_{\text{bins}}} X(t_j) \exp(-i\omega t_j) \right|^2$$

$$P_c(\omega) = \frac{1}{N_{\text{bins}}} \left\{ \left[\sum_{i=1}^{N_{\text{bins}}} X(t_i) \sin(\omega t_i) \right]^2 + \left[\sum_{i=1}^{N_{\text{bins}}} X(t_i) \cos(\omega t_i) \right]^2 \right\}, \quad (6.25)$$

where the final P_c is higher if a said frequency ω is equal or near the expected frequency ω_0 of the dataset $\{X(t_i)\}$, having an analogous explanation. This can be interpreted as a random walk problem, in which for random frequencies, every new step will point to a random direction and, after a total of N_{bins} steps, the resulting position will be placed near the origin. Alternatively, for frequencies near the expected frequency ω_0 , every new step will point to the same direction, resulting in a final position far from the origin. The evenly time-distributed data is interpreted as the step size, where uneven step sizes, analogous to an unevenly distributed dataset, will result in misleading P_c values.

The binned Rayleigh power (equation 6.22) is very similar to the classic periodogram (equation 6.25): both can be interpreted as a random walk problem, and both need an evenly distributed dataset¹², but most importantly, they differ in the way the calculated values P_c or P_R^{bin} are interpreted. The power P_c is relative to the magnitude of the measurements $\{X(t_i)\}$, while the binned Rayleigh power is calculated based on the number of events in each bin, the latter being an absolute measurement that can be compared to the probability of being pure noise.

6.8.3 The Lomb-Scargle method

The Lomb-Scargle method [95–97] generalizes the classic periodogram definition in order to be used to detect periodicity in unevenly sampled data signals. As such, this formalism is an extension of the classic periodogram, and it consists in calculating the power spectra

$$P_{LS}(\omega) = \frac{1}{2\sigma^2} \left\{ \frac{\left[\sum_{i=1}^N (X_i - \bar{X}) \cos(\omega t_i - \phi) \right]^2}{\sum_{i=1}^N \cos^2(\omega t_i - \phi)} + \frac{\left[\sum_{i=1}^N (X_i - \bar{X}) \sin(\omega t_i - \phi) \right]^2}{\sum_{i=1}^N \sin^2(\omega t_i - \phi)} \right\}. \quad (6.26)$$

In equation 6.26, ω is a selected frequency, σ is the variance, $X_i = \{X_1, X_2, \dots, X_N\}$ is the dataset, which encompasses a total of N data points, \bar{X} is simply the average of all data points

$$\bar{X} = \frac{1}{N} \sum_{i=1}^N X_i, \quad (6.27)$$

¹²This is the reason for the use of the average duty cycle $\langle t \rangle$ of the detector when calculating the X_i terms in equation 6.22 instead of using the real number of events for each month: $X_i = R_i \langle t \rangle$ produces equally sized bins.

and the variance is defined as

$$\sigma = \sqrt{\frac{1}{N-1} \sum_{i=1}^N (X_i - \bar{X})^2}. \quad (6.28)$$

The power spectra P_{LS} is calculated for a range of different values of ω . Sampled frequencies with periodicity values shorter than the minimum time interval between 2 data points Δt cannot be used, as there may be infinite sinusoidal solutions that could fit within the sampled signal¹³. As such, the range of tested frequencies must be limited to

$$\omega_k = \frac{\pi}{N\Delta t}k; \quad k = \{1, 2, \dots, N\}, \quad (6.29)$$

in which the highest frequency value is known as the Nyquist limit.

The power of both the classic periodogram and the Lomb-Scargle method is relative to the magnitude of the data points $\{X(t_i)\}$, being not trivial to assess the likelihood of a said periodic result when compared to random noise.

¹³This problem, in which frequencies with smaller periodicities than the time interval between 2 data points may yield high P_{LS} values, is also referred to as aliasing.

Chapter

Multiple-muon physics results

This Chapter presents the results of the multiple-muon physics analysis, whose purpose is to measure and better understand their seasonal variation effect. The results are presented in 2 main categories: *i*) using different choices of time bins for the data (daily, weekly, monthly, week of year, and month of year) and *ii*) broken down by different variables, such as track separation, zenith angle, angle between tracks, and multiplicity. The correlation coefficient α_T , which connects the seasonal modulation of the effective temperature of the atmosphere with the cosmic ray muon rate measured by the NO ν A Near Detector is also presented. In the case of multiple-muons, the value is not as important as its sign. The premise of the model used to describe muon seasonal variations outlined in Section 3.3 considers only the decay of secondary pions and kaons into muons. Multiple-muons are produced in different regions of the atmosphere by secondary and further hadronic decays, encompassing more complications for the calculation of the effective temperature. As such, α_T may not be a good method for quantifying the effect, but the sign of α_T is a clear indication that the multiple-muon data obeys a direct or inverted correlation with atmospheric temperature oscillations. In addition, a Lomb-Scargle frequency analysis is performed over the data to verify the periodicity of the signal. The seasonal variations are broken down using different variables and their seasonal trends are quantified using the binned Rayleigh power.

7.1 Periodicity consistency checks

The Lomb-Scargle method was applied to both multiple-muon rate and effective temperature data as a function of time using daily bins. As such, it is expected that the highest peak for P_{LS} , considering that the data follows a yearly periodicity, must yield a result close to the expected value

$$\omega_{\text{exp}} = \frac{2\pi}{365.24} \simeq 0.0172. \quad (7.1)$$

The results are presented in figure 7.1, with both datasets showing a yearly seasonality, as the highest peaks found by the power spectra analysis are at $\omega_{\mu} \simeq 0.0181$ and $\omega_{T_{\text{eff}}} \simeq 0.0173$,

representing a periodicity of $T_\mu \simeq 347$ days, and $T_{T_{\text{eff}}} \simeq 363$ days, for the multiple-muon and effective temperature data, respectively. Given the width of both peaks, an annual effect with the expected frequency is seen unambiguously.

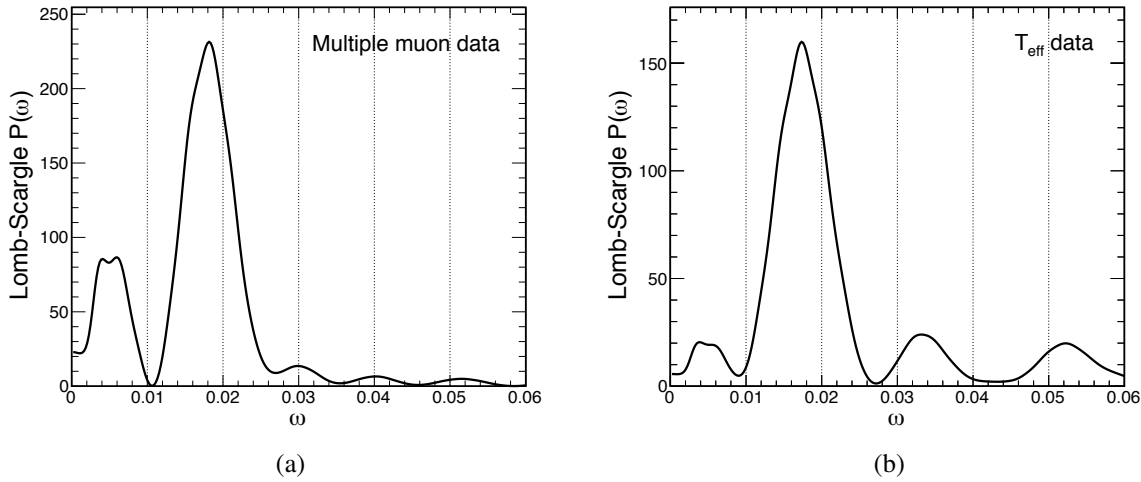


Figure 7.1 | Lomb-Scargle results for both multiple-muon rate and T_{eff} data

Lomb-Scargle power spectra for different values of ω for both (a) multiple-muon and (b) effective temperature data. The value of the frequency for each peak is (a) $\omega_\mu \simeq 0.0181$ and (b) $\omega_{T_{\text{eff}}} \simeq 0.0173$, yielding a periodicity of $T_\mu \simeq 347$ days for (a), and $T_{T_{\text{eff}}} \simeq 363$ days for (b). These results are close to the expected frequency for a perfect yearly periodicity, which is $\omega_{\text{exp}} \simeq 0.0172$. Considering the width of the peaks, the annual effect is confirmed.

7.2 Seasonal variations using different time bins

The multiple-muon rate at the NO ν A ND is expected to fluctuate around the order of 10^{-1} s^{-1} , resulting in roughly 10^4 events per day. Therefore, daily bins have enough statistics to provide a clear verification of a seasonal effect, as is shown in figures 7.2 (a) and (b), with the first one showing the daily multiple-muon rates as a function of time, along with the global average rate (solid red line), while the second presents the percent variation of each daily data point with respect to the global average rate. The same set of plots is shown for the daily effective temperature data from ECMWF, and is presented in figures 7.2 (c) and (d). The multiple-muon seasonality verified by the NO ν A Near Detector has an inverted phase with respect to the temperature data, in agreement with the results presented by MINOS [55]. The daily α_T coefficient is achieved by combining plots 7.2 (b) and (d) and calculating the linear best fit (figure 7.2 (e)). The negative slope of α_T is a clear confirmation of the opposite modulation phases between the multiple-muon and effective temperature data.

Other bin sizes, which encompass weeks and months, are presented as well. Longer binning intervals provide a better view of the seasonal modulation, while removing short period oscil-

lations that are especially high during winter months. The results for weekly and monthly bins are presented, respectively, in figures 7.3 and 7.4.

Note that the multiple-muon rate presents a more prominent depletion during the summer of 2015 with respect to the same period of 2016. The reason for this is not clear. Nevertheless, there is a very likelihood of it being an atmospheric effect instead of a change in the detector itself. Two main arguments support this statement. The first is seen in figure 6.20, which compares normalized distributions of the data for each year separately. No clear differences are seen in any reconstructed variable and, as such, no effective changes in the electronics, nor the trigger, have occurred within both years of operation. The second reason is that the effective temperature shows a warmer summer during 2015 when compared to the respective period in 2016, hence providing plausible link of causation, in which the more intense seasonal effect detected in the multiple-muon rate may be due to the larger atmospheric temperature variations. This is obvious when figures 7.3 (a) and (c) are compared.

Next, both years are also folded in bins of week of year and month of year. The multiple-muon and atmospheric effective temperature in the form of week of year, along with α_T , are shown in figure 7.5, while the results using the month of year representation are seen in figure 7.6. All the fitted α_T values, for each bin size, are summarized in table 7.1.

Bin size	Fitted α_T
Daily	-2.78 ± 0.05
Weekly	-3.04 ± 0.05
Monthly	-3.48 ± 0.05
Week of year	-4.8 ± 0.1
Month of year	-4.1 ± 0.6

Table 7.1 | Multiple-muon α_T fitted values according to different time bins

The table shows resulting fitted temperature correlation coefficients for each bin size presented.

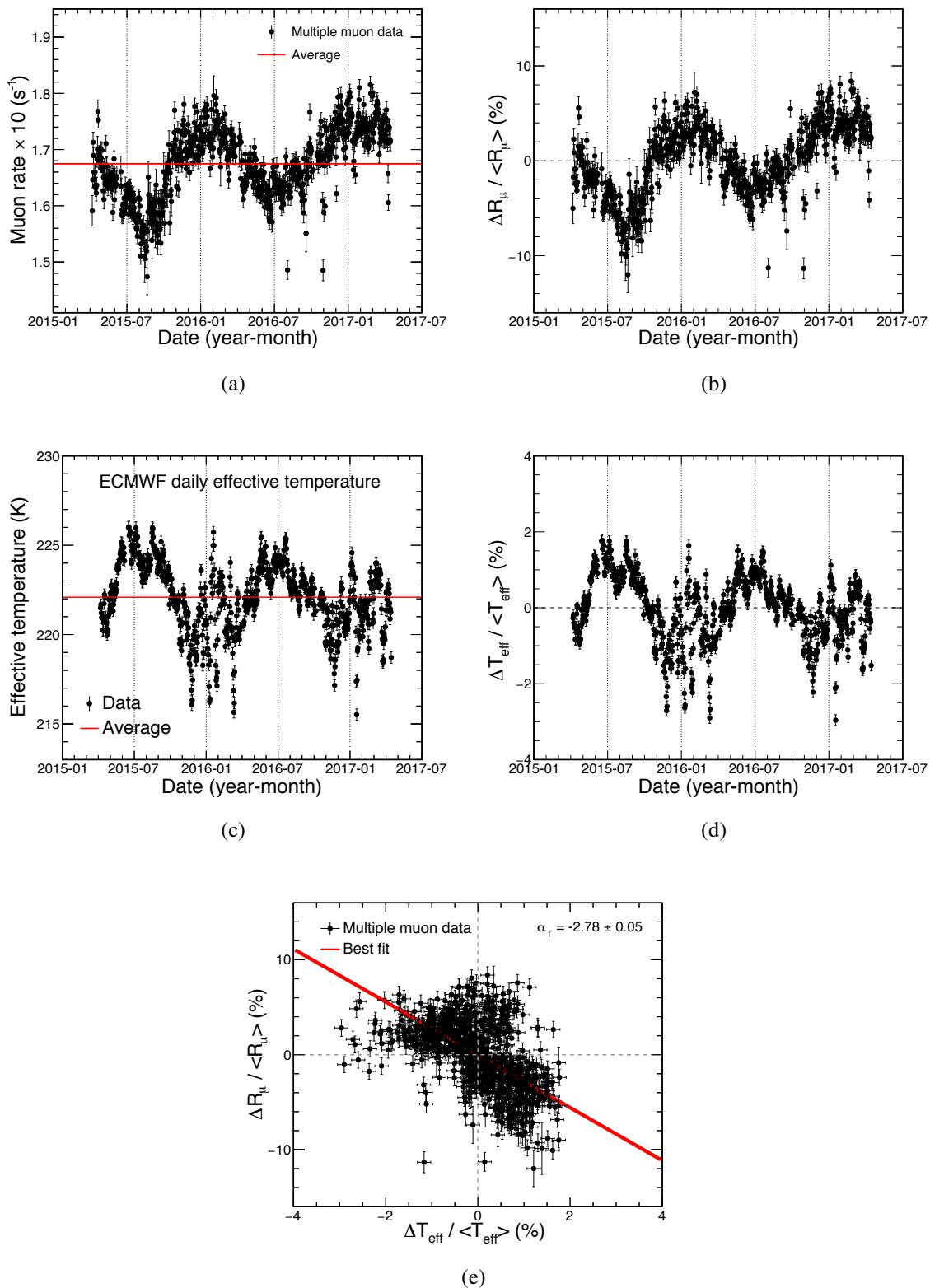


Figure 7.2 | Daily multiple-muon and effective temperature seasonalities, and α_T

(a) Daily multiple-muon rates as a function of time, along with the average rate (solid red line). (b) Percent variation of the daily multiple-muon rate with respect to the average rate. In (a) and (b) the error bars represent the statistical uncertainties. (c) Daily effective temperature for the NOVA Near Detector location as a function of time, along with the average effective temperature (solid red line). (d) Percent variation of the daily effective temperature with respect to the average. (e) Multiple-muon daily percent variations as a function of the percent variation of the daily effective temperature, along with the linear best fit (solid red line).

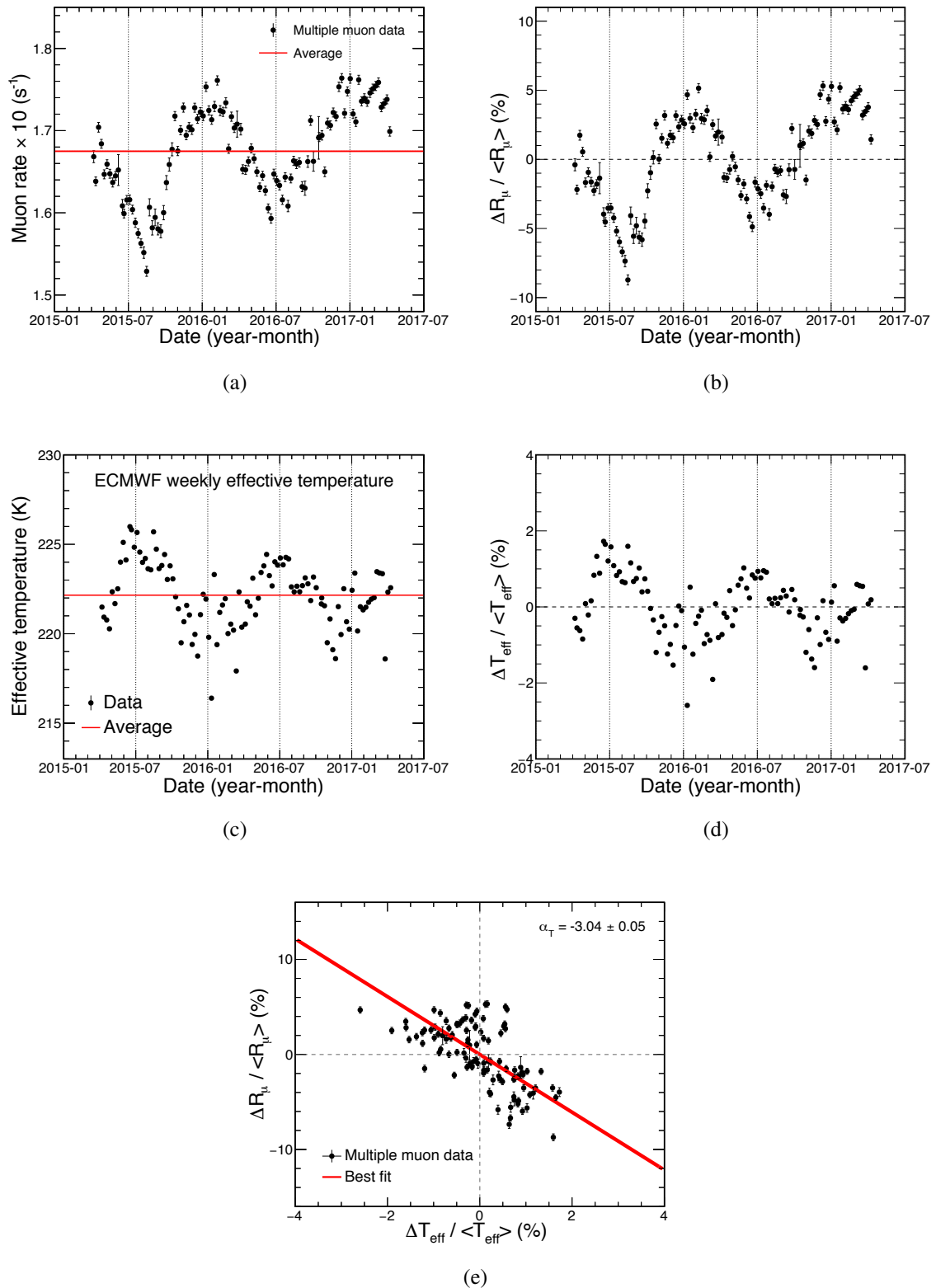


Figure 7.3 | Weekly multiple-muon and effective temperature seasonalities, and α_T

(a) Weekly multiple-muon rates as a function of time, along with the average rate (solid red line). (b) Percent variation of the weekly multiple-muon rate with respect to the average rate. In (a) and (b) the error bars represent the statistical uncertainties. (c) Weekly effective temperature for the NO ν A Near Detector location as function of time, along with the average effective temperature (solid red line). (d) Percent variation of the weekly effective temperature with respect to the average. (e) Multiple-muon weekly percent variations as a function of the percent variation of the weekly effective temperature, along with the linear best fit (solid red line).

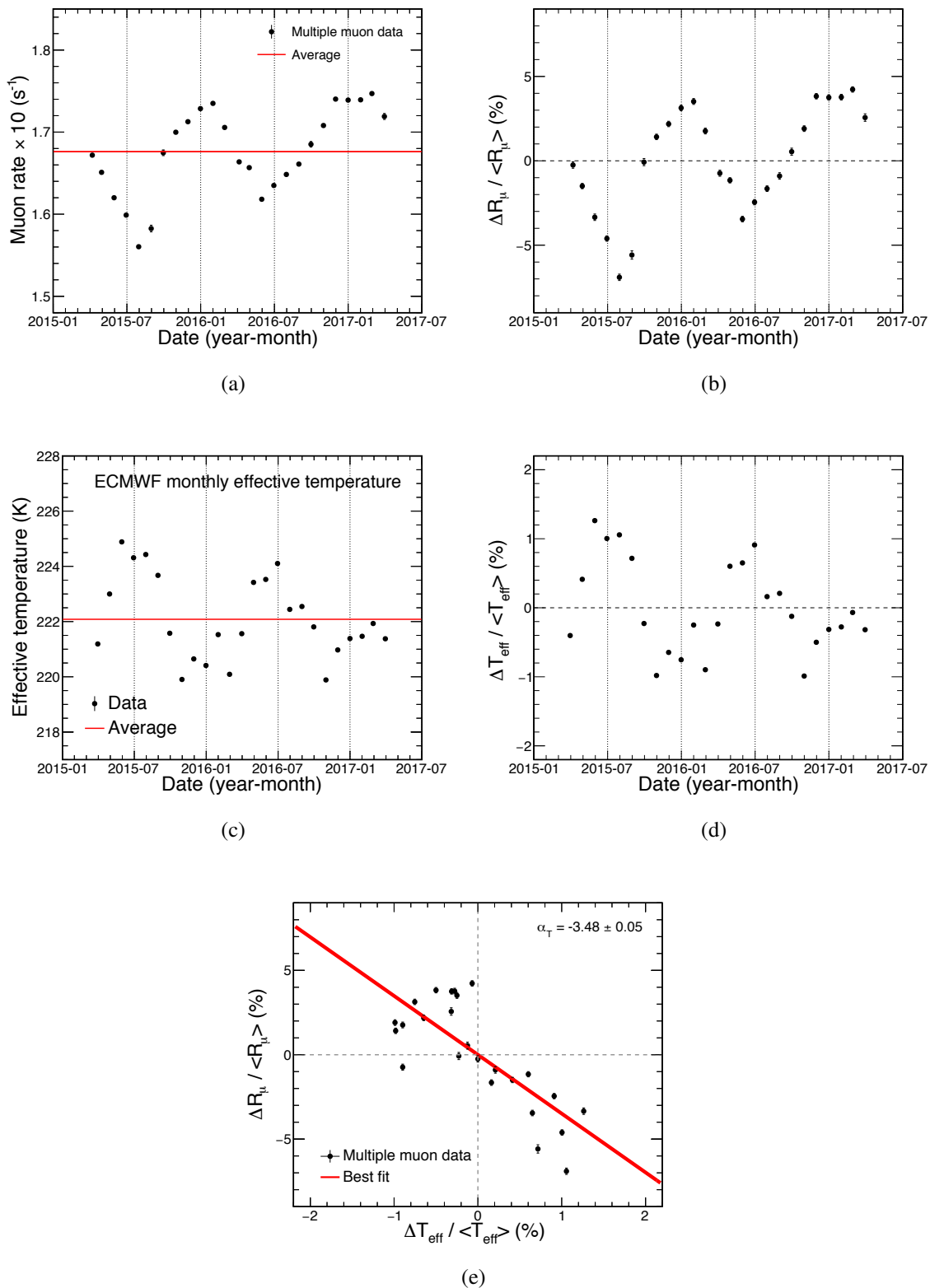


Figure 7.4 | Monthly multiple-muon and effective temperature seasonalities, and α_T

(a) Monthly multiple-muon rates as a function of time, along with the average rate (solid red line). (b) Percent variation of the monthly multiple-muon rate with respect to the average rate. In (a) and (b) the error bars represent the statistical uncertainties. (c) Monthly effective temperature for the NO ν A Near Detector location as a function of time, along with the average effective temperature (solid red line). (d) Percent variation of the monthly effective temperature with respect to the average. (e) Multiple-muon monthly percent variations as a function of the percent variation of the monthly effective temperature, along with the linear best fit (solid red line).

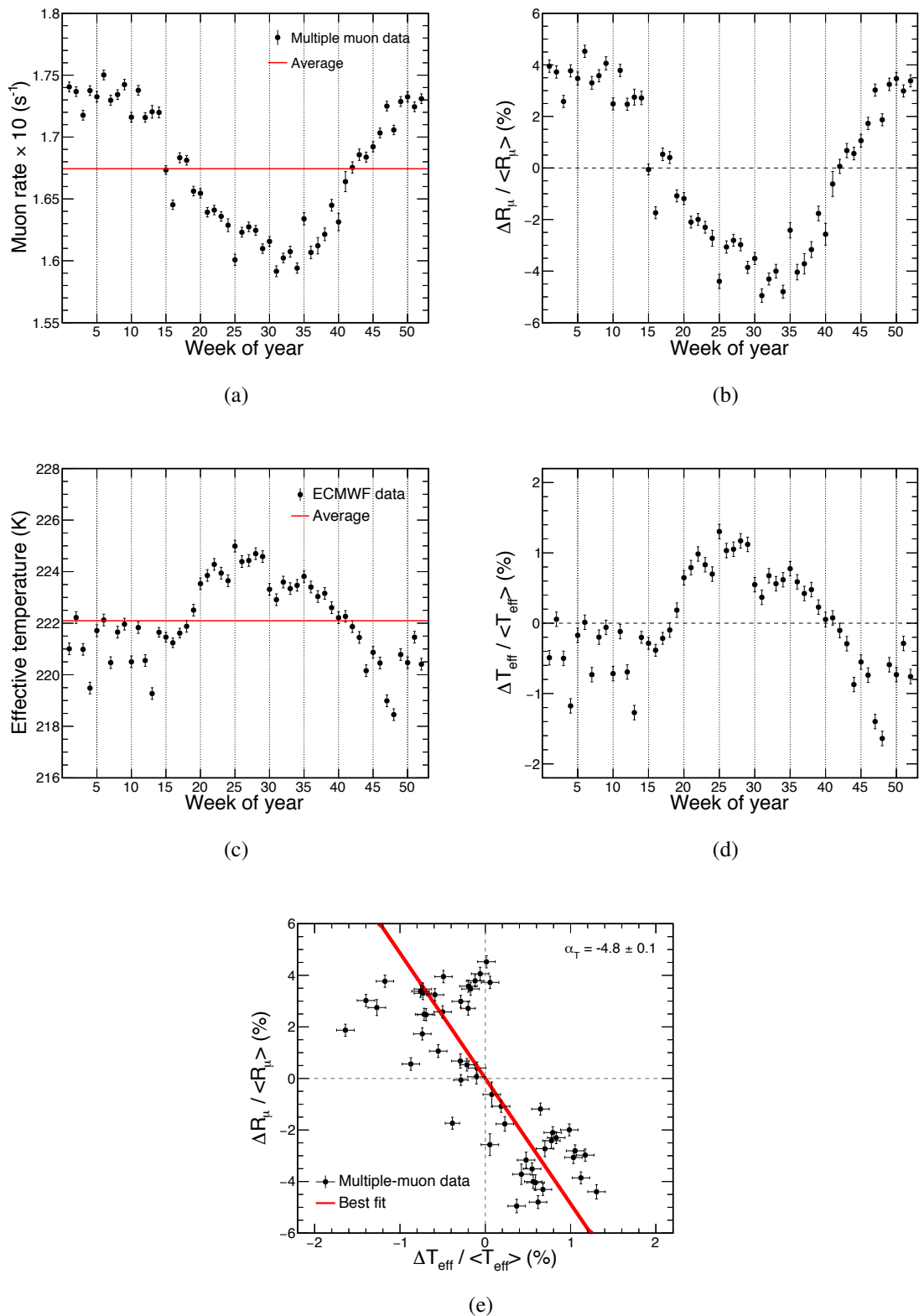


Figure 7.5 | Week of year multiple-muon and effective temperature seasonalities, and α_T
 (a) Week of year multiple-muon rates as a function of time, along with the average rate (solid red line). (b) Percent variation of the week of year multiple-muon rate with respect to the average rate. (c) Week of year effective temperature as a function of time, along with the average effective temperature (solid red line). (d) Percent variation of the week of year effective temperature with respect to the average. (e) Multiple-muon week of year percent variations as a function of the percent variation of the week of year effective temperature and the linear the best fit (solid red line).

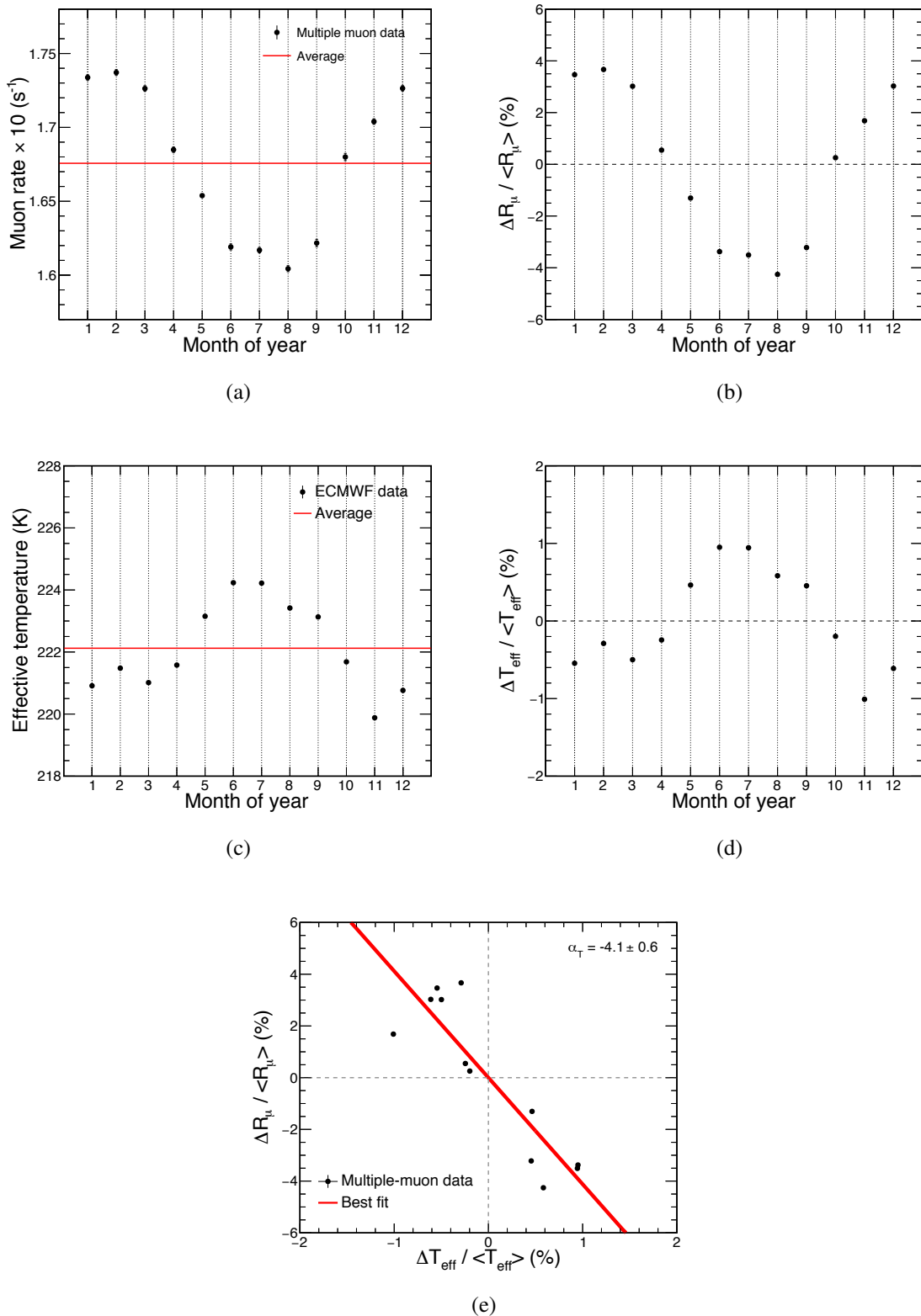


Figure 7.6 | Month of year multiple-muon and effective temperature seasonalities, and α_T
 (a) Month of year multiple-muon rates as a function of time, along with the average rate (solid red line). (b) Percent variation of the month of year multiple-muon rate with respect to the average rate. (c) Month of year effective temperature as a function of time, along with the average effective temperature (solid red line). (d) Percent variation of the month of year effective temperature with respect to the average. (e) Multiple-muon month of year percent variations as a function of the percent variation of the month of year effective temperature and the linear best fit (solid red line).

7.3 Seasonal variations as a function of different event variables

This section breaks down the multiple-muon seasonal variations by a set of event parameters. The goal is to search for any specific trend in the multiple-muon modulation signal that leads to a better understanding of the phenomenon. The multiple-muon rate as a function of time is plotted for different regions of track separation, zenith angle, angle between tracks, and multiplicity, with each variable being described in its own subsection.

A periodicity analysis using the binned Rayleigh power is performed in order to quantify the seasonal effect and search for trends in each of the aforementioned variables. For the results presented in this Thesis, monthly bins have been chosen. Therefore, $\omega = 2\pi/12 \text{ months}^{-1}$ represents the frequency of a yearly periodicity. For the bin width $\langle t \rangle$ (see equation 6.23), since the data encompasses 24 months and the average duty cycle of the detector is at the 86% level (see Section 6.5.1), $\langle t \rangle = 2.3 \times 10^6 \text{ s}$.

7.3.1 By track separation

The seasonal modulation signal for different track separations was studied by the MINOS experiment, which presented a similar study for both its ND and FD [55]. The reason for the muon track separation study is due to its link with their parent cosmic ray energy, in which the angle is larger if the energy is lower. As a result, muons traversing the detector with larger track separation come, on average, from less energetic parents.

As discussed in Section 3.4.2, the published MINOS results divided the track separation distribution into 3 regions of equal statistics and verified the multiple-muon seasonal effect for each of the three regions. Said results showed no correlation between the track separation and the seasonality of the multiple-muons for the MINOS ND, but showed an anticorrelation between short and large track separation distances in the FD data. In the FD case, small separations followed the same trend seen in the ND, in which the multiple-muon seasonal variation has an inverted phase with respect to the effective temperature modulation signal, whereas for large track separations the trend followed a direct correlation with the effective temperature, being the same as the single muon data. The NO ν A ND has a similar size and is built tens of meters away from the MINOS ND.

The track separation is calculated in pairs (i.e. for a 4 muon event, 6 track separation distances are computed) by taking the perpendicular distance between every pair of tracks. The distance between tracks is simply

$$\Delta L = \sqrt{(\Delta X)^2 + (\Delta Z)^2} \cos \bar{\theta}, \quad (7.2)$$

where X and Z are the NuMI coordinates of the starting vertices of each track, and $\bar{\theta}$ is the

average zenith angle of both tracks. The data is divided into three track separation squared regions (namely A, B, and C) with roughly equal statistics, as it is shown in figure 7.7 (a), which presents the track separation squared for different multiplicities, along with the limits of each region, found to be at $102,375 \text{ cm}^2$ and $305,250 \text{ cm}^2$. The plot was normalized for easier comparison between each multiplicity distribution. There are no evident differences between them.

The multiple-muon seasonal modulation for each track separation squared region is presented in figures 7.7 (b), (c), and (d), which show no clear differences in the phases of the seasonalities. The magnitude of the effect is very similar, as it is clear from 7.7 (e), which presents the percent variation of the seasonal effect according to the average ($\Delta R_\mu / \langle R_\mu \rangle$) as a function of time for all three regions. The binned Rayleigh power results for each region are also computed and presented in table 7.2. These values do not show any obvious trend. The data from figure 7.7 (e) is folded and presented in month of year bins in figure 7.7 (f), which also includes the best fit of each region. The fitting function is

$$f(t) = A + B \cos(\omega t + \phi), \quad (7.3)$$

where A , B , ω , and ϕ are the fitted constant, amplitude, frequency, and phase parameter, respectively. It is important to stress the fact that there is no particular reason for the fit choice in equation 7.3, except for being a general sinusoidal function. As such, the data may not follow said specific fit, as more variables may play important roles¹, but the amplitude, frequency, and phase are still physically meaningful. The fitting parameters found for each region are presented in table 7.3.

The combination of figures 7.7 (e) and 7.4 (d) provides the measured α_T for each region of track separation squared, with the results being presented in figure 7.8 and summarized in table 7.4.

The results found by the NO ν A Near Detector are in accordance with the conclusion published by the MINOS Collaboration [55], which did not detect any noticeable change in the modulation phase of the signal for different track separations in its Near Detector.

¹One example of an extra effect could be the inclusion of a term that represents a possible detector degradation over time.

Region	Limits $\times 10^3$ (cm)	Binned Rayleigh power	Number of events
A	[< 102.375]	4,224	3,497,360
B	[102.375, 305.250]	3,861	3,497,210
C	[> 305.250]	4,162	3,496,770

Table 7.2 | Binned Rayleigh power results for each track separation squared region

The table shows results for the binned Rayleigh power (equation 6.22) for each region of track separation squared. No clear trends are seen in the data.

Region	Constant (%)	Amplitude (%)	Frequency (month ⁻¹)	Phase (rad)
A	-0.24 ± 0.08	4.41 ± 0.08	0.5611 ± 0.0008	-0.99 ± 0.06
B	-0.19 ± 0.08	3.75 ± 0.08	0.5600 ± 0.0009	-0.93 ± 0.07
C	-0.31 ± 0.07	4.35 ± 0.08	0.5695 ± 0.0008	-1.08 ± 0.06

Table 7.3 | Best fit values for each region of track separation

The table shows the best fitted values from equation 7.3 for each region of track separation squared. No clear differences are noticed.

Region	Fitted α_T
A	-4.6 ± 0.1
B	-3.6 ± 0.1
C	-4.5 ± 0.1

Table 7.4 | Multiple-muon α_T fitted values according to different regions of track separation

The table shows resulting fitted temperature correlation coefficients for each region of track separation squared.

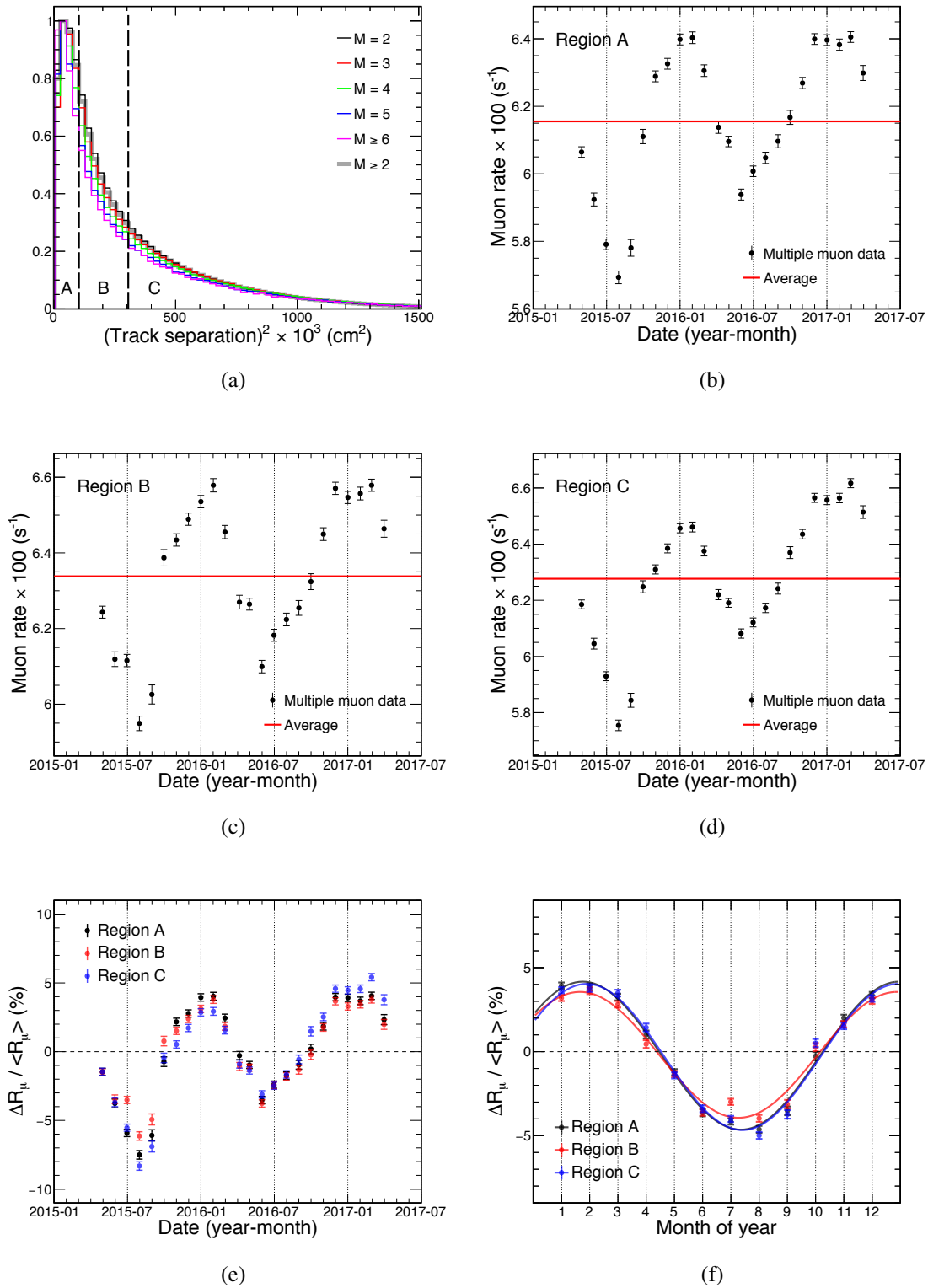


Figure 7.7 | Multiple-muon seasonal variations for different regions of track separation

(a) Track separation squared for each pair of multiple-muon tracks of every event, separated by different multiplicities. The distribution is normalized and divided into three regions of roughly equal statistics (namely, regions A, B, and C), whose limits are specified by the vertical dashed lines. Figures (b), (c), and (d) show the multiple-muon seasonal variations according to each track separation squared region. Figure (e) compares the $\Delta R_{\mu} / \langle R_{\mu} \rangle$ of each region, and (f) shows the same data in a month of year representation, along with the best fits. The error bars represent the statistical uncertainties.

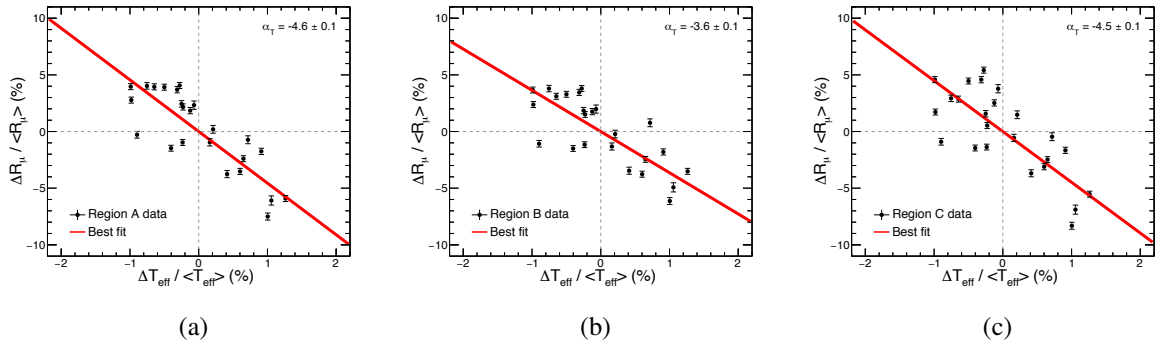


Figure 7.8 | Calculated α_T for each region of track separation squared

Figure shows the fitted α_T value for each region of track separation squared, which is achieved by combining figures 7.7 (e) and 7.4 (d), resulting in $\alpha_T^{(A)} = -4.6 \pm 0.1$, $\alpha_T^{(B)} = -3.6 \pm 0.1$, and $\alpha_T^{(C)} = -4.5 \pm 0.1$ for regions A, B, and C, respectively.

7.3.2 By zenith angle

The motivation to study the multiple-muon modulation signal as a function of zenith angle is based on the fact that the total overburden encountered by a cosmic ray muon increases by a factor of $1/\cos\theta$, as the zenith angle θ increases. As such, the threshold energy for muons to reach the detector is also

$$E_{\text{th}}(\theta) = \frac{E_{\text{th}}(0)}{\cos\theta}, \quad (7.4)$$

where $E_{\text{th}}(0)$ is the muon vertical threshold energy for a given depth, and whose value is 54 GeV in the case of the NO ν A Near Detector. The muon threshold energy at the detector level is a rough indication of the primary energy and, therefore, the dependence of the zenith angle is used as a direct indication of how the multiple-muon seasonal effect changes as a function of muon energy, and as an indirect indication of primary energy.

The cosine distribution of the zenith angle of every muon is plotted and divided into three regions of roughly equal statistics (namely, regions 1, 2, and 3), as well as broken down by multiplicity, as shown in figure 7.9 (a). The limits of the regions are placed at 0.73 and 0.87. The shape of the distribution remains similar for most multiplicities, but it is more broad for $M = 2$, which indicates that dimuons in the detector are more likely to occur over a larger range of zenith angles.

The seasonal modulations for each of these 3 regions are presented in figures 7.9 (b), (c), and (d), showing no broad discrepancies between them. The magnitude of the effect is very similar for every region, as it is noticed in figure 7.9 (e), which presents each region's muon rate percent variation according to the average ($\Delta R_\mu / \langle R_\mu \rangle$) as a function of time. The binned Rayleigh power results for each of the three $\cos(\text{zenith})$ regions are presented in table 7.5, also showing no clear trends. Figure 7.9 (f) folds the data presented in (e) in order to provide a month of year view of the data, and includes the best fit found for each of the regions presented.

The best fitting function used is the same as in equation 7.3, and the best fit values found are shown in table 7.6. The combination of figure 7.9 (e) and 7.4 (d) provides the measured α_T for each $\cos(\text{zenith})$ region, which are presented in figure 7.10 and table 7.7.

Region	Limits	Binned Rayleigh power	Number of events
1	[< 0.73]	4,007	5,882,700
2	[0.73, 0.87]	4,172	5,882,910
3	[> 0.87]	3,949	5,882,070

Table 7.5 | Binned Rayleigh power results for each $\cos(\text{zenith})$ region

The table shows results for the binned Rayleigh power (equation 6.22) for each region of $\cos(\text{zenith})$. No clear trends are seen in the data.

Region	Constant (%)	Amplitude (%)	Frequency (month^{-1})	Phase (rad)
1	-0.20 ± 0.07	3.93 ± 0.08	0.5530 ± 0.0009	-0.91 ± 0.07
2	-0.17 ± 0.07	3.80 ± 0.08	0.5522 ± 0.0009	-0.91 ± 0.07
3	-0.31 ± 0.07	3.90 ± 0.08	0.5823 ± 0.0008	-1.12 ± 0.06

Table 7.6 | Best fit values for each region of $\cos(\text{zenith})$

The table shows the best fitted values from equation 7.3 for each region of $\cos(\text{zenith})$. No clear differences are noticed.

Region	Fitted α_T
A	-3.9 ± 0.1
B	-3.6 ± 0.1
C	-3.9 ± 0.1

Table 7.7 | Multiple-muon α_T fitted values according to different regions of $\cos(\text{zenith})$

The table shows resulting fitted temperature correlation coefficients for each region of $\cos(\text{zenith})$.

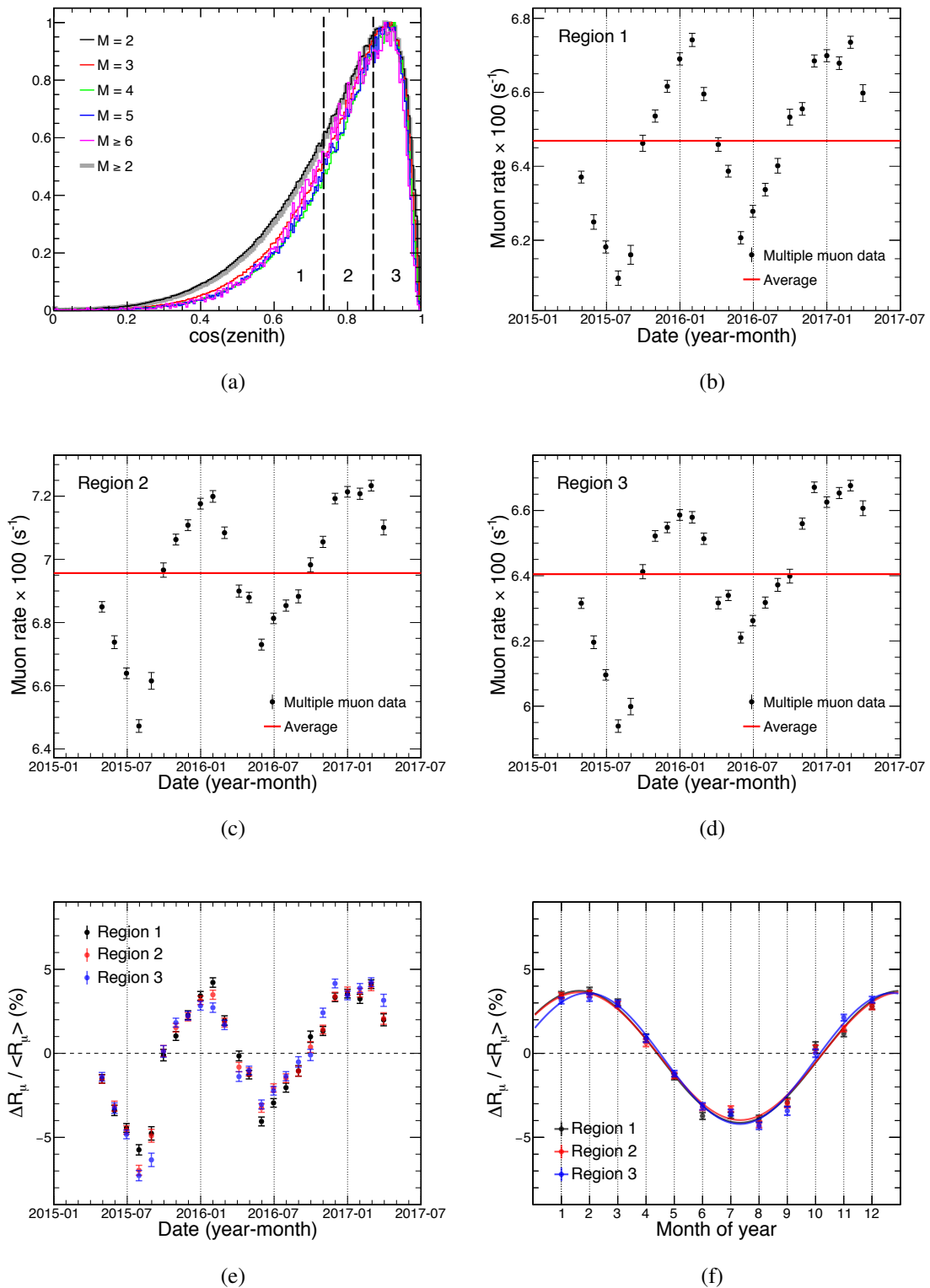


Figure 7.9 | Multiple-muon seasonal variations for different regions of $\cos(\text{zenith})$

(a) $\cos(\text{zenith})$ of each muon of every multiple-muon event, separated by different multiplicities. The distributions are normalized and divided into three regions of roughly equal statistics (namely, regions 1, 2, and 3), whose limits are specified by the vertical dashed lines. Figures (b), (c), and (d) show the multiple-muon seasonal variations for each region, along with each average muon rate (solid red line). All three signals are very similar, as shown in (e), which shows the $\Delta R_{\mu} / \langle R_{\mu} \rangle$ for each region. Figure (f) folds figure (e) into month of year bins and presents the best fit for each region. The error bars represent the statistical uncertainties.

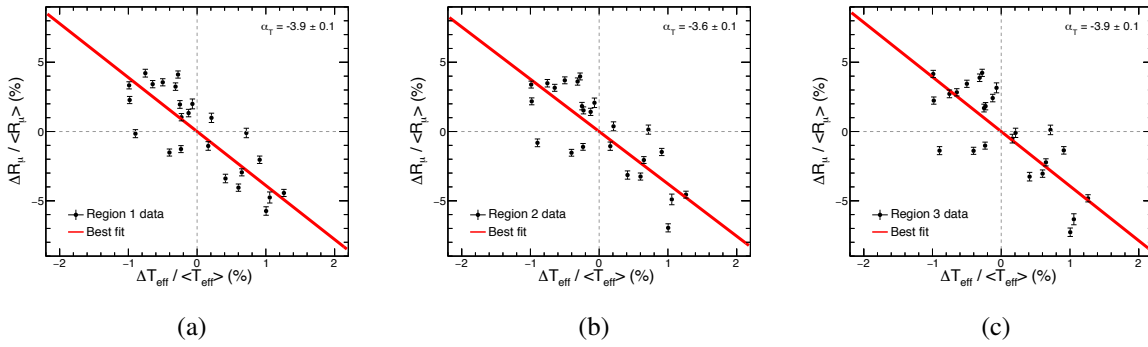


Figure 7.10 | Calculated α_T for each region of $\cos(\text{zenith})$

Figure shows the fitted α_T value for each region of $\cos(\text{zenith})$, which is achieved by combining figures 7.9 (e) and 7.4 (d), yielding $\alpha_T^{(1)} = -3.9 \pm 0.1$, $\alpha_T^{(2)} = -3.6 \pm 0.1$, and $\alpha_T^{(3)} = -3.9 \pm 0.1$ for regions 1, 2, and 3, respectively.

7.3.3 By angle between tracks

The motivation for searching for seasonal trends in different regions of angle between tracks is the correlation between the muon multiple scattering through the rock and its primary energy. The scattering of cosmic ray muons when traversing the rock overburden is the most prominent effect that may cause angle differences between tracks. Since this effect is proportional to $1/E_\mu$, and the muon energy is related to the primary energy, higher angles between tracks come, on average, from less energetic primaries.

The angles between tracks are calculated in a pair by pair basis by simply computing

$$\theta_{AB} = \cos^{-1} \left(\frac{\vec{A} \cdot \vec{B}}{|\vec{A}| |\vec{B}|} \right), \quad (7.5)$$

where \vec{A} and \vec{B} are vectors representing the directions of each pair of tracks in every multiple-muon event. The final distribution of angle between pairs of tracks is presented in figure 7.11, which is also separated by multiplicity. All distributions are very similar, although there seems to be a small trend for angle separations above 3° and below 30° , in which the amount of track pairs with higher angle separations increases according to the multiplicity of the event.

The first attempt to verify any trends in the angular separation considered 3 regions of roughly equal statistics and showed a possible trend at larger angle differences. This outcome resulted in a more detailed test using thrice the amount of regions. As such, nine regions of roughly equal statistics (namely, regions α , β , γ , δ , ϵ , ζ , η , θ , and ι) were separated and presented in figure 7.12 (a), with their boundaries being defined by the dashed vertical lines, whose limits are at 1.19° , 1.95° , 2.74° , 3.68° , 4.90° , 6.64° , 9.48° , and 15.55° . Since the angle separation distribution is very narrow, the y axis of figures 7.11 (b) and 7.12 (a) are presented in logarithmic scale.

The results of the seasonal modulation of each of the aforementioned regions is presented in figures 7.12 (b) through (j), showing no large differences between each case. The magnitude of the effect is again very similar for every region, as it is noticed in figure 7.12 (k), which shows small differences in the percent variations in the muon rate ($\Delta R_\mu / \langle R_\mu \rangle$) for each region. Figure 7.12 (l) folds (k) into month of year bins and includes the best fit found for each region of angle separation using equation 7.3. The numerical values extracted from the fits are shown in table 7.9.

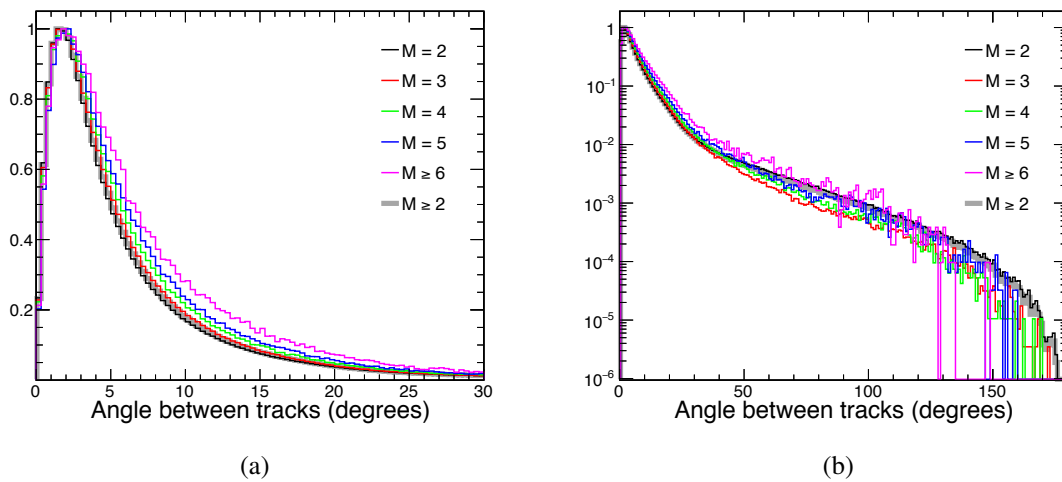


Figure 7.11 | Angular separation between tracks for different multiplicities

Both figures show the angular separation between every multiple-muon track pair according to different multiplicities. Figure (a) presents the distribution up to 30° , while (b) provides a full view of the distribution spectrum. Since the distribution is very narrow, the y axis in (b) is presented in logarithmic scale. The similarity between all distributions shows that the angle between tracks has no dependency with multiplicity.

The binned Rayleigh power values for each region are shown in table 7.8, which presents a slight decrease in power as angular differences increase, suggesting a possible trend for larger angle separations. The combination of figure 7.12 (k) and 7.4 (d) provides the measured α_T for each region of angular separation, which are presented in figure 7.13 and table 7.10.

Region	Limits (degrees)	Binned Rayleigh power	Number of events
α	[< 1.19]	644	1,206,880
β	[1.19, 1.95]	565	1,206,350
γ	[1.95, 2.74]	607	1,207,880
δ	[2.74, 3.68]	572	1,206,870
ϵ	[3.68, 4.90]	582	1,206,560
ζ	[4.90, 6.64]	541	1,206,540
η	[6.64, 9.48]	591	1,206,590
θ	[9.48, 15.55]	593	1,206,570
ι	[> 15.55]	333	1,200,510

Table 7.8 | Binned Rayleigh power results for each angle between tracks region

The table shows results for the binned Rayleigh power (equation 6.22) for each region of angle between tracks. The last region presents the smaller number of events. There is a possible trend in which the seasonality of the effect decreases for higher angular separations.

Region	Constant (%)	Amplitude (%)	Frequency (month ⁻¹)	Phase (rad)
α	0.0 ± 0.1	4.5 ± 0.1	0.53 ± 0.01	-0.7 ± 0.1
β	-0.1 ± 0.1	4.3 ± 0.1	0.54 ± 0.01	-0.8 ± 0.1
γ	-0.3 ± 0.1	4.4 ± 0.1	0.57 ± 0.01	-1.0 ± 0.1
δ	0.0 ± 0.1	4.4 ± 0.1	0.52 ± 0.01	-0.7 ± 0.1
ϵ	-0.4 ± 0.1	4.3 ± 0.1	0.57 ± 0.01	-1.0 ± 0.1
ζ	-0.2 ± 0.1	4.2 ± 0.1	0.55 ± 0.01	-0.9 ± 0.1
η	-0.4 ± 0.1	4.5 ± 0.1	0.58 ± 0.01	-1.1 ± 0.1
θ	-0.4 ± 0.1	4.5 ± 0.1	0.57 ± 0.01	-1.1 ± 0.1
ι	-0.5 ± 0.1	3.6 ± 0.1	0.62 ± 0.02	-1.4 ± 0.1

Table 7.9 | Best fit values for each region of angular separation

The table shows the best fitted values from equation 7.3 for each region of angular separation. The last region has a smaller amplitude with respect to the other regions.

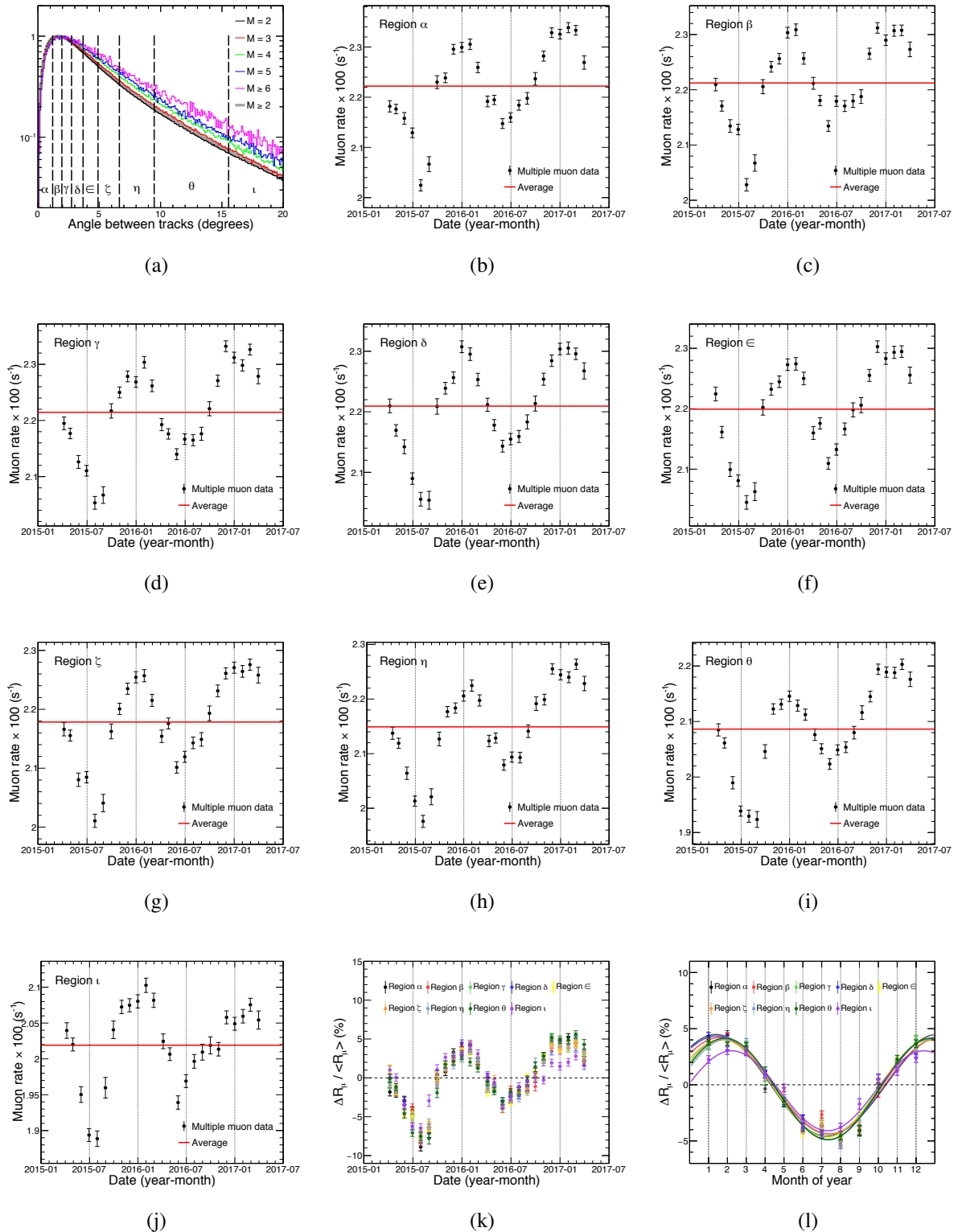


Figure 7.12 | Multiple-muon seasonal variations for different regions of angular separation

(a) Angle between each pair of multiple-muon tracks of every event, separated by different multiplicities. The distributions are normalized and divided into 9 regions of roughly equal statistics (namely, regions $\alpha, \beta, \gamma, \delta, \epsilon, \zeta, \eta, \theta,$ and ι), whose limits are specified by the vertical dashed lines and defined in table 7.8. Figures (b) through (j) show the multiple-muon seasonal variations for each angle between tracks region, along with each average muon rate (solid red line). (k) $\Delta R_{\mu} / \langle R_{\mu} \rangle$ for each region, showing little difference between each signal. Figure (l) folds (k) into month of year bins and fits the data accordingly. The error bars represent the statistical uncertainties.

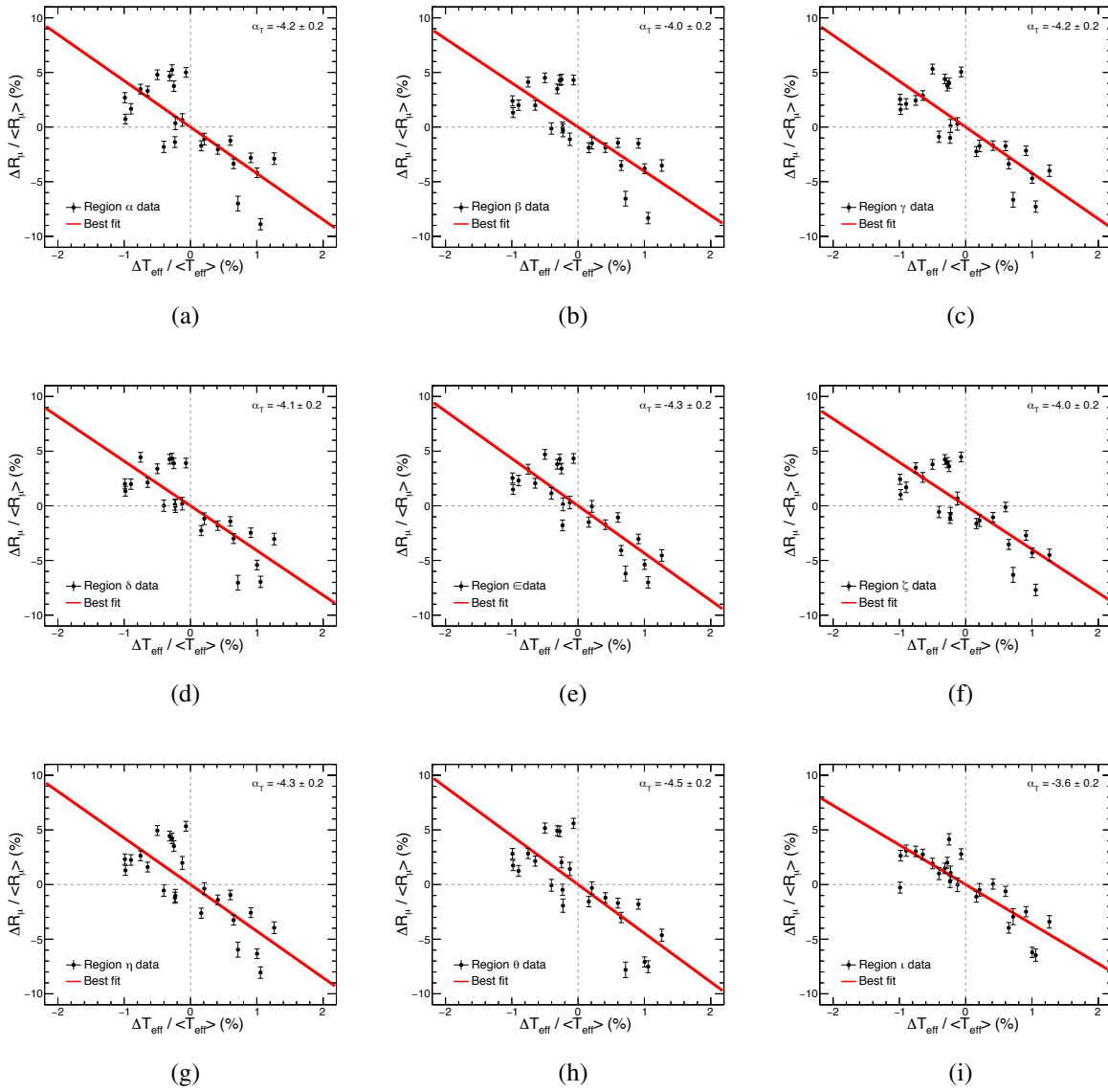


Figure 7.13 | Calculated α_T for each region of angular separation

Figure shows the fitted α_T value for each region of angular separation, which is achieved by combining figures 7.12 (k) and 7.4 (d). The α_T values found for each region are summarized in table 7.10.

Angular separation region				
Fitted α_T				
α	β	γ	δ	ϵ
-4.2 ± 0.2	-4.0 ± 0.2	-4.2 ± 0.2	-4.1 ± 0.2	-4.3 ± 0.2
ζ	η	θ	ι	
-4.0 ± 0.2	-4.3 ± 0.2	-4.5 ± 0.2	-3.6 ± 0.2	

Table 7.10 | Multiple-muon α_T values according to different regions of angular separation
The table shows resulting fitted temperature correlation coefficients for each region of angular separation.

7.3.4 By multiplicity

As described in Section 3.4.2, there is a possible anticorrelation between secondary and further hadron decays and the effective temperature of the atmosphere. Similarly to the previous sections, the multiplicity of a measured multiple-muon event at the detector depth is another variable that is related to the energy of the primary particle. As such, measuring effects versus multiplicity could be related to changes with increasing primary energy.

The vast majority of events recorded have $M = 2$, as can be seen in figure 7.11 and table 7.14.

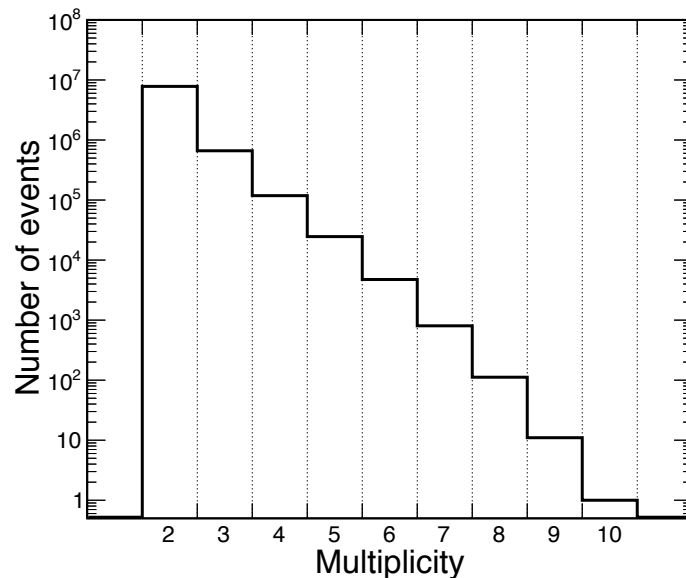


Figure 7.14 | Number of events as a function of multiplicity

Figure shows the number of events for each multiplicity, with the highest multiplicity being one event with $M = 10$.

The highest reconstructed multiplicity in the 2 years of detector exposure is a single event with $M = 10$ (showed in figure 7.15). In this scenario, the multiplicities were chosen to be sepa-

Multiplicity	Number of events (fraction)
≥ 2	8,628,936 (1.0000)
2	7,818,369 (0.9061)
3	661,884 (0.0767)
4	118,389 (0.0137)
5	24,617 (0.0028)
6	4,749 (0.0005)
7	804 (0.0001)
8	112 (10^{-5})
9	11 (10^{-6})
10	1 (10^{-7})

Table 7.11 | Total number of events according to multiplicity

The table shows the total number of multiple-muon events ($M \geq 2$), along with the number of events and fraction for each multiplicity, which reaches a maximum of $M = 10$.

rated until $M = 5$, while, for statistical reasons, the rest of the data is gathered and presented as $M \geq 6$. Since the absolute rate of each multiplicity is a less useful form of comparison, the data is presented as $\Delta R_\mu / \langle R_\mu \rangle$, which is the percent variation with respect to the global average rate. Also, to avoid data point cluttering and to smooth out yearly differences for a better fit, the comparison of the seasonal variations for different multiplicities is presented in month of year bins, as seen in figure 7.16 (a). Said figure includes the best fit for each multiplicity, which was carried forward using the function defined in equation 7.3. The findings show that as the multiplicity increases the seasonal variation effect becomes more prominent, as there is a clear trend in the resulting fitted amplitudes seen in table 7.12, which gathers the extracted values from the best fit for each multiplicity. The increase in the fitted amplitude values is also presented in figure 7.16 (b), that shows the fitted amplitude value as a function of multiplicity.

Multiplicity	Constant (%)	Amplitude (%)	Frequency (month ⁻¹)	Phase (rad)
2	-0.20 ± 0.05	3.75 ± 0.05	0.567 ± 0.006	-0.91 ± 0.04
3	-0.3 ± 0.2	5.4 ± 0.2	0.56 ± 0.01	-1.0 ± 0.1
4	-0.6 ± 0.4	7.2 ± 0.4	0.59 ± 0.02	-1.2 ± 0.2
5	-0.9 ± 0.7	10.7 ± 0.9	0.59 ± 0.03	-1.5 ± 0.2
≥ 6	-2 ± 1	14 ± 2	0.64 ± 0.04	-1.5 ± 0.3

Table 7.12 | Best fit values for each multiplicity

The table shows the best fitted values from figure 7.16 (a) using the fitting function defined in equation 7.3 for each multiplicity. The amplitude of the modulation signal increases with multiplicity.

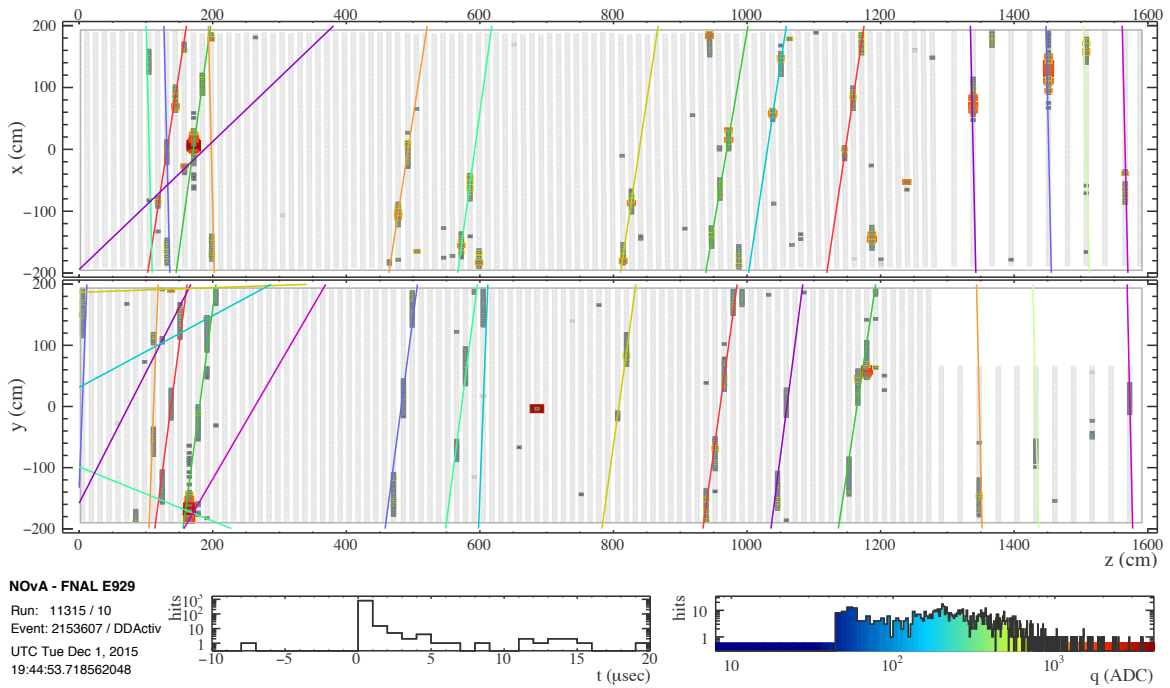


Figure 7.15 | The multiple-muon event with the highest reconstructed multiplicity
 Figure shows the event with the highest reconstructed multiplicity, which reached a total of 10 reconstructed 3D tracks, along with all Multi-Hough 2D lines found by the Multi-Hough Transform.

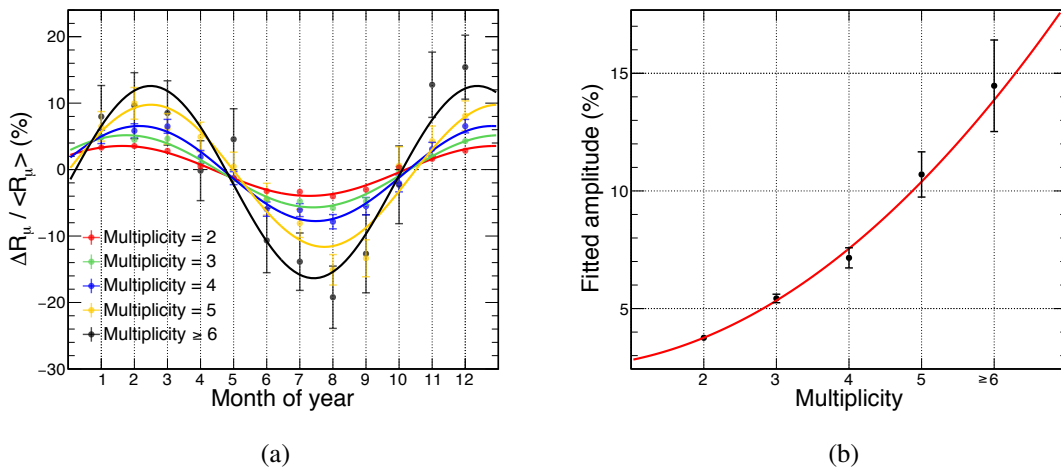


Figure 7.16 | Multiple-muon seasonal variations for different multiplicities
 (a) Percent variation with respect to the average rate of the multiple-muon seasonal modulation broken down by different multiplicities, along with their respective cosine fits. For statistical reasons, all events above $M = 5$ are gathered and presented as $M \geq 6$. The error bars represent the statistical uncertainties. (b) Fitted amplitudes according to each multiplicity, showing that the multiple-muon seasonal modulation effect is more sensitive to atmospheric temperature variations for events with higher multiplicities, which is an approximation for higher energy primaries. The error bars represent the resulting uncertainties from the fitted amplitudes.

Chapter 8

Conclusions

The dynamics of extensive air showers is intrinsically connected to the conditions of the atmosphere, which is subject to a yearly seasonal temperature pattern. As such, the effect that atmospheric temperature variations produce in the observed single muon flux at a given underground depth is explained and quantified using a model that considers only the decay of secondary charged pions and kaons into muons and neutrinos. Said model predicts the variation in the muon flux given a change in the effective temperature of the atmosphere. The limitation of the model is mainly rooted in the premise that the flux is originated solely by the decay of secondary mesons. This model that is well suited for single muons, since the muon energy distribution is rapidly falling as a function of $E^{-\gamma}$, but it has less physical meaning for multiple-muon results.

The multiple-muon experimental results presented by MINOS [55] showed an inversion of the modulation phase with respect to the effective temperature seasonality which has not been predicted. In the ND the phase was unambiguously inverted, while the FD presented a dependency with the track separation, with tracks with smaller separations showing an inverted phase and large separation showing a similar phase as to the temperature modulation. The not fully understood multiple-muon results were compared to 4 hypotheses, in which one is the most likely explanation for the phase inversion. Said hypothesis considers that the anticorrelation between temperature and muon flux arises from the higher probability of secondary mesons to interact in the atmosphere during winter time, producing more mesons further down in the atmosphere and increasing the overall muon count underground. Given that further interactions imply in a smaller fraction of the primary energy being passed on to further hadrons, only higher energetic primaries are likely to produce observable multiple-muon showers underground.

In order to measure the anomalous effect on NO ν A, two years of Near Detector exposure are used as the dataset of the analysis, ranging from April 8th, 2015, to April 16th, 2017. The analysis provided the following conclusions:

- The multiple-muon rate measured by the NO ν A ND is unambiguously inverted with respect to the effective temperature seasonal variation phase, in agreement with the results

previously reported by the nearby MINOS ND.

- The multiple-muon phase does not have a dependency on track separation, recovering the same conclusion presented by the MINOS ND. Given the similar size of both detectors, the results are in agreement.
- A set of new results with the intent to search for new trends in the multiple-muon modulation phase according to different variables was presented. Different regions of zenith angle, angle between tracks, and multiplicity were explored, and showed the following:
 - There is no phase dependency as a function of zenith angle.
 - There may or may not be a dependency with the angle separation.
 - There is a strong correlation with multiplicity, in which the seasonal effect is more prominent as the event multiplicity increases.

The results presented by the MINOS Far Detector showed an inversion in the modulation phase between short and large track separations. As higher separations imply in higher p_T , and as a result, lower muon energy, it is possible to pinpoint the region where the phase flips. The lack of inversion in the NO ν A Near Detector means that a larger detector, to encompass larger track separations, could have verified that.

The zenith angle results have no correlation with the size of the detector. As such, the fact that the zenith angle shows no change in the seasonal effect is a strong indication that the longer path traveled by higher zenith angle particles has little to no effect in the modulation phase itself.

The higher $\Delta R_\mu / \langle R_\mu \rangle$ found for higher multiplicities indicates an anticorrelation between secondary and further hadronic decays, as outlined in subsection 3.4.2. During summer, as most hadrons decay, there is the need for cosmic ray events with a certain energy to produce enough secondary mesons that will yield a said multiplicity underground. Alternatively, during winter, the copious production of particles at further hadronic interactions imply that less energetic primaries will be able to reach the same said multiplicity. As the flux of primaries decrease with energy according to a power law, the rate of events that produce such multiplicity during winter is higher than during summer. The more prominent effect for higher multiplicities is an indication that there is an increase in the energy gap between the energy of primaries that produce a said multiplicity during summer and the energy of primaries that produce the same multiplicity during winter.

The seasonal effect observed by the NO ν A Near Detector is unambiguously inverted for any multiplicity above 1. As such, in order to verify any changes in the trend within different multiplicities, a detector located at a shallower depth, with a smaller $\langle E_{\text{th}} \cos \theta \rangle$, may be necessary.

The NO ν A Far Detector, due to being located at surface level, has too much contamination of low energy muons¹, being unlikely for a single muon analysis to be done, as it would yield an $\alpha_T \approx 0$. Alternatively, its top surface area is ~ 15 times larger when compared to the Near Detector², being able to explore much larger track separations and much higher multiplicities. In this scenario, the NO ν A Far Detector opens the possibility for pinpointing the multiplicity in which modulation phase inverts and provides a mean to estimate at which primary energy range it should happen by confronting the experimental result with cosmic ray Monte Carlo simulations.

¹The average muon rate at the FD is about $155 \times 10^3 \text{ s}^{-1}$.

²The exact numbers are $A_{\text{ND}}^{\text{top}} = 62.4 \text{ m}^2$ for the ND, and $A_{\text{FD}}^{\text{top}} = 909.8 \text{ m}^2$ for the FD, resulting in $A_{\text{FD}}^{\text{top}}/A_{\text{ND}}^{\text{top}} = 14.58$.

Appendix

List of acronyms and abbreviations

AMANDA	Antarctic Muon and Neutrino Detector Array experiment.
APD	Avalanche Photodiode.
CDF	Collider Detector at Fermilab.
CKM	Cabibbo-Kobaiashi-Maskawa matrix.
CORSIKA	Cosmic Ray Simulation for KASCADE.
CP	Charge and Parity symmetry. The violating phase is usually denoted as δ_{CP} .
DAQ	Data Acquisition system. May also represent a type of detector data file.
DCM	Data Concentrator Module.
DDT	Data-Driven Trigger.
EAS	Extensive Air Shower(s).
ECMWF	European Center for Medium-range Weather Forecast.
FEB	Front-End Board.
FD	Far Detector.
GERDA	Germanium Detector Array experiment.
GPS	Global Position System.
GZK	Greisen-Zatsepin-Kuzmin suppression.

HiRes	High Resolution Fly's Eye experiment.
INFN	<i>Istituto Nazionale di Fisica Nucleare</i> (National Institute for Nuclear Physics).
Kamiokande	Kamioka Neutron Decay Experiment.
KASCADE	Karlsruhe Shower Core Array Detector experiment.
LINAC	Linear Accelerator.
LNGS	<i>Laboratori Nazionali del Gran Sasso</i> (Gran Sasso National Laboratories).
LVD	Large Volume Detector experiment.
MACRO	Monopole, Astrophysics, and Cosmic Ray Observatory experiment.
MC	Monte Carlo.
MI	Main Injector. One of the circular accelerators of Fermilab.
MINOS	Main Injector Neutrino Oscillation Search experiment.
MTDU	Master Time Distribution Unit.
ND	Near Detector.
NOνA	NuMI Off-axis ν_e Appearance experiment.
NuMI	Neutrinos at the Main Injector.
PMNS	Pontecorvo-Maki-Nakagawa-Sakata matrix.
PVC	Polyvinyl Chloride.
RFQ	Radio Frequency Quadrupole.
SNEWS	SuperNova Early Warning System.
SSW	Sudden Stratospheric Warming effect.
STDU	Slave Time Distribution Unit.
TEC	Thermoelectric Cooler.
TDU	Time Distribution Unit.
WLS	Wavelength-Shifting fiber.

Bibliography

- [1] Carlson, P. and De Angelis, A. **Nationalism and internationalism in science: the case of the discovery of cosmic rays**. arXiv: 1012.5068v2. 2011.
- [2] Rossi, B. **Cosmic Rays**. McGraw-Hill, New York. 1964.
- [3] Patrignani, C. *et al.* **Particle Data Group**. Chin. Phys. C **40**, 100001. 2016.
- [4] Gaisser, T. K. **The cosmic-ray spectrum: from the knee to the ankle**. Journal of Physics: Conference Series **47**, p. 15. 2006.
- [5] Naganot, M. *et al.* **Energy spectrum of primary cosmic rays above 10^{17} eV determined from extensive air shower experiments at Akeno**. J. Phys. G: Nucl. Part. Phys. **18**, 423. 1992.
- [6] Mostafa, M. **Ultra High Energy Cosmic Rays**. XXXI Physics in Collision, Vancouver, Canada. 2011.
- [7] Zatsepin, G. T.; Kuz'min, V. A. **Upper limit of the spectrum of cosmic rays**. J. Exp. Theor. Phys. Lett. **4**, p. 78. 1966.
- [8] Abbasi, R. U. *et al.* **First Observation of the Greisen-Zatsepin-Kuzmin Suppression**. Phys. Rev. Lett. **100**, 101101. 2008.
- [9] Abraham, J. *et al.* **Observation of the suppression of the flux of cosmic rays above 4×10^{19} eV**. Phys. Rev. Lett. **101**, 061101. 2008.
- [10] Fermi, E. **On the Origin of the Cosmic Radiation**. Phys. Rev. Lett. **75**, 1169. 1949.
- [11] Baring, M. G. **Diffusive shock acceleration: the Fermi Mechanism**. Proceedings of the 32nd Rencontres de Moriond: High-Energy Phenomena in Astrophysics, Les Arcs, France. 1997.; ArXiv: 9711177.
- [12] Grashorn, E. W. **Astroparticle Physics in the MINOS Far Detector**. Ph.D. Thesis. University of Minnesota, USA. 2008.

- [13] Auger, P., *et al.* **Extensive Cosmic Ray Showers**. Rev. Mod. Phys. **11**, 288. 1939.
- [14] Kampert, K. H. Watson, A. A. **Extensive Air Showers and Ultra High-Energy Cosmic Rays: A Historical Review** EPJ H **37**, p. 359. 2012.
- [15] Cazon, L. **Extensive Air Showers: from the muonic smoking guns to the hadronic backbone**. International Symposium on Very High Energy Cosmic Ray Interactions. arXiv:1301.3340. 2012.
- [16] Heitler, W. **The Quantum Theory of Radiation**. Oxford University Press, London. 1954.
- [17] Matthews, J. **A Heitler model of extensive air showers**. Astropart. Phys. **22**, p. 387. 2005.
- [18] Shukla, P. **Energy and angular distributions of atmospheric muons at the Earth**. arXiv:1606.06907. 2016.
- [19] Reichembacher, J. Goodman, M. **Differences in dE/dX for μ^+ and μ^- and its Effect on the Underground Charge Ratio**. Proceedings of the 30th International Cosmic Ray Conference, vol. **5**, p. 1229. Mexico City, Mexico. 2008.
- [20] Barry, R. G. and Chorley, R. J. **Atmosphere, Weather and Climate**. 8th ed. Routledge. Taylor and Francis Group. ISBN 0-203-42823-4. 2004.
- [21] Andrew, D. G. **An Introduction to Atmospheric Physics**. 2nd ed. Cambridge University Press. ISBN 978-0-521-87220-1. 2010.
- [22] Trenberth, K. E. and Smith, L. **The Mass of the Atmosphere: A Constraint on Global Analyses**. Journal of Climate **18**, p. 864. 2005.
- [23] Gaisser, T. K. **Cosmic Rays and Particle Physics**. Cambridge University Press. ISBN 0-521-32667-2. 1990.
- [24] Grashorn, E. W. **Astroparticle Physics in the MINOS Far Detector**. Ph.D. Thesis. University of Minnesota. 2008.
- [25] Duperier, A. **The Meson Intensity at the Surface of the Earth and the Temperature at the Production Level**. Proc. Phys. Soc. A **62**, 684. 1949.
- [26] Barrett, P. *et al.* **Interpretation of Cosmic-Ray Measurements Far Underground**. Rev. Mod. Phys. **24**, 133. 1952.
- [27] Sherman, N. **Atmospheric Temperature Effect for μ Mesons Observed at a Depth of 846 m.w.e.** Phys. Rev. **93**, 208. 1954.
- [28] Barrett, P. *et al.* **Atmospheric Temperature Effect for Mesons Far Underground**. Phys. Rev. **95**, 1573. 1954.

-
- [29] Fenton, A. G. *et al.* **Cosmic Ray Observations at ~ 2 m.w.e. Underground at Hobart, Tasmania.** *Il Nuovo Cim. B* **22**, 285. 1961.
- [30] Castagnoli, G. C. and Dodero, M.A. **Temperature Effect of the Muon Component Underground and Pion Attenuation Length.** *Il Nuovo Cim. B* **51**, 525. 1967.
- [31] Humble, J. E. *et al.* **Variations in atmospheric coefficients for underground cosmic-ray detectors.** Proceedings of the 16th International Cosmic Ray Conference, Vol. **4**, p. 258. Kyoto, Japan. 1979.
- [32] Cutler, D. J. *et al.* **Meteorological effects in cosmic ray muon production.** Proceedings of the 17th International Cosmic Ray Conference, vol. **4**, p. 290. 1981.
- [33] Yasue, S. *et al.* **Observation of cosmic ray intensity variation with Matsushiro underground telescope.** Proceedings of the 17th International Cosmic Ray Conference, vol. **4**, p. 290. 1981.
- [34] Sagisaka, S. **Atmospheric Effects on Cosmic-Ray Muon Intensities at Deep Underground Depths.** *Il Nuovo Cim. C* **9**, p. 809. 1986.
- [35] Andreyev, Yu. M. *et al.* **Season and daily variations of the intensity of muons with $E_\mu \geq 220$ GeV.** Proceedings of the 21st International Cosmic Ray Conference, vol. **7**, p. 88. Adelaide, Australia. 1990.
- [36] Munakata, K. *et al.* (Matsushiro and Kamiokande II Collaborations) **Time Variation of the Cosmic Ray Muon Flux in Underground Detectors and Correlation with Atmospheric Temperature.** *J. Phys. Soc. Jpn.* **60**, 2808. 1991.
- [37] Munakata, K. *et al.* (Matsushiro and Kamiokande II Collaborations) **Time Variation of the Cosmic Ray Muon Flux in Underground Detectors.** Proceedings of the 22nd International Cosmic Ray Conference, vol. **3**, p. 671. Dublin, Ireland. 1991.
- [38] Ambrosio, M. *et al.* (MACRO Collaboration) **Seasonal variations in the underground muon intensity as seen by MACRO.** *Astropar. Phys.* **7**, 109. 1997.
- [39] Bouchta, A. *et al.* (AMANDA Collaboration) **Seasonal variation of the muon flux seen by AMANDA.** Proceedings of the 26th International Cosmic Ray Conference, vol. **2**, p. 108. Salt Lake City, USA. 1999.
- [40] Goodman, M. C. *et al.* (Soudan 2 Collaboration) **Seasonal Variations in Soudan 2.** Proceedings of the 26th International Cosmic Ray Conference, vol. **2**, p. 324. Salt Lake City, USA. 1999.

- [41] Selvi, M. *et al.* (LVD Collaboration) **Analysis of the seasonal modulation of the cosmic muon flux in the LVD detector during 2001-2008**. Proceedings of the 31st International Cosmic Ray Conference. Łódź, Poland. 2009.
- [42] Tilav, S. *et al.* (IceCube Collaboration) **Atmospheric Variations as observed by IceCube**. Proceedings of the 31st International Cosmic Ray Conference. Łódź, Poland. 2009.
- [43] Osprey, S. *et al.* **Sudden stratospheric warmings seen in MINOS deep underground muon data**. *Geophys. Res. Lett.* **36**, L05809. 2009.
- [44] Adamson, P. *et al.* **Observation of muon intensity variations by season with the MINOS Far Detector**. *Phys. Rev. D* **81**, 012001. 2010.
- [45] Grashorn, E. W. *et al.* **The Atmospheric charged kaon/pion ratio using seasonal variation methods**. *Astropart. Phys.* **33**, 140. 2010.
- [46] D'Angelo, D. *et al.* (Borexino Collaboration) **Seasonal modulation in the Borexino cosmic muon signal**. Proceedings of the 32nd International Cosmic Ray Conference, vol. **2**, p. 26. Beijing, China. 2011.
- [47] Desiati, P. *et al.* (IceCute Collaboration) **Seasonal Variations of High Energy Cosmic Ray Muons Observed by the IceCube Observatory as a Probe of Kaon/Pion Ratio**. Proceedings of the 32nd International Cosmic Ray Conference, vol. **1**, p. 78. Beijing, China. 2011.
- [48] Bellini, G. *et al.* (Borexino Collaboration) **Cosmic-muon flux and annual modulation in Borexino at 3800 m water-equivalent depth**. *JCAP* 1205 (2012) 015. 2012.
- [49] Adamson, P. *et al.* (MINOS Collaboration) **Observation of muon intensity variations by season with the MINOS near detector**. *Phys. Rev. D* **90**, 012010. 2014.
- [50] Agostini, M. *et al.* (GERDA Collaboration) **Flux modulations seen by the muon veto of the Gerda experiment**. *Astropart. Phys.* **84**, 29. 2016.
- [51] Malgin, A. S. **Seasonal Modulations of the Underground Cosmic Ray Muon Energy**. *J. Exp. Theor. Phys.* (2015) 121: 212. 2016.
- [52] Abrahão, T. (Double Chooz Collaboration) **Cosmic-muon characterization and annual modulation measurement with Double Chooz detectors**. *JCAP* 1702 (2017) n. 02, 017. 2017.
- [53] An, F. P. (Daya Bay Collaboration) **Seasonal Variation of the Underground Cosmic Muon Flux Observed at Daya Bay**. Submitted to *JCAP*. arXiv: 1708.01265. 2017.

-
- [54] De Ridder, S. *et al.* (IceCube Collaboration) **Seasonal variation of the muon multiplicity in cosmic rays at South Pole**. Proceedings of the 33rd International Cosmic Ray Conference. Rio de Janeiro, Brazil. 2013.
- [55] Adamson, P. *et al.* (MINOS Collaboration) **Observation of seasonal variation of atmospheric multiple-muon events in the MINOS Near and Far Detectors**. Phys. Rev. D **91**, 112006. 2015.
- [56] Ronga, F. **Seasonal variations of the rate of multiple-muons in the Gran Sasso underground laboratory**. 6th Roma International Conference on Astroparticle Physics. EPJ Web Conf. **136**, 05004. 2017.
- [57] Bergeson, H. E. *et al.* **Operational Characteristics of the Utah Anisotropy Detector**. Proceedings of the 15th International Cosmic Ray Conference, vol **2**, p. 176. Plovdiv, Bulgaria. 1977.
- [58] Heck, D. Knapp, J. Capdevielle, J. N. Schatz, G. Thouw T. **CORSIKA: A Monte Carlo Code to Simulate Extensive Air Showers**. Forschungszentrum Karlsruhe Report FZKA **6019**. 1998.
- [59] The NO ν A Collaboration. **Proposal to Build a 30 Kiloton Off-Axis Detector to Study $\nu_{\mu} \rightarrow \nu_e$ Oscillations in the NuMI Beamline: NO ν A – NuMI Off-Axis ν_e Appearance Experiment**. 2005. Available at <http://nova-docdb.fnal.gov/cgi-bin/ShowDocument?docid=593>.
- [60] Souter, L. (NO ν A Collaboration) **NuMI off-axis electron neutrino appearance**. Talk presented at the 48th Annual Fermilab Users Meeting. 2015. Available at <http://nova-docdb.fnal.gov/cgi-bin/ShowDocument?docid=13469>
- [61] Giunti, C. and Kim, C. K. **Fundamentals of Neutrino Physics and Astrophysics**. Oxford University Press. 2007.
- [62] Adamson, P. *et al.* (MINOS Collaboration) **The NuMI neutrino beam**. Nucl. Instr. Meth. A **806**, 279-306. 2016.
- [63] Livingston, M. S. **Analysis of Charge-Exchange Injection for NAL**. Fermilab Report No. FN-194. 1969.
- [64] Gomes, R. A. **Uma Investigação Sobre o Decaimento $\Xi^0 \rightarrow \Sigma^+ \mu^- \bar{\nu}_{\mu}$ e a sua Observação**. Ph.D. Thesis, State University of Campinas, São Paulo, Brazil. 2005.
- [65] Rauffer, T. M. **A Study of Neutrino Oscillations in MINOS**. Ph.D. Thesis, University College, Oxford. 2007.

- [66] Flumerfelt, E. **DAQ Software Contributions, Absolute Scale Energy Calibration and Background Evaluation for the NO ν A Experiment at Fermilab**. Ph.D. Thesis, The University of Tennessee, Knoxville. 2015.
- [67] Sachdev, K. **Muon Neutrino to Electron Neutrino Oscillation in NO ν A**. Ph.D. Thesis, University of Minnesota. 2015.
- [68] Niner, E. **Observation of electron neutrino appearance in the NuMI beam with the NO ν A Experiment**. Ph.D. Thesis, Indiana University. 2015.
- [69] Xin, T. **Observing muon neutrino to electron neutrino oscillations in the NO ν A Experiment**. Ph.D. Thesis, Iowa State University. 2016.
- [70] Bays, K. (NO ν A Collaboration) **Status of the NO ν A Experiment**. Talk presented at the Lake Louise Winter Institute, Alberta, Canada. 2015. Available at <http://nova-docdb.fnal.gov/cgi-bin/ShowDocument?docid=10770>
- [71] Sepulveda-Quiroz, J. (NO ν A Collaboration) **The NO ν A Near Detector: An Overview**. Talk presented at the APS April Meeting. 2015. Available at <http://nova-docdb.fnal.gov/cgi-bin/ShowDocument?docid=13176>
- [72] Wang, Z. **Search for Magnetic Monopoles with the NO ν A Far Detector**. Ph.D. Thesis, University of Virginia. 2015.
- [73] Mufson, S. L. and Fox, W. R. (NO ν A Collaboration) **APD module drawings**. Internal report. DocDB-3012. 2010.
- [74] (NO ν A Collaboration) **The NO ν A Neutrino Experiment**. NO ν A brochure. 2015. Available at http://www-nova.fnal.gov/NOvA_FactSheet.pdf
- [75] Lein, S. M. **Muon Neutrino Contained Disappearance in NO ν A**. Ph.D. Thesis, University of Minnesota. 2015.
- [76] Kephart, K. (NO ν A Collaboration) **Near Detector Under Ground (NDUG) Parameters**. Internal report. DocDB-9860. 2014.
- [77] Oshinowo, B. **Fermilab Coordinate Systems**. Internal report. Beams-Doc-1148. 1997. Available at <http://ppd.fnal.gov/align/beams-doc-1148.html>
- [78] Baird, M. D. **An analysis of muon neutrino disappearance from the NuMI beam using an optimal track fitter**. Ph.D. Thesis, Indiana University. 2015.
- [79] Dixon, S. (NO ν A Collaboration) **WBS 2.1 Far Detector Building Drawings (15-1-3B)**. Internal report. DocDB-1128. 2012.

-
- [80] Bu, X. (NO ν A Collaboration) **The NO ν A Experiment**. Public presentation. 2013. Available at <http://nova-docdb.fnal.gov/cgi-bin/ShowDocument?docid=10407>
- [81] Dixon, S. (NO ν A Collaboration) **Far Detector Assembly Progress Graphic**. Internal report. DocDB-8698. 2014.
- [82] Frank, M. (NO ν A Collaboration) **Trigger Rate Review**. Internal report. DocDB-11004. 2014.
- [83] Davies, G. *et al.* (NO ν A Collaboration) **Data Driven Trigger**. Internal report. DocDB-10514. 2014.
- [84] Norman, A. *et al.* (NO ν A Collaboration) **NO ν A DAQ Data Formats**. Internal report. DocDB-4390. 2015.
- [85] Zamorano, B. (NO ν A Collaboration) **Continuity in Activity trigger**. Internal report. DocDB-12382. 2014.
- [86] Zamorano, B. (NO ν A Collaboration) **Revisiting the parameters of the Activity trigger**. Internal report. DocDB-13132. 2015.
- [87] Hough, P. V. C. **Methods and means for recognizing complex patterns**. U.S. Patent 3,069,654. 1962.
- [88] Ballard, D. H. **Generalizing the Hough Transform to Detect Arbitrary Shapes**. Pattern Recognition **13**, N. 2, 111. 1981.
- [89] Fernandes, L. A. F. and Oliveira, M. M. **Real-time line detection through an improved Hough transform voting scheme**. Pattern Recognition **41**, 299. 2008.
- [90] Baird, M. (NO ν A Collaboration) **Global Vertex Reconstruction beginning with a Modified Hough Transform**. Internal report. DocDB-8241. 2012.
- [91] Haggmann, C. Lange, D. and Wright, D. **Cosmic-ray shower generator (CRY) for Monte Carlo transport codes**. Nuclear Science Symposium Conference Records, vol 2 (IEEE), 1143-1146. 2007.
- [92] Dee, D. P. *et al.* **The ERA-Interim reanalysis: configuration and performance of the data assimilation system**. Q. J. R. Meteorol. Soc. **137**, Issue 656, Part-A, 553. 2011.
- [93] Mardia, K. V. **Statistics of directional data**. Academic Press Inc. (London) Ltd. ISBN 0-12-471150-2. 1972.
- [94] Lewis, D. A. **Detection of weak signals in TeV gamma-ray astronomy: dc excess vs. periodic amplitude**. Astron. Astrophys. **219**, 352. 1989.

- [95] Lomb, N. R. **Least-squares frequency analysis of unequally spaced data**. *Astrophysics and Space Science* **39**, 447. 1976.
- [96] Scargle, J. D. **Statistical aspects of spectral analysis of unevenly spaced data**. *Astrophys. J.* **263**, 835. 1982.
- [97] VanderPlas, J. T. **Understanding the Lomb-Scargle Periodogram**. arXiv: 1703.09824. 2017.